DYNAMICS OF EXCITED STATES AND TRANSIENT SPECIES IN SELF ASSEMBLED MEDIA

By

BISWAJIT MANNA

CHEM01201404003

Bhabha Atomic Research Centre, Mumbai

A thesis submitted to the

Board of Studies in Chemical Sciences

In partial fulfillment of requirements

for the Degree of

DOCTOR OF PHILOSOPHY

of

HOMI BHABHA NATIONAL INSTITUTE

June 2017

Homi Bhabha National Institute

Recommendations of the Viva Voce Committee

As members of the Viva Voce Committee, we certify that we have read the dissertation prepared by Biswajit Manna entitled "Dynamics of Excited States and Transient Species in Self Assembled Media" and recommend that it may be accepted as fulfilling the thesis requirement for the award of Degree of Doctor of Philosophy.

Chairman - P. D. Naik — **Date:** 11/9/17

Guide / Convener – D. K. Palit — **Date:** 11/09/2017

Examiner - Prof. A. Samanta — **Date:** 11.9.2017

Member 1- H. Pal — **Date:**

Member 2- S. K. Nayak — **Date:** 11/9/2017

Member 3- P. A. Hassan — **Date:** 11-09-2017

I/We hereby certify that I/we have read this thesis prepared under my/our direction and recommend that it may be accepted as fulfilling the thesis requirement.

Date:

Place: Mumbai

11/09/2017

Dr. Dipak Kumar Palit

Guide

Though I could not present personally in the PhD. viva-voce examination, however, based on my experiences in the previous review meetings till the synopsis presentation, I have full consent on the conduction of the viva-voce presentation and decision of the PhD Review committee.

13/9/17
(H. PAL)

STATEMENT BY AUTHOR

This dissertation has been submitted in partial fulfillment of requirements for an advanced degree at Homi Bhabha National Institute (HBNI) and is deposited in the Library to be made available to borrowers under rules of the HBNI.

Brief quotations from this dissertation are allowable without special permission, provided that accurate acknowledgement of source is made. Requests for permission for extended quotation from or reproduction of this manuscript in whole or in part may be granted by the Competent Authority of HBNI when in his or her judgment the proposed use of the material is in the interests of scholarship. In all other instances, however, permission must be obtained from the author.

Biswajit Manna

Biswajit Manna

DECLARATION

I, hereby declare that the investigation presented in the thesis has been carried out by me. The work is original and has not been submitted earlier as a whole or in part for a degree/diploma at this or any other Institution / University.

Biswajit Manna

Biswajit Manna

List of Publications Arising from the Thesis

Journal

1. In Stationary Regime, Electron Transfer Rates in RTIL Media are Diffusion Controlled: Experimental Evidence from Pulse Radiolysis Study; B. Manna, R.Ghosh and D. K. Palit; Journal of Physical Chemistry B, 117(2013), 5113-5120.
2. Exciton dynamics in anthraces nenanoaggregates; B. Manna, R. Ghosh and D. K. Palit; J. Phys. Chem. C, 119(2015), 10641-10652.

3. Ultrafast Energy Transfer Process in Doped-Anthracene Nanoaggregates is Controlled by Exciton Diffusion: Multiple Doping Leads to Efficient White Light Emission; B. Manna, R. Ghosh and D. K. Palit; J. Phys. Chem. C, 120(2016), 7299-7312.

Symposia/Conference

1. Exciton Dynamics of Anthracene Nanoaggregates:Synthesis, Charecterization and Photophysics; B. Manna, R. Ghosh and D. K. Palit; NLS-21(2013), CP-05-13, 64
2. Study of Exciton Dynamics in Perylene Nanoparrticles, produced by a Facile Solvochemical Method; B. Manna, R. Ghosh and D. K. Palit; NSRP(2013), PC-7
3. Exciton Diffusion Assisted FRET Study in Doped Anthracene Nanoaggregates; B. Manna, R. Ghosh and D. K. Palit; TSRP, PC-96 (2014), 237-238.
4. Study of exciton-exciton annihilation process and estimation of exciton diffusion parameters in anthracene and perylene nanoaggregates; B. Manna, R. Ghosh and D. K. Palit ; UFS-2014, PC-2, Manipal Univesity
5. Exciton Dynamics in Phthalocyanine Nanoaggregates. S. Kakde, B. Manna, R. Ghosh, D. K. Palit. The International Conference on Fiber Optics and Photonics, OSA, 2016.

Publication from Other Topics

1. Carrier recombination dynamics through defect states of ZnO nanocrystals: From nanoparticles to nanorods; A. Layek, B. Manna, A. Chowdhury; Chemical Physics Letters, 539–540 (2012), 133–138

2. Synthesis of Rare Earth Doped ZnONanorods and their Defect Dopant Correlated Enhanced Visible Orange Luminescence; A. Layek, S. Banarjee, B. Manna, A. Chowdhury; RSC Adv., 6(2016), 35892

DEDICATIONS

TO MY LOVING PARENTS

AND

RESPECTED TEACHERS

ACKNOWLEDGEMENTS

I would like to take this opportunity to thank everyone, who supported me throughout in my work for this thesis.

At first, I wish to begin by expressing my deepest and sincere gratitude to my guide, Dr. Dipak K. Palit for his aspiring guidance, constant encouragement, and motivation. His wide knowledge and logical way of thinking and reasoning on scientific problems greatly helped me during the work. His dedication towards scientific works always motivates me to put best efforts. I am thankful to him for sharing his knowledge and scientific understanding during the fruitful discussions with me throughout the work.

I am privileged to thank Dr. S. Nath, for his unstinted support and encouragement. Your advice and comments have been priceless and great value for me, which played a major role in shaping my thesis work.

I would like to express my sincere regards and deepest appreciation to Dr. R. Ghosh. His invaluably constructive criticism and friendly suggestions on an academic and personal level has always been extremely helpful to me.

My special thanks go to my lab mates Amitabha Nandi, Snehal Kakade and Araynak sarkar for their cooperative attitude, diversified help, and several funs which I will always cherish in my life.

I am grateful to Dr. M. Kumbhakar, Dr. S. Adhikari, Dr. J. A. Mondal, Dr. Prbhat K. Singh and A. Mora for their moral support, stimulating discussions and constructive criticisms, which have substantially helped me in my research work.

I also gratefully acknowledge the cooperative attitude and support provided by all the members of RPCD. Their spirited research oriented approach has always been a source of inspiration and morale booster.

I thank all my friends and batch mates in BARC for their support and the wonderful moments we spent together. I greatly value their friendship and deeply appreciate their belief in me.

I would like to take this opportunity to thank LINAC staff (Shri S. A. Nadkarni, Smt. M. A. Toley, Shri S. J. Shinde, Shri B. B. Chaudhari) of RPCD, whose has immensely helped me in carrying out the pulse radiolysis experiments. I am also thankful to Dr. R. Ganguly, Dr. V. sudarshan and B. G. Vats for their kind help in DLS, AFM and XRD measurements, respectively.

It gives me immense pleasure to thank the respected and distinguished members of the doctoral committee, Dr. B. N. Jagatap (Former Chairman), Dr. P. D. Naik (Chairman), Dr. H. Pal (Member), Dr. S. K. Nayak (Member), Dr. P. A. Hassan (Member) for their critical reviews and suggestions during the progress reviews and pre-synopsis presentation.

I cannot imagine my current position without the blessings of my teachers, and will always be indebted to them. Most importantly, I owe my heartfelt gratitude to my parents for their encouragement and love. Finally, I would like to express my endless thanks and appreciations to my wife, Mitali, for her support, encouragement and care.

June, 2017

Biswajit Manna, RPCD, BARC, Mumbai

CONTENTS

Page No.

Chapter 1: Introduction

Chapter 2: Experimental Techniques and Instrumentation

Chapter 3: Effect Of Microscopic Heterogeneity On The Electron Transfer And Triplet Energy Transfer Reactions Associated With Long Lived Transients

Chapter 4: Dynamics in Anthracene Nanoaggregates

Chapter 5: Diffusion Controlled Energy Transfer Process In Doped Anthracene Nanoaggregates: Multiple Doping Leads To Efficient White Light Emission

Chapter 6: Exciton Dynamics in Pyrene and Perylene Nanoaggregates

Chapter 7: Exciton Dynamics in Nanoaggregates of Phthalocyanines and their Zinc Derivatives

Chapter 8: Summary and Future Direction

SYNOPSIS

A molecule is subjected to different kinds of intermolecular forces when it is placed in a condensed medium. The nature and strength of intermolecular forces acting between the solute molecules themselves as well as between the solute and the solvent molecules are the deciding factors for its existence in the monomeric form or the self-assembled form of the solutes in this condensed medium. The organic molecules self-assembling to form aggregates in solution phase is considered as one of such self-assembled media. Here, the interaction force acting between the solute molecules is much stronger than the solute-solvent interaction forces leading tothe aggregation process energetically feasible. In some of the cases, a big solvent molecule itself, because of the presence of both ionic and nonionic parts in it, undergoes self-assembling. Such kinds of self-assembly creates microscopic pockets of two distinct polarities, one ionic and another non-ionic, inside a single medium. Solvent molecules of room temperature ionic liquids (RTILs) possess this characteristic and may be thought of self-assembling to create microscopic pockets of different polarities..[1-3]Although, RTILs are known to possess microheterogeneity, this kind of self-assembling has not yet been exclusively discussed.

These self-assembled media are well known since long back and have been shown to be very useful for applications in different fields of science and technology. In this thesis, we have made an attempt to explore the dynamics of the transient species generated in these self-assembled media following excitation by light or electron beam using time resolved absorption and emission techniques. These investigations lead to the basic understanding about nature of such media and it may be extended to the applicability of these media in different purposes.

Herein we have carried out our scientific investigations in two different kinds of self-assembled media. Firstly, we have explored the self-assembling behavior of RTIL media. RTILs are highly viscous liquids at ambient temperature. These liquids may have different combinations of counter ions and the properties can be tuned in desired manner. That is why these solvents are known as designer solvents. During the last two decades, RTILs have drawn a huge attention due to its environment friendliness and possibility of wide scale applications in multiple fields, e.g. organic synthesis, photovoltaic applications, separation sciences, nuclear reprocessing, etc.[4-12]

Huge research efforts have been invested in recent years to explore the microscopic nature of RTIL media. There are several groups, who have reported the presence of microscopic heterogeneity in these solvents. These solvents are probed through the study of some basic chemical processes, like hydrogen atom transfer, electron transfer(ET), energy transfer (ENT), solvation dynamics, etc.[13-28]Electron transfer processes in RTIL have been studied by several research groups . In most of the cases, it has been found that the electron transfer rate is faster by about almost one order than the diffusion controlled rate. The faster electron transfer rates observed in most of the cases, has been explained by the reactants movement through local low viscosity pockets. However, Maroncelli and coworkers as well as Vauthey and coworkers demonstrated that, the faster ET rates observed in RTIL media were really not associated with some special property of RTIL.[27,28] Instead, they showed that this feature might also be observed in the case of the conventional organic solvents having comparable viscosities. They propose that, in those cases, the ET process takes place in '*transient quenching regime,* as the transients used there has lifetime in ns regime. They also suggest that the diffusion controlled reaction can only observed at '*stationary quenching regime'*. In the case of highly viscous solvents, like RTIL, the stationary condition can be achieved only after a few hundreds of nanoseconds. Therefore, to measure the actual diffusion controlled rate, reactions involving long lived transient reactants, e.g. anion radicals or molecules in the excited triplet states, need to be investigated. Herein, we report electron transfer and triplet - triplet energy transfer studies to observe diffusion controlled processes involving long lived transient species, say, anion radicals and triplet states. We could probe the microscopic heterogeneity of the RTIL media and could estimate the microscopic viscosity of the nonionic pockets of the RTIL media.

The second part of this thesis is focused on the studies of exciton dynamics in various kinds of organic nanoaggregates. Organic molecules are known to form aggregates because of intermolecular interactions, such as van der Waals interaction, H-bonding interaction, π-π interaction, etc.[29-33]The excited state properties and dynamics of the molecules change significantly in the self-assembled form of moleculesas compared to those in the solution phase. Organic semiconductors in the form of film or aggregates are considered as potential materials for applications in photovoltaic devices (PV), organic light emitting diodes (LED), biological or chemical sensor, etc.[34-40] However, the efficient use of these materials in optoelectronic devices relies on the basic understanding of the excited processes. In this part of the thesis, we have focused on the synthesis of the organic nanoaggregates using facile solvent route and morphological as well as photophysical characterization of these materials.[41,42] We have employed time resolved absorption and fluorescence spectroscopic techniques to explore the exciton dynamics and estimate the exciton diffusion parameters.

Time resolved spectroscopic techniques have been extensively used to monitor the excited state dynamics in real time in order to understand the mechanisms of the excited state processes at the molecular level. In 1949, Norris and Porter invented the microsecond flash photolysis technique to detect and study the transient species in photochemical reactions for the first time. Time resolution of this technique further could be improved to nano, pico and femtosecond time scales because of invention of pulsed laser systems in the following years..[43,44] Prof. Ahmed Zewail revolutionized the field of chemical reaction dynamics by application of the femtosecond time resolved pump –probe technique to understand the microscopic dynamics of the bond-breaking process in simple molecules as well as many other kind of fundamental chemical processes. For his pioneering work in this field, he was honoured by the prestigious Nobel Prize in 1999. Now the spectroscopic studies can also be carried out down to the sub fs time resolution.

Time resolved spectroscopic techniques have been applied very effectively to study the dynamics of excitons and the excitonic processes following generation of excitonic states in crystals and nanoaggregates. The most important phenomenon, which occurs at high exciton density is the exciton - exciton annihilation process.[45, 47]This process is diffusion controlled and the annihilation rate is directly related to the exciton diffusion coefficient in the matrix. Therefore, it is possible to estimate the exciton diffusion parameters by studying the exciton–exciton annihilation process. In fact after photogeneration of excitons it should diffuse to the donor-acceptor interface where the charge separation takes place in a photovoltaic device. Therefore, long exciton lifetime and larger value of exciton diffusion coefficient may provide better charge separation yield. Efficient solar light absorption, long exciton lifetime and exciton diffusion lengths are some primary criteria for a good organic solar cell material. On the other hand, for LED device the material should possess long exciton lifetime, high emission yield and better color tunability. The second part of the thesis is dedicated to explore these aspects in some specific organic molecules.

For the convenience of presentation and discussion, the content of this thesis has been organized in eight chapters. Chapter 1 describes the introduction to the general aspects of self-assembled media, which are the main focus of this thesis. The motivation and objective of the present research work is also discussed here. The second Chapter discusses about the instrumentation and experimental techniques used for the research works presented in this thesis. The third Chapter is dedicated to the electron transfer and triplet- triplet energy transfer study in RTIL media. On the other hand, particular aspects of synthesis, characterization and relaxation dynamics of the photoexcited states in molecular nanoaggregate systems are presented in self contained manner from Chapter 4to Chapter 7. A concise description of the contents of the thesis is provided below.

Chapter 1

This chapter provides detailed discussion on the basic principles and concepts related to the present studies reported in this thesis. Relevance and motivation of the present research work have also been discussed in this chapter. Since the thesis deals mainly with the self-assembly of molecular systems, we have provided about a detailed account of various kinds of molecular self-assemblies and the driving force of formation of such assemblies. A brief introduction to the nature, importance, application of ionic liquids have been presented here. Since the major part of the thesis deals with organic nanoaggregates, an introductory discussion has been provided about these systems, for example, basic differences in properties of organic and inorganic nanoaggregates, types of organic nanoaggregates, basic introduction to excitons, photophysical processes which occur in the molecular and nanoaggregate systems as well as the exciton dynamics in these nanoaggregates.. We have also described the basic working mechanisms of organic photovoltaic and organic light emitting diodes to emphasize the importance of the present studies on exciton lifetime and exciton diffusion properties. Further, we have explained about the exciton - excion annihilation process, occurring at high exciton density condition. We have also provided the basic steps of estimation of exciton diffusion length and explain some basic criteria of a good solar cell material in this chapter.

Chapter 2

This chapter provides the details of various methods of synthesis of organic nanoaggregates and the morphological characterization techniques of the nanoaggregates. It provides a detailed discussion on the working principles of these characterization tools. It describes the procedures of spectroscopic measurements of the nanoaggregate materials and RTIL samples. The basic principles of of steady state absorption and emission measurement techniques and the spectrometers are described here. Most of the research works being reported here have been carried out using time resolved fluorescence and absorption techniques. Therefore, brief descriptions of the experimental setups, for example, time correlated single photon counting spectrometer, fluorescence up-conversion spectrometer, nano-second flash photolysis set up and sub-picosecond time resolved transient absorption spectrometer have been provided. The details of the nanosecond pulse radiolysis also have been described in this chapter.

Chapter 3

In several papers published earlier, the electron transfer (ET) or energy transfer (ENT) rates in RTIL media were shown to be faster than the diffusion controlled rate. This observation was explained by considering the diffusion of the reactants through low viscous pockets inside RTIL media. However, Maroncelli and coworkers as well as Vauthey and coworkers assigned these observations by the transient quenching effect.[27,28]They also predicted that the diffusion controlled ET or ENT processes could be observed only in the stationary quenching regime. Therefore, in this work, we have investigated the ET processes from the long-lived radical anions of pyrene and benzophenone to molecular acceptors, say, benzophenone and fluorenone, respectively, in two RTIL media, namely, [BMIM][PF_6] and [BMIM][BF_4], as well as a few other conventional organic solvents using the nanosecond pulse radiolysis technique. Anion radicals have lifetimes longer than 1 μs. Therefore, it is expected that, stationary quenching regime may be achieved in these viscous ionic liquids using the long-lived transients and diffusion controlled reaction process may possibly be observed. Here, decay of the donor radical anion and concomitant formation of the acceptor radical anion ensure a bimolecular ET process. The rate constants for the bimolecular ET process in both normal organic solvents and RTIL solvents have been found to be nearly equal to diffusion controlled rate calculated using the bulk viscosity of the corresponding solvents. This suggests that even in highly viscous RTIL solvents, diffusion controlled reaction may be observed, if the transient species possess sufficiently long lifetime to achieve the stationary condition.

It was also discussed earlier that, the microscopic heterogeneity was more prominent with the RTIL solvents having long alkyl substitution. Therefore in the next step, we have studied the ET and triplet-triplet energy transfer (TET) processes in RTILs having alkyl substituents with various chain lengths to observe the effect of microscopic heterogeneity in the rate of the reactions occurring at the stationary condition. TET and ET processes involving a few long-lived (lifetime is about a few microsecond) triplet states as energy donors and radical anions as electron donors, respectively, have been investigated here in a series of 1-alkyl-3-methyl-imidazolium cation based ionic liquids, SDS micelle as well as in conventional solvents. Long lifetimes of the transient donors ensure occurrence of these processes in the 'stationary quenching regime' even in highly viscous RTIL solvents. Results of our molecular dynamic simulations reveal that self-organization of the RTIL solvent molecules, which creates nonionic and ionic pockets in RTIL, becomes more significant as the alkyl chain length increases. In the cases, where both the reactants are neutral molecules, which prefer to stay inside the nonionic or nonpolar pockets, the diffusive motion of the reactants experiences much lower microscopic viscosity as compared to the bulk or macroscopic viscosity of the solution. However, if one of the two reactants is ionic and the other is nonionic, they reside at ionic and nonionic pockets of the RTIL solution, respectively and the motion of the reactants occur through different regions of the RTIL solution. Therefore, the resultant viscosity experienced by the reactants become equal to the macroscopic viscosity of the solution and the reaction rates show a linear relationship with inverse of viscosity of the solution (Smoluchowski equation). Our estimated ET and TET rates also indicate that the viscosity of the nonionic pocket in 1-decyl-3-methyl-imidazolium cation based ionic liquid is nearly equal to that of the core of the SDS micelle.

Chapter 4

In this chapter photophysical properties of the anthracene nanoaggregates have been discussed. Anthracene is a well-known polyacene molecule having absorption in the near UV region and emission in the violet-blue region with significantly large emission yield. Polyacene molecules are well-known as organic semiconductors and can form aggregates due to π-π interaction. These molecules even arrange in various crystalline forms having widely varied photophysical properties. Significantly large absorption coefficient and emission yield also make these materials suitable for application in photovoltaic or light emitting devices. Anthracene being one of such simple molecules have been chosen for studying the photophysical properties of organic nanoaggregates. Anthracene nanoaggregates(NA) have been synthesized using well known reprecipitation method in the presence of PVA stabilizer.[41,42]Dynamic light scattering (DLS) and Atomic Force Microscopy (AFM)techniques have been employed to reveal that the particles of anthracene nanoaggregates have shapes of nanodiscs with the average diameter and height of about 260 nm and 50 nm, respectively. Maxima of the 0 - 0 vibronic bands in both the absorption and emission spectra of the NA are red-shifted by about20 nm as compared to the corresponding one in the monomeric absorption and emission bands. Time-resolved emission studies show wavelength dependent dynamics, which originates from the distribution of particle size as well as the orientational heterogeneities in the aggregate leading to different kinds of defect sites and hence population of the excimeric states of different conformations. Ultrafast transient absorption studies reveal nonexponential dynamics of the singlet excitonic state due to exciton-exciton annihilation reaction at high excitation intensity. On the other hand, nanosecond laser flash photolysis studies reveal significant population of the triplet exciton, which also undergoes exciton - exciton annihilation reaction. Rate constants of exciton - exciton annihilation reactions undergone by the singlet and the triplet excitons have been determined as 3.7×10^{-9} cm^3 s^{-1} and 2.2×10^{-13} cm^3 s^{-1}, respectively and exciton diffusion lengths to be about 13.2 and 6.5 nm, respectively. While the value of the exciton diffusion length for the singlet excitonis comparable to, but that for the triplet exciton is significantly shorter than, those reported in the case of the anthracene crystals. These observations have been rationalized by predicting more disordered structure in the self-assembled nanoaggregates as compared to those parameters for the crystals of anthracene.

Chapter 5

In this chapter, synthesis and photophysical properties of doped anthracene nanoaggregates have been discussed. Singlet states of polyacene molecules e.g. perylene, tetracene and pentacene, are characterized with large emission yields and the combination of the emission spectra of these molecules cover the entire visible region of the spectrum of electromagnetic radiation.. Molecular structures of these molecules also are very similar to that of anthracene molecule and therefore they are suitable for doping in anthracene nanoaggregate matrix. In addition, absorption spectrum of each of these molecules in the nanoaggregate has good overlap with the emission spectrum of anthracene nanoaggregate and hence, anthracene nanoaggregate doped with those polyacene hydrocarbons are suitable for fluorescence resonance energy transfer study. Considering the possible application of the doped anthracene nanoaggregates in white light generation, singly and combinedly doped antrhracene nanoaggregates have been synthesized using reprecipitation technique. Following photoexcitation of anthracene molecule in the nanoaggregate, anthracene exciton transfers energy to the dopant molecule(s).Energy transfer (ET) efficiency of about 98% could be achieved with the concentration of about 6 x 10^{-3} mol. dm^{-3} for perylene or tetracene as the acceptor and about 92% efficiency with the doping concentration of about 5 x 10^{-2}mol dm^{-3} for pentacene as the acceptor. Very fast energy transfer rates (~3 - 6 x 10^{11} dm^3 $mol^{-1}s^{-1}$) observed here could not be explained by invoking onlyFörster's mechanism. However, the rate of diffusion of anthracene exciton, determined experimentally using exciton – exciton annihilation reaction in anthracene nanoaggregate matrix, has been shown to agree well with the ET rate. This observation leads us to conclude that the ET rate in the nanoaggregate matrix is controlled by exciton diffusion. Using those three dopants with proper concentration ratios, efficient white light emission has been achieved following optical excitation of the nanoaggregate sample at the absorption band of the anthracene molecule.

Chapter 6

Polyacene molecules may arrange in two different crystalline phases, known as α and β phase.[48]Anthracene has beenfound to arrange in β phase. On the other hand, pyreneordperylene has tendency to form α phase which is suitable for excimer formation. Therefore, depending upon the molecular arrangement in the crystal or nanoaggregate, the excited state dynamics maybe affected significantly and hence also applicability of these materials in devices. To delineate this issue, we have carried out photophysical studies in pyrene and perylene nanoaggregates and these aspects have been discussed in this chapter. Nanoaggregates of pyrene and perylene have been prepared in presence of PVA stabilizer using reprecipetation method. It has been found that, the average sizes of the nanoaggregates are about 120 and 140 nm for pyrene and perylene, respectively. The characteristic features of vibronic bands present in the absorption spectra of these molecules in solution change significantly in the nanoaggregate. These two molecules are well-known to show excimer emission in highly concentrated solution. The bulk solid in crystal also shows excimer emission upon photoexcitation in the near UV range. The fluorescence spectra of the nanoaggregates of both these molecules are characterized mainly by excimer emission. The excimer emission of pyrene is highly efficient and may have wide scale applications in LED and display systems. However emission from perylene excimer is quite weak in nature and may not be suitable for above applications. TCSPC technique has been employed to estimate the life times of the excimeric states(28 ns and 11 ns for pyrene and perylene, respectively). Formation of the excimeric state occurs with the time constants of1.1±0.2 ns and 4±0.4 ns for perylene and pyrene, respectively, at room temperature. Formation time constant has been found to decrease with increase in sample temperature and indicates presence of energy barrier in the formation of the excimeric state from the excitonic state for both nanoaggregates. In both the cases, excitation intensity dependent exciton–exciton annihilation process has been analyzed to estimate the exciton diffusion parameters for these nanoaggregates.

Chapter 7

In this chapter, focus has been made on the comparative studies of excited state dynamics of the nanoaggregates of pthalocyanin (PC), Zn-ion complexes of PCs and its derivatives. These molecules are also useful for photovoltaic applications. We have carried out comparative study of exciton dynamics to get idea about the effect of enlarged π-conjugation, metal ion inclusion in these dyes and also substitution of tertiary butyl group on the aromatic ring. In all these cases, we observe formation of disc shaped nanoaggregates having diameter varying in the range200-400 nm and height of 40-50 nm. The steady state absorption spectra of the nanoaggregates show both Soret and Q-band and the absorption band shows mainly bathocromic shift as compared to that of the monomer. This suggests formation of J aggregates of these dyes.[47] The excited state dynamics studies have been carried out following photoexcitationof the monomers and nanoaggregates at 390 nm. Our pump-probe measurements on the nanoaggregates show excited state absorption in the wavelength region of 450-600 nm region and the ground state bleaching in the 650-750 nm region for all the nanoaggregates. The exciton dynamics has been found to follow nonexponential dynamics, which has been fitted using tri-exponential fitting functions. The exciton decay rates are found to depend upon the exciton densities and indicate involvement of exciton-exciton annihilation process. The exciton density dependent annihilation process has been analyzed to estimate the exciton diffusion coefficient and diffusion length of the material. It has been observed that the metal ion complex formation and enlarged π-conjugation causes faster exciton diffusion process and elongated exciton diffusion length which is better for photovoltaic application. On the other hand, substitution with t-butyl group probably causes inefficient packing i.e. intermolecular distance increases and this causes slower exciton diffusion and shorter exciton diffusion lengths.

Chapter 8

The work summarized above leads to the conclusion that, the diffusion controlled ET or TET process maybe observed in RTIL media with using long lived transients e.g. anion radicals or triplet excited states of molecules. Our investigation also reveals that the RTILs form nonionic and ionic pockets and it is more evident if the chain length of alkyl substituent is long. Nonionic molecules prefer to be solvated in the nonionic pocket; on the other hand ionic reactants remains mostly in the ionic region. The nonionic molecules present in the nonionic pockets of the RTILs faces lower viscosity as compared to that of the bulk viscosity of the RTILs. The ET and ENT rates observed here indicate that, the viscosity of the nonionic pocket is equivalent to the viscosity of the core of SDS micelle.

The second part of the thesis leads us to the conclusion that, organic nanoaggregates can be easily synthesized using facile solvent route. Aggregates may have different photophysical properties depending upon the molecular arrangement and type of intermolecular interaction inside the nanoaggregate matrix. We have explained different photophysical properties and exciton dynamics for the polyacene nanoaggregates. The excimer formation dynamics and effect of excimer formation on the possibility of device applications also has been explained. We have also chosen other kind of dyes, which also form J or H aggregate and have absorption in the different wavelength region of the solar spectrum. The exciton density dependent annihilation process has been studied extensively to estimate the exciton diffusion parameters and prospects of these materials in photovoltaic application have been discussed.

References

1. Samanta. A.*J. Phys. Chem. B.* **2006,** *110*, 13704**.**
2. Li, S.;Bañuelos, J. L.; Guo, J.; Anovitz, L.; Rother, G.; Shaw, R. W.; Hillesheim, P. C.; Dai, S.; Baker G. A.; Cummings,P. T.*J. Phys. Chem. Lett.***2012**, *3*, 125.
3. Hardacre, J. D.;Holbrey, S. E.;McMath, J.; M. Nieuwenhuyzen, M.; *ACS Symposium Series***2009**, *818* (Chapter-31), 400.
4. Rogers R. D.;Voth, G. A.; *Acc. Chem. Res.***2007**, *40***,** 1077.
5. Fischmeister, C.; Bruneau, C.*TopOrganomet. Chem.***2015**, *51*, 287
6. Dupont, J.;Kollár, L. Eds.;*Ionic Liquids (ILs) in Organometallic Catalysis,* Springer-Verlag, Berlin, Heidelberg, **2015**.
7. Torriero, A. A. *J. Ed.Electrochemistry in Ionic Liquids*, Vol. 2: Applications, Springer International Publishing Switzerland, **2015**.
8. Mora-Pale, M.;Meli, L.; Doherty, T. V.;Linhardt, R. J.Dordick, J. S. *Biotech.Bioeng.***2011**, *108*, 1229.
9. De Los Rios, A. P. Fernandez, F. J. H. (Eds.) *Ionic Liquids in Separation Technology*, Elsevier B. V. **2014**.
10. Welton, T. (Ed.) *Green Chemistry*, **2011**, *13* (2) (Spcial Issue), RSC Publishing.
11. Ha, S. H.; Menchavez, R. N.; Koo, Y. M. *J. Chem. Engg.***2010**, *27*, 1360.
12. Venkatesan, K. A.;SrinivasanT. G.; Rao, P. R. *J. Nucl. Radiochem. Sci.***2009**, *10*, R1.
13. Grodkowski, J.; Neta,P.; Wishart, J. F.*J. Phys. Chem. A***2003**, *107***,** 9794**.**
14. Skrzypczak,A.;Neta, P. *J. Phys. Chem. A,* **2003**, *107***,** 7800**.**
15. Paul, A.;Samanta, A.*J. Phys. Chem. B* **2007**, *111*, 1957**.**
16. Sarkar, S.; Pramanik, R.; Seth, D.; Setua,P.;Sarkar,N.*Chem*. Phys. Lett. **2009**, *477*, 102.
17. Sarkar, S.; Pramanik, R.; Ghatak, C.; Rao, V. G.;Sarkar, N.*J. Chem. Phys*. **2011,***134*, 74507.
18. Vieira, R. C.; Falvey, D. E.*J. Am. Chem. Soc.***2008**, *130***,** 1552.
19. Vieira, R. C.;Falvey, D. E. *J. Phys. Chem. B* **2007,***111*, 5023
20. Wishart, J. F.; Neta, P. *J. Phys. Chem. B* **2003,***107*, 7261**.**
21. Behar, D.; NetaP.; Schultheisz, C. *J. Phys. Chem. A* **2002,***106*, 3139.
22. Lee, C.; Winston, T.; Unni, A.; PagniR. M.; Mamanto, G.*J. Am. Chem. Soc.* **1996,***118*, 4919.
23. Liang, M.; Kaintz, A.; Baker, G. A.; Maroncelli, M. *J. Phys. Chem. B***2012**, *116***,** 1370.
24. Koch, M.; Rosspeintner, A.; Angulo, G.; Vauthey, E. *J. Am. Chem. Soc.***2012,** *134*, 3729.

25. Gordon C. M. McLean, A. J.*Chem. Commun.***2000,** 1395.

26. McLean, A. J.; Muldoon, M. J.; Gordon, C. M.; Dunkin, I. R.*Chem. Commun.***2002,** 1880.

27. Liang, M.; Kaintz, A.; Baker, G. A.; Maroncelli, M*J. Phys. Chem. B.***2012**, *116*, 1370.

28. Koch, M.; Rosspeintner, A.; Angulo, G.; Vauthey, E. *J. Am. Chem. Soc.***2012**, *134,* 3729.

29. Eisfeld, A.; Briggs, J. S. *Chem. Phys*. **2006**, *324*, 376.

30. M. Kasha, H. R. Rawls, M. A. El-Bayoumi, *Pure Appl. Chem.***1965**, *11*, 371

31. Sautter, A.; Thalacker, C.; Heise, B.; Würthner, F. *Proc. Natl. Acad. Sci. U. S. A.***2002**, *99*, 4993.

32. Gao, Y.; Zang, X.; Ma, C.; Li. X.; Jiang, J. *J. Am. Chem. Soc.***2008**, *130*, 17044.

33. Hunter, C. A.; Sanders, J. K. M. *J. Am. Chem. Soc.***1990**, *112*, 5525.

34. Cheng, Y. J.; Yang, S. H.; Hsu, C. S. *Chem. Rev*. **2009**, *109*, 5868.

35. Kalyani, N. T.; Dhoble, S. J. *Renewable and Sustainable Energy Reviews*. **2012,***16*,2696.

36. Brütting, W.; Frischeisen, J.; Schmidt, T. D.; Scholz, B. J.; Masr, C. *Phys. Status. Solidi A***2013**, *210*, 44.

37. Scholz, S.; Kondakov, D.; Lüssem, B.; Leo, K. *Chem. Rev.***2015**, *115*, 8449.

38. Sessole, M.; Bolink, H. J. *Adv. Mater*.**2011**, *23*, 1829.

39. Yu, J. Y.; Chen, I. W. P.; Chun-hsien Chen, C. H.; Lee, S. J.; Chen, I. C.; Lin, C. S.; Cheng, C. H. *J. Phys. Chem. C* **2008**, *112*, 3097.

40. Liang, W. W.;Chang,C. Y.; Lai, Y. Y.; Cheng, S. W.; Chang, H. H.; Yin-Yu Lai, Y. Y.; Cheng, Y. J.; Wang, C. L.; Hsu, C. S. *Macromolecules* **2013**, *46*, 4781.

41. Chung, H. R.; Kwon, E.; Oikawa, H.; Kasai, H.; Nakanishi, H. *J. Crystal growth* **2006**, *294*, 459.

42. Seko, T.; Ogura, K.; Kawakami, Y.; Sugino, H.; Tanaka, J. *Chem. Phys. Lett.* **1998**, *291*, 438.

43. Zewail, A. H. "*Femtochemistry: Ultrafast Dynamics of the Chemical Bond*", vol. 1&2 World Scientific Pub., Singapore, **1994**.

44. De Schryver, F. C.; De Feyter, S.; Schweitzer, G. Eds. "*Femtochemistry*", Wiley-VCH, Weinheim, **2001**.

45. Yago, T.; Tamaki, Y.; Furube, A.; Katoh, R. *Phys. Chem. Chem. Phys*. **2008,** *10*, 4435.

46. Paillotin, G.; Swenberg, C. E.; Breton, J.; Geacintov, N. E. *Biophys. J.* **1979,** *25*, 513.

47. Kakade, S.; Ghosh, R.; Palit, D. K. *J. Phys. Chem. C* **2012**, *116*, 15155.

48. Rohatgi-Mukherjee, K. K. "*Fundamentals of Photochemistry*", Wiley Estern Ltd. India, **1986.**

LIST OF ABBREVIATIONS

AFM: Atomic Force Microscopy

ADC: Analog to Digital Converter

BBO: Beta Barium Borate

BMIM/C_4MIM: 1-butyl-3-methyl-imidazolium

CCD: Charge Coupled Device

CFD: Constant Fraction Discriminator

CPA: Chirp Pulse Amplification

DLS: Dynamic Light Scattering

DMSO: Dimethylsulfoxide

DMIM/C_{10}MIM: 1-decyl-3-methyl-imidazolium

EEA: Exciton – Exciton Annihilation

EMIM/C_2MIM: 1-ethyl-3-methyl-imidazolium

ESA: Excited State Absorption

ET: Electron Transfer

FCS: Fluorescence Correlation Spectroscopy

FRET: Fluorescence Resonance Energy Transfer

FWHM: Full Width at Half Maxima

GSB: Ground State Bleaching

HOMO: Highest Occupied Molecular Orbital

HMIM/C_6MIM: 1-hexyl-3-methyl-imidazolium

IC: Internal Conversion

ICCD: Intensified Charge Couple Device

IRF: Instrument Response Function

ISC: Inter System Crossing

LINAC: Linear Accelerator

LUMO: Lowest Unoccupied Molecular Orbital

MCA: Microchannel Analyzer

MD: Molecular Dynamics

PMT: Photomultiplier Tube

NA: Nanoaggregate

OPV: Organic Photovoltaic

OLED: Organic Light Emitting Diode

PVA: Poly Vinayl Alcohol

PL: Photoluminescence

RTIL: Room Temperature Ionic Liquid

SAXS: Small Angle X-ray Scattering

SDS: Sodium Dodecyl Sulfate

SE: Stimulated Emission

SHG: Second Harmonic Generation

SV: Stern Volmer

TA: Transient Absorption

TAC: Time to Amplitude Converter

TET: Triplet Energy Transfer

TCSPC: Time Correlated Single Photon Counting

THF: Tetrahydrofuran

TRES: Time Resolved Emission Spectra

TRANES: Time Resolved Area Normalized Emission Spectra

UTA: Ultrafast Transient Absorption

XRD: X-Ray Diffraction

LIST OF FIGURES

Page No.

LIST OF TABLES

Page No.

. *CHAPTER 1*

INTRODUCTION

1.1. GENERAL INTRODUCTION

"Chemistry" is a part of science, which deals with the study of molecular structure, property and chemical transformation of materials. Chemical science has been practiced knowingly or unknowingly from the ancient age of civilization. With the progress of time, scientists have been interested to have better understanding about the chemical processes leading to development of this brunch of science. During the last several decades, many sophisticated instrumentation techniques have been devolved in order to obtain molecular level understanding of physical and chemical processes. Detail understanding about the molecular structure, properties and reaction pathways in naturally occurring systems guided the scientist community to develop artificial chemical devices to service the mankind. Spectroscopy is one of such techniques, which provide us information about the molecular energy levels and their reactivity. Thus spectroscopic techniques have become an indispensable tool for qualitative and quantitative analysis. Different frequency ranges of electromagnetic radiation may be used to introduce transitions in different kinds of molecular energy levels and various kinds of spectroscopic techniques may be used to obtain deeper understanding about the energy levels and reactivities of molecular systems.[1,2] Development of theoretical simulation techniques of molecular systems has also complimented these efforts immensely to unfold the fundamental details of the matters.[3,4]

Science has come across a long way to reach the present status. This journey has been completed to fulfill the need and necessity of the human civilization. During this process, researchers aspired to understood the underneath molecular and physical mechanism and out of this curiosity leading to the development of the fundamental science. Therefore in the present day research, emphasis is put in understanding the basic molecular level properties of the materials as well as mechanism of interactions related to a particular application of the materials.

Therefore, in this present thesis, we discuss synthesis of new materials, characterization of the spectroscopic properties of these materials to explore their possible applications.

The environmental pollution has become a serious problem towards the human civilization. Pollution from chemical industry is one of the major contributors in different kinds of environmental pollution. Therefore, scientist community has put huge efforts to replace those conventional solvents which are major players in polluting the environment. In the last century, a new kind of solvent systems, popularly known as room temperature ionic liquids (RTIL), has been discovered. These were considered as green solvents as these solvents have less pollution hazards and can have wide scale applications.[5,6] However, recently the environment friendliness of RTILs are also doubted.

The efficient application of this new class of solvents needs understanding of their microscopic properties and their role in different kinds of chemical processes conducted using these solvents. Here, we made an attempt to address the issue of microscopic nature of RTILs and their effects on some basic reactions e.g. energy transfer and electron transfer processes. Long lived transients have been used to monitor the reactions in stationery conditions in these viscous liquid systems.

The second part of the work is mainly focused on the investigations of the phophysical properties of various kinds of organic nanoaggregate materials having possibility of use for photovoltaics, display devices and other optoelectronic devices. Extraction of energy in the useable form has been a field of active research of interest during the last several decades. The increasing demand of electrical power in the modern age makes this research field alive till date. Decrease in the reserves of natural gas and coal resources has emerged the surge of more intensive search for renewable energy resources. Solar energy harvestation is one of such renewable energy sources whose efficient use itself can fulfill the present daily energy demand. Photosynthesis process observed in plants occurs through solar light absorption, which inspires us to mimic such systems, which can absorb solar light and convert it to the electrical energy. Inorganic, organic and hybrid inorganic-organic materials are being tried for solar energy harvestation.[7-14] Inorganic semiconductor materials are extensively used in the form of thin film and nanomaterial for solar cell applications.[7-12] However application of organic molecules for solar cell applications are mostly limited to conducting polymers and some specific molecules.[15,16] So there are plenty of unexplored area which can be explored for this purpose.

In addition to efficient energy extraction, efficient use of the extracted energy is also essential to meet the energy demand in the recent age. In this context different light emitting and display devices have come into the market. Light emitting diode is considered as one of the most potential device for such applications.[17-19] Significant research effort has been put to search suitable material for this application.[20-22] Both inorganic and organic materials have been used for such uses. Organic LED materials are low cost, efficient and flexible and therefore considered as potential materials for next generation LED devices.[20-22] Therefore organic semiconductor materials possess the applicability for energy harvestation and lightening devices. However, efficient device applications always require basic understanding of underneath mechanism of device operation and photophysical properties of the material. Ease of processing of those materials for device application is also required to make these materials more cost effective. Major part of the present thesis is focused on the study of exciton dynamics, exciton diffusion parameters and other excited state properties of different organic nanoaggregates to explore the prospect of these materials for above device applications. But before going to the rigorous discussion about the work it is essential to provide some basic concepts related with the thesis. In this chapter we will give a brief introduction about those basic concepts and the objectives of the thesis.

1.2. SELF ASSAMBLED MOLECULAR SYSTEMS

Self assembled molecular systems are formed due to the involvement of a number of non-covalent interaction forces, which cause this self organization process thermodynamically feasible and make the molecular self assembly systems enough stable in the ambient condition.[23-25] In nature, there are several kinds of self assembled molecular systems which are indispensible for their biochemical functionality. For example, molecular self assembly can be observed in the DNA, chloroplast, aggregates of proteins, cellular membranes, micelles formed by surfactants and many others. These self-assembled systems considered meta-stable forms of the materials. As these self organizations are thermodynamically driven, there are less probabilities of impurity incorporation and is quite robust for application purpose.

As discussed earlier, many biological structures are nothing but structurally well-defined aggregates arranged through noncovalent interactions. The aggregate formation involves stepwise interactions leading to formation of numerous noncovalent weak chemical bonds. These noncovelent bonds are typically hydrogen bonds, ionic bonds, and van der Waals bonds which are associated with the molecules to form well-defined and stable macroscopic structures.[23-25] Although these bonds are weak in nature, the collective interactions may result in very stable structures and materials.[26-28] Self assembly systems present in the biological systems and there efficient functionality motivates the scientific community to biomimic and design such self organized materials for wide scale applications. The efficient use of a material relies upon the basic understanding about its nature, its physicochemical properties. Therefore, it is the primary need to understand the interaction forces which are involved to make such molecular self assembled systems. In the next sub-section we have provide a brief description of such noncovalent interaction forces.

1.2.1. INTERACTION FORCES GOVERNING MOLECULAR SELF-ASSEMBLY FORMATION

Non covalent interaction forces responsible for self-organization of molecules include van der Waals force, H-bonding, π-π interaction, etc. The stabilization energy associated with such noncovalent interactions is not very large but sufficient for the self-assemblies to exist in the ambient condition. Few important and widely studied interactions forces described in this thesis are as follows.

Van der Waals Interactions: Van der Waals forces include attractions and repulsions between atoms, molecules, and surfaces, as well as other intermolecular forces.[29,30] These are the most fundamental interactions present between any two atoms or molecules and are generally divided into following categories.

- Force exists between two permanent dipoles (Keesom force)
- Force exists between a permanent dipole and a corresponding induced dipole (Debye force)
- Force exists between two instantaneously induced dipoles (London dispersion force).

Van der Waals forces are relatively weak in nature as compared to the force between two atoms/ions/molecules linked by covalent or ionic bonds, but play a fundamental role in various fields such as supramolecular chemistry, polymer science, structural biology, surface science, nanotechnology and condensed matter physics. Van der Waals forces are major driving force of many properties of organic compounds, including their solubility in polar and non-polar media, etc.

Hydrogen bonding: Traditionally, hydrogen bonds have been defined as D─H···A, wherein both the donor D and acceptor A are highly electronegative atoms, such as N, O, or F.[30,31] Since there is no strictly defined cut-off for an atom's ability to participate in hydrogen bonding, this concept has been extended to weaker donor atoms such as carbon (in all three hybridization states) or unusual acceptors such as π-systems. These bonds are formed when an acidic hydrogen atom attached to donor, interacts with the acceptor atom having nonbonding electron lone pairs. The intermolecular H-bondings have the advantage of selectivity and directionality, which are important in building biological nanostructures. The strength of the bond depends on the number as well as the sequence of the H-bonds. Many examples of containing this type of bond-mediated self assembled moieties are present in nature as well as in the synthesized materials. Hydrogen bonding not only initiates the self-assembly but also helps in designing unique organized structures, which were impossible otherwise. The most important example of hydrogen bond assisted self-assembly is the base pairing within nucleotides resulting in the formation of DNA helixes.

***π-π* interactions:** The term refers to the attractive, noncovalent interactions between two aromatic rings resulting in alignment of positive electrostatic potential of one ring with negative electrostatic potential of another ring forming an offset stack. Well known example is formation of benzene dimer through *π*–*π* stacking.[32] These interactions are important in nucleobase stacking within DNA and RNA molecules, protein folding, template-directed synthesis, materials science, and molecular recognition. Intermolecular interactions involving aromatic rings are key processes in both chemical and biological systems.[33-34]

These kinds of interactions are responsible for many diverse phenomena such as the vertical base-base interactions, which also stabilize the double helical structure of DNA, the intercalation of drugs into DNA, the packing of aromatic molecules in crystal, the tertiary structures of proteins, the conformational preferences and binding properties of polyaromatic macrocycle, complexation in many host-guest systems and aggregations in π-conjugated organic macrocycles like porphyrins and phthalocyanines.[35-42] π-π attractions of these molecules are not limited to self-aggregation, but it also extends to the π-stacking seen with a wide variety of covalently attached π-systems in organic solvents. Studies carried out in this area suggests that π-stacking within molecules depends on many factors like solvo-phobic effect favoring the geometry of maximum π-overlap.[43] The π-π interaction also can provide the strong electronic interaction between an electron donor and an electron acceptor. They are characterized either by charge-transfer transitions in the UV-visible absorption spectrum or by a broadened UV-visible spectrum.[44] It has also been suggested that the attraction arises from the uneven charge distribution across π-systems. In a particular orientation of two π-systems, positively charged atoms on one molecule may be aligned with negatively charged atoms on the other, so that there is an attractive electrostatic interaction.[45]

In this thesis, aggregation of polyacene molecules, phthalocyanine and its derivative molecules have been described in the following chapters. The π-π interactions play the major role in the co-facial stacking of these molecules upon each other.

1.2.2. ROOM TEMPERATURE IONIC LIQUID (RTIL): SELF ASSMBLED MEDIA FORMING MICROSCOPIC POCKETS

RTILs belong to a class of low temperature molten salts which have melting points below 100 °C. The development of ILs started in 1914 when Paul Walden described the synthesis and properties of the “first” IL, ethylammonium nitrate (melting point =14°C).[46] In the late 1970s, Osteryoung group and Wilkes et. al. synthesized chloroaluminate melts liquid at room temperature, but these fluids are found to suffer from their high sensitivity to atmospheric moisture.[47-52] However, in 1990s, a significant milestone was achieved when the RTILs comprising of imidazolium as cation and tetrafluoroborate, hexafluorophosphate as anions were synthesized.[53-57] Unlike haloaluminate based ILs, this new generation of ILs were relatively resistant to hydrolysis and could be prepared, stored, and handled outside a glove box.[53-57] RTILs are reported to possess unique physicochemical properties such as high polarity, negligible vapour pressure, high ionic conductivity and excellent radiation and thermal stability.[58-65] All these properties make them good substitutes for conventional organic solvents. In addition, these solvents can solubilise most of the inorganic and organic reagents and possess a large electrochemical window, which make them useful for synthesis, and solar cell applications.[66-69] Due to their good radiation stability, they are expected as future solvents for nuclear fuel cycle including actinide electro-refining, and solvent extraction.[70-72] Owing to these, a surge in the interest of the scientific community (especially in the last two decades) can be observed from the exponential growth in the number of publications on RTILs.

Further, these media are often referred to as "designer" solvents. This is due to the fact that by altering the cation-anion combination, the characteristics associated with ionic liquids, such as hydrophobicity, miscibility (with other solvents), polarity and other physicochemical properties can be easily tuned, as desirable for a specified task.[54-56,73,74] According to Plechkova et. al. pairing of all known anion and cation combinations can obtain approximately 10^6 types of different ILs.[75] Nevertheless, till now, most of the research has been focused on RTILs with commonly used cation-anion combinations. The structures of some of these cations and anions are shown in Figure 1.1.

RTILs are composed of ions. However they are different from the molten salts, which have much higher melting point temperatures. Essentially, melting point of a crystal is a synergistic effect of the cation and the anion as both influence its lattice energy. The low melting points of RTILs are the result of weak inter-ionic interactions due to inefficient packing of irregularly shaped ions and diffuse charged nature of counter ions.

Cations	**Anions**
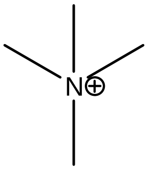 Ammonium 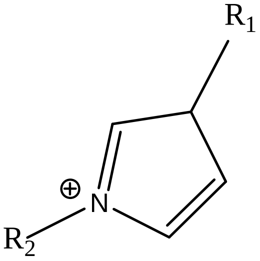 Imidazolium 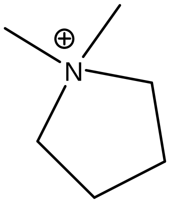 Pyrrolidinium 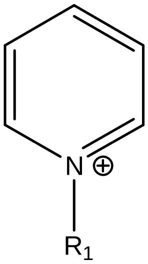 Pyridinium 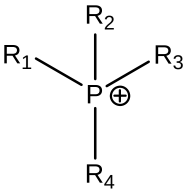 Phosphonium	Cl^-, Br^-, I^- Halides NO_3^- Nitrate BF_4^- Tetrafluoroborate PF_6^- Hexafluorophosphate $CH_3CO_2^-$ Acetate $C_2H_5SO_4^-$ Ethayl Sulfate $CF_3SO_3^-$ Trifluoromethanesulfonate $[(CF_3SO_2)_2N]^-$ Bis(trifluoromethylsulfonyl) imide 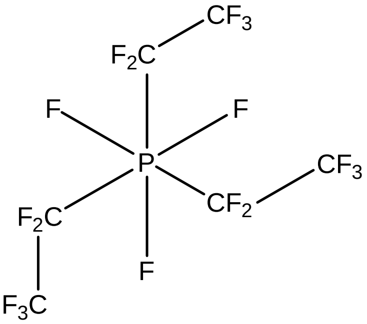 Tris(pentafluoroalkyl)trifluorophosphate

Figure 1.1: The structures of some of the cations and anions for commonly available RTILs.

RTILs are different from the conventional organic solvents with respect to their structure and physicochemical properties (mentioned earlier). Specially, the microscopic nature of the RTILs is reported to be not homogeneous, unlike most of the conventional organic solvents. [76-92] Within an IL, there are many correlation length scales present between the ion pairs. [93] These are due to a various inter-ionic interactions co-existing in these fluids as a result of complex interplay of forces such as Coulombic, van der Waals (dipole -dipole, dipole-induced dipole,and dispersion), hydrogen bond, and π-π stacking interactions.[94-96]

It is also reported that, RTILs with long alkyl substituent may have significant effect on microscopic pocket formation due to favourable hydrophobic interaction of long alkyl substituents. We want to probe such microscopic pocket formation by observing energy and electron transfer processes or observe the effect of microscopic pocket formation on the reaction rates.

1.2.3. SELF-ASSEMBLY BY AGGREGATION

Gunter Scheibe and Edwin E. Jelley in the late 1930s independently investigated the photochemistry of cyanine dyes and it led to the first discovery of aggregate formation of organic dye molecules.[97-98] Organic dye molecules with extended π-conjugation favour to go for self aggregation and form larger sized nanoaggregates.[26-28] This bottom-up approach used for synthesis of the nanoaggregates gives one of the efficient methods for the synthesis of organic nanoparticles. Formation of molecular aggregates depends upon various factors such as concentration, temperature, solvent medium, and many other factors.[27, 99-101]

Precise arrangement of monomers in aggregate leads to strong intermolecular interaction, which causes the differences in the photophysical behavior of the aggregate and corresponding monomer. Hence aggregates may possess new functions that are not observed in their monomeric form.[26-28] The change in the photophysical properties first observed in the UV–visible absorption spectra, which arises due to the intermolecular interaction and excitonic coupling present in the aggregates.[26-28]

The molecular aggregates are broadly classified into two types depending upon the molecular stacking pattern present in the aggregate. Aggregates, where molecular transition dipoles are arranged in head-to-tail configuration, are known as J-aggregates (shown in Figure 1.2). This name was given after the name of the scientist, Jelly, who reported the J-aggregate formation for the first time.[102] In the case of J-aggregates, the absorption band shows red shift i.e. absorption maximum is shifted to the longer wavelength region as compared to that of the corresponding monomer.[102] The newly developed band is also well known as J-band, which is sharp and intense as compared to the monomeric absorption band. J-aggregates are also characterized by their red shifted strong emission.[102]

Another class of the aggregates, which are frequently observed, is known as H-aggregates. Here molecular transition dipoles arranged in face-to-face configuration (shown in Figure 1.2).[102] These aggregates show blue shift in the absorption band i.e. the absorption maximum of the aggregated species is shifted to lower wavelength region as compared to that of the monomeric form.[103] Since these aggregates shows 'hypsochromic shift' they are named as H-aggregates. Unlike to the J-aggregates, H-aggregates show broader absorption band also known as 'H-band' and are nearly nonfluorescent, when compared with the corresponding monomeric species.[103]

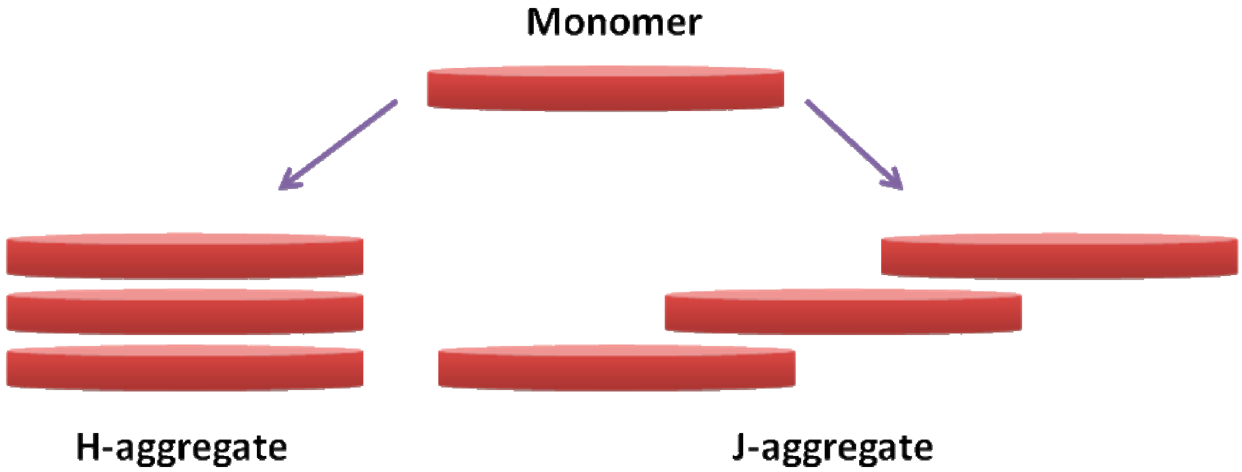

Figure 1.2: Type of stacking in molecular aggregates.

The above mentioned shifts in the absorption spectra of these aggregates may be explained following the Kasha-McRae exciton model for the dimeric molecules.[103] The model explains the allowed and forbidden electronic transitions after excitation of the aggregates depending on the angle between the transition dipole moments of two interacting molecules. In the case of face-to-face stacking (seen in H-aggregates), where the two transition dipoles are parallel to each other, the energy level diagram is given in Figure 1.3. Here the ovals correspond to the molecular profile, and the double arrow indicates the polarization axis for the considered molecular electronic transition. E' and E" are the excitonic states formed by the splitting of the excited state level and E represents the energy level of the monomer. The out-of-phase dipole arrangement corresponds to an electrostatically interacted lower of energy level, so E' lies lower than the van der Waals displaced states of the component molecules. The in-phase dipole interaction gives repulsion, so energy level possesses higher values, and E" is displaced upwards from the displaced origin. The transition moment is nothing but the vector sum of the individual transition dipole moments of the component molecules. Thus, transition from the ground state to the excitonic state E' appears to be forbidden (transition moment ~0), while transition from the ground state to the excitonic state E" is allowed (transition moment non zero). Thus this model clearly explains the reason of blue-shift in the singlet-singlet transition of the dimer (transition to higher energy level).[102]

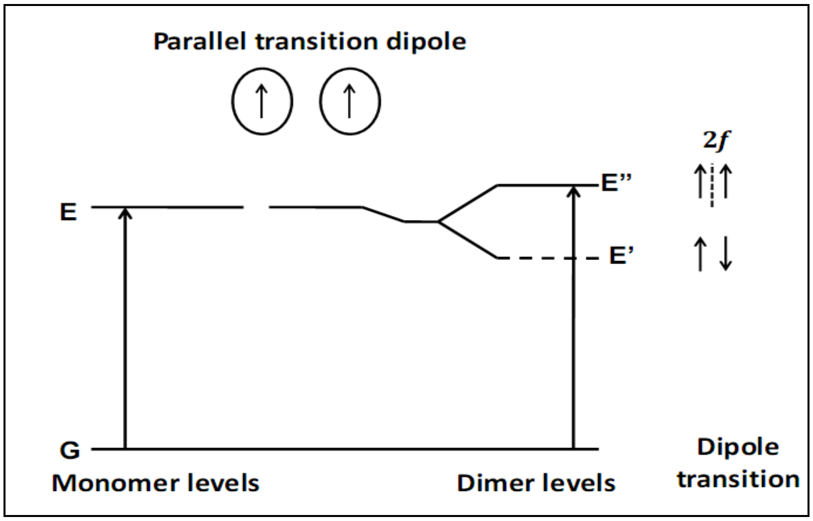

Figure 1.3: Splitting of energy levels in case of H-aggregates (blue shift case) taken from ref 103.

Following excitation to the allowed upper excitonic singlet state as shown in the figure 1.3, the rapid internal conversion between the singlet states dominates over the radiative transition from the allowed excitonic state to the ground state. As a result, the fluorescence signal from the allowed state to the ground state is rarely observed. The radiative transitions from the lower excitonic state to the ground electronic state are formally forbidden and thus these aggregates appear as non-fluorescent. However in a few rare cases, emissive H-aggregates are observed due to the distortions in the aggregate geometry leading to a small probability of transition, corresponding to lifetimes in the nano-second range.[104]

In the case of J-aggregates, the transition dipoles are polarized along the axis of a unit molecule (in-line in the dimer). Dimer with in-line transition dipoles lead to the excitonic energy level diagram shown in the following figure 1.4. From the diagram, it is clear that the in-phase arrangement of transition dipoles leads to an electrostatic attraction or stabilization as compared to the monomer energy level and produce the excited state E' of Figure 1.4, whereas the out-of-phase arrangement of transition dipoles causes repulsion, producing the state E". On the other hand, the transition moments possess nonzero value for electric dipole transitions from the ground state to E', and zero for the state E" from the ground state. Hence, in J-aggregates, lower energy transitions are allowed and they are responsible for the observed red shift in the absorption band.[103] The emission also comes from the low lying E′ state, since the radiative transition is allowed from this state to the ground state. Thus the J-aggregates show intense emission feature.

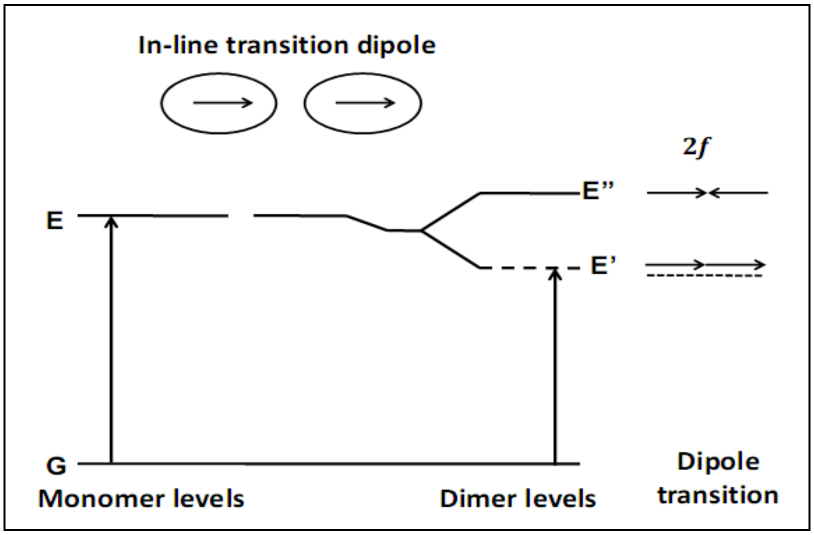

Figure 1.4: Splitting of energy levels in the case of J-aggregates (red shift case) taken from ref 103.

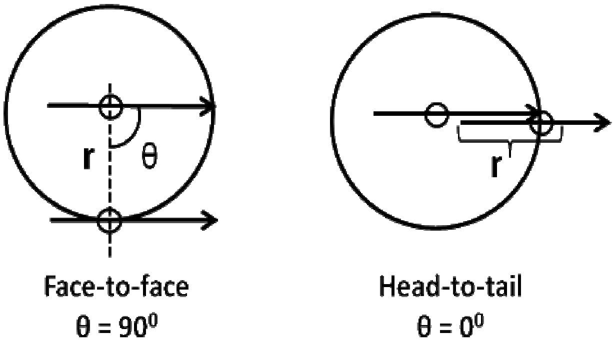

Figure 1.5: Two transition dipoles in the "face-to-face" (θ = 90◦) and "head-to-tail" (θ=0◦) orientations taken from ref 105.

In real case the molecular transition dipole may have different angles. Figure 1.5 illustrates the overall situation of the transition dipole and orientation factor in different aggregates.[105] It is seen that the orientation factor becomes zero at $\theta=54.7^0$, the so-called "magic angle". In the larger angle region ($90^0 > \theta > 54.7^0$), a blue-shifted band is observed, whereas a red-shifted band is observed in the smaller angle region ($54.7^0 > \theta > 0^0$).

The splitting of the excitonic energy levels is given by $\Delta E = E' - E''$, which can also be represented in the form of equation showing direct relation with transition moment, relative angle.[105]

$$\Delta E = \frac{2\,|M|^2}{r^3{}_{uv}} \;(\cos \propto \; + \; 3\cos^2 \theta) \qquad (1.1)$$

Where M is the transition moment for the singlet—singlet transition in the monomeric form, r_{uv} is the centre to centre distance between two molecules u and v, α is the angle between polarization axes for the component absorbing units and θ is the angle made by the polarization axes of the unit molecule with the line of molecular centers. The transition moments to the excitonic states E' and E" are given by:

$$M' = \sqrt{2M\cos\theta} \qquad (1.2)$$

$$M'' = \sqrt{2M\sin\theta} \qquad (1.3)$$

A characteristic feature of exciton theory is illustrated by equation (1.1). It is seen that the splitting of the excitonic energy levels is directly related to the square of the transition moment for the component molecules. Thus, the greater the intensity of light absorption in the unit molecule, the greater is the excitonic band splitting. Also the splitting of enrgy levels is inversely proportional to the cube of the intermolecular distance. The square of the transition moment, M, is a measure of the oscillator strength, f, for the transition.

The above described theoretical approach explains the change in the photophysical behavior of the nanosized molecular aggregates from the bulk materials or monomers. The difference is mainly caused due to the newly generated excitonic levels through splitting of the single molecular electronic transition level. The excited state relaxation dynamics in the aggregates are dominated by the characteristic excitonic decay processes. A concise account of the theory related to exciton dynamics is given in the next section of the chapter.

1.3. PHOTOINDUCED EXCITED STATE PROCESSES

1.3.1. PHOTOCHEMISTRY IN MOLECULAR SYSTEMS

Asorption of Light, and Electronic Transitions in Molecules: When an atom or a molecule is exposed to the electromagnetic radiation, the electric filed generated by the radiation induces an oscillating dipole within the atom or molecule by disturbing its surrounding electronic cloud. When the frequency of the incident radiation (ν) matches with the natural frequency (ν_n) of the oscillating dipole, the light gets absorbed by the atom or molecule and it is transferred to the electronically excited state having higher energy.[1]

$$\nu_n = \frac{E_n - E_i}{h} = \frac{\Delta E}{h} \qquad (1.4)$$

Where, $\Delta E = E_n - E_i$ is the energy difference between the initial (E_i) and final (E_n) energy states of the molecule and *h* is the Planck's constant.

The rate of photon absorption is governed by the Lambert-Beer's Law which states that, light absorbed by a medium is independent of the intensity of incident radiation (I_0) but proportional to the number of molecules absorbing the radiation, i.e, concentration (C) and path length (l).[1]

$$-\frac{dI}{I} = \alpha_\nu c\, dl \qquad (1.5)$$

Where α_ν is the proportionality constant, c is the concentration and dl is the thickness of the medium. Solution the above differential equation provides,

$$\ln\frac{I_0}{I} = \alpha_\nu\, C\, l \quad or \quad \log\frac{I_0}{I} = \varepsilon_\nu\, Cl \; = OD \qquad (1.6)$$

Where, $\varepsilon_\nu = \alpha_\nu/2.303$ is molar exctinction coefficient and is the function of the absorption frequency ν. This quantity, $\log I_0/I$ is called as absorbance (A) or optical density (OD) of the medium.

Absorption of light by a molecule leads to its excitation to the higher electronic level. The transition depends upon the nature of the molecular orbitals involved in the process. A convenient notation, developed by M. Kasha, is used to express the electronic states in terms of the initial and final orbitals involved in the transition.[1,107] Commonly, organic molecule possesses σ, π and n orbitals depending upon the electronic overlap between the two atomic orbitals. An electron from any one of the lower occupied orbitals get transferred to the higher unoccupied orbitals e.g. σ^* or π^*, following absorption of light of suitable energy. The n-electrons (nonbonding electrons) are excitable with relatively lower energy radiation and give rise to the longest wavelength absorption band. When an n-electron is excited to a π^* orbital, it is designated as ($n\rightarrow\pi^*$) transition. When a π electron is promoted, it may be a ($\pi\rightarrow\pi^*$) or ($\pi\rightarrow\sigma^*$) transition, depending on the final energy level of π^* and σ^* respectively. The ($\sigma\rightarrow\sigma^*$) transitions are also possible but require much higher energy and may appear in the far UV region. Schematic of these transitions are shown in Figure 1.6. The work presented here mainly focused on $\pi\rightarrow\pi^*$ and $n\rightarrow\pi^*$ transitions in molecules and aggregates.

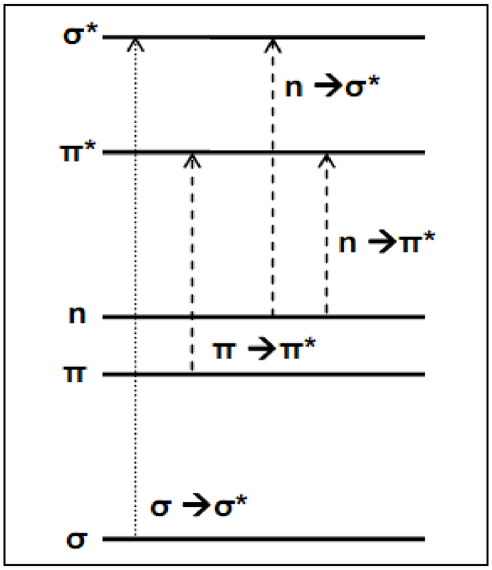

Figure 1.6: Approximate energy level diagram showing different types of transitions in organic molecules.

Electronic states signify the properties of all the electrons in all of the orbitals. Transition of an electron from one orbital to another will result in a change in the electronic state of the molecule. Hence proper designation and characterization of these states is necessary. The representation considering the overall symmetry of the corresponding MO is the most useful way to designate an electronic energy state of a molecule. However, this method can produce difficulties for polyatomic molecules, where the details of the electronic structures are not known. The most common method for such complex molecules is to denote the energy states simply by their spin multiplicity, defined as 2S+1, where S is the spin quantum number. Thus, an electronic state with all its electrons spin-paired has S = 0, multiplicity = 1. Such electronic states are referred as the *singlet states* and denoted by the symbol "S". While electronic states with two electrons having parallel spin i.e. S = 1, multiplicity = 3, called *triplet states* and represented by "T". For most of the organic molecules the ground electronic state is singlet and conventionally denoted by S_0. The higher electronically excited singlet states are represented as S_1, S_2, S_3 etc., where the subscript refers to the energy ranking of the state relative to the ground state. Triplet states are represented as T_1, T_2, T_3 etc. T_1 state has lower energy than that of the lowest singlet excited state, S_1. This lowering of the T_1 state energy is due to the spin correlation. The presence of two parallel electrons in the triplet state in two different orbitals reduces the electron-electron repulsion that is present in the singlet state. This reduction in repulsion energy makes the triplet state lower in energy as compared to the corresponding singlet state.

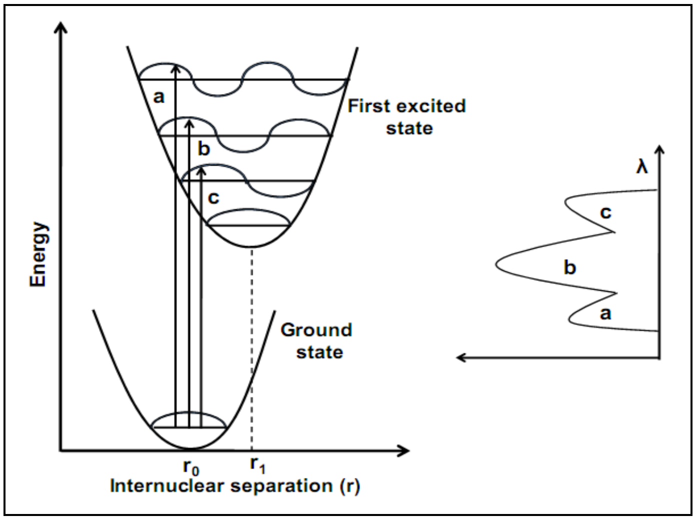

Figure 1.7: A schematic illustration of Franck-Condon principle. According to Franck-Condon principle, the electronic transition takes place so rapidly that the internuclear distances in a molecule do not change to any appreciable extent during transition.[106-109] This is because the electrons are thousand times lighter than nuclei. Thus, at the time of excitation, the internuclear separations in the excited state remain the same as that in the initial ground state. Alternatively, Franck-Condon principle can be stated as: "*transition between two electronic states occur vertically in the potential energy diagram.*"

The intensity of a vibronic transition depends directly on the probabilities of finding the molecule in the two respective vibrational levels involved in the lower and higher electronic states. For a particular vibronic transition, if the wave functions of the two vibrational levels of the lower and higher excited states have better spatial overlap, the transition will be stronger. If the spatial overlap of the two vibrational states involved is poor, the transition will be weaker. Figure 1.7 illustrates a few electronic transitions in accordance with the Franck-Condon principle. According to this figure, the transition ‘b’ is the most intense one whereas the transitions ‘a’ and ‘c’ are relatively much weaker. It is clear from Figure 1.7 that if the equilibrium internuclear separation in the two electronic states involved in the transition remains the same (i.e. r_0=r_1) the 0-0 vibrational transition will be the most intense one.

Generally, molecular transitions follow some selection rules, which govern the possibility of transition between two given energy states.[106-109]

(i) $\Delta l = 0, \pm 1$ i.e. during an electronic transition, the total orbital angular momentum (Δl) either does not change or changes by ± 1.

(ii) $\Delta S = 0,$ i.e. during an electronic transition, total spin angular momentum, (S), is conserved. As a consequence, transitions are allowed only between singlet-singlet and triplet-triplet states. The singlet-triplet transitions are forbidden, unless some perturbing influences bring about spin-orbit coupling.

(iii) Symmetry properties of the energy states must be conserved.

1.3.2. EXCITED STATE PROCESSES IN THE MOLECULE

A molecule excited to higher energy state eventually returns to the ground state, without losing its identity unless it is involved in any photochemical reaction. For a polyatomic molecule, in condensed phase (e.g solutions, liquids and solids) there are more than one pathways available for the excited molecule for dissipation of its excitation energy. These different modes of de-excitation are grouped under photophysical processes occurring in the electronically excited molecules. Some of them are intrinsic properties of the molecule and are unimolecular while some others depend on the external perturbations and involve bimolecular interactions.

The characteristics of the excited states of the molecule determine the photophysical processes taking place following photoexcitation. Even the chemical reactivity of the molecule changes with the change in its electronic state. Thus a complete knowledge of the photophysical processes and especially the partitioning of the absorbed photon energy in different channels are necessary to understand and formulate a detailed mechanism of a photochemical reaction.

These de-excitation pathways are often classified into two broad groups: (1) radiative processes, that involve the emission of electromagnetic radiation by the excited state molecules and (2) non-radiative processes, in which the depopulation of the excited states takes place without accompanying any photoemission. Radiative and non-radiative processes mentioned here are usually unimolecular processes. Different unimolecular photophysical processes that an excited molecule may undergo are represented by famous Jablonsky diagram (Figure 1.8).

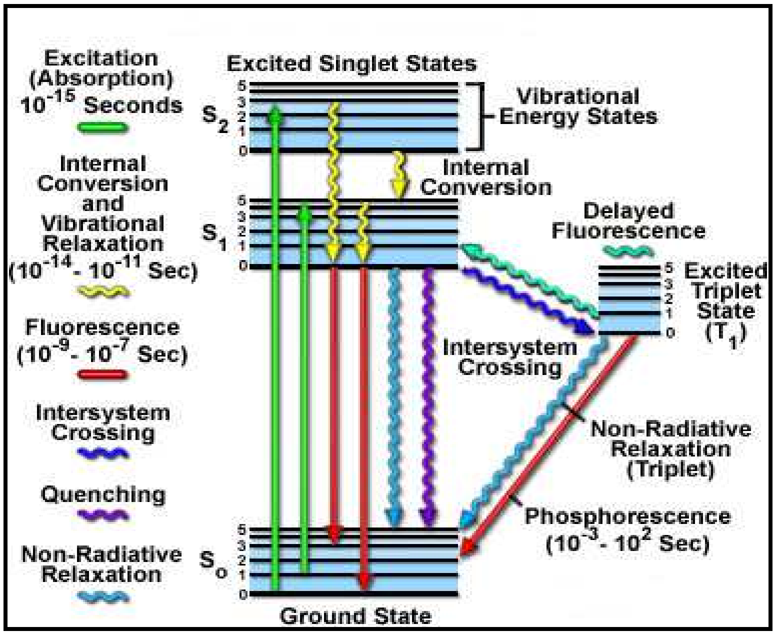

Figure 1.8: Jablonski diagram describing photophysical processes in organic molecules.

Kinetic parameters associated with these processes, e.g. rate of the reaction, lifetimes, etc may be given as follows.

Table 1.1: Reactions along with their rate constants for different unimolecular processes taking place during de-excitation of the excited molecule.

	Process	Reaction	Rate
I	Excitation	$S_0 + hv \rightarrow S_n$	I_a
Ii	S_n to S_1 Internal Conversion (IC)	$S_n \rightarrow S_1 + heat$	$k_{IC}[S_n]$
Iii	S_1 to S_0 Internal Conversion (IC)	$S_1 \rightarrow S_1 + heat$	$k_{IC}[S_1]$
Iv	Fluorescence	$S_1 \rightarrow S_0 + hv_f$	$k_f[S_1]$

V	S_1 to T_1 Intersystem Crossing (ISC)	$S_1 \rightarrow T_1 + heat$	$k_{ISC}[S_1]$
Vi	Phosphorescence	$T_1 \rightarrow S_0 + h\nu_p$	$k_p[T_1]$

In the above equations, S_n, S_1, S_0, and T_1 denote the respective electronic states of the molecule.

Under photostationary conditions, we get, rate of formation = rate of decay

$$I_a = k_{IC}[S_n] = \{k_f + k_{IC} + k_{ISC}\}[S_1] \tag{1.7}$$

$$or, [S_1] = \frac{I_a}{k_f + k_{IC} + k_{ISC}} \tag{1.8}$$

By definition, fluorescence quantum yield (ϕ_f) is given by

$$\phi_f = \frac{rate\ of\ fluorescence}{rate\ of\ light\ absorption} = \frac{k_f[S_1]}{I_a} \tag{1.9}$$

Introducing the value of $[S_1]$ from equation 1.8 into the equation 1.9 we get,

$$\phi_f = \frac{k_f}{k_f + k_{IC} + k_{ISC}} \tag{1.10}$$

Similarly, quantum yield for the triplet system (ϕ_T) is given by

$$\phi_T = \frac{k_{isc}[S_1]}{I_a} = \frac{k_{ISC}}{k_f + k_{IC} + k_{ISC}} \tag{1.11}$$

The observed fluorescence lifetime (τ_f) is the lifetime of the fluorescing state (usually S_1 state) and can be expressed as

$$\tau_f = \frac{1}{k_f + k_{IC} + k_{ISC}} = \frac{1}{k_f + k_{NR}} \tag{1.12}$$

Where, $k_{NR} = k_{IC} + k_{ISC}$ and represents the total nonradiative rate constant. The fluorescence and nonradiative rate constants can be calculated by using following expressions.

$$k_f = \frac{\phi_f}{\tau_f} \qquad (1.13)$$

$$k_{NR} = k_{IC} + k_{ISC} = \tau_f^{-1} - k_f \qquad (1.14)$$

Similarly, rate of intersystem crossing i.e. formation of the triplet state may be obtained from eq. 1.15,

$$k_{ISC} = \frac{\phi_T}{\tau_f} \qquad (1.15)$$

The values for ϕ_f, ϕ_T and τ_f may be obtained experimentally. The rate constant for internal conversion may be calculated as,

$$k_{IC} = \frac{1 - (\phi_T + \phi_f)}{\tau_f} \qquad (1.16)$$

The above mentioned processes are the most common excited state unimolecular diexcitation processes. However, there may be some other kind of photophysical processes e.g. structural relaxation, charge transfer, solvation etc. for different molecules in different kinds of solvent systems.[106-112] Molecules also may undergo bimolecular diexcitation processes e.g. photochemical reaction, quenching via resonance energy transfer, excimer or exciplex formation etc.[106] In this thesis, the systems presented are found to have significant contributions of these bimolecular processes in the di-excitation process.

1.3.3. PHOTOINDUCED EXCITED SPECIES IN MOLECULAR AGGREGATES: EXCITONS AND ITS DYNAMICS

Exciton is considered as a bound state of an electron and a hole, which are bound to each other through the electrostatic Coulomb force.[106] It is an electrically neutral quasiparticle that exists in insulators and semiconductor materials. When these materials are excited through photon absorption or thermally the excitons are generated and it is regarded as an elementary excitation of condensed matter that can transport energy without transporting net electric charge.[106]

Generally the excitons are of two types, (1) Wannier excitons and (2) Frankel excoitons.[106,113, 114] Wannier excitons are mostly associated with the inorganic semiconductors, quantum dots or metallic nanoparticles.[113] These materials possess high dielectric constants due to their columbic interaction between the counter ions. It causes weak interaction between the electron and the hole associated with a single exciton. As a result, these excitons possess low exciton binding energy and the exciton Bohr radius, which is the average radius between electron and hole is quite long (few nm). Here the excited electron distribution function covers many lattice sites.

Molecular excitons, also known as Frenkel excitons where the electron-hole pairs are strongly bound to each other.[114] Organic semiconductors are generally low dielectric materials and as a result the coulambic force existing between the electron and the hole are very strong and the exciton Bohr radius is very short. The exciton binding energy for Frankel excitons are in the order of eV range. On the other hand the binding energies of Wannier excitons are almost one to two orders smaller. In this present thesis as we are mainly interested about the exciton dynamics of organic nanoaggregates. Therefore, only Frenkel excitons are considered in further discussion in this thesis.

The spectroscopic properties of molecular aggregates is related with their collective excited states, characterized by molecules interacting together to capture or redistribute excitation energy. Excitons are quasiparticles exist at those collective excited states. These excitons can be formed by association of free charge carrier units (e.g. electron and electron hole) or by direct photoexcitation. For an aggregate of N molecular units, the excitonic band will consist of N discrete excitonic states; again characteristically, only one or a very few (equal in number to the number of molecules per unit cell) of these excitonic states for the aggregate can be reached by allowed electric-dipole transitions. Photoexcitation creates an electron in the conduction band, leaving a ‘hole’ in the valence band. If the interaction between the electron and hole is assumed to be negligible, which is justified when each wavefunction is spread over an expanse of atoms, then the pairs are free carriers. On the other hand, an attractive coulombic interaction between the electron and hole ‘quasi-particles’ binds them into an exciton.

The decay dynamics of the excitonic state decides the application of these molecular systems.[115] The assemblies where the electron and the hole recombine with each other through emission of a photon and having high emission yield can be used in organic light-emitting diode technologies. Again, materials where the excitons, that are formed through photoexcitation, may dissociate into free carriers (unbound electrons and holes), are useful in photovoltaic and solar cell device applications.

The well known example of involvement of excitons is the natural light harvesting assembly, i.e. photosynthesis units comprising of aggregated chlorophyll molecules which absorb the visible light and stored it in the form of chemical energy.[116] The process takes place through many steps and can be briefly summarized as, light absorption causes generation of excitons in the chlorophyll molecular aggregate. The photogenerated excitons migrate in the next step via different molecular units in a light-harvesting complex towards a reaction center. These excitons undergo charge separation at the interface of the reaction centre producing a positively and a negatively charged species. These charged species set off a series of chemical reactions, which eventually end in conversion of part of the incident solar energy into chemical energy. This rapid exciton migration within such aggregate systems leading to efficient conversion of excitons into charged species has inspired for utilization in organic based photovoltaic cells for solar energy hervestation.[10-12]

Molecules having long π-conjugated systems are considered as organic semiconductors absorb in the near UV and visible region. Stacking of π-electron clouds in these molecular systems favors to form stable molecular aggregates. Self assembled molecular aggregates of polyacene, phthalocyanine and porphyrin derivatives aggregated into structures, which are analogues to such light harvesting systems and contain π-stacked molecules that can provide pathways for efficient exciton and charge transport.[117] These materials have strong optical absorption, which can extend into the red part of the solar spectrum to a wavelength as long as 800 nm. Therefore these materials are of great interest for application in photovoltaic devices, organic light emitting diodes etc.[10-12, 118, 119] Detailed photophysical study based on the aggregation of polyacenes and phthalocyanines are presented in the following chapters of this thesis. Excited state relaxation dynamics of these aggregates are dominated by the exciton dynamics or the excited states of the aggregates. Hence it is necessary to understand the basic concepts and the factors affecting the exciton dynamics processes.

1.3.4. Exciton - Exciton Annihilation in Molecular Aggregates

It is already discussed that, upon photoexcitation of molecular aggregates Frenkel excitons are generated and start to hop from one center to other. This hoping of excitons results exciton diffusion process. During this exciton diffusion process, if the density of the photo-generated excitons is large enough, then there is a possibility that two excitons can come to a distance where they can interact with each other and can participate in the energy transfer process. At large exciton density, one of the most common second order photophysical processes is the exciton - exciton annihilation reaction.[120-128] The annihilation process becomes evident from a decrease in the excited-state lifetime and a decrease in integrated fluorescence quantum yield with increasing excitation intensity.[120-123]

The annihilation process may occure by the interaction of excitons having same or different spin multiplicities. However, following photoexcitation singlet - singlet exciton annihilation process becomes dominating in the initial 10-100 ps time domain. The triplet - triplet exciton annihilation process is also highly probable for aggregates having sufficiently high triplet exciton quantum yield. The interaction between the singlet and triplet excitons are relatively less favored and has negligible contribution. During the annihilation process, one exciton transfer its energy to the other and goes back to the ground state non-radiatively. tThe second exciton excited to higher excited state, which further decays through vibrational relaxation and IC process to the lowest excited state level.[129] Thus annihilation process added as an alternative decay path for excitons along with their natural decay processes. Here, we have represented the excited state processes which take place under high exciton density after photoexcitation of molecular aggregates.

Free S_1 excitonic state undergoes the following photophysical processes.

$$S_1 \xrightarrow{k_1} S_0 \qquad (1.17)$$

$$S_1 + S_1 \xrightarrow{k_2} S_0 + S_n \qquad (1.18)$$

The generation of two triplet excitons from the annihilation reaction between two singlet excitons is possible form spin multiplicity conservation rule but in general it is rarely observed for molecular aggregates. The reaction scheme presented in equation 1.18 is the most probable and we have focused on this reaction scheme for analysis of the works presented in this thesis. In this thesis, the major part has been attributed to the exciton dynamics. Thus, at high exciton density, exciton annihilation reaction may have a significant contribution to the exciton decay process. Not only that, the exciton – exciton annihilation process is diffusion controlled and directly related to the exciton diffusion parameters. Therefore, estimation of excton – exciton annihilation rate constant and exciton diffusion parameters become important. The estimation of exciton – exciton annihilation rate constant is possible by solving the differential equation representing the rate of change of S_1 excitons.[129] The expression for the rate of change of concentration of the S_1 excitonic state for the above case may be written as,

$$\frac{d[S_1]}{dt} = -k_1[S_1] - \frac{k_2[S_1]^2}{2} \qquad (1.19)$$

Here k_1 represents the annihilation free decay of the excitonic state. k_2 is the rate constant for the exciton – exciton annihilation reaction. Solution of the eq. 1.19 gives us the concentration of the S_1 excitonic state at a particular time t, $[S_1]_t$.

$$[S_1]_t = [S_1]_0 \frac{\exp(-k_1 t)}{(1 + k'_2\, t)} \qquad (1.20)$$

Here $k_2' = k_2 [S_1]_0 / 2$ (1.21)

Any signal, which is proportional to the S_1 excitonic state population, will also follow the equation. The signal may be the fluorescence emission from the S_1 excitonic state or the excited state absorption signal. We may observe time dependence of these signals and fit the experimental data using equation 1.20 to find out the value of k_2'. The slope of k_2' vs. $[S_1]_0$ plot can be used to estimate the exciton - exciton annihilation rate constant. According to the equation 1.21 the k_2' vs. $[S_1]_0$ plot should pass through the origin when, $[S_1]_0$ become 0. But in reality at low exciton density, the k_2' value become zero even when $[S_1]_0$ possess non-zero value. This exciton density may be considered as the threshold of annihilation and useful for estimation of the exciton annihilation radius of the material. When the exciton density is less than this threshold value, there is a little chance for excitons to come sufficiently close to participate in the exciton - exciton annihilation process.[120,129]

Exciton diffusion, diffusion parameters and their importance

Excitons produced under photoexcitation generally do not remain restricted to one molecular centre in molecular aggregates. Instead it hops from one center to the other following random walk model. The exciton diffusion property is quantified by exciton diffusion coefficient of the material. As we have mentioned earlier that, exciton – exciton annihilation process take place through exciton diffusion and basically it is a diffusion controlled process. Therefore the exciton – exciton annihilation rate constant (k_2) has a direct relation with the exciton diffusion coefficient (D) of the material.[120, 129] The relation is presented as,

$$k_2 = 8\pi D R_a \qquad (1.22)$$

Here, R_a represents the exciton annihilation radius for that material.

Now, this exciton diffusion coefficient is also directly related with the exciton hopping time (τ_{Hopp}) and exciton diffusion length (L_d) by equations 1.23 and 1.24. These are two important parameters of the material for optoelectronic or photovoltaic applications. The exciton hopping time basically indicates the average time required for excitons to transfer from one center to the other residing at its neighborhood. The lower value of τ_{Hopp} indicates faster hopping of excitons and favorable for efficient optoelectronic application. On the other hand, the exciton diffusion length is defined as the mean distance traveled by excitons during its lifetime.[120,129] For photovoltaic application, specifically after photogeneration of excitons, it needs to travel through diffusion to the donor acceptor interface where charge separation can take place. The excitonic processes, which occur in a photovoltaic device, are schematically represented in Figure 1.9. Therefore, a material having long exciton diffusion length is always desired for photovoltaic application, because there will be more chance for the excitons to reach to the donor – acceptor interface where charge separation will take place and may provide larger photovoltaic efficiency.[130,131]

$$\tau_{Hopp} = \frac{d^2}{6D} \qquad \text{(Here, d is the inter molecular separation)} \qquad (1.23)^{132}$$

$L_D = (6D\tau)^{1/2}$ (1.24)

The equation for exciton diffusion length represented here is valid for three dimensional exciton diffusion in the material.[129] If the exciton diffusion restricted to one or two dimensional then the constant number 6 needs to be replace by 2 or 4, respectively.[120,129, 132]

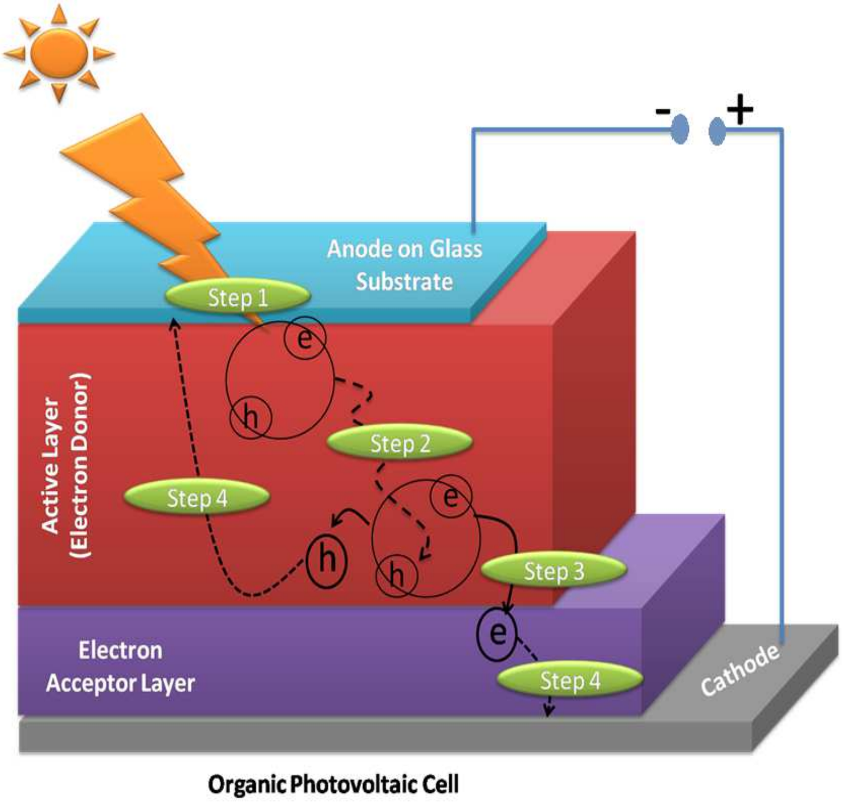

Figure 1.9: Excitonic processes involved in the photovoltaic device.

1.4. SCOPE OF THE THESIS

1.4.1. PROBING MICROSCOPIC NATURE OF RTIL SOLVENTS AND ITS EFFECT ON ELECTRON AND ENERGY TRANSFER REACTIONS

Several groups have tried to probe the heterogeneous nature of these solvents, by studying some basic chemical processes like hydrogen atom transfer, electron transfer, solvation dynamics, etc.[133-146] Electron transfer (ET) being the soul of a redox process, several reports have been published on the study of ET processes in RTIL media.[134-144] Skrzypczak and Neta have reported that the ET rate in a RTIL is about an order of magnitude larger as compared to the calculated diffusion controlled rate in the same medium.[134] To explain the reason for this difference, they predicted the existence of voids in ionic liquids and the possibility that diffusion of reacting species took place through movement of segments of the ions while the viscosity was related to the movement of the whole ions. Paul and Samanta observed that the rate of photo-induced electron transfer (PET) reactions is 2-4 fold higher than the diffusion-controlled value and they suggested that the microviscosity around the electron donor and acceptor was different from the bulk viscosity of the RTILs.[135]

Recently Maroncelli and co-workers showed that, like in RTIL, the faster rate of an ET process could also be observed in conventional organic solvents of similar viscosity.[143] They proposed a model to explain that the following two factors were responsible for faster ET rate in highly viscous solvents. Firstly, the quenching took place in the transient regimes due to the short-lived nature of the transients and hence the diffusion controlled ET process was not observed. Secondly, the reactants possessed lower hydrodynamic radius than that of the solvent and hence they could diffuse much faster than the expected diffusion rate. Hence, they recommended that ET reaction involving long-lived transients should be an ideal probe to observe the ET process in the diffusion controlled regime.

In a recent communication, Vauthey and co-workers described the dynamics of PET reaction between N,N-dimethylaniline and the excited state of 3-cyanoperylene in three RTILs [namely, 1-ethyl-3-methyl-imidazolium dicyanamide (BMIDCA), 1-butyl-3-methyl-imidazolium dicyanamide (EMIDCA) and 1-ethyl-3-methyl-imidazolium ethylsulfate (EMIES)] as well as in the binary mixtures of two conventional solvents (DMSO and Glycerin) of similar viscosities.[144] They concluded that in all these cases, the diffusive motion of the reactants was very similar in RTILs and conventional solvents of comparable viscosity. They assigned the reason for the faster ET process in RTILs to the highly viscous nature of the solvents, but not related to the ionic nature of the RTILs. Faster ET rate in highly viscous solvents was explained by considering three quenching regimes, namely, *static, transient and stationary*. In the case of highly viscous solvents, transients having lifetimes of a few nanoseconds get quenched mainly in the *static and transient regime* and the average ET rate appears faster than the diffusion controlled rate.

Vauthey and coworkers used the diffusional encounter theory (DET) to calculate the time-dependence of the ET rate, which decreases steadily while passing through the static and transient regimes and the stationary value is attained after more than a few nanoseconds in the solvents of low viscosities.[143,144] The most important results reported by Vauthey and co-workers revealed that while the rate of intrinsic ET reaction occurring in the static and transient regime is controlled by the free energy of reactions, solvent dynamics and concentration, the rate of the ET reaction as well as the onset of the stationary quenching regime, depend entirely on the viscosity of the solvent and not on its dipolar or ionic nature. Time dependence of the rate coefficients calculated using DET revealed that the stationary value, k_{diff}, is attained only after few hundred nanoseconds in the case of solvents of very large viscosity (say, ~100 cP). In the *stationary regime*, quenching is only possible after substantial diffusion and an equilibrium between the diffusional formation of the reactant pairs and their decay upon reaction is attained, giving rise to a constant reaction rate.[144]

Therefore to observe the reaction process in the stationary condition in these viscous RTIL media one should have long lived transients e.g. excited triplet state, anion radicals etc.[106, 119] We can generate these long lived species by using flash photolysis and/or pulse radiolysis techniques and monitor the energy transfer or electron transfer reaction in the stationary conditions. So in these present thesis, we have tried the same using the above two techniques and observe the triplet energy transfer and electron transfer reactions. First we have aimed to verify, whether we could see the diffusion controlled reaction rate in RTILs media by using such long lived transients. Secondly, we would like to observe the effect of the presence of long alkyl chain substituents in the cataionic part of the RTILs in the microscopic pocket formation. We observed how the above reaction rate constants were affected by this microscopic domain formation. We could also provide some insight about the microscopic viscosity of these pockets.

1.4.2. EXPLORATION OF EXCITON DYNAMICS AND ESTIMATION OF EXCITON DIFFUSION PARAMETRS IN ORGANIC NANOAGGREGATES

As we mentioned earlier that the organic nanoaggregates are potential material for optoelectronic, photovoltaic device applications.[118,147,148] Working efficiency of these devices mainly depends upon the excitonic property and, therefore, exploration of exciton dynamics and exciton diffusion parameters are essential.[115] However, for this purpose, plenty of verities of organic dyes are available. But for our primary investigations, we have chosen some basic polyacene molecules namely, anthracene, pyrene, perylene etc. These are extended π-conjugated systems and suitable for π-π interaction. These molecules can produce stable aggregates, have strong absorption in the near UV-Visible region, possess high emission yield, can arrange in different crystalline phase.[106] Thus we can understand different aspects of the aggregates, and corresponding effect on the exciton dynamics and excited state photophysics. Depending upon their emission spectral range, emission yield and other related issues, we may infer their applicability in emission or display devices. On the other hand, depending upon the exciton lifetime and exciton diffusion properties, we may provide some ideas about the suitability of their applications in photovoltaic devices. In the last part, our focus will be on the study of exciton dynamics and diffusion properties of aggregates of different phthalocyanine derivatives. We observe the effect of introduction of bulky ^{t}Bu group and one more π-conjugated aromatic ring in the four peripheral positions, Zn^{2+} ion complex formation upon the above mentioned properties.

1.5. REFERENCES

1. Banwell. C. N.; McCash, E. M. *Fundamental of Molecular Spectroscopy*, Tata McGraw-Hill Education, Fourth Edition, London, **1994**.

2. Struve, W. S. *Fundamental of Molecular Spectroscopy*, A Wiley-Interscience Publication, New York, **1989**.

3. Hohenberg, P.; Kohn, W. "Inhomogeneous electron gas". *Phys. Rev.* **1964**, *136 (3B)*: B864.

4. Runge, E.; Gross, E. K. U. "Density-Functional Theory for Time-Dependent Systems". *Phys. Rev. Lett.* **1984**, *52 (12):* 997.

5. Kerton, F.; Marriott, R. *Aternative Solvents for Green Chemistry: edition 2*. RSC Publishing, **2013**

6. Rogers, R. D.; Seddon, K. R. *Ionic Liquids as Green Solvents*, ACS Symposiym Series, **2003**, 856.

7. Miles, R. W.; Zoppi, G.; Forbes, I. *Mateials Today*, **2007**, *10*, 20.

8. Hagfeldt, A.; Boschloo, G.; Sun, L.; Kloo, L.; Pettersson, H. *Chem. Rev*. **2010**, *110*, 6595.

9. Carrey, G. H.; Abdelhady, A. L.; Ning, Z.; Thon, S. M.; Bakr, O. M.; Sargent, E. H. *Chem. Rev*. **2015**, *115*, 12732.

10. Günes, S.; Neugebauer, H.; Sariciftci, N. S. *Chem. Rev.* **2007**, *107*, 1324.

11. Clarke, T. M.; Durrant, J. R. *Chem. Rev.* **2010**, *110*, 6736.

12. Lu, L.; Zheng, T.; Wu, Q.; Schneider, A. M.; Zhao, D.; Yu, L. *Chem. Rev.* **2015**, *115*, 12666.

13. Lin, J. F.; Tu, G. Y.; Ho, C. C.; Chang, C. Y.; Yen, W. C.; Hsu, S. H.; Chen, Y. F.; Su, W. F. *ACS Appl. Mater. Interfaces*, **2013**, *5*, 1009.

14. Ikeda, N.; Koganezawa, T.; Kajiya, D.; Saitow, K. I. *J. Phys. Chem. C.* **2016**, *120*, 19043

15. Tsao, J. Y.; Saunders, H. D.; Creighton, J. R.; Coltrin, M. E.; Simmons, J. A. *J. Phys. D: Appl. Phys.* **2010**, *43*, 354001

16. Narukawa, Y.; Ichikawa, M.; Sanga, D.; Sano, M.; Mukai, T. *J. Phys. D: Appl. Phys.* **2010**, *43*, 354002

17. Kim, J. H.; Han, C. Y.; Lee, K. H.; An, K. S.; Song, W.; Kim, J.; Oh, M. S.; Do, Y. R.; Yang, H. *Chem. Mater.* **2015**, *27*, 197.

18. Yantara, N.; Bhaumik, S.; Yan, F.; Sabba, D.; Dewi, H. A.; Mathews, N.; Boix, P. P.; Demir, H. V.; Mhaisalkar. S. *J. Phys. Chem. Lett.* **2015**, *6*, 4360.

19. Bolink, H. J.; Coronado, E.; Sessolo, M. *Chem. Mater*. **2009**, *21*, 439.

20. Lo, S. C.; Burn, P. L. *Chem. Rev.* **2007**, *107*, 1097.

21. Buckley, A. *Organic Light-emitting Diodes*, Woodhead Publishing Limited, **2013**.

22. Sekine, C.; Tsubata, Y.; Yamada, T.; Kitano, M.; Doi, S. *Sci. Tech. Adv. Mat.* **2014**, *15*, 034203

23. Lehn, J. M. *Science,* **1993**, *260*, 1762.

24. Whitesides, G. M.; Mathias, J. P.; Seto, C. T. *Science,* **1991**, *254*, 1312.

25. Ball, P. *Nature*, **1994**, *367*, 323.

26. Latterini, L.; Roscini, C.; Carlotti, B.; Aloisi, G. G.; Elisei, F.; *Phys. Stat. Sol. A* **2006**, *203*, 1470.

27. Chung, H. R.; Kwon, E.; Oikawa, H.; Kasai, H.; Nakanishi, H. *J. Crystal growth* **2006**, *294*, 459.

28. T.; Ogura, K.; Kawakami, Y.; Sugino, H.; Tanaka, J. *Chem. Phys. Lett.* **1998**, *291*, 438.

29. London, F. *Transactions of the Faraday Society* **1937**, *33*, 8.

30. Ehli, C.; Rahman, G. M. A.; Jux, N.; Balbinot, D.; Guldi, D. M.; Paolucci, F.; Marcaccio, M.; Paolucci, D.; Melle- Franco, M.; Zerbetto, F.; Campidelli, S.; Prato, M. *J. Am. Chem. Soc.* **2006**, *128*, 11222

31. Prins, L. J.; Reinhoudt, D. N.; Timmerman, P. *Angew. Chem. Int. Ed.* **2001**, *40*, 2383.

32. Rich, C. C.; McHale, J. L. *Phys. Chem. Chem. Phys.* **2012**, *14*, 2362

33. Sinnokrot, M. O.; Valeev, E. F.; Sherrill, C. D. *J. Am. Chem. Soc.* **2002**, *124*, 10887

34. Da Silva, C. H. T. P.; Campo, V. L.; Carvalho, I.; Taft, C. A. *J. Mol. Graphics Modell.* **2005**, *25*, 169.

35. Dougherty, D. A. *Science,* **1996**, *271*, 163.

36. Saenger, W.; *Principles of Nucleic Acid Structure,* Springer-Verlag: New York, **1984**, 132.

37. Wakelin, L. P. G. *Med. Res. Reo.* **1986**, *6*, 275.

38. Desiraju, G. R.; Gavezzotti, A. *Chem. Commun.* **1989**, 621.

39. Meyer, E. A.; Castellano, R. K.; Diederich, F. *Angew. Chem. Int. Ed.*, **2003**, *42*, 1210.

40. Hunter, C. A.; Leighton, P.; Sanders, J. K. M. *J. Chem. Soc., Perkin Trans.***1989**, *1*, 547.

41. Wang, K.; Qi, D.; Wang, H.; Cao, W.; Li, W.; Jiang, J. *Chem. Eur. J.* **2012**, *18*, 15948.

42. Contakes, S. M.; Beatty, S. T.; Dailey, K. K.; Rauchfuss, T. B.; Fenske, D. *Organometallics*, **2000**, *19*, 4767.

43. Gallivan, J. P.; Dougherty, D. A. *J. Am. Chem. Soc.* **2000**, *122*, 870.

44. Koizumi, T.; Tsutsui, K.; Tanaka, K.; *European Journal of Organic Chemistry* **2003**, *23*, 4528

45. Hunter, C. A.; Sanders, J. K. M.; *J. Am. Chem. Soc.***1990**, *112*, 5525

46. Walden, P. *Bull. Acad. Imp. Sci. St. Petersbourg*, **1914**, *8*, 405-422.

47. Evans, D. F.; Yamauchi, A.; Roman, R.; Casassa, E. Z. *J. Colloid Interface Sci.,***1982**, *88*, 89

48. Karpinski, Z. J.; Osteryoung, R. A. *Inorg. Chem.,* **1984**, *23*, 1491.

49. Zawodzinski, T. A.; R. A. Osteryoung, R. A. *Inorg. Chem.,* **1990**, *29*, 2842.

50. Mantz, R. A.; Trulove, P. C.; Carlin, R. T.; Osteryoung, R. A. *Inorg. Chem.,* **1995**, *34*, 3846.

51. Wilkes, J. S.; Levisky, J. A.; Wilson, R. A.,; Hussey, C. L. *Inorg. Chem.,* **1982**, *21*, 1263.

52. Wilkes J. S.; Zaworotko, M. J. *J. Chem. Soc., Chem Commun.,***1992**, 965.

53. Fuller, J.; Carlin, R. T.; De Long, H. C.; Haworth, D. *Chem Commun*., **1994**, 299.

54. Welton, T. *Chem. Rev*., **1999**, *99*, 2071.

55. Pârvulescu V. I.; Hardacre, C. *Chem. Rev*., **2007**, *107*, 2615.

56. Hallett. J. P.; Welton, T. *Chem.Rev*., **2011**, *111*, 3508.

57. Hapiot, P.; Lagros, C.; *Chem. Rev.* **2008**, *108*, 2238.

58. Welton, T. *Chem. Rev.* **1999**, *99*, 2071.

59. Wasserscheid, P.; Keim, W.*Angew. Chem., Int. Ed.***2000**, *39*, 3772.

60. Dupont, J.; de Suza, R. F.; Suarez, P. A. Z. *Chem. Rev.* **2002**, *102,* 3667.

61. Buzzeo, M. C.; Evans, R. G.; Compton. R. G. *Chem. Phys. Chem.* **2004**, *5*, 1106.

62. Chiappe, C.; Pieraccini, D. *J. Phys. Org. Chem.* **2005**, *18*, 275.

63. Rogers, R. D.; Seddon, K. R. *Science* **2003**, *302*, 792.

64. Seddon, K. R. *Nature Mater.* **2003**, *2*, 363.

65. Castner, E. W.; Wishart, J. F. *J. Chem. Phys.* **2010**, *132*, 120901.

66. Hallett, J. P.; Welton, T. *Chem. Rev.* **2011**, *111*, 3508.

67. Bai, Y.; Cao, Y.; Zhang, J.; Wang, M.; Li, R.; Wang, P.; Zakeeruddin, S. M.; Grätzel, M. *Nat. Mater.* **2008**, *7*, 626.

68. Bai, Y.; Zhang, J.; Wang, Y.; Zhang, M.; Wang, P. *Langmuir* **2011**, *27,* 4749.

69. Hardin, B. E.; Sellinger, A.; Moehl, T.; Humphry-Baker, R.; Moser, J. E.; Wang, P.;Zakeeruddin, S. M.; tzel, M.; McGehee, M. D. *J. Am. Chem. Soc.* **2011**, *133*, 10662.

70. Berthon, L.; Nikitenko, S. I.; Bisel, I.; Berthon, C.; Faucon, M.; Saucerotte, B.; Zorz, N.; Moisy. P. *Dalton Trans.* **2006**, 2526.

71. Thied, R. C.; Etter, J. E. H.; Seddon, K. R.; Pitner, W. R.; Rooney, D. W.; Hebditoh, D. *World Pat*., WO01/13379A1, 18 August **1999**

72. Dietz,M. L.; Dzielawa, J. A. *Chem. Commun,* **2001**, 2124.

73. Hapiot, P.; Lagros, C. *Chem. Rev.* **2008**, *108*, 2238.

74. Plechkova N. V.; Seddon, K. R. *Chem. Soc. Rev.,* **2008**, *37*, 123.

75. Li, S.; Bañuelos, J. L.; Guo, J.; Anovitz, L.; Rother, G.; Shaw, R. W.; Hillesheim, P. C.; Dai, S.; Baker, G. A.; Cummings, P. T. *J. Phys. Chem. Lett.* **2012**, *3*, 125.

76. Hardacre, C.; Holbrey, J. D.; McMath, S. E. J.; Nieuwenhuyzen, M. *ACS Symposium Series* **2009**, *818* (Chapter-31), 400.

77. Russina, O.; Triolo, A.; Gontrani, L.; Caminiti, R. *J. Phys. Chem. Lett.* **2012**, *3*, 27.

78. Aoun, B.; Goldbach, A.; González, M. A.; Kohara, S.; Price, D. L.; Saboungi, M. L. *J. Chem. Phys.* **2011**, *134*, 104509.

79. Urahata, S. M.; Ribeiro, M. C. C. *J. Phys. Chem. Lett.* **2010**, *1*, 1738.

80. Russina, O.; Gontrani, L.; Fazio, B.; Lombardo,D.; Triolo, A.; Caminiti, R. *Chem. Phys. Lett.* **2010**, *493*, 259.

81. Hardacre, C.; Holbrey, J. D.; Mullan, C. L.; Youngs, T. G. A.; Bowron, D. T. *J. Chem. Phys.* **2010**, *133*, 074510.

82. Bodo, E.; Gontrani, L.; Caminiti, R.; Plechkova, N. V.; Seddon K. R.; Triolo, A. *J. Phys. Chem. B* **2010**, *114*, 16398.

83. Annapureddy, H. V. R.; Kashyap, H. K.; Biase, P. M. D.; Margulis, C. J. *J. Phys. Chem. B* **2010**, *114*, 16838.

84. Habasaki, J.; Ngai, K. L. *J. Chem. Phys.* **2008**, *129*, 194501.

85. Wang, Y.; Jiang, W.; Yan, T.; Voth, G. *Acc. Chem. Res.* **2007**, *40*, 1193.

86. Triolo, A.; Russina, O.; Bleif H. F.; Cola, E. D.;*J. Phys. Chem. B* **2007**, *111*, 4641.

87. Xiao, D.; Rajian, J. R.; Li, S.; Bartsch, R. A.; Quitevis, E. L. *J. Phys. Chem. B* **2006**, *110*, 16174.

88. Wang, Y.; Voth,G. A. *J. Phys. Chem. B* **2006**, *110***,** 18601.

89. Lopes, J. A. C.; Padua, A. A. H. *J. Phys. Chem. B* **2006**, *110*, 3330.

90. Hu, Z.; Margulis, C. *Proc. Natl. Acad. Sci. U. S. A.* **2006**, *103*, 831.

91. Patra, S.; Samanta, A. *J. Phys. Chem. B* **2012**, *116*, 12275.

92. Sasmal, D. K.; Mandal, A. K.; Mondal, T.; Bhattacharyya, K. *J. Phys. Chem. B* **2011,** *115***,** 7781.

93. Greaves, T. L.; Drummond, C. J. *Chem. Soc. Rev.,* **2013**, *42*, 1096.

94. Lopes, J. N. C.; Shimizu, K.; Pádua, A. A. H.; Umebayashi, Y.; Fukuda, S.; Fujii, K.; Ishiguro, S. *J. Phys. Chem. B*, **2008**, *112*, 1465.

95. Hardacre, C.; Holbrey, J. D.; Mullan, C. L.; Nieuwenhuyzen, M.; Youngs, T. G. A.; Bowron, D. T. *J. Phys. Chem. B*, **2008**, *112*, 8049.

96. Castner Jr., E. W.; Margulis, C. J.; Maroncelli, M.; Wishart, J. F. *Annu. Rev. Phys. Chem.*, **2011**, *62*, 85-105

97. Scheibe, G. *Angew. Chemie* **1937**, *50*, 212.

98. Jelley, E. E. *Nature* **1937**, *139*, 639.

99. Conga, F.; Li, J.; Maa, C.; Gaob, J.; Duana, W.; Dua, X. *Spectrochimica Acta Part A* **2008**, *71*, 1397.

100. FitzGerald, S.; Farren, C.; Stanley, C. F.; Beeby, A.; Bryce, M. R. *Photochem. Photobiol. Sci.* **2002**, *1*, 581.

101. Wang, Y.; Liang, D. *Adv. Mater.* **2010**, *22*, 1521

102. Kasha, M.; Rawls, H. R.; Ashraf El-Bayoumi, M. *Pure Appl. Chem.,* **1965**, *11*, 371.

103. MacRae, E. G.; Kasha, M. "*The Molecular Exciton Model in Physical Processes in Radiation Biology*". Academic Press, New York, **1964**, 23.

104. Farren, C.; FitzGerald, S.; Beeby, A.; Bryce, M. R. *Chem. Commun*. **2002**, 572

105. Satake, A.; Kobuke, Y. *Org. Biomol. Chem.* **2007**, *5*, 1679

106. Rohatgi-Mukherjee, K. K. "*Fundamentals of Photochemistry*", Wiley Estern Ltd. India, **1986**

107. Jaffe, H. H.; Orchin, M.; *Theory and Application of Ultraviolet Spectroscop*y, Wiley, New York, **1962**.

108. Rice,O. K. *Electronic Structure and Chemical Bonding*, McGraw Hill, **1940**.

109. Murrell, J. N. *Theory of the Electronic Spectra of Organic Molecules*, Chapmann and Hall, **1970**

110. Simons, J. P. "*Photochemistry and Spectroscopy*", Wiley, New York, **1971**.

111. Parker, C. A. "*Photoluminescence in Solution*", Elsevier, Amsterdam, **1968**.

112. Lim, E. C. (ed), "*Excited States*", Academic Press, New York, Vol.1 1974; Vol.2, **1975**.

113. Wannier, G. H. *Phys. Rev.* **1937**, *52*, 191

114. Frenkel, J. *Phys. Rev.* **1931**, *37*, 17

115. Marinova, N.; Valero, S.; Delgado, J. L. *J. Colloid and Interface Science*, **2017**, *488*, 373.

116. Scholes, G. D.; Fleming, G. R. *Adv. Chem. Phys.* **2005**, *132*, 57.

117. Liu, J.; Zhang, H.; Dong, H.; Meng, L.; Jiang, L.; Jiang, L.; Wang, Y.; Yu, J.; Sun, Y.; Hu, W.; Heeger. A. *J. Nature Comm.* **2015**, *6*, 10032.

118. Liang, W. W.; Chang, C. Y.; Lai, Y. Y.; Cheng, S. W.; Chang, H. H.; Lai, Y. Y.; Cheng, Y. J.; Wang, C. L.; Hsu, C. S. *Macromolecules* **2013**, *46*, 4781.

119. Yu, J. Y.; Chen, I. W. P.; Chen, C. H.; Lee, S. J.; Chen, I. C.; Lin, C. S.; Cheng,C. H. *J. Phys. Chem. C* **2008**, *112*, 3097.

120. Paillotin, G.; Swenberg, C. E.; Breton, J.; Geacintov, N. E. *Biophysics J.* **1979**, *25*, 513.

121. Gulbinas, V.; Chachisvilis, M.; Persson, A.; Svanberg, S.; Sundström, V. *J. Phys. Chem.* **1994**, *98*, 8118.

122. Barzda, V.; Garab, G.; Gulbinas, V.; Valkunas, L. *Biochim. Biophys. Acta* **1996**, *1273*, 231.

123. Sundström, V.; Gillbro, T.; Gadonas, R.; Piskarskas, A. *J. Chem. Phys.* **1988**, *89*, 2754.

124. Gilbro, T.; Sandström, A.; Spangfort, M.; Sundström, V.; von Grondelle, R. *Biochim. Biophys. Acta* **1988**, *934*, 369.

125. Suna, A. *Phys. Rev B.* **1970**, *1*, 1716.

126. Siebbeles, L. D. A.; Huijser , A.; Savenije, T. J. *J. Mater. Chem.* **2009**, *19*, 6067.

127. Lunt, R. R.; Benziger, J. B.; Forrest, S. R. *Adv. Mater.* **2010**, *22*, 1233.

128. Rim, S.; Fink, R. F.; Schoneboom, J. C.; Erk, P.; Peumans, P. *Appl. Phys. Lett.* **2007**, *91*, 173504.

129. Kakade, S.; Ghosh, R.; Palit, D. K. *J. Phys. Chem. C* **2012**, *116*, 15155.

130. Lunt, R. R.; Benziger, J. B.; Forrest, S. R. *Adv. Mater.* **2010**, *22*, 1233.

131. Rim, S.; Fink, R. F.; Schoneboom, J. C.; Erk, P.; Peumans, P. *Appl. Phys. Lett.* **2007**, *91*, 173504

132. Makhnenko, O. V.; Blom, P. W. M.; Nguyen, T. Q. *Energy Environ. Sci.* **2015**, *8*, 1867.

133. Grodkowski, J.; Neta, P.; Wishart, J. F. *J. Phys. Chem. A.* **2003**, *107*, 9794**.**

134. Skrzypczak, A.; Neta, P. *J. Phys. Chem. A.* **2003**, *107*, 7800**.**

135. Paul, A.; Samanta, A. *J. Phys. Chem. B.* **2007**, *111*, 1957**.**

136. Sarkar, S.; Pramanik, R.; Seth, D.; Setua, P.; Sarkar, N. *Chem*.Phys. Lett. **2009**, *477***,** 102.

137. Sarkar, S.; Pramanik, R.; Ghatak, C.; Rao, V. G.; Sarkar, N. *J. Chem. Phys.* **2011**, *134***,** 74507.

138. Vieira, R. C.; Falvey, D. E. *J. Am. Chem. Soc.* **2008**, *130***,** 1552.

139. Vieira, R. C.; Falvey, D. E. *J. Phys. Chem. B* **2007**, *111*, 5023.

140. Wishart, J. F.; Neta, P. *J. Phys. Chem. B.* **2003**, *107*, 7261**.**

141. Behar, D.; Neta, P.; Schultheisz, C. *J. Phys. Chem. A* **2002**, *106*, 3139.

142. Lee, C.; Winston, T.; Unni, A.; Pagni, R. M.; Mamanto, G. *J. Am. Chem. Soc.* **1996**, *118*, 4919.

143. Liang, M.; Kaintz, A.; Baker, G. A.; Maroncelli, M. *J. Phys. Chem. B.* **2012**, *116*, 1370.

144. Koch, M.; Rosspeintner, A.; Angulo, G.; Vauthey, E. *J. Am. Chem. Soc.* **2012**, *134***,** 3729.

145. Gordon, C. M.; McLean, A.J. *Chem. Commun.* **2000**, 1395.

146. McLean, A. J.; Muldoon, M. J.; Gordon, C. M.; Dunkin, I. R. *Chem. Commun.* **2002**, 1880.

147. Chao, Y. C.; Chung, C. H.; Zan, H. W.; Meng, H. F.; Ku, M. C. *Appl. Phys. Lett.* **2011,** *99*, 233308.

148. Zhao, Y. S.; Zhan, P.; Kim, J.; Sun, C.; Huang, J. *Acs Nano* **2010**, *4***,** 1630.

CHAPTER 2

EXPERIMENTAL TECHNIQUES AND INSTRUMENTATION

2.1 INTRODUCTION

Transformation of reactants into products through a chemical reaction has been a subject of intensive investigations from ancient times. This gave birth to the Arrhenius equation, which was formulated to calculate the rate of a particular reaction.[1] In 1949, Norrish and Porter developed the flash photolysis technique to investigate the spectroscopy and lifetime of the transient molecular species, which are the short lived intermediates between the reactants and products in millisecond time scale in order to formulate the mechanism of the chemical reaction.[2,3] Since then spectroscopy has become an indispensible tool for identification and characterization of the various transient species and intermediates generated in the course of a chemical reaction as well as to determine the rates of reactions of these intermediates. High resolution or ultrafast time resolution as well as high sensitivity and accuracy of the spectrometers developed over time, have been the real work horses for microscopic understanding of the physical and chemical processes at the atomic or molecular level. Spectroscopic techniques have been immensely developed because of availability of highly sophisticated laser and optical detection systems. On one hand, lasers with extremely narrow bandwidth have made possible the high resolution atomic and molecular spectroscopy (resolution <0.1 cm^{-1}), on the other hand, ultrashort laser pulses have made possible detection of intermediates with lifetimes as short as less than a femtosecond (10^{-15} s), generating the possibility of studies of very fast dynamical processes, such as breaking or forming of chemical bonds following absorption of photons.[4] Ultrashort (picosecond and femtosecond) laser pulses have effectively been used to initiate and monitor the cascade of events that occur when the light is absorbed by the molecule.[4,5] In addition, high intensity as well as short duration laser pulses have been helpful in development of numerous nonlinear spectroscopic techniques, which have been very effectively used in investigation of the processes in the excited states of molecules and materials.

Among various experimental techniques available now-a-days to monitor the physico-chemical processes occurring in the excited states of the molecules and materials, those based on optical spectroscopy are extremely popular. Techniques used in the present thesis are mainly based on absorption or emission of light by the chemical species in the excited states. Both steady-state and time-resolved absorption and fluorescence spectroscopic techniques have been used here to carry out the investigations presented in the thesis. The thesis is based on the studies of the photophysical properties of the transients created in various kinds of self assembled media. Techniques used for the characterization of the nanoaggregates are also described in this chapter.

2.2 STEADY-STATE ABSORPTION AND FLUORESCENCE MEASUREMENTS

The electronic transition of most of the organic chromophores occurs through absorption of photons in UV-visible region. Therefore UV-Visible absorption spectroscopy is considered as one of the basic and widely used technique to obtain the information about the ground state absorption of the sample. Wavelength region and extinction coefficient of absorption of a chromophore is considered as its characteristic signature and absorption spectroscopy is one of the powerful techniques for both qualitative and quantitative analysis of the samples.[5] When a molecule undergoes monomer to aggregate transition then the associated electronic energy levels also undergo significant changes and this effect is directly monitored through absorption spectroscopy by observing the changes in the positions of spectral lines or bands, broadening or sharpening of the absorption bands or changes in the extinction coefficient.[6] Present thesis contains a major portion of the work based on organic nanoaggregates. Therefore the UV-Visible absorption spectroscopy may be considered as an essential tool for characterization of the nanoaggregate systems.

The UV-Visible absorption spectra were recorded using a Jasco model V-670 spectrophotometer. Absorbance (A) of a species having concentration C in a chemical system and molar absorption or extinction coefficient ε_λ at wavelength λ is given by the equation 2.1.

$$A = \log\frac{I_0}{I} = \varepsilon_\lambda C l \qquad (2.1)$$

Here, I_0 and I are the intensities of the transmitted light after passing through the blank cell and a cell with sample, respectively and l is the path length of the light beam passing through the sample. For UV-Visible absorption measurements, samples were taken in a quartz cuvette of 1 cm path length. The schematic diagram of a dual-beam UV-Visible absorption spectrophotometer is provided in Figure 2.1.

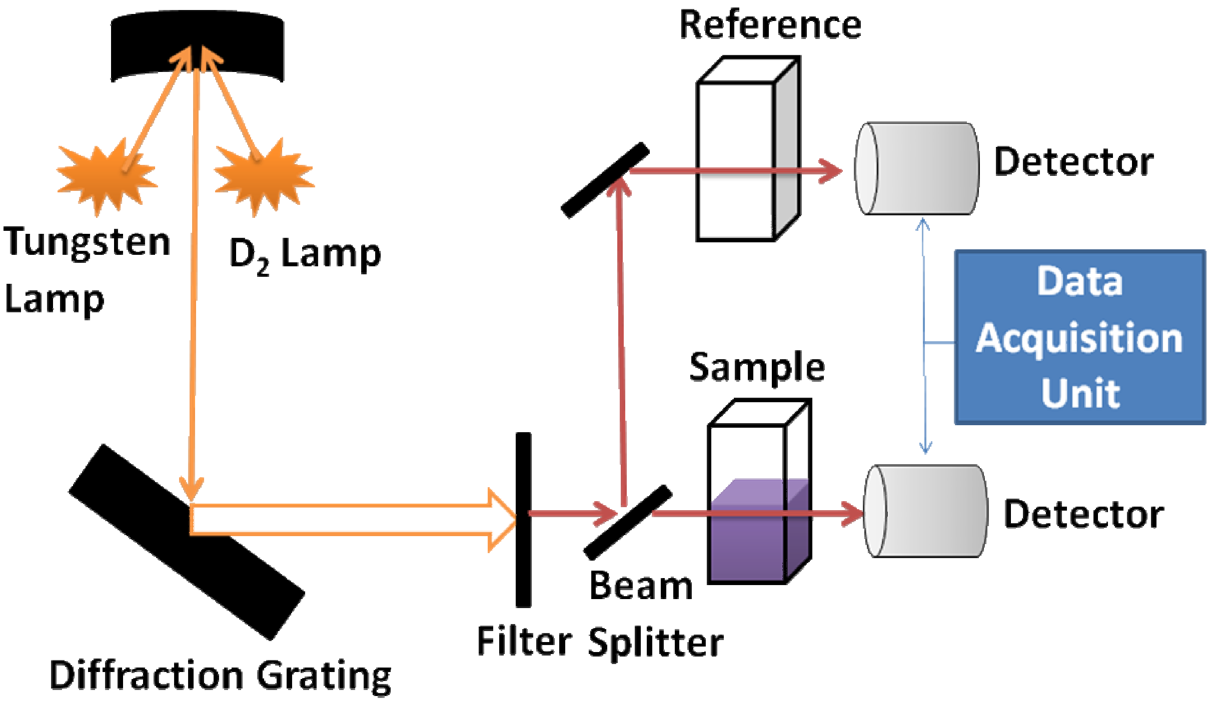

Figure 2.1: Schematic diagram of UV-Visible absorption spectrophotometer.

The steady state photoluminescence measurement is another most useful technique for characterization of electronically excited states of the chromophores. At room temperature (~25^o C or 298 K), photoluminescence observed from the organic molecules are mainly fluorescence emission and fluorescence spectroscopy is a very popular and sensitive technique for characterization of the excited states of luminescent samples.[5] We have used steady state emission technique frequently to characterize the nanoaggregate samples. Fluorolog 3 spectrofluorometer (Horiba JobinYvon, France), has been used for recording room temperature photo-luminescence (PL) spectra of the nanoaggregate samples. The instrument uses a 450 watt continuous powered high pressure xenon lamp as the excitation source and the desired excitation wavelength is selected using an excitation monochromator. Sample is excited in a 1 cm x 1 cm suprasil quartz cuvette and the fluorescence is measured in a perpendicular direction with respect to the direction of the excitation beam. The emission wavelengths are selected using an emission monochromator and detected by R-928F (Hamamatsu) photomultiplier tube (PMT) as the photodetector. The schematic diagram of the fluorescence spectrometer is provided in Figure 2.2. The interference from the excitation and scattered radiation is eliminated using appropriate filters put in the light beam before the emission monochromator. Emission spectra are corrected by multiplying the correction factor to the uncorrected spectra. The correction factor is generated by using the correction kit provided by Horiba.

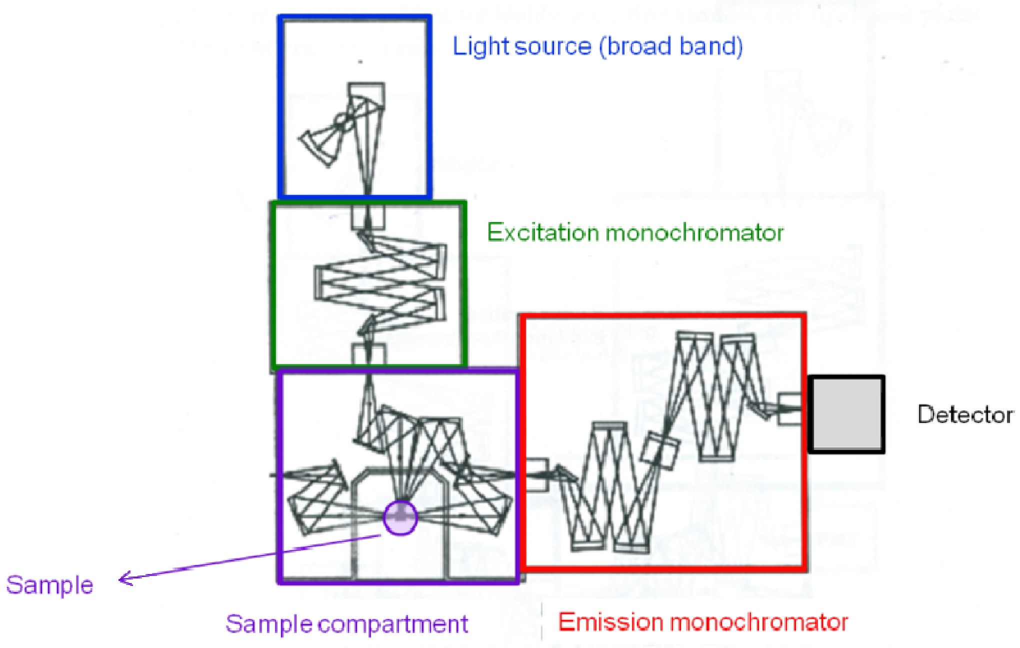

Figure 2.2: Schematic diagram of Fluorolog 3 spectrofluorometer (Horiba JobinYvon)

The emission quantum yield of a material is also an important photophysical parameter for the application purpose. We have estimated the emission quantum yield for the samples using the comparative emission yield estimation method.[7] Here we have chosen some reference samples having known emission quantum yield and could be excited using light of the same wavelength as it is used for the sample. The emission yield could be estimated using equation 2.2.

$$\phi_{sample} = \frac{A_{reference}}{F_{reference}} \times \frac{F_{sample}}{A_{sample}} \times \frac{\eta^2_{sample}}{\eta^2_{reference}} \times \phi_{reference} \qquad (2.2)$$

Where $A_{reference}$ and A_{sample} are the absorbances at the excitation wavelength, $F_{reference}$ and F_{sample} are the integrated fluorescence intensities and $\eta_{reference}$ and η_{sample} are the refractive indices for the reference and the sample solutions, respectively. To minimize the self absorption effect and other ambiguities, absorbances of both the sample and reference sample are kept ≤ 0.1.[7] For nanoaggregates, all the steady state absorption and emission measurements were carried out using aqueous dispersion of the sample.

2.3 CHARACTERIZATION TECHNIQUES FOR NANOAGGREGATES

2.3.1 Dynamic Light Scattering[8,9]

Dynamic light scattering (DLS) is a well known technique which is very routinely used by the material chemists for several decades. This technique is useful to obtain the size distribution of micron to nanometer size particles suspended in a liquid medium.[8,9] In a basic light scattering experiment, one measures the average scattered intensity 'I_s' (that is the average rate of flow of energy per unit area of cross section) or the energy spectrum of intensity $S(\omega)$ where ω is the angular frequency of the scattered light. Both I_s and $S(\omega)$ are measured at various angles as they are angle dependent. The I_s bears information about the static properties of the scatterer whereas $S(\omega)$ bears information regarding the dynamics of the scatterer.

When light photons hit small particles, there is a significant probability to undergo Rayleigh scattering as long as the particles are small compared to the wavelength of the light. In solution phase, small particles undergo Brownian motions and so the distance between the scatterers in the solution is constantly changing with time. The scattered light then undergoes either constructive or destructive interference by the surrounding particles, and within this intensity fluctuations observed by the detector, information is contained about the time scale of movement of the scatterers.

The dynamic information about the particles is derived from an autocorrelation of the intensity traces recorded during the experiment. The second order autocorrelation curve is generated from the intensity traces as follows:

$$g^2(q,\tau) = \frac{<I(t)I(t+\tau)>}{<I(t)>^2} \qquad (2.3)$$

Where $g_2(q;\tau)$ is the second order autocorrelation function at a particular wave vector, q, and delay time, τ, and I is the intensity. The angular brackets <> denote the expected value operator.

At the initial time delays, the correlation remains high because the particles do not have a chance to move to a great extent from the initial state that they were in. The two signals are thus essentially remain unchanged when compared after a very short time interval. As the time delay becomes longer, the correlation decays exponentially, meaning that, after a long time period there must not be any correlation between the scattered intensity of the initial and final states. This exponential decay is related to the motion of the particles, specifically to the diffusion coefficient. To fit the decay (i.e., the autocorrelation function), numerical methods are used, based on calculations of assumed distributions. If the sample is monodisperse then the decay is simply a single exponential. The Siegert equation relates the second-order autocorrelation function with the first-order autocorrelation function $g^1(q;\tau)$ as follows:

$$g^2(q,\tau) = 1 + \beta[g^1(q,\tau)]^2 \qquad (2.4)$$

Here the parameter β is a correction factor that depends on the geometry and alignment of the laser beam.

For a suspension of monodispersed, rigid, spherical particles undergoing Brownian diffusion, the first-order correlation function decays exponentially and is given as,

$$g^{(1)}(\tau) = \exp\,(-Dq^2\tau) \qquad (2.5)$$

Where D is the translational diffusion coefficient and q is the magnitude of the scattering wave vector given by equation 2.6,

$$q = \frac{4\pi n}{\lambda}\ \sin\frac{\theta}{2} \qquad (2.6)$$

Here, *n* is the refractive index of the solvent, λ is the wavelength of light, and θ is the scattering angle. For small, dilute, non-interacting spheres the hydrodynamic radius, R_h, can be obtained from the translational diffusion coefficient using the Stokes-Einstein relationship.[5]

$$D = \frac{k\,T}{6\,\pi\eta R_h} \qquad (2.7)$$

Where k is the Boltzmann constant, η is the solvent viscosity, and T is the absolute temperature.

For the present work, DLS measurements were carried out using a Malvern 4800 Autosizer employing 7132 digital correlator. He–Ne laser operated at 632.8 nm with a power output of 15 mW was used as light source for these experiments. All measurements were carried out at an angle of 130° between the source and the detection light paths. The general set up for the DLS instrument is presented in Figure 2.3.

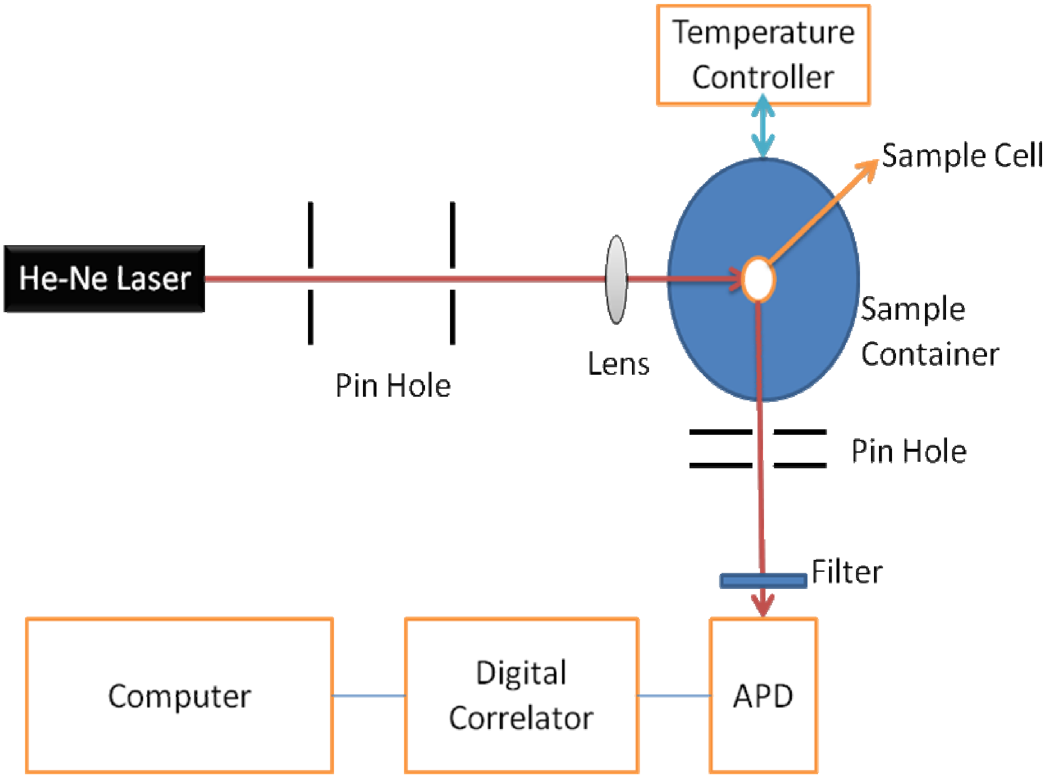

.

Figure 2.3: Block diagram of a typical DLS instrument.

2.3.2 Atomic Force Microscopy[10,11]

Atomic force microscopy (AFM) is a scanning probe microscopic technique with the maximum resolution of fractions of a nanometer, which is 1000 times better than the optical diffraction limit. It is one of the preferred tools for imaging, measuring, and manipulating surface of the material at the nanoscale.[10] It can also be used to measure forces, which is important for the study for biological molecules like proteins, nucleic acids etc.[11] Figure 2.4 presents the schematic layout of AFM instrument.

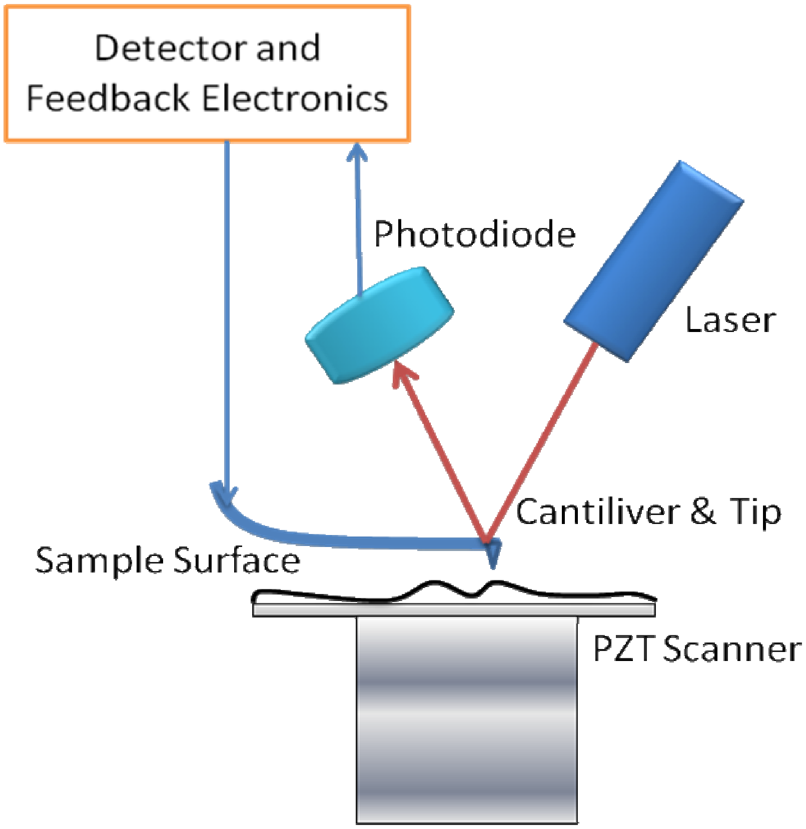

Figure 2.4: Schematic layout of AFM instrument.

The AFM basically consists of a cantilever with a sharp tip (probe) at its end; that is used to scan the specimen surface. The cantilever is typically Si or Si_3N (silicon nitride) with a tip radius of curvature on the order of nanometers. When the tip is brought into proximity of a sample surface, force between the tip and the sample leads to a deflection of the cantilever according to Hooke's law. The deflection of the cantilever is generally measured using a laser spot reflected from the top surface of the cantilever into an array of photodiodes. Scanning the tip at a constant height can cause damage to the tip due to collision of the tip with the surface. Hence, in most cases a feedback mechanism is employed to adjust the tip-to-sample distance to maintain a constant force between the tip and the sample. Conventionally, the sample is mounted on a piezoelectric tube that can move the sample in the *z* direction for maintaining a constant force, and in the *x* and *y* directions for scanning the sample.

The AFM tip is able to scan extremely small interaction area using a tip of 5-50 nm which gives it high sensitivity. This technique is used as a tool for creating the three dimensional micrographs for the samples with resolution down to the nanometer scale. AFM measurements included in the present thesis are carried out on instruments namely, NT-MDT, Solver Model.

Samples for AFM analysis were prepared by following method. The aqueous dispersion of aggregate to be analyzed were drop casted on the piece of the clean mica sheets and spin coated at 5000 rpm speed to get homogeneous distribution of aggregates over the mica sheet. Then the samples were allowed to dry under IR lamp.

2.3.3 X-Ray Diffraction[12, 13]

Max von Laune first discovered that, crystalline substances act as three dimensional diffraction gratings for X-ray light, as the wavelength of X-ray and the inter planer spacing in crystal lattice are in the same range.[13] X-ray diffraction caused by crystalline sample causes constructive and destructive interference at different angles.

X-ray diffraction required monochromatic X-ray source. In general X-rays are generated by a cathode ray tube, filtered to produce monochromatic radiation. The beam is further collimated and directed towards the sample with particular incident angle. Constructive inference take place when the condition satisfy Bragg's law ($n\lambda = 2d \sin\theta$). This equation relates the wavelength of X-ray with the diffraction angle and lattice spacing. The diffracted X-rays are detected for a range of $2\theta = 5$ to70^0 and all possible diffraction angles are attended to obtain the crystal structural feature.[13]

For our present thesis we have mainly used powder XRD technique as a tool of structural analysis of molecular aggregates. Powder XRD is a rapid analytical technique where the analyzed material is finely ground, homogenized and crystalline phase of the material is identified.

In general, X-ray diffractometers consist of three basic elements: an X-ray tube, a sample holder, and an X-ray detector. X-rays are generated in a cathode ray tube. In this tube a filament is heated to produce electrons which are further accelerated by applying voltage and bombard on a target material. Cu, Fe, Mo, Cr these are some common material used as target. The bombard electrons possess high energy to dislodge inner shell electrons and it causes inner orbital electron transfer to provide characteristic X-ray from the material. These spectra consist of several components, the most common being K_α and K_β. K_α consists, in part, of $K_{\alpha1}$ and $K_{\alpha2}$. $K_{\alpha1}$ has a slightly shorter wavelength and twice the intensity as compared to that of the $K_{\alpha2.}$ Monochromatic X-ray is obtained by filtering, with foils or crystal monochrometers. Copper is the most common target material for single-crystal diffraction, with CuK_α radiation = 1.5418Å. These X-rays are collimated and directed onto the sample. As the sample and detector are rotated, the intensity of the reflected X-rays is recorded. The schematic diagram of XRD setup is provided in Figure 2.5.

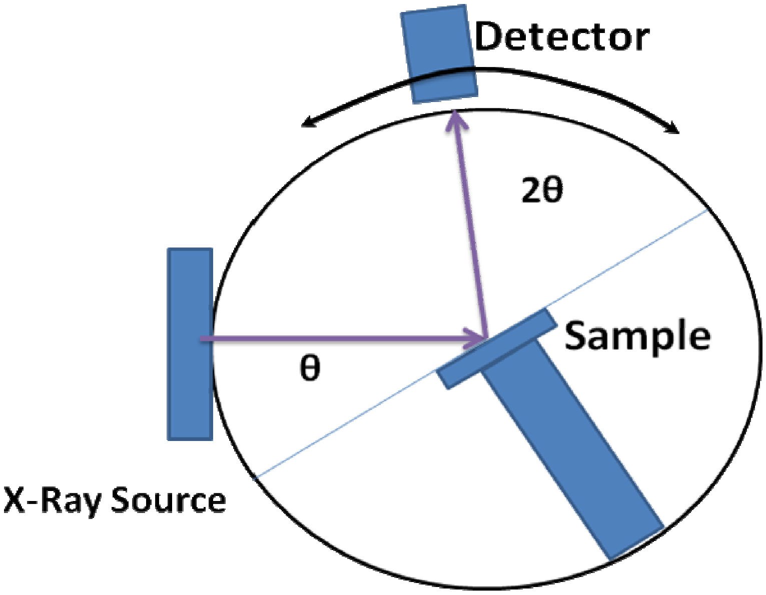

Figure 2.5: Schematic diagram of XRD setup.

The XRD pattern of our nanoaggregate samples were recorded on a Agilent Super Nova X-ray diffractometer using Cu-k_α radiation (λ = 1.5418 Å), over the two theta range of 5-50^0 for the vacuum dried powder samples.

2.4 Time Resolved Emission

When a molecule absorbs a light photon, one of its excited states is populated following which the latter decays back to the ground state through several photophysical processes, the details of which have already been discussed in Chapter 1. Fluorescence emission is one of such processes, which occurs, in general, because of the radiative transition from the S_1 to S_0 state. The fluorescence signal observed after certain time of excitation of a sample is directly proportional to population of the S_1 state at that particular time. Therefore, the time resolved fluorescence measurement may provide us direct information about the lifetime of the corresponding state.

In the works presented here, we have used two different time resolved emission techniques, (1) Time Correlated Single Photon Counting (TCSPC) and (2) Fluorescence Up-conversion techniques.[7] These techniques differ in the working principle as well as in the time resolution. The first one is used for samples with lifetimes in the range of few picosecend to a few microsecond time scale.[7,14] On the other hand, the second one may achieve a few tens of a femtosecond time resolution.[7] The basic working principles about these experimental techniques are described in the following subsections.

2.4.1 Time Correlated Single Photon Counting (TCSPC) Technique [7]

TCSPC is a well established technique, which has been used to monitor the time-resolved emission. The principle and operation can be described as follows.

This technique involves the excitation of the sample with pulses from a pulsed laser or light emitting diode (LED) or a flash lamp and the detection system monitors the time difference between the excitation pulse and the first fluorescence photon from the sample. The prerequisite for this measurement is that only one photon is observed for a large number of excitation pulses i.e. one photon is observed for < 2 % of the total number of excitation pulses. That is the reason; the technique is called as 'single photon counting'. In this situation, the statistics follows the Poisson distribution and a true time-resolved emission profile is obtained. A schematic diagram of TCSPC setup is represented in Figure 2.6.

An excitation pulse (optical pulse) source is splitted into two parts; the major part is used to excite the sample and other fraction of it is used to initiate the detection system. The process is done in the following way: a small part of the light from the excitation source is directed to a START PMT (Photomultiplier tube) to generate the electrical *START* signal, which is routed through a Constant Fraction Discriminator (CFD) to the START input of a Time to Amplitude Converter (TAC), which initializes charging operation of TAC. In the mean time, the major part of the light from the source optical pulse excites the sample, which subsequently gives the fluorescence emission. The emission photons are then detected by a STOP PMT (at right angle to the direction of excitation) to generate an electrical *STOP* signal. The *STOP* pulse is then routed through another CFD and a variable delay line to the STOP input of the TAC. After receiving the *STOP* signal the charging operation of the TAC is stopped and it generates an electrical output pulse (TAC-output) which has amplitude proportional to the time difference (Δt) between the *START* and *STOP* pulses arriving to the TAC. The TAC output pulse is then given to the input of a Multichannel Analyzer (MCA). The MCA is having an analog to digital converter (ADC), which generates a numerical value ($n_{\Delta t}$) corresponding to the amplitude of the TAC output and a count is added up in an appropriate channel (say $n_{\Delta t}^{th}$ of the MCA, selected by the number ($n_{\Delta t}$) generated in the ADC. This cycle (from excitation to data storage) is repeated for a large number of times to generate a histogram of counts against the channel number of the MCA. Since the collection of the emission photons in the stop PMT is kept very low (<0.02 photons/excitation pulse) the distribution of counts in the MCA channels (i.e. the histogram) exactly represents the probability of emission of a single photon after an excitation event and thus the fluorescence decay of the sample. Since the MCA channels are calibrated with respect to time, the fluorescence lifetime of the sample may be obtained by the analysis of the observed histogram in the MCA.

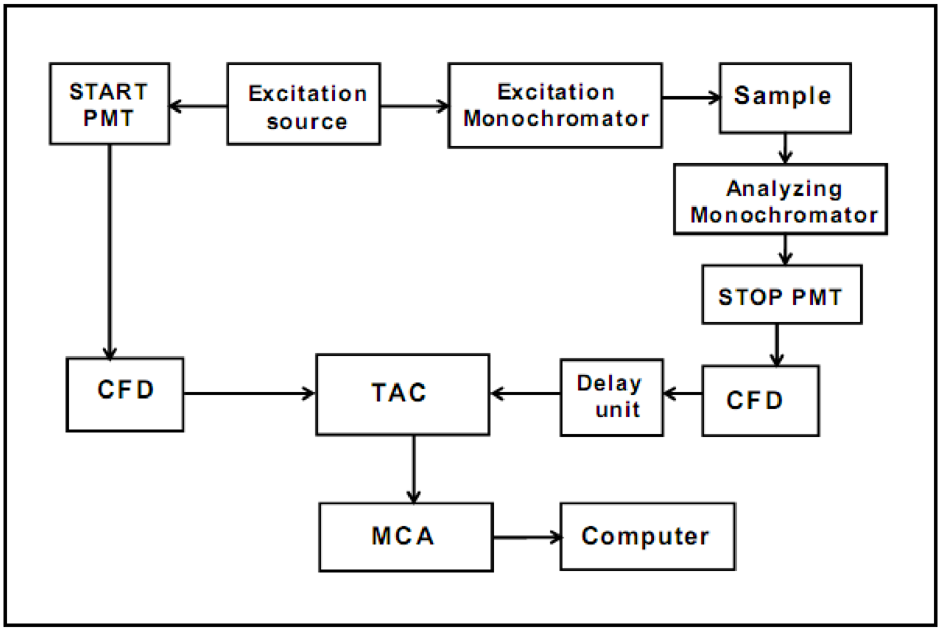

Figure 2.6: A schematic block diagram of the TCSPC spectrometer.

All kinetic measurements, in case of laser excitation, have been performed by keeping the excitation polarizer at the vertical position and the emission polarizer at the magic angle (54.7°) with respect to the excitation polarizer. Thus the fluorescence collected at the magic angle with respect to the excitation polarization remains free from any anisotropy components and represents the actual total fluorescence intensity decay. All the measurements represented in this thesis are done in a condition such that the counts at the peak of the time-resolved fluorescence decay are larger than 5000. Appropriate cut-off filters were placed just before the focusing lens to remove any scattered exciting light entering the monochromator from the sample chamber. The emission decay thus observed is de-convoluted with the instrument response to get the actual lifetime. The instrument response function (IRF) is measured using a scatterer solution placed in place of the sample. The TCSPC measurements and analyses carried out in this thesis have been performed by using an instrument of make IBH, U.K. The excitation wavelength was set considering the absorption spectrum of the sample. The fluorescence decay profiles thus recorded using the TCSPC technique were fitted using the IBH DAS 6.2 software.

2.4.2 Fluorescence Up-conversion Technique[15-18]

This is an advanced technique used for the time-resolved emission studies with femtosecond time resolution. To achieve ultra short time resolution, it is mandatory to have a light source which generates femtosecond excitation pulses and the detection technique needs also not to be limited to electronics response time of the detector. Here, ultrashort light pulse used to create the emissive excited state and monitoring of the fluorescence transient by time gating using the nonlinear frequency mixing technique.[15,16] The emission light (frequency ω_{fl}) collected from the sample following its excitation with an ultra-short laser pulse and a suitably delayed intense laser pulse, known as the gate pulse (frequency ω_g), are focused into a thin nonlinear crystal, whose optic axis is oriented at an appropriate angle with respect to the ω_g and ω_{fl} light beams. The sum-frequency photons (frequency ω_s) are generated only during that time for which the ultra-short gate pulse is present at the crystal along with the comparatively long lived fluorescence light. Thus, frequency mixing occurs only for a thin temporal slice of the fluorescence decay and accordingly acts as a light gate, providing time-resolution quite comparable to the width of the gate pulses used. The sum frequency generation is also called as photon upconversion process and thus this technique gets the name 'up-conversion'.[16]

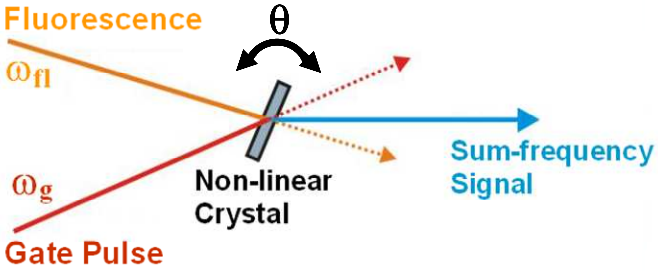

Figure 2.7: Schematic representation of sum frequency generation in a nonlinear crystal.

The efficiency of the up-conversion process, which is a three photon mixing process, largely depends upon the phase matching condition among the wave vectors ($\vec{k}$) of these three light beams (ω_g, ω_{fl}, and ω_s), that interact in the nonlinear crystal. The sum-frequency generation process needs to follow two important criteria, the "*energy conservation*" as well as the "*momentum conservation*" and these are achieved only at the "*phase matching condition*" among the interacting lights in the nonlinear crystal.[16-18] The energy conservation criterion gives us the following relation among the frequencies of the different light involved.

$$\omega_g + \omega_{fl} = \omega_s \tag{2.8}$$

Similarly, the phase matching condition suggests the following relation among all the wave vectors involved in the nonlinear phenomenon for the most efficient sum-frequency generation.

$$\vec{k}_s = \vec{k}_g + \vec{k}_{fl} \tag{2.9}$$

Here $\vec{k}_g$, $\vec{k}_{fl}$ and $\vec{k}_s$ are the wave vectors for the gate, fluorescence and the sum frequency lights. In accordance with relation 2.9, the closeness to the phase matching condition for sum-frequency generation is often expressed by the parameter called phase mismatch, $\Delta\vec{k}$, and is expressed by the following equation.

$$\Delta\vec{k} = \vec{k}_s - (\vec{k}_g + \vec{k}_{fl}) \tag{2.10}$$

For the co-linear propagation of the gate and the fluorescence beams, the above expression for the phase mismatch for the sum-frequency generation can be simplified as,

$$\Delta\vec{k} = \vec{k}_s - (\vec{k}_g + \vec{k}_{fl}) = \frac{1}{c}(n_s\omega_s - n_g\omega_g - n_{fl}\omega_{fl}) \tag{2.11}$$

Here c is the velocity of light in vacuum and n_s, n_g and n_{fl} are the refractive indices of the sum frequency, gate and fluorescence lights, in the non-linear medium. Obviously, the true phase matching condition suggests that the $\Delta\vec{k}$ value should be equal to zero. It is thus clear that the smaller is the $\Delta\vec{k}$ value, more closer is the situation for the true phase matching condition and accordingly the better should be the efficiency for the fluorescence up-conversion process.[16-18] Such an ideal situation is, however, not possible to achieve practically, because none of the light beams used are monochromatic in nature. Thus, for all practical purposes in the fluorescence up-conversion measurements, the best efforts are made to achieve the lowest possible phase mismatch condition such that the intensity of the sum-frequency light becomes the maximum. To achieve this, the optical axis of the nonliner crystal is rotated with respect to the polarization direction and the direction of propagation of the gate and the fluorescence light pulses until the intensity of the sum-frequency light becomes the maximum for a selected ω_{fl} value (i.e. the monitoring emission wavelength). The selection of ω_{fl} or the monitoring emission wavelength is easily achieved by setting the wavelength of the monochromator in front of the photodetector corresponding to the sum-frequency light ω_s that is expected according to eq. 2.8 for the selected ω_{fl} and the fixed ω_g for the gate pulses used. Thus, by selecting different emission wavelengths for the measurements and accordingly tuning the optical axis of the non-liner crystal for the maximum sum-frequency light for each of these selections, one can easily carry out the time-resolved fluorescence up-conversion measurements for a wide range of wavelengths covering the whole fluorescence spectrum of the sample. A proper selection of the non-linear crystal is, however, essential to achieve this because different nonlinear materials have different spectral ranges for their suitability and efficiency to up-convert the fluorescence light by mixing it with the gate laser light. Among different non-linear crystals, the β-barium borate (BBO) is mostly used as nonlinear crystal in the fluorescence up-conversion measurements, because it has a high transmittance over a wide spectral range (covering most of the UV-visible spectral region) and a reasonably high non-linear efficiency for the sum-frequency generation process.

Since the beam size of the fluorescence collected from the sample is always quite large, it is always required to focus the fluorescence beam on to the non-linear crystal with a broad cone. Thus, the nonlinear crystal used for up-conversion measurement should have quite high phase matching acceptance angle, $\Delta\theta$ such that the maximum of the fluorescence light can be utilized in the up-conversion process. For a nonlinear crystal, the phase matching acceptance angle, $\Delta\theta$, is expressed by the following relation.

$$\Delta\theta = \frac{4\pi}{d}\left(\frac{\partial \Delta \vec{k}}{\partial\theta}\right) \qquad (2.12)$$

Here d is the thickness of the nonlinear crystal. It is evident from the above equation that the smaller the thickness of the crystal, the larger is the $\Delta\theta$ value. Thus, the thinner is the non-linear crystal, the easier is the tuning of the crystal axis for the efficient sum-frequency generation. However, with very thin crystal the integrated intensity of the sum-frequency light becomes very low and accordingly the system becomes overall inefficient. Thus, in all practical systems, there is a compromise to select the optimum crystal thickness. Crystals with thickness of about 0.5 mm are quite commonly used in most fluorescence up-conversion measurements, without sacrificing much on the acceptance angle and at the same time not sacrificing much on the time resolution of the measurements.

Brief description of the present fluorescence up-conversion setup

The block diagram of the femtosecond fluorescence up-conversion instrument used for our experiments is shown in Figure 2.9. In this instrument, the ultra short laser pulses (wavelength around 780 nm, pulse duration of ~100 fs, at a repetition rate of 1kHz) obtained from an amplified ultrafast laser system have been used. The output laser beam is first passed through a harmonic generator unit, where the 2nd harmonic (390 nm) of the laser light is generated using β--BBO crystals and by proper tuning of their optic axis for the required phase matching conditions. The higher harmonic light thus produced is separated from the residual fundamental light by using a dichroic mirror and is used for the excitation of the samples of our interest. The intensity of the higher harmonic light is normally kept reasonably low to ensure that the fluorescence intensity remains linearly dependent on the excitation laser intensity. This is also required to minimize the photo-degradation of the samples during the measurements of the fluorescence decays.

In our experimental arrangement, the sample solution is generally kept in a rotating quartz cell of 1 mm thickness. The sample cell is rotated continuously during the measurement to prevent localized heating of the sample and consequently to minimize its photo-decomposition. A cut-off filter is used immediately after the sample cell to prevent the residual excitation light and/or Raman light to reach the detection system. The transient fluorescence originating from the sample is then focused onto an up-conversion crystal (0.5 mm thick BBO crystal), using two parabolic mirrors. The residual fundamental beam is used as the gate pulse is first directed to an optical delay line and subsequently focused onto the up-conversion crystal.

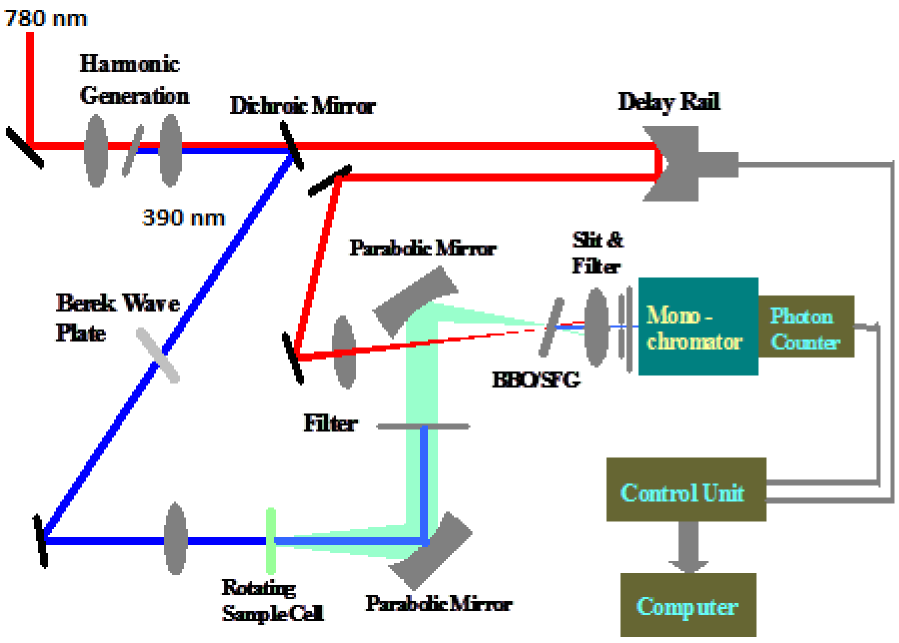

Figure 2.8: The Schematic diagram of the fluorescence up-conversion spectrometer. .

A translational stage, driven by a stepper motor with a step size of 0.1 µm, is used to change the delay of the gate pulse. Each step of the translational stage changes the optical path length of the gate pulse by 0.2 µm, thus delaying the pulse by 0.66 femtosecond per step. The gate pulse is focused onto the up-conversion crystal using a lens to mix with the fluorescence signal and thus to generate the sum-frequency or the up-converted signal. The upconverted light is focused onto a slit of a double monochromator after passing through a UV band pass filter (UG 11) that eliminates the gate and the unused fluorescence light but transmits the up-converted light. This up-converted light is finally detected by using a photomultiplier tube connected to a photon counting system (CDP Inc. Russia).

A variable wave plate (Berek Compensator) in the path of the excitation beam is used to control the polarization direction of the excitation pulses relative to the horizontally polarized gate pulses. Fluorescence up-conversion measurements are normally carried out under magic angle condition to avoid the rotational depolarization effect of the probe molecules on the observed fluorescence decays.

2.5 Time Resolved Transient Absorption Spectroscopy

Following absorption of a photon, the properties and the recativities of the excited states of the molecules become significantly different from those of the ground state because of different electron density distributions in the excited states. These states are of short lifetimes and commonly called as '*transients*'. Since the electron density of the molecule is significantly different from that in the ground state, the absorption spectrum associated with these transient species significantly differs from that of its initial form. Therefore the transient absorption spectroscopic technique is useful for characterization of the transient species in a way similar to the technique of characterization of the ground state species using steady state absorption technique.[5] Since these transients are short lived, the time resolution of the transient absorption technique should be fast enough to monitor the growth and decay kinetics of the transients and sensitive enough to record their spectra during their lifetime. We have used two different transient absorption techniques, the basic principle of which is very similar, but differs in the time resolution and hence the experimental setup. One of these is used for transient absorption measurements in the ns to ms time range after photoexcitation of the samples. This technique is commonly known as 'laser flash photolysis', because in general a nanosecond laser is used for sample excitation or photolysis, following which another light flash is used for optical detection of the transients.[2,3] The time resolution of the set up is dependent not only on the duration of the excitation pulse but also the time response of the detector, a fast photomultiplier or photodiode. The second one may have the time resolution down to few fs or sub-picosecond level and is well known as 'ultrafast pump – probe transient absorption technique'.[19-21] The later technique is known as pump-probe spectroscopy, because, here one highly intense 'pump' beam is used to produce the transient species and another weakly intense beam used to 'probe' the transient species at different delay times between the pump and probe.[22-25] Time resolution of the spectrometer, however, depends only on the duration of the excitation pulse, but not on the time response of the detector, which is really a slow and integrating photodiode. However, to obtain information in femtosecond time domain precision delay line of sub-micron distance resolution is essential to be able to delay the probe pulse with respect to the pump pulse by a few fs. The probe beam may be generated in different spectral region e.g. visible, infra red, terahertz etc.[26-29] In the present thesis we have mainly used UV-visible pump and UV-visible-near IR probe spectroscopy to characterize the transient species.

In the transient absorption experiments described above, there can be three different contributions to the transient absorption signals. The electronic transitions associated with these three different type of TA signals are represented in Figure 2.9. First the strong pump pulse excites the molecules from the ground state (S_0) to a higher excited state S_1 or S_n. Then, the molecules in the excited state absorb probe light, called as excited state absorption (process A in Figure 2.9).[22-25] This is seen as decrement in the probe light and hence there is an increase in ΔA. The probe pulse may also excite the molecules from the ground state to the excited state, which will result in a bleaching of the ground state, process C in Figure 2.9. This will be seen as an increase in the detected probe intensity in presence of pump compared to that in absence of pump, which eventually appears as negative ΔA.[22-25] Finally there may be stimulated emission from the excited molecule, which can be seen as process B in Figure 2.9 and this will be detected as a decrease in the ΔA.[22-25]

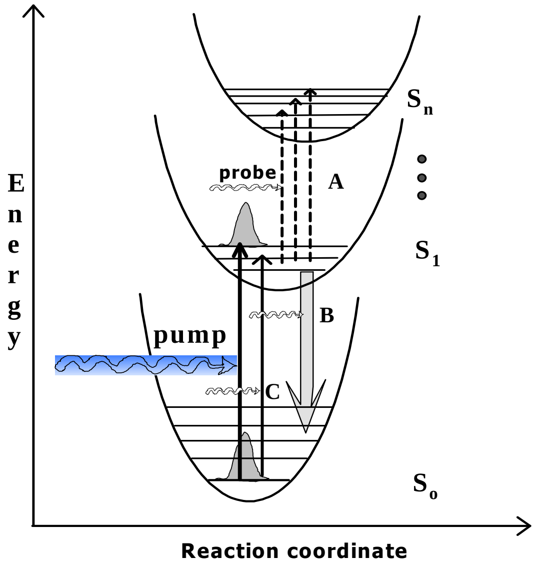

Figure 2.9: Scheme of the states involved in a pump probe experiment in a dye solution. (A) Excited state absorption (B) Stimulated emission. (C) Bleaching.

Brief description about the experimental setup and working principles of the two transient absorption spectroscopic techniquesare provided in the following sub sections.

2.5.1 Nanosecond Flash Photolysis

Photoinduced long lived transients (e.g. long lived singlet, triplet excited state, radical cation, anion etc.) can be monitored by laser flash photolysis experiment.[2,3] The technique was introduced by Porter and Norris in 1949 and since then it has become a basic tool in the study of the photochemical and photophysical properties of compounds under the effect of light irradiation. The sample is excited by the intense pulse of the pump source (normally a laser) to create the excited state population with sufficiently high concentration. The spectral and temporal properties of these excited state molecules are monitored by a white probe light from a pulsed xenon lamp passed through the sample at right angles to the path of the exciting pulse. After passing through the sample the probe light is directed to a monochromator / spectrograph. The transmitted probe light is then measured either by a single detector (for kinetic analysis at a single wavelength) e. g. PMT or by an array detector (for spectral analysis at a given time). The transmission intensity of the sample before, during, and after the exciting pulse are converted by the detector into electrical signals and measured by an oscilloscope (in the case of the single detector) or acquired by a CCD camera (in the case of an array detector). The changes in the transmission intensity are normally converted into changes of optical density. The basic layout of the set up is shown in Figure 2.10.

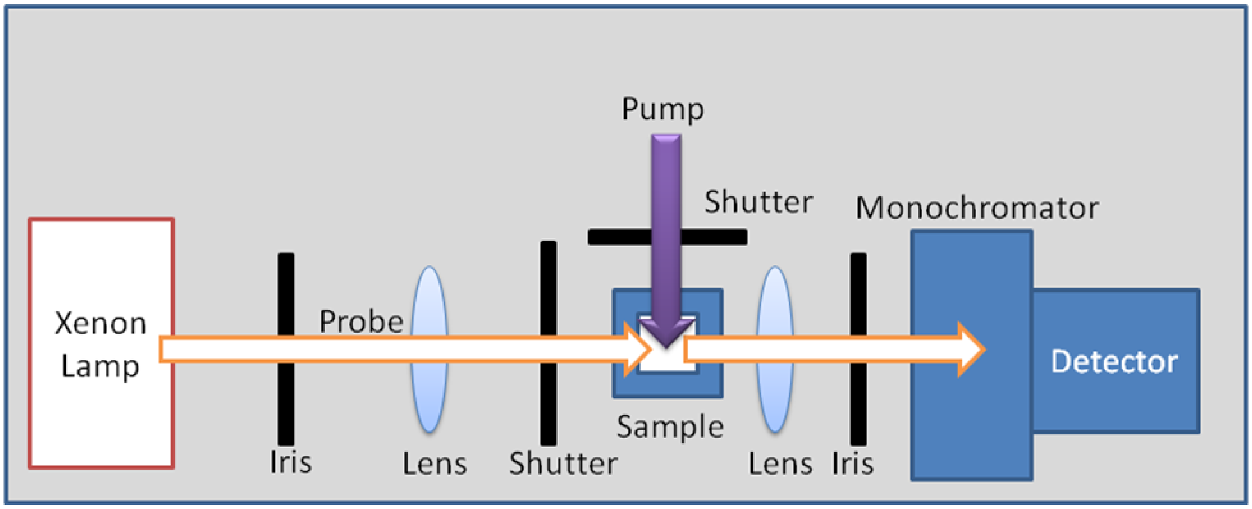

Figure 2.10: Basic layout of nanosecond flash photolysis experimental setup

In this present thesis, the flash photolysis experiments with about 5 ns time resolution were performed using a Laser Kinetic Spectrometer (Edinburgh Instruments, UK, model LP920). The sample in a 1 cm × 1 cm quartz cuvette was excited using second or third harmonic of

Nd:YAG laser (Thales Laser SA, France, model: SAGA), i.e. 532 nm and 355 nm, respectively; having laser pulse width of ~5 ns duration and ~20 mJ/pulse energy . Continuum light (250 – 1000 nm) from a pulsed 450 W xenon arc lamp was used as the optical probe. Time-resolved transient absorption spectra in the 300 - 850 nm region were recorded using an ICCD camera (Andor, UK, Model: iStar-320T) and the temporal absorption profiles at selected wavelengths were recorded using photomultiplier tube (Hamamatsu R920) connected to a 200 MHz digital oscilloscope.

2.5.3 Ultrafast transient absorption spectrometer

This is one of the most useful techniques to resolve the excited state dynamics in the sub-picosecond time regime.[19,20] Achievement of such ultrafast time resolution required a source which can provide the pump and probe lights having pulse width ≤ 100 fs. Invention of ultrafast laser systems resolved the issue of such short pulse sources.[30,31] Ti-Sapphire crystal having broad stimulated emission band are considered as most suitable laser material for this purpose and mostly used for the ultrafast spectroscopy.[24, 32] Er^{3+} doped fiber laser also provide short pulses having pulse width of ~80 fs. These materials possess broad stimulated emission band and provide large gain bandwidth which is an essential condition for ultrashort pulse generation. In Ti:Sapphire crystal the basic principle of femtosecond pulse generation relies on Kerr lensing effect of the Ti-Sapphire gain medium which leads to self focusing of the Gaussian laser beam passing through it. The Kerr lens forms a passive 'intracavity' aperture and introduces power dependent loss and intence longitudianal modes are locked to generate fs light pulses.[32]

The output energy from these ultrafast laser oscillators and in range of few nJ. This small energy/pulse is not suitable to generate significant concentration of transient species. Therefore, the energy of the output beam required to be amplified which is carried out following the chirped pulse amplification (CPA) technique.[32] This technique is employed in order to avoid the damage of the gain medium by the high-intensities pulses. For example, a 3 mJ, 80 fs pulse focused to a 100 μm spot size has a peak fluence of $\sim 4 \times 10^{12}$ W/cm2, which is ~ 1000 times higher than the damage threshold of most optical materials (GW/cm2). The peak power reduction is done by temporal stretching of femtosecond pulses. The stretched pulses are then safely amplified, followed by recompression to the femtosecond duration.

An ultrashort laser pulse is characterized by the broad spectral distribution. By using a combination of gratings and/or lenses, the individual frequencies within an ultrashort pulse is separated (stretched) from each other in time (see Figure 2.8). The longer component wavelength (red part) is diffracted at larger angle as compared to blue part. This wavelength dependent divergence creates a path difference between the red and blue part of pulse leading to temporal stretching of the incoming pulse. The duration of the incoming femtosecond pulse is usually stretched (chirped) up to few hundred ps. The resulting chirped pulse is ready to be amplified, since peak power of a stretched pulse after amplification is lower than the damage threshold of the amplification crystal.

The most widely used approach of pulse amplification is the regenerative and the multipass techniques. The regenerative amplification traps the pulse to be amplified in a laser cavity until the gain is saturated. Trapping and dumping the pulse in and out of the resonator is performed by a fast-switching Pockel cell and a broad-band polarizer. Amplification done by excitation of gain medium with powerful Nd:YAG (or similar laser) laser source. The Pockel cell consists of a birefringent crystal, which can change the polarization of a traveling laser field by applying a voltage on it and controls the injection and extraction of laser pulses from the regenerative amplification cavity. Further amplification carried out using multipass amplification technique where different passes are geometrically separated to one another.

After amplification the pulse is recompressed back to its original duration by a conjugate dispersion line in the compressor (Figure 2.8). The main challenge for a compressor is to recover not only the initial pulse duration and quality, but also to compensate the dispersion introduced in the amplification stage itself. To achieve this goal, the distance between gratings in the compressor is set longer than that in the stretcher. This will compensate overall second-order dispersion and help in producing relatively short pulses, but at the expense of introducing higher-order dispersion terms, which usually create extra temporal features in the compressed pulse such as prepulses and/or wings.

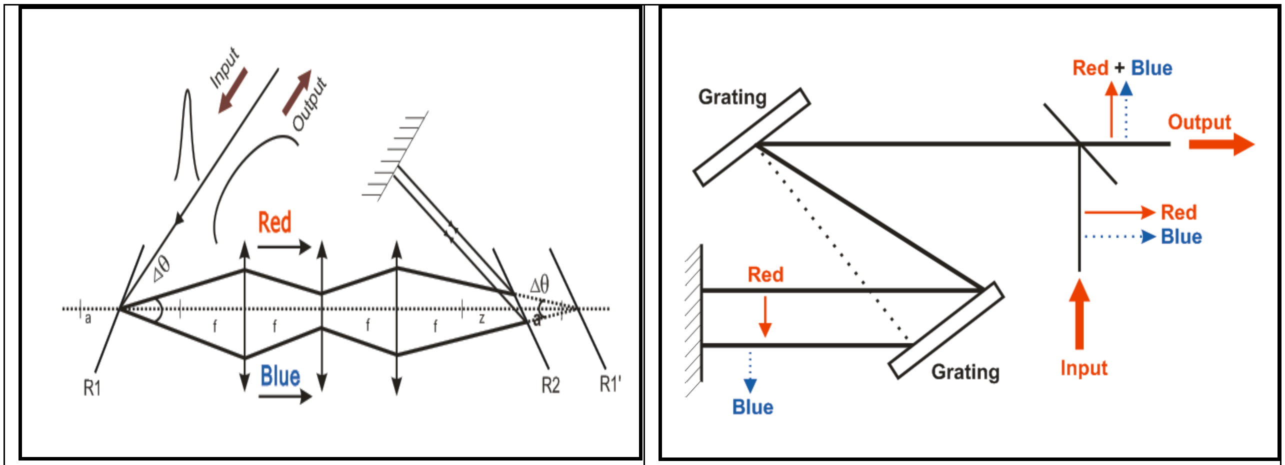

A

B

Figure 2.11: (A) Schematic diagram of pulse chirping and (B) Schematic diagram of pulse compression.

Fundamental wavelength of 800 nm or 780 nm light obtained from the femtosecond amplified laser source is not suitable for excitation, as most organic chromophores absorb in UV and visible region. To obtain femtosecond pulses of 400 nm or 390 nm, which are suitable for photoexcitation of large numbers of organic and inorganic molecular systems, second harmonic generation (SHG) technique was employed. Type I BBO crystal of 0.5 mm thickness is used for generating second harmonic generation. The second harmonic generated is polarized perpendicular to the fundamental (type I phase matching). This 400 nm or 390 nm wavelength light is used for sample excitation in most of the transient absorption studies presented in the thesis. The second harmonic and the fundamental also can be used further to generate third harmonic light. Pyrene nanoaggregates are excited with third harmonic 266 nm light.

In pump probe spectroscopy, it is necessary to have continuum of light to probe the photogenerated transient species. In the experimental setup presented here, white light is generated by focusing small part of fundamental (~2 μJ) with a lens on to a sapphire or rotating CaF_2 window of 1.5 mm thickness. Self phase modulation of the 800 nm or 780 nm laser pulse leads to generation of higher and lower frequencies leading to spectral broadening covering visible and near-infrared region.[32]

During pump –probe spectroscopy the second harmonic, third harmonic or the fundamental having major energy is passes though the sample as the pump beam to create the transients. The probe light pass through same region of samples at different relative delay times and detected by the detector. Photodiode with band pass filter or spectrograph with CCD is frequently used as detectors in this instrument. The relative delay between pump and probe beam is maintained by passing one of the above beams through the controlled delay rail system. The polarization of the pump and probe beam are maintained in the magic angle conformation to avoid the rotational dipolarization effect.

We have used two different ultrafast transient absorption setups. The brief description provided below. One of present work carried out using Ti-Sapphire based oscillator purchased from Thales Lasers SA, France.[33] In brief, laser pulses of 5 nJ energy and 50 fs in duration at 800 nm are generated from the Ti: Sapphire oscillator, which is pumped by diode pumped solid state laser (DPSS). The pulses obtained from the oscillator are amplified based on chirped pulse amplification (CPA) technique. After amplification, pulses with energy of 200 μJ and duration of 70 fs centered at 800 nm are obtained. Pulses at 800 nm, as well as its second harmonic, 400 nm (generated in a β barium borate (BBO) crystal) are used as pump pulse and the white light continuum (generated by focusing the fundamental on a sapphire window) is used as probe. The pump-probe method is used for the generation and detection of the transients. The schematic digram of our transient absorption setup is provided in Figure 2.12

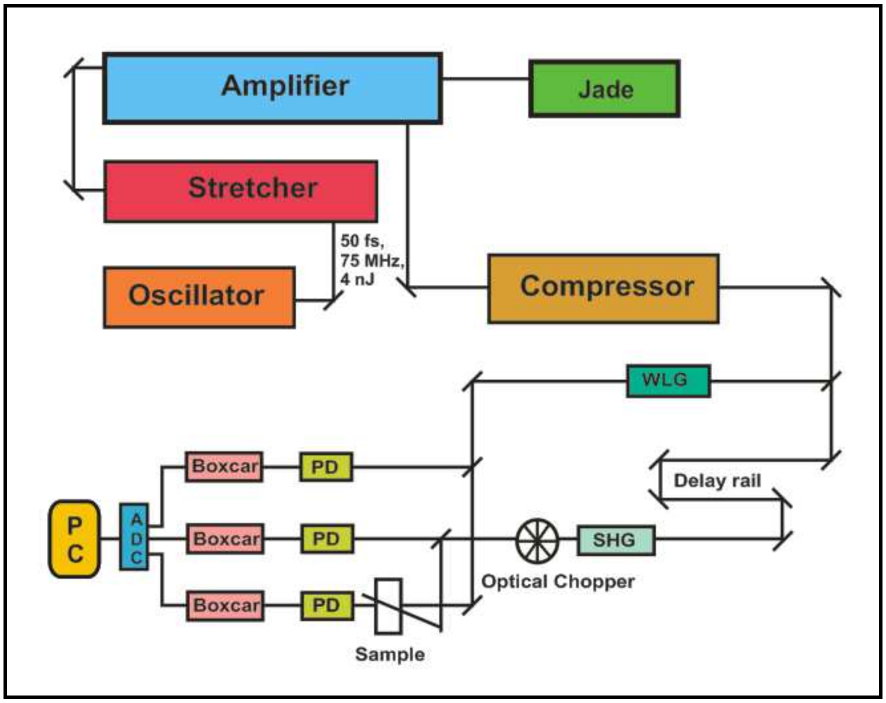

Figure 2.12: Optical layout of our old transient absorption spectrometer.

Other experiments are carried out with our new transient absorption spectrophotometer.[34] In this setup, the fiber laser 'C-fiber' procured from Menlo, Germany, provide the seed pulse. The fiber laser provide wide band stimulated emission output with a central wavelength of 1560 nm which is further frequency doubled inside the Menlo oscillator module and provide the final output with central wavelength of 780 and a pulse width of 80 fs with 90 mW power and 102 MHz repetition rate. Further the seed laser pulse taken for chirp pulse amplification. The final output from the amplified laser system (Amplitude, France) possesses 3 mJ per pulse energy having the central wavelength at 780 nm with pulse duration of ~90 fs at a 1 kHz repetition rate. The pulse width of the amplified laser output was inspected through using autocorrelator module.

One part of this laser beam (about 2 µJ per pulse) is used to generate continuum probe light (340–1100 nm) after passing through a 2 mm thick rotating CaF_2 or sapphire plate following self phase modulation mechanism. Other two parts of the laser beam is passed through nonlinear crystal for second and third harmonic generation having output energy of about ~12 and ~15 µJ per pulse, respectively. The transient absorption signal is recorded using a spectrograph and a CCD detector. Samples of about 1 mm thickness (absorbance is about 0.3-0.5 at 390 nm or 260 nm, which are the excitation wavelengths) taken in a rotating cell were used for sub-picosecond pump–probe measurements. The temporal profiles were recorded at different wavelengths and time resolved spectra were constructed from the decay kinetics after correction of the zero delay time. The temporal profiles were fitted to multi-exponential decay and/or growth functions convoluted with a Gaussian function having an FWHM of 150 fs. The intensity dependent experiments of the nanoaggregates were carried out using 390 nm light with variable pump pulse energy in the range of 3-12 µJ per pulse. The excitation intensity dependent measurements of pyrene nanoaggregates were carried out with 260 nm light pump with energy in the range of 10-20 µJ per pulse. The excitation energy could be changed by using neutral density filters. The schematic diagram of the spectrometer used for monitoring the transient species in femtosecond time-domain is represented in figure 2.13.

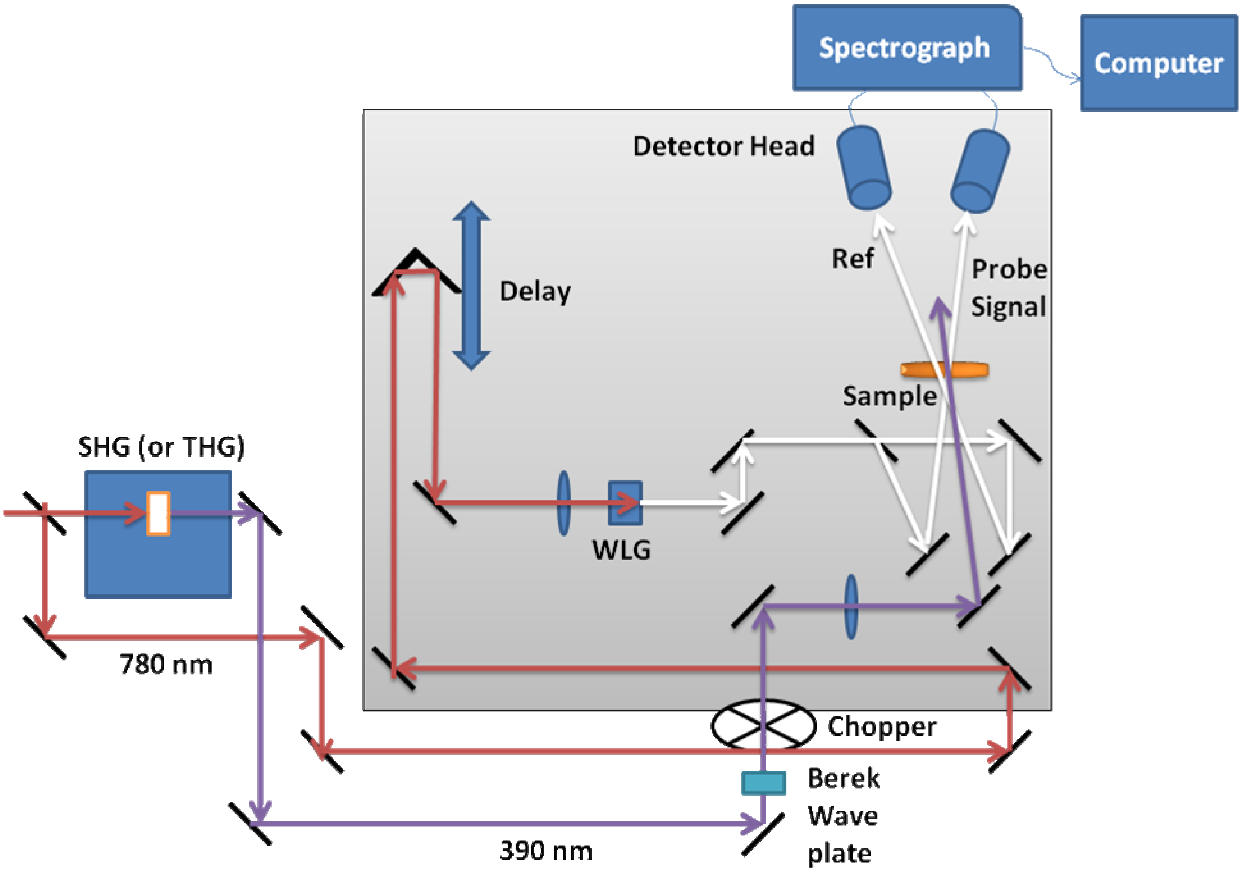

Figure 2.13: Optical layout of our new ultrafast pump-probe setup.

2.6. Nanosecond Pulse Radiolysis

In pulse radiolysis, the system under investigation is generally irradiated with an intense pulse of electrons to generate a significant concentration of transient species.[35-40] The resulting transient species are then monitored online by a suitable physical technique, such as optical absorption, conductivity, electron spin resonance or fluorescence.[35-40] Typically, electron pulse should be of sufficiently high energy to produce an adequate concentration of the transient chemical species in the irradiated sample.[41] A schematic of the pulse radiolysis set up used in the experiments for the present thesis is shown in Figure 2.14.[42]

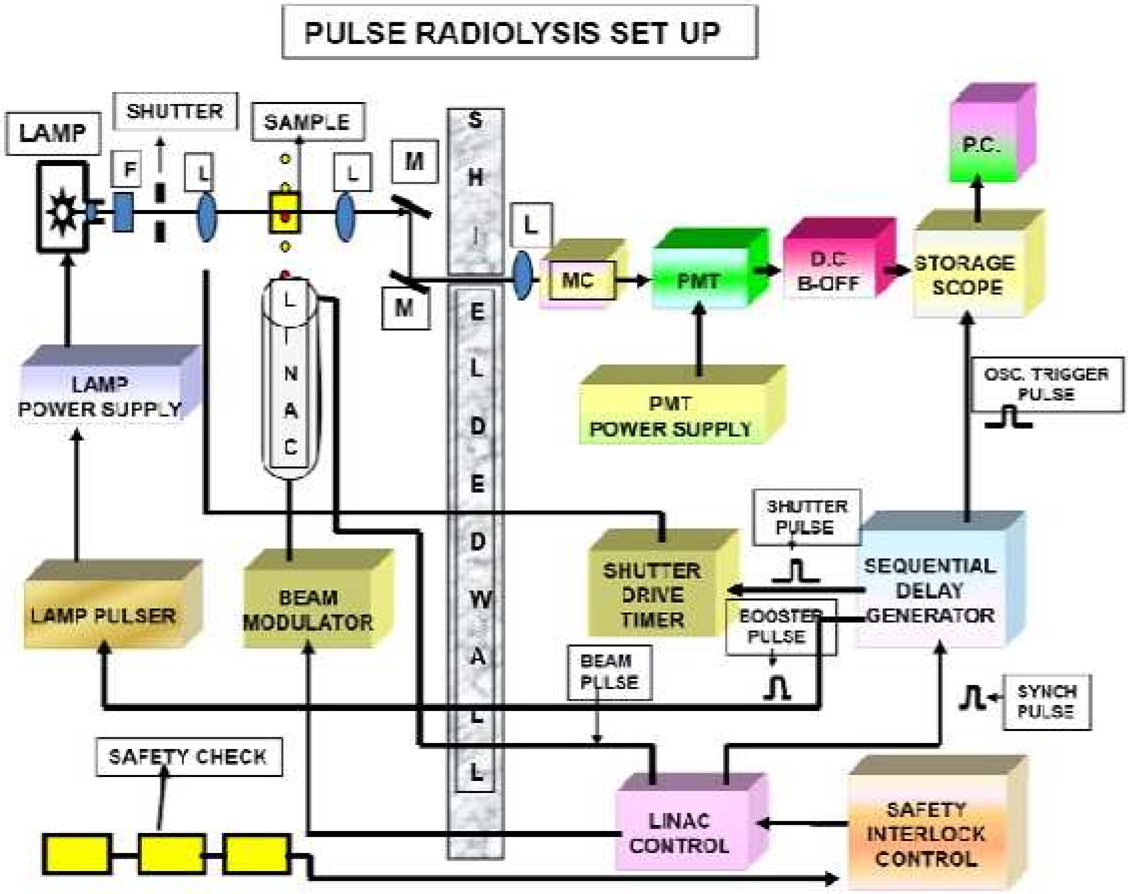

Figure 2.14: Schematic diagram of the nanosecond pulse radiolysis setup used for the experiments presented in this thesis.

Herein, the sample solutions are taken in a quartz cuvette (1cm × 1 cm) and are kept at a distance of ~12 cm from the titanium electron beam window of the linear accelerator system (LINAC), where the beam diameter is ~ 1 cm. The sample solutions are then irradiated with 7 MeV electron pulse sourced from the LINAC. Subsequently, a collimated light beam from a pulsed 450 W Xenon arc lamp is used to monitor the changes in the absorbance of the irradiated solution. The transmitted (after passing through the sample cell) light beam is directed to the spectrophotometer through a tunnel in the wall by making use of the fused silica lenses and mirrors. The light beam is then focused on the entrance slit of a monochromator, on the exit slit of which a photomultiplier (PMT, model no. Hamamatsu R 955) is fixed. PMT signal is then fed into a storage oscilloscope from which traces are transferred to a computer. Details of the LINAC and kinetic spectrophotometer are given in the following sections.

Linear accelerator (LINAC): Accelerator is the main component of pulse radiolysis system as it provides short pulse, high energy electrons which are essential to generate the transient species. The LINAC system was obtained from Viritech Ltd., U. K. The components of this machine are discussed in brief as follows. The schematic diagram of the LINAC is provided in Figure 2.15.

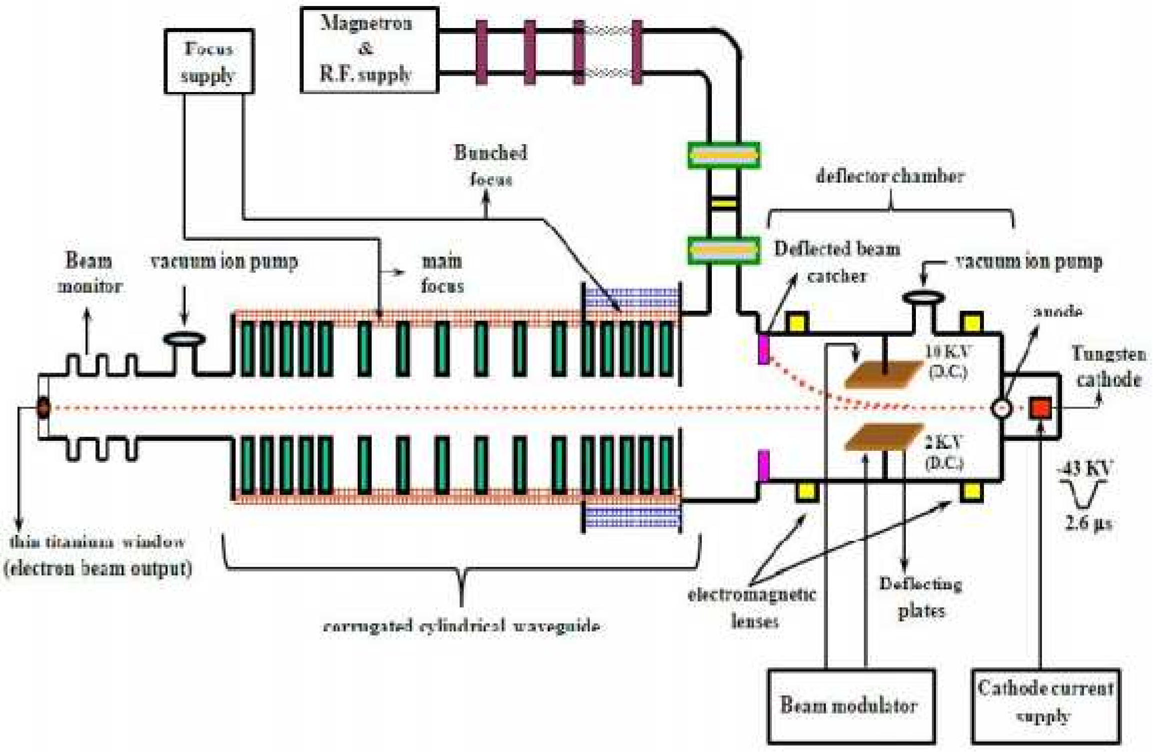

Figure 2.15: Schematic diagram of LINAC system

Electron gun: A tungsten electrode in the form of a pellet is continuously heated by electrons from the filament of the gun kept at a potential of -6.0 KV (DC) with respect to the cathode. The cathode potential is varied for 2 µs at amplitude of 43 KV. As a result of this, 2 µs electron pulse of energy 43 KeV is generated in the system initially. This electron pulse is focused into a deflector chamber with the help of electromagnetic lenses before it enters into a cylindrical wave guide.

Wave guide: A magnetron with 3 GHz frequency and 1.8 MW peak power produces a synchronous traveling R.F. (radio frequency) field of 2 µs pulse width. The electrons produced in the electron gun assembly are allowed to enter into the wave guide in a phase synchronous with the R.F. field, wherein the electrons are accelerated in vacuum to a final energy of 7 MeV. A well-defined uniform beam of accelerated electrons are obtained after focusing by electromagnetic coils and comes out from the wave guide through a titanium window with mean diameter of ~ 2 mm. Electron pulses of various widths from 50 ns to 2 μs with peak current ranging from 1.56 A to 70 mA can be produced by this machine. The nano-second pulses are obtained with the help of deflector plates placed between the anode of the electron gun and the corrugated wave guide. The 43 KeV electrons emitted from the electron gun are deflected and collected by a beam catcher.

Dosimeters for pulse radiolysis

The electron dose applied to the sample during pulse radiolysis is considered as one important parameter. Thiocyanate dosimeter is commonly used to measure the absorbed dose per pulse for pulse radiolysis experiment.[43] It is an aerated aqueous 0.01 mol dm^{-3} potassium thiocyanate (KCNS) solution. The species such as e^-_{aq} and H-atom generated upon electron beam irradiation of the sample solution are scavenged by the dissolved oxygen. Therefore, the hydroxyl (•OH) radical only exist and it oxidizes SCN^- ions to produce $(SCN)_2^{\bullet -}$ radicals. Involved reactions are shown below.[43]

$SCN^- + {}^\bullet OH \rightarrow SCN^\bullet + OH^-$ [2.13]

$SCN^\bullet + SCN^- \; (SCN)_2^{\bullet -}$ [2.14]

The radiation dose is estimated from the maximum absorbance (ΔOD) of the radical $(SCN)_2^{\bullet -}$ at 475 nm. The G-value and the extinction coefficient (ϵ) of this radical is reported to be 3.3 per 100 eV of absorbed dose and 7600 $dm^3\ mol^{-1}\ cm^{-1}$, respectively at 475 nm.[43] From the measured ΔOD, the absorbed dose per pulse (D) is computed from the following equation.[43]

$$D = \frac{9.648 \times 10^6 \Delta OD}{G \epsilon l \rho}\ Gy \qquad [2.15]$$

Here, l and ρ are path length of the light and density of the solution, respectively.

The experiments represented in this thesis are mostly carried out with a dose in the range of 30 ± 5 Gy and pulse width used are mostly 100 or 200 ns. The samples are irradiated after purging the solution for 10-15 min. with the IOLAR grade nitrogen gas. The electron transfer reactions were monitored using donor concentration almost one order higher than the acceptor concentration. It minimise the formation of the radical anion of the acceptor by direct electron capturing and enhance the possibility of observation of bimolecular electron transfer process.

2.6. Materials and Methods

2.6.1. Materials: The details of the source and quality of the materials used for the work presented in this thesis are provided here.

Chapter 3 comprises of the experiments based on electron and triplet energy transfer study in room temperature ionic liquid medium. RTIL solvents (each of them is HPLC grade), namely, 1-ethyl-3-methyl-imidazoliumtetrafluoroborate ([EMIM][BF_4] or C_2Mim), 1-butyl-3-methyl-imidazolium-tetrafluoroborate ([BMIM][BF_4] or C_4Mim), 1-butyl-3-methyl-imidazolium-hexafluorophosphate ([BMIM][PF_6]), 1-hexyl-3-methyl-imidazoliumtetrafluoroborate ([HMIM][BF_4] or C_6Mim) and 1-decyl-3-methyl-imidazoliumtetrafluoroborate ([DMIM][BF_4] or C_{10}Mim), (with >99% purity, <100 ppm water content and <100 ppm halide ion concentration) were procured from IoLiTec, Germany. They were used here without any purification. Another group in our division verified the water content of the ionic liquids by using Karl Fischer titration with the aid of a Metrohm 831 KF Coulometer and found to be within the limits specified by the manufacturers.[44, 45] They also indicated negligible effect of these impurities on fluorescence studies. All the ionic liquids chosen for this study were colourless. Therefore, we made a consideration that these ionic liquids containing permissible amount of water and halide ions should have no effect on the rates of the photo and radiation chemical processes studied here.

Spectroscopic grade acetonitrile and ethylene glycol, were purchased from Spectrochem, India or Sigma-Aldrich, USA and were used as received without further purification. Sodium dodecyl sulfate (SDS), benzophenone (BP), naphthalene (NP), biphenyl (BIP) anthracene (AN), pyrene (PY), tris-(bypyridine)-ruthenium ($[Ru(bpy)_3]^{2+}$, $RuBPY^{2+}$) chloride and methyl viologen (MV^{2+}) chloride were procured from Sigma-Aldrich, USA. These chemicals were of better than 99% purity and used as received. Solutions, which were used for laser flash photolysis and electron pulse radiolysis experiments, were purged with IOLAR grade nitrogen for about 15 minutes to ensure complete removal of oxygen dissolved in the solutions and properly sealed.

Chapter 4 describes the exciton dynamics study in anthracene nanoaggregates. Scintillation grade anthracene (purity > 99%) procured from Fluka was further purified by recrystallization from toluene followed by vacuum sublimation. Purity of the sample was verified using NMR spectroscopy as well as comparing the absorption and fluorescence excitation spectra recorded in cyclohexane. Perfect matching between these absorption and excitation spectra ensured the high purity of the sample used for the experiments. Spectroscopic grade acetonitrile from Spectrochem (India) Pvt. Ltd. was used as received. Millipore water was used for preparation of anthracene and all other nanoaggregates. Polyvinyl alcohol (PVA; 99+% hydrolyzed), which was used as stabilizer in preparation of all the nanoaggregates, was purchased from Sigma-Aldrich and was used without any further purification.

Chapter 5 deals with the energy transfer study in dopped anthracene nanoaggregates. For this work, scintillation grade anthracene (An) purchased from Fluka (purity > 99%) was further purified by recrystallization from toluene followed by vacuum sublimation. Perylene (Pe) (purity > 99%), tetracene (Te) (purity > 97%) and pentacene (Pn) (purity > 97%) were procured from Sigma-Aldrich and used after purification through re-crystallization and vacuum sublimation. Spectroscopic grade tetrahydrofuran (THF) has been procured from Spectrochem Pvt. Ltd., India, and used as received.

Chapter 6 describes the exciton dynamics study of pyrene and perylene nanoaggregates. Scintillation grade pyrene and perylene were purchased from Sigma-Aldrich, andspectroscopic grade dimethyl sulphoxide (DMSO) procured from Spectrochem Pvt. Ltd. (India) All these reagents were used as received without further purification.

Chapter 7 presents the studies based on exciton dynamics in pthalocyanine nanoaggregates. Zinc Phthalocyanine (purity ≥97 %), Zinc 2,9,16,23-tetra-*tert*-butyl-29*H*,31*H*-phthalocyanine (purity ≥96 %), 2,9,16,23-Tetra-*tert*-butyl-29*H*,31*H*-phthalocyanine (purity ≥97 %), 2,11,20,29-Tetra-tert-butyl-2,3-naphthalocyanine (NPC) (purity ≥97 %), Zinc 2,11,20,29-tetra-tert-butyl-2,3-naphthalocyanine (NPC) (purity ≥90 %), Solvent tetrahydrofuran (HPLC grade) all are procured from Sigma Aldrich and are used without further purification.

2.6.2. Synthesis methods of Nanoaggregates: Several procedures for synthesis of organic nanoaggregates already have been reported.[46-50] Among these methods, reprecipitation method has become the most popular because of its simplicity and facileness.[46-48] Anthracene nanoaggregates have been prepared using reprecipitation method, where acetonitrile and water have been used as the good and poor solubility solvents, respectively. 10 mM anthracene solution in acetonitrile and 1mg/ml PVA solution in millipore water were prepared. 200 µl aliquot of the former solution was injected into the 10 ml PVA solution (1 mg/ml) under vigorously stirring condition. After 15 minutes of stirring, anthracene nanoaggregate dispersed in water was obtained. PVA acts as the stabilizer for the nanoaggregates and also limits the size distribution of the nanoaggregates. PVA with same concentration has been used as stabilizer during the synthesis of all the other nanoaggregates presentend in the thesis. The good solubility solvent, the concentration, volume ratios of the poor and good solubility solvents are changed in system to system depending upon the solubility requirement or for generation of small size nanoaggregates.

For doped anthracene nanoaggregates, we prepared an anthracene solution (1 x 10^{-2} mol dm^{-3}) in THF (good solvent). Solution of the acceptor (or dopant) molecule (i.e. tetracene, pentacene or perylene) was also prepared in tetrahydrofuran (THF) and the solutions of anthracene (donor) and the dopant were mixed together to get the proper donor – acceptor concentration ratio (D/A) or donor concentration. Finally, 200 µl of the above solution is injected into 10 ml of the aqueous PVA solution and sonicated for 10 minutes to get aqueous dispersion of nanoaggregates. Perylene and tetracene molecules have good solubility in THF and hence we can change concentration of the dopant up to about 0.25 mol. dm^{-3} or more. However, pentacene is sparingly soluble in THF and hence we could change the concentration up to about 7.2 x 10^{-2} mol. dm^{-3}.

Pyrene and perylene nanoaggregate were synthesized using dimethyl sulfoxide (DMSO) as the good solubility solvent and water as the poor solubility solvent. 100 µl of DMSO solution containing 1 mM of the aromatic hydrocarbon was injected into 10 ml aqueous solution of PVA and was sonicated for about 10 minutes to obtain aqueous dispersion of perylene or pyrene nanoaggregate.

A stock solution of the phthalocyanine derivatives (1 mg/ml) in THF was prepared (concentration ~1.0 x 10^{-3} mol dm^{-3}) and 500 µl of this solution was added to 10 ml of aqueous

PVA solution under mild stirring condition for 15 minutes. This method produces stable dispersion of aggregates of phthalocyanines in water.

REFERENCES

1. Arrhenius, S. *Z. Phys. Chem. (Leipzig),* **1889**, *4,* 226

2. Norrish, R. G. W.; Porter, G. *Nature* **1949**, *164*, 658.

3. Porter, G. *Chemsitry in Microtime*, Imperial College Press: London, **1997**

4. Zewail, A. H. *Femtochemistry-Ultrafast Dynamics of the Chemical Bond*, World Scientific, New Jersey, Singapore, **1994**, volumes I & II and references therein

5. Rohatgi-Mukherjee, K. K. "*Fundamentals of Photochemistry*", Wiley Estern Ltd. India, **1986**

6. *Kasha, M.; Rawls, H. R.; Ashraf El-Bayoumi, M. Pure Appl. Chem.,* **1965**, *11, 371.*

7. Lakowicz, J. R. *Principles of Fluorescence Spectroscopy*, Plenum Press, New York**, 1983**.

8. Pecora, R. *The Scattering of Light and Other Electromagnetic Radiation*, Academic Press, New York, **1969**, pp 482.

9. Verma, G.; Aswal, V. K.; Fritz-Popovski, G.; Shah, C. P.; Kumar, M.; Hassan, P. A. *Journal of Colloid and Interface Science* **2011**, *359*, 163

10. Binnig, G.; Quate, C. F. *Physical Review Letters*, **1986**, *56*, 930.

11. Skoog, D. A.; Holler, J. F.; Crouch, S. R. *Principles of Instrumental Analysis, 6th Ed.* Brooks/Cole Pub Co**, 2006.**

12. Shih, K. *X-Ray Diffraction: Structure*, Principles and Applications, Nova Science, **2013**.

13. West, A. R. *Basic Solid State Chemistry*, John Wiley & Sons, 2nd editio., **1999**.

14. Holzwarth, U.; Gibson, N. *Nat. Nanotechnol.*, **2011**, *6*, 534.

15. Mahr, H.; Hirch, M. D. *Opt. Commun*. **1975**, *13*, 96.

16. Duguay, M. A. *Progress in OpticsAmsterdam*, Netherlands, **1976**, Vol. XIV.

17. Duguay, M. A.; Hansen, J. M. *Opt. Commun* **1969**, *1*, 254.

18. Kahlow, M. A.; Jarzeba, W.; DuBruil, T. P.; Barbara, P. F. *Rev. Sci. Instrum.* **1988**, *59,* 1098.

Chem. 2000, **104**, 5661.

20. Zewail, A. H. *J. Phys. Chem. A* **2000**, *104,* 5660

21. Fleming, G. R. *Chemical Applications of Ultrafast Spectroscopy (International Series of Monographs on Chemistry)*, Oxford University Press, **1986**.

22. Fleming, G. R.; Kaufman, L. J. *Ultrafast Spectroscopy*, John Wiley and Sons.

23. Manz, J.; Wöste, L. *Femtosecond Chemistry*, Vols. I and II, VCH , New York, **1994**.

24. Siegman, E. *Lasers*, University Science Books, Mill Valley, CA, **1986**.

25. George, P. A.; Strait, J.; Dawlaty, J.; Shivaraman, S.; Chandrashekhar, M.; Rana, F.; Spencer, M. G. *Nano. Lett.* **2008**, *8,* 4248.

26. Ghosh, R.; Mora, A. K.; Nath, S.; Palit, D. K. *J. Phys. Chem. B.* **2017**, *121,* 1068.

27. Kakade, S.; Ghosh, R.; Palit, D. K. *J. Phys. Chem. C* **2012**, *116*, 15155.

28. Berera, R.; Grondelle, R. V.; Kennis, J. *Photosynthesis Research*, **2009**, *101*, 105.

29. Ruckebusch, C.; Sliwa, M.; Pernot, P.; Huan, A. D.; Tauler, R. *J. Photochem. Photobiol. C: photochem. Rev.* **2012**, *13*, 1.

30. Manz, J.; Wöste, L. *Femtosecond Chemistry*, Vols. I and II, VCH , New York, **1994**.

31. Svelto, O. *Principles of Lasers*, 3rd. ed. Plenum Press, New York, **1989**.

32. Rulliere, C. *Femtosecond Laser Pulses; Principles and Experiments*, Springer, **1998**.

33. Ghosh, R.; Mandal, J. A.; Palit, D. K. *J. Phys. Chem. B* **2010**, *114*, 12129.

177

34. Ghosh, R.; Nandi, A.; Palit, D. K.*Phys. Chem. Chem. Phys*. **2016**, *18*, 7661.

35. Yoshida, Y.; Tagawa, S.; Tabata, Y. *Pulse Radiolysis*, CRC Press, **1990**.

36. Baxendale, J. H.; Busi, F.; Eds., *The Study of Fast Processes and Transient Species by Electron Pulse Radiolysis*, Springer Netherlands, Dordrecht, Holland, **1982**.

37. Hummel, A. *Adv. Radiat. Chem*., **1974**, *4*, 1-102.

38. Yoshida, Y.; Tagawa, S.; Tabata, Y.*Radiat. Phys. Chem*., **1984**, *23*, 279.

39. Smaller, B.; Remko, J. R.; Avery, E. C. *J. Chem. Phys*., **1968**, *48*, 5174.

40. Schmidt, K. H.; Buck, W. L. *Science*, **1966**, *151*, 70.

41. Tabata, Y. *Pulse Radiolysis of Irradiated Systems*, CRC Press, **1991**.

42. Guha, S. N.; Moorthy, P. N.; Kishore, K.; Naik, D. B.; Rao, K. N. *Proc. Indian Acad. Sci.(Chem. Sci.)* **1987**, *99*, 261

43. Buxton, G. V.; Stuart, C. R. *J. Chem. Soc. Faraday Trans*., 1995, **91**, 279.

44. S. R. Prabhu, S. R.; Dutt, G. B. *J. Phys. Chem. B* **2014**, *118*, 13244.

45. V. Gangamallaiah, V.; Dutt, G. B. *J. Phys. Chem. B* **2014**, *118*, 13711.

46. Liang, W. W.; Chang, C. Y.; Lai, Y. Y.; Cheng, S. W.; Chang, H. H.; Lai, Y. Y.; Cheng, Y. J.; Wang, C. L.; Hsu, C. S. *Macromolecules* **2013**, *46*, 4781.

47. Yu, J. Y.; Chen, I. W. P.; Chen, C. H.; Lee, S. J.; Chen, I. C.; Lin, C. S.; Cheng, C. H. *J. Phys. Chem. C* **2008**, *112*, 3097.

48. Latterini, L.; Roscini, C.; Carlotti, B.; Aloisi, G. G.; Elisei, F. *Phys. Stat. Sol. A* **2006**, *203*, 1470.

49. Chung, H. R.; Kwon, E.; Oikawa, H.; Kasai, H.; Nakanishi, H. *J. Crystal growth* **2006**, *294*, 459.

50. Seko, T.; Ogura, K.; Kawakami, Y.; Sugino, H.; Tanaka, J. *Chem. Phys. Lett.* **1998**, *291*, 438.

CHAPTER 3

EFFECT OF MICROSCOPIC HETEROGENEITY ON THE ELECTRON TRANSFER AND TRIPLET ENERGY TRANSFER REACTIONS ASSOCIATED WITH LONG LIVED TRANSIENTS

3.1. INTRODUCTION

Room temperature ionic liquids (RTIL), which are often referred to as ‘designer solvents’, are considered as the novel solvents of interest and the green alternatives to conventional organic solvents. They have been the great focus of the scientists in various fields, since they can be tuned for diverse applications due to their unusual physical and chemical properties like high thermal stability, inflammability, low volatility, chemical stability and excellent solubility for many organic compounds.[1 – 7] Due to good radiation stability of RTILs, these solvents are also being considered as future solvents for nuclear fuel cycle and can be used in actinide electro-refining and solvent extraction.[8, 9]

In spite of huge research efforts in recent years, the properties of RTIL are not yet well understood. Several groups have reported the presence of microscopic heterogeneities in these solvents.[10 - 16] Significant efforts have been put to explore the microscopic nature of these solvents using fundamental chemical processes as the probe, like hydrogen atom transfer, electron transfer, energy transfer, solvation dynamics, etc.[17- 32] Energy transfer (ENT) and electron transfer (ET) reactions have particularly been used by different research groups, who found that the rates of these processes conducted in RTILs were faster by about one to two order than the diffusion controlled rates. These observations have been explained by the presence of local low viscosity pockets in RTIL solutions.

Maroncelli and coworkers as well as Vauthey and coworkers demonstrated that the faster ET rates observed in RTIL media were really not associated with some special property of RTILs.[28, 29] Instead, they showed that this feature might also be observed in the case of the conventional organic solvents having comparable viscosities. They proposed presence of three distinct quenching regimes appearing at three different time scales. If the reactants stay very close to each other, e.g. at very high concentration of the quencher, they form a contact complex and they need not to diffuse for the reaction and the reaction rate falls in the '*static quenching regime*'. In this regime, the reaction rate is governed by the activation energy. If the ET process has low or zero activation barrier, the reaction rate is quite fast in this quenching regime. Subsequently, the '*transient quenching regime'* appears where reactants need to diffuse towards each other for reaction to occur. However, even in this quenching regime, equilibrium condition is not achieved. The '*stationary quenching regime'* is attained at longer time domain, when the rate of diffusion and the rate of reaction are equal to achieve an equilibrium condition. Therefore, the diffusion controlled reaction can only be observed after achieving the stationary condition. In the case of highly viscous solvents, like RTIL, the stationary condition can be achieved only after a few hundreds of nanoseconds.[36] If the excited state undergoing ET reaction has lifetime shorter than 10 ns, the observed quenching process occurs mainly in the static and transient quenching regimes. As a result, the average reaction rates appeared to be faster than the diffusion controlled rate. Therefore, to measure the actual diffusion controlled rate, reactions involving long lived transient reactants, e.g. anion radicals or molecules in the excited triplet states, need to be investigated. In order to delineate this aspect, we have tried to observe the electron transfer rate between two different pairs of radical anions and neutral molecules, namely, pyrene (PY) radical anion – benzophenone (BP) and BP radical anion – fluorenone, using nanosecond electron pulse radiolysis technique in two very common RTIL solvents and few other conventional solvents having different viscosities.

Dutt and coworkers studied rotational diffusion process for neutral and charged fluorophores and suggested the existence of polar and nonpolar pockets in solutions of RTIL.[33] There are several other reports which also indicates presence of such microscopic pockets inside RTIL media. Here in the second part we want to explore the effect of long alkyl substituents of RTILs on such microscopic pocket formation by observing the TET and ET processes using a few neutral and / or ionic donor -acceptor pairs reaction schems are provided in supplementary data (SD) section (S3.1). We also wish to probe the microscopic viscosities of these pockets.

3.2. RESULTS AND DISCUSSION

3.2.1. Establishing the fact that, diffusion controlled ET process can be observed with long lived transients

3.2.1.1. Radiolysis of ionic liquid and characterization of radical anions: Several studies on pulse radiolysis of ionic liquids in nanosecond time domain,[20, 27, 28, 36- 40] as well as in picosecond time domain,[41-44] have been published. These works indicate that, for the imidazolium ionic liquids, the electrons produced by ionization are rapidly scavenged by the solvent molecules before they become fully solvated, while the electrons in the ammonium ionic liquids are solvated quickly to form the solvated electrons. Neta and his coworkers recorded the absorption spectra of the transient species formed upon pulse irradiation of deoxygenated liquid [BMIM][PF_6].[33] The spectrum recorded at 1 μs following irradiation using electron pulses of <1 μs duration exhibited a maximum at 325 nm and a shoulder near 370 nm. They have predicted that in the radiolysis of this RTIL, the energy deposited in the liquid is possibly absorbed by $BMIM^+$ (~53%) and by PF_6^-(~47%), according to their relative electron densities. In both cases, the first step is ionization, forming a thermalized electron and the remaining radical.

$$\mathbf{BMIM^+ \rightarrow BMIM^{\cdot 2+} + e^-} \qquad (3.1)$$

$$\mathbf{PF_6^- \rightarrow PF_6^{\cdot} + e^-} \qquad (3.2)$$

Geminate recombination of the primary radical species leads to formation of the excited states and subsequently C-H and C-C bond scission reactions in the methyl and butyl groups lead to formation of H· atoms and alkyl radicals, respectively. In addition, formation of PF_5, F· and F^- are also expected from the dissociation reaction of PF_6^- and $PF_6^{\cdot}$ species. Thermal electrons thus produced may or may not be solvated but these electrons and H· atoms react with $BMIM^+$ to from BMIM· radical (equation 3.3) and H· atom adduct (equation 3.4), respectively, and F· reacts very rapidly, possibly via addition to the ring or oxidation. These processes are complete within <10 ns and their products are observed immediately at the end of the sub-microsecond pulse. However, these radiolysis products have negligible absorption in the wavelength region of our interest (i.e. >400 nm).

$$\mathbf{BMIM^+ + e_{aq}^- \rightarrow BMIM^{\cdot}} \qquad (3.3)$$

$$\mathbf{BMIM^{+} + H^{\cdot} \rightarrow H - BMIM^{\cdot}} \qquad (3.4)$$

Pulse radiolysis technique has been frequently used for generation, characterization as well as studying reactions of radical anions in solutions.[20, 27, 28, 45, 46] Wishart and Neta reported that dry electron capture by aromatic solutes, such as benzophenone and pyrene, is very efficient in ionic liquids, while the reactions of the solvated electron with the same compounds are diffusion limited, and slower due to the high viscosity of the ionic liquid.[27] In this work, we have used this technique to generate and characterize the spectroscopic properties of the radical anions of pyrene, benzophenone and fluorenone in [BMIM][PF_6] and [BMIM][BF_4]. 5 x 10^{-2} mol dm^{-3} of the solute dissolved in an RTIL was subjected to electron pulse irradiation and the decay kinetics of the transient species were recorded in the 400 – 770 nm region. The time resolved transient spectra were constructed using these decay traces.

The time resolved transient spectra recorded following pulse radiolysis of the solutions of these solutes in [BMIM][PF_6] are presented in Figure 3.1. The transient absorption spectrum recorded at 0.5 μs following electron pulse radiolysis of pyrene in this solvent has the absorption maxima at 490 nm and a shoulder at 450 nm, which can be assigned to pyrene radical anion, $Py^{\cdot -}$, and radical cation, $Py^{\cdot +}$, respectively.[45] Simultaneous formation of both the pyrene radical cation and radical anion, has been observed by pulse radiolysis of pyrene in DMSO and RTIL.[20, 45] We mentioned earlier that the yield of solvated electron is small in imidazolium ionic liquids because the electrons are rapidly scavenged by the solvent molecules before they become fully solvated. Therefore, in the present case, formation of these radicals can be predicted by the reactions with the dry and / or solvated electron and $BMIM^{\cdot 2+}$, respectively. Wishart and Neta reported that dry electron capture by aromatic solutes, such as benzophenone and pyrene, is very efficient in ionic liquids.[27] Therefore, formation of $Py^{\cdot +}$, and $Py^{\cdot -}$ can be predicted via the reactions 3.5 and 3.6. Since the absorption coefficients of these two radicals are very similar (~2.2 x 10^4 dm^3 mol^{-1} cm^{-1}), the relative heights of the peaks at 495 and 450 nm clearly suggest much larger yield of the radical anion.[42]

$$\mathbf{Py + e^{-}(Th) \rightarrow Py^{\cdot -}} \qquad (3.5)$$

$$\mathbf{Py + BMIM^{\cdot 2+} \rightarrow Py^{\cdot +}} \qquad (3.6)$$

Formation of the radical anions of benzophenone and fluorenone is also confirmed by the absorption bands with the maxima at 680 nm and 530 nm (and a shoulder at 470 nm), respectively (Figures 3.1B and 3.1C).[27, 46] While, the time evolution of the transient spectra reveals that the radical anion of pyrene decays monotonously without formation of any other radiolysis products (inset of Figure 3.1A), the decay of the benzophenone radical anion band with the maximum at 680 nm leads to the concomitant rise of another band with the maximum at 540 nm. The latter can be attributed to the formation of ketyl radical of benzophenone.[47] In the case of fluorenone also, the change in the shape of the time-resolved spectra during the course of decay of the fluorenone radical anion is a clear indication of formation of ketyl radical of fluorenone, which has already been characterized by an absorption spectrum with the maxima at 350 and 500 nm.[47] Formation of ketyl radicals of benzophenone and fluorenone can be envisioned by the reaction of the anion radical with the H· atom generated by radiolytic C-H bond scission of the methyl and butyl group of [BMIM][PF_6] (vide supra).

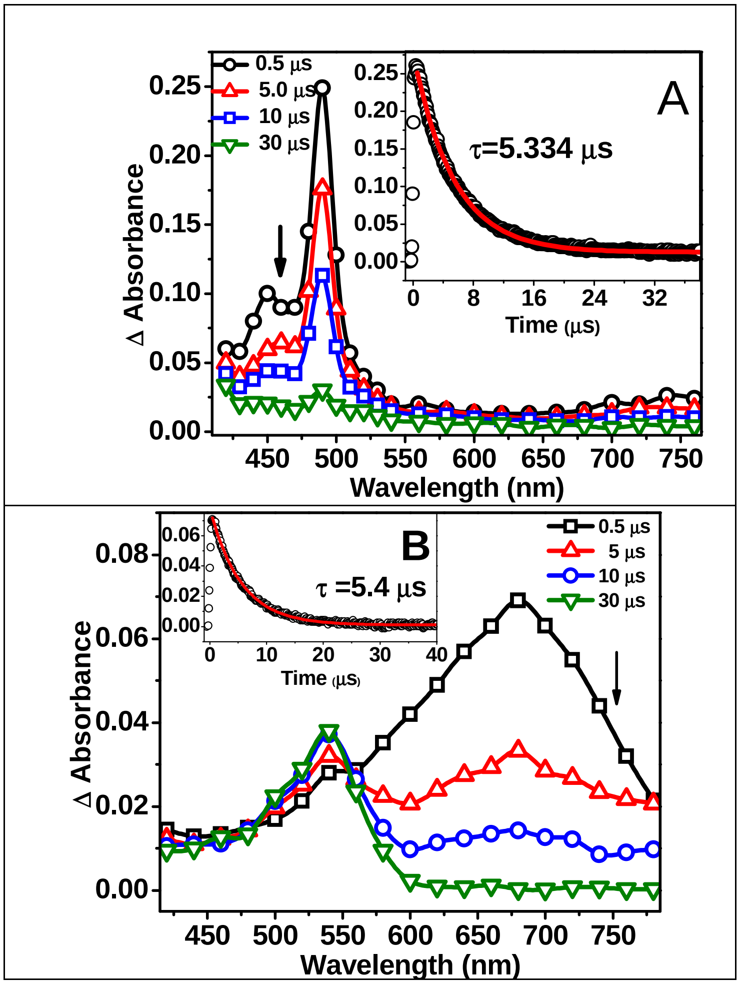

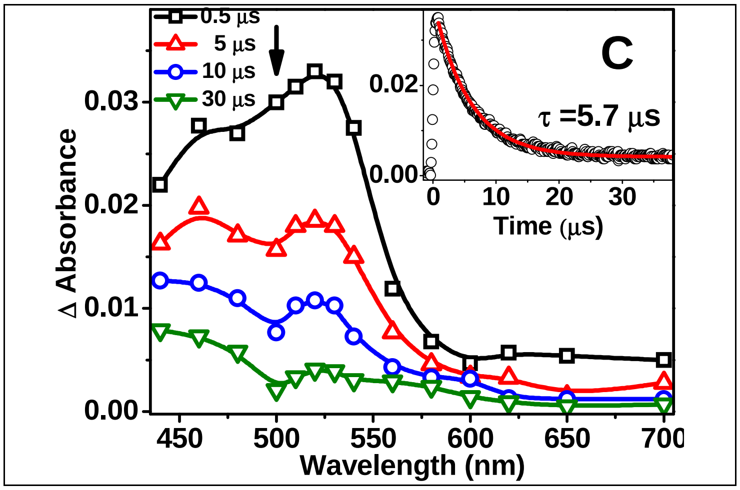

Figure 3.1: Time resolved absorption spectra and decay traces at corresponding λ_{max} of the radical anions of pyrene (A), benzophenone (B) and fluorenone (C).

For determination of the lifetimes of these radical anions, we have analyzed the decay profiles recorded at several wavelengths of the absorption spectra and found that each of them could be well-fitted using an exponential function with a single lifetime component. Only one decay trace, recorded at the wavelength of maximum absorption of each of the radical anions is given in the insets of Figure 3.1 along with the best fit single exponential function and the associated lifetime. The lifetimes of the anion radicals of pyrene, benzophenone and fluorenone in [BMIM][PF$_6$] are 5.3, 5.4 and 5.7 μs, respectively. We discussed earlier that for investigation of the electron transfer processes occurring in the diffusion controlled regime in viscous RTIL media, the electron donor needs to be long-lived enough to survive for several hundreds of nanoseconds. Therefore, these radical anions could be used as promising electron donors for this purpose.

Characteristics of the radical anions of these solutes have also been studied in [BMIM][BF$_4$]. Absorption spectra of the anions in this solvent have been found to be very similar to those recorded in the other RTIL. The lifetimes have been determined to be in the range of few microseconds.

3.2.1.2 Electron Transfer Study: We have investigated the dynamics of ET from a radical anion, which is formed by capturing a thermal electron, to an acceptor molecule in the ground electronic state. We have chosen the donor – acceptor pairs of molecules on the basis of the consideration that the absorption band of the donor radical anion does not have significant overlap with that of the radical anion of the acceptor molecule so that the decay of the former and formation of the later can be monitored without any interference. Therefore, we have chosen Pyrene - Benzophenone and Benzophenone - fluorenone pairs for our study. In these systems, concentration used for pyrene (or benzophenone) (3 or 5 x 10^{-2} mol dm^{-3}) is about ten times larger than that of the acceptor molecule, benzophenone (or fluorenone) (varying in the range 1 – 8 x 10^{-3} mol dm^{-3}). In this condition, the thermal electrons are preferentially captured by pyrene (or benzophenone) to form the radical anion, which transfers its extra electron to benzophenone (or fluorenone). The ΔG values for these two pairs of donor radical anion and molecular acceptor systems have also been calculated using equation 3.7 (Table 3.1) and has been found to be negative, suggesting the fact that these pairs are suitable for study of ET process in RTILs.

$$\Delta G = -E_{red}(A/A^{-}) + E_{red}(M/M^{-}) \qquad (3.7)$$

Where $E_{red}(M/M^{-})$ and $E_{red}(A/A^{-})$ are the reduction potentials for the quencher molecule and the radical anion, respectively. In the present case, since one of the reactants undergoing ET reaction and one of the products formed are neutral molecules, the work function term arising due to columbic interaction between the ionic species will have negligible contribution and is not considered here.

We have recorded the temporal profiles for the transient species formed following radiolysis of 3 x 10^{-2} mol dm^{-3} of pyrene and 3 x 10^{-3} mol dm^{-3} of benzophenone in [BMIM][PF_6] in the 420 – 770 nm region and the time-resolved spectra of the transient species thus constructed using these temporal profiles are shown in Figure 3.2. We find a rapid decay of the transient absorption band with the maximum at 490 nm and the concomitant growth of a transient absorption band with the maximum at 680 nm. This time evolution of the transient spectra suggests the transfer of an electron from the radical anion of pyrene to benzophenone forming the benzophenone radical anion. This has been further confirmed by monitoring the decay of the pyrene radical anion at 490 nm and the growth of the benzophenone radical anion at 680 nm following pulse radiolysis of the solutions containing pyrene of fixed concentration (3 x 10^{-2} mol dm^{-3} of pyrene) but varying concentrations of benzophenone in the range 1.6 -6.8 x 10^{-3} mol dm^{-3}. The results have been presented in Figure 3.3, which clearly reveals that the decay rate of pyrene radical anion increases with the increasing concentration of benzophenone in solution.

This observation confirms the electron transfer interaction between the pyrene radical anion and benzophenone in its ground electronic state.

The decay traces are fitted single exponentially and the pseudo first order rate constants (the inverse of the corresponding lifetimes) for the ET reaction in the presence of different concentrations of benzophenone are determined (Table 3.1). The bimolecular rate constant for the ET process from pyrene radical anion to benzophenone molecule in [BMIM][PF$_6$] has been determined from the slope of the plot of the pseudo first order rate constants vs the concentration of benzophenone. The rate constant thus determined is 5.7 x 10^7 dm^3 mol^{-1} s^{-1}.

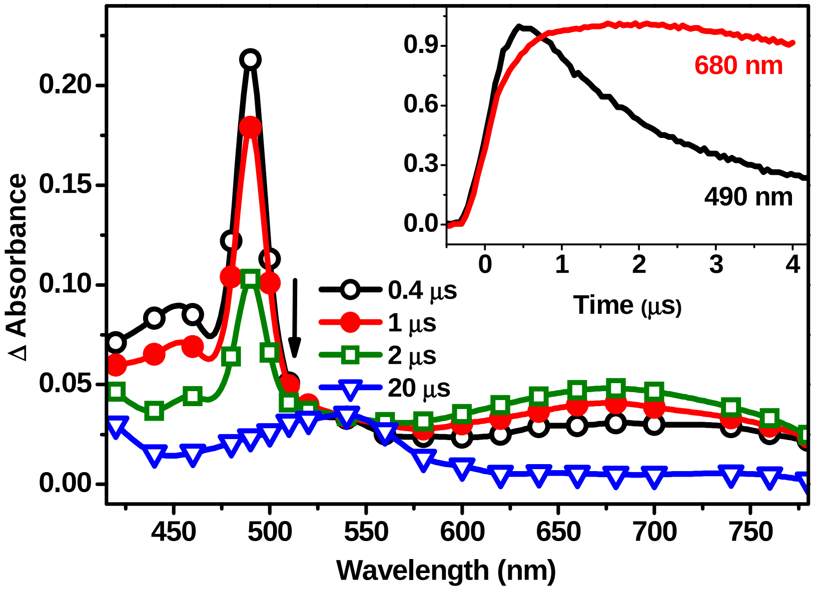

Figure 3.2: (a) Time-resolved transient spectra following pulse radiolysis of 3 x 10^{-2} mol dm^{-3} of pyrene and 3 x 10^{-3} mol dm^{-3} of benzophenone in [BMIM][PF$_6$], (b) Decay trace of pyrene anion radical at 490 nm and formation of benzophenone radical anion at 530 nm.

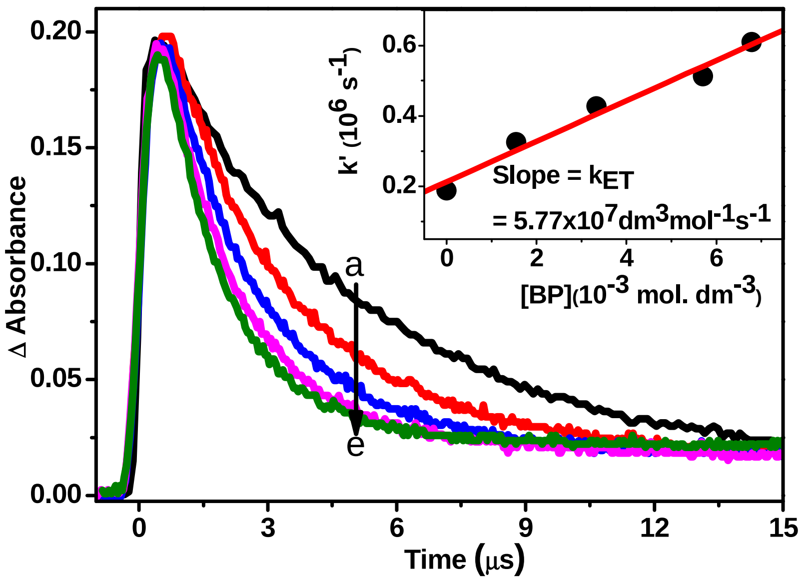

Figure 3.3: Decay of pyrene radical anion measured at 490 nm in absence of benzophenone (a), and in presence of 1.6 (b), 3.3 (c), 5.7 (d) and 6.8 (e) x10^{-3} mol dm^{-3} of benzophenone in acetonitrile. Inset: Linear plot of the pseudo-first order rate constants vs the concentration of Benzophenone ([BP]) in [BMIM][PF_6].

Quenching of benzophenone radical anion as the electron donor has been studied using fluorenone as the electron acceptor in [BMIM][PF_6]. Figure 3.4 presents the time-resolved spectra of the transients following pulse radiolysis of 5 x 10^{-2} mol dm^{-3} of benzophenone and 5 x 10^{-3} mol dm^{-3} of fluorenone in this RTIL. We determined the bimolecular rate constant for the ET reaction between benzophenone radical anion and fluorenone using different concentrations of fluorenone in the range 2 - 8 x 10^{-3} mol dm^{-3} as the quencher (Figure 3.5).

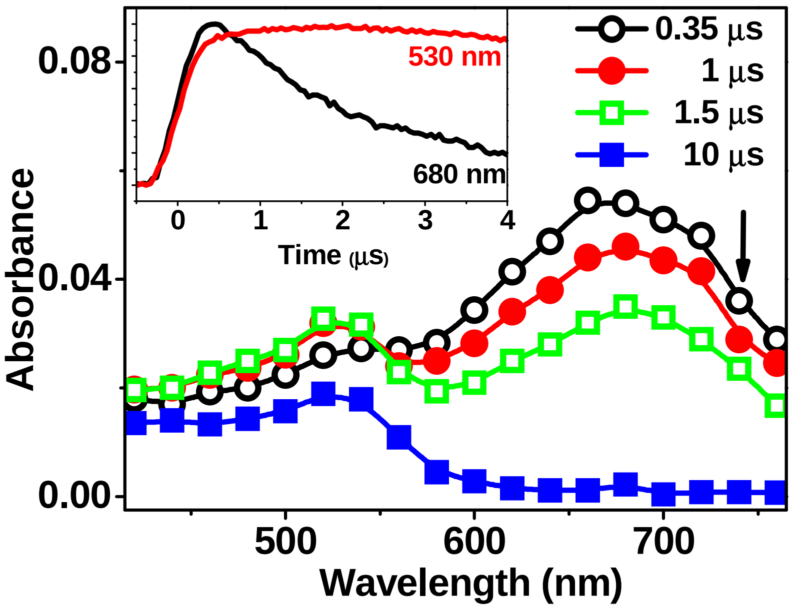

Figure 3.4: Time-resolved transient spectra following pulse radiolysis of 5 x 10^{-2} mol dm^{-3} of benzophenone and 5 x 10^{-3} mol dm^{-3} of flurenone in [BMIM][PF_6], Inset: Decay trace of benzophenone radical anion at 680 nm and formation of fluorenone radical anion at 530 nm.

Similar studies as described in the earlier sections using [BMIM][PF_6] as the solvent were extended for the other RTIL, namely, [BMIM][BF_4], as well as other conventional solvents, namely, acetonitrile, 1-pentanol and 1-decanol as well as ethylene glycol (EG) and ethylene glycol – glycerol (GL) solvent mixtures. The bimolecular rate constants for the ET reactions for the pyrene – benzophenone and benzophenone - fluorenone pairs have been estimated. Results obtained are presented in Table 3.1.

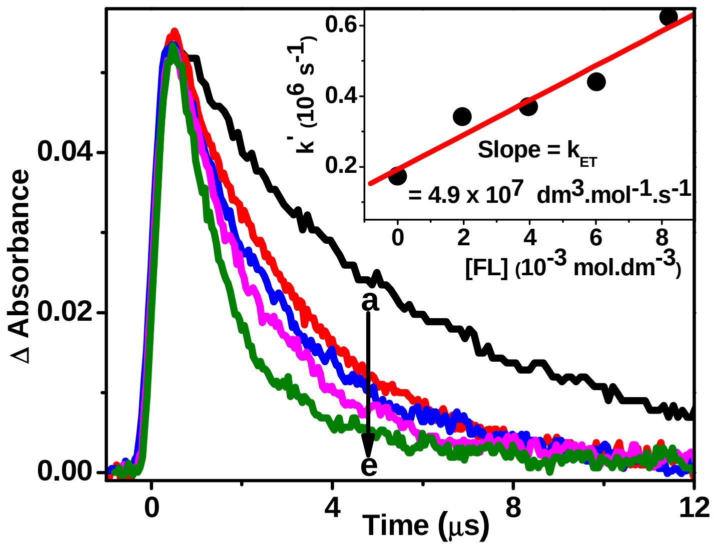

Figure 3.5: Decay of benzophenone radical anion measured at 680 nm in absence of fluorenone (a) and in presence of 1.9 (b), 3.8 (c), 6.0 (d) and 8.0 (e) x10^{-3} mol dm^{-3} of fluorenone in acetonitrile. Inset: Linear plot of the pseudo-first order rate constants vs the concentration of fluorenone ([FL]) in [BMIM][PF_6].

In a first approximation, i.e. assuming spherical reactants of identical radii, we have calculated the diffusion controlled reaction rate constants (k_{diff}) for all those solvents and solvent mixtures used in the present study (Table 3.1) using the equation 3.8 and the values are given in Table 3.1,[31,48,49]

$$k_{diff} = \frac{8\ x\ 10^6}{3\eta} RT \qquad (3.8)$$

Where *R* is the gas constant (8.3144 J K^{-1} mol^{-1}), T the room temperature (25°C) and η is bulk or macroscopic viscosity of the solvent in cP unit. At 25°C, the bulk viscosities of the pure solvents as well as the solutions in the presence of the highest concentrations of the donor and acceptor molecules have been measured and the values are given in Table 3.1. We find that in the presence of the donor and acceptor molecules, the bulk viscosities of both the RTILs used here are reduced significantly, e.g. the viscosity of pure [BMIM][PF_6] at 298 K is 270 cP, but the viscosity of the RTIL decreases to 212 cP in the presence of 3 x 10^{-2} mol dm^{-3} of pyrene and 5 x 10^{-3} mol dm^{-3} of benzophenone and to 196 cP in the presence of 5 x 10^{-2} mol dm^{-3} of benzophenone and 5 x 10^{-3} mol dm^{-3} of fluorenone. Here we have assumed that due to variation of the concentration of the acceptor molecule in the range 1.5 – 8 x 10^{-3} mol dm^{-3}, the viscosities of the solutions do not change significantly. Conventional solvents, e.g. acetonitrile, 1-pentanol, 1-decanol and EG, have much lower viscosities as compared to those of RTILs and ethylene glycol-gycerol mixtures have moderate viscosities. We have also observed that the radiation dose used here do not change the viscosities of the solvents.

Table 3.1: Standard free energy changes (ΔG^0) for the ET reaction between the anions and the quenchers, viscosities of the solutions, experimentally determiined rates of ET reactions (k_{ET}), the rates of diffusion controlled reactions calculated using equation 3.8 (k_{diff}) and the ratio between k_{ET} and k_{diff}.

A. Pyrene- Benzophenone pair

Solvent	ΔG^0(eV)	Viscosity (cP)[a]	k_{ET} ($dm^3.mol^{-1}s^{-1}$)	k_{diff},(dm^3 mol^{-1} s^{-1})	k_{ET} /k_{diff}
[BMIM][PF_6]	-0.26	208	5.7 ± 0.5 x 10^7	3.2x10^7	1.78
[BMIM][BF_4]		80.7	10.3 ± 1 x 10^7	8.2 x10^7	1.26
EG + GL (0.5:0.5)		75.2	1.3 ± 0.2 x 10^8	8.8 x 10^7	1.47
EG + GL (0.7:0.3)		38.1	2.3 ± 0.2 x 10^8	1.73 x 10^8	1.33
EG		15.4	4.7 ± 0.1 x 10^8	4.3 x 10^8	1.09
1-decanol		11.8	8.1 ± 0.2 x 10^8	5.6 x 10^8	1.44
1-Pentanol		3.35	2.7 ± 0.3 x 10^9	1.97 x10^9	1.37
Acetonitrile		0.35	1.8± 0.2 x 10^{10}	1.89x10^{10}	0.95

B. Benzophenone –Flurenone pair

Solvent	ΔG^0(eV)	Viscosity (cP)[a]	k_{ET} ($dm^3.mol^{-1}s^{-1}$)	k_{diff}, (dm^3 mol^{-1} s^{-1})	k_{ET} /k_{diff}
[BMIM][PF_6]	-0.54	195.4	4.9 ± 0.5 ×10^7	3.4 × 10^7	1.44
[BMIM][BF_4]		76.2	12.7 ± 0.7 ×10^7	8.7×10^7	1.46
EG + GL (0.5:0.5)		75.3	1.2 ± 0.2 x 10^8	8.8 x 10^7	1.36
EG + GL (0.7:0.3)		38.2	1.4 ± 0.2 x 10^8	1.73 x 10^8	0.81
EG		15.6	3.9 ± 0.5 x 10^8	4.23 x 10^8	0.92
1-decanol		12	5.7 ± 0.2 × 10^8	5.5 × 10^8	1.04
1-Pentanol		3.34	1.5 ± 0.2 ×10^9	2 ×10^9	0.75
Acetonitrile		0.353	1.4 ± 0.1×10^{10}	1.87 ×10^{10}	0.75

[a] Average viscosity of the solution is considered here.

In Table 3.1, we observe that the ratios of the experimentally determined values of k_{ET} and the calculated values of k_{diff} using equation 8 for all the solvents and solvent mixtures used in our study vary in the range from 0.75 to 1.64, which leads us to consider that the experimentally determined ET rates are nearly equal to the diffusion controlled rate within the experimental error. This leads us to conclude that, like in the case of conventional solvents, the rates of ET reactions between anions and a neutral solute molecules in RTIL are diffusion controlled.

Vauthey and coworkers observed time-dependence of the rates of bimolecular quenching reactions in RTIL as well as in other viscous solvents and explained the phenomenon by predicting the existence of three distinct quenching regimes.[31] In the '*static*' regime, the reactant pairs are already in contact with each other and no diffusion is necessary for the reaction to take place and the quenching rate is the intrinsic ET rate, k_0. In the next regime, namely the '*non-stationary* or *transient*' regime, the reaction rate constantly decreases with time, because of the fact that immediately after the reactions between the reactants in close contact, the hole created by the reaction in the pair distribution distance between the reactants gradually increases and the reactants needs to diffuse to react. This continues as long as an equilibrium is established between the rate at which the intrinsic reaction occurs and the rate of diffusion of the reactants to give rise to a constant reaction rate. This is called the 'stationary' regime. The duration of the static regime depends on the intrinsic ET rate constant, k_0, whereas that of the transient regime depends on the viscosity of the solvent. Therefore, while the stationary regime may be reached after a few nanoseconds in the case of low viscous solvents, such as acetonitrile, it may take several hundreds of nanoseconds to reach the same regime in the case of viscous solvents, like RTIL.[31] In the case of highly viscous solvents, the reaction rate (here k_{ET}), which is controlled entirely by the rates of approach of the reacting pairs through diffusion to the optimal distance to form an encounter complex (and can be represented as k_{diff}), is significantly slower than the intrinsic ET rate constant, k_0.

In the present study, because of long duration of the electron pulse (~500 ns), the static and transient quenching regime is not resolvable and hence the value of k_0 could not be determined even in the case of conventional solvents of low viscosity. But the long lifetimes of the donor radical anions allow us to monitor the quenching rates in the *stationary regime* and the transient decay of the donor radical anions appears to follow single exponential kinetics. This suggests that the rate of the bimolecular ET process is determined only by the diffusion rate of the reactants in all kinds of solvents. We observe that, like in conventional organic solvents, the ET process is diffusion controlled in RTILs too.

3.2.2. Probing the Effect of Long Alkyl Substituent on the Microscopic Heterogenity and its Effect upon Electron Transfer and Energy transfer Reactions

3.2.2.1. TET Studies System using Nanosecond Laser Flash Photolysis Technique: The lowest excited triplet (T_1) states of BP and RuBPY$^{2+,}$ which have been used here as photosensitizers, are populated via intersystem crossing process with a quantum yield of near unity following photoexcitation to the excited states in the singlet manifold and the T_1 states are very long-lived (lifetimes are about 1 μs or longer) in normal organic solvents.[50, 51] Spectroscopic and kinetic properties of the T_1 states of these molecules could be effectively used for investigation of the reactions or photophysical processes in RTIL occurring in the stationary quenching regime (vide infra).

TET Process BP-NP and BP-BIP: In this work, we have estimated the rates of TET process occurring from the T_1 state of BP (E_T ~ 2.95 eV) to the T_1 state of NP (E_T ~ 2.64 eV) or to BIP (E_T ~ 2.82 eV) in homogeneous solutions, SDS micelle as well as in four RTIL solvents. Like in the case of common organic solvents, the triplet-triplet (T-T) absorption spectrum of BP recorded in C_4Mim appears in the 420 - 650 nm region with the maximum at 525 nm (S3.2 in SD section).[52] Temporal profiles recorded at 525 nm have been fitted single exponentially with the lifetime of 1.5 μs but with some residual absorption beyond delay times longer than 6 μs. Latter may be attributed to formation of the long-lived ketyl radical of BP by abstraction of hydrogen atom from the alkyl group of the RTIL by the T_1 state of BP.[52, 53] Muldoon et. al. established the mechanism of hydrogen atom abstraction by BP triplet from the alkyl chain of the RTIL solvent molecule to form benzophenone ketyl radical (BPH•)[53] We find that the T_1 state of BP in RTIL is sufficiently long-lived to make it a suitable probe for our purpose (vide infra).

Not only that the lower energy of the T_1 state of NP or BIP with respect to that of BP makes the former a good acceptor, but also the position of the T - T absorption band of NP or BIP is distinctly different from that of the BP triplet and this gives a clear advantage in determining the rate of the TET process by monitoring the decay of the donor triplet and also the rise of the acceptor triplet. Maximum of the T – T absorption spectrum of NP appears at around 415 nm and that of BIP at 360 nm.[51] Since the absorption coefficient of the RTIL solvents is quite large below 380 nm, monitoring the rise of the BIP triplet has not been possible, but the decay of the BP triplet monitored at 525 nm provides information about the TET rate in the case of BP– BIP pair.

TET process is a widely used photophysical process (e.g. in photosensitization reaction), which is allowed under Wigner's spin conservation rule. Therefore, the rate of this process is solely governed by the rate of diffusion of the reactants in solution. In turn, the latter depends upon the macroscopic viscosity (η), if the reaction is conducted in homogeneous solution and the rate of the TET process is directly correlated with the viscosity of the solution. However, in heterogeneous media, such as micelles and RTILs, rate of the TET process is expected to depend upon the microscopic viscosity of the site, at which the donor and acceptor molecules are preferentially located in the medium.

In Figure 3.6, we have presented the time-resolved transient absorption spectra of the T_1 state of BP in the presence of 4.8 mol dm^{-3} of NP in deaerated solution of C_4Mim following photoexcitation at 355 nm (NP molecule does not absorb at this wavelength). The transient absorption spectrum with the maximum at 525 nm recorded immediately after the ns laser pulse has the characteristics of the BP triplet only. However, with increase in delay time, the absorption band due to the BP triplet decays with the concomitant development of an absorption band with the maximum at 415 nm, which is the characteristic of the NP triplet. The temporal profiles shown in the inset of this figure ensure that the triplet state of NP is populated via transfer of energy from the triplet state of BP to that of NP.

We determined the decay rate constants of the donor triplet (k') in the presence of different quencher concentrations varying in the range of 0 – 1.4 x 10^{-2} mol dm^{-3}. Faster rates of the decay of the BP triplet in the presence of higher concentrations of NP provide the direct evidence of the TET process. Each of the temporal profiles recorded at 525 nm is fitted with a single exponential function, $OD(t) = a_1 \exp(-k't) + OD(\infty)$, assuming quenching process follows pseudo-first order kinetics. The factor $OD(\infty)$ represents the residual absorption due to formation of a long-lived reaction product, e.g. the benzophenone ketyl radical in the present case. Slope of the best fit line to the plot of k' vs quencher concentration provides the value of k_{TET}.

We adopted similar approach to determine the rate constants of the TET process for BP – NP and BP – BIP pairs in those four RTIL solvents, SDS micelle and two other conventional solvents (Table 3.2). Residual distributions for the fit functions for BP - NP pair in four RTIL solvents are given in S3.3 in SD section.

In conventional liquids, the value of k_{Diff} can be calculated using the simple Smoluchowski equation,[54, 55] If we assume that the reactants are of spherical shapes of identical radii, Smoluchowski equation may be simplified to equation 3.8 to obtain the values of k_{Diff} with reasonable accuracy.

Bulk viscosities of the solutions containing both the donor and the acceptor molecules have been measured at 298 K and thus the values of k_{Diff} are calculated and given in Table 3.2. We observe that, in the cases of the TET processes for both the BP – NP and BP – BIP pairs, the k_{TET}/k_{Diff} ratio is increased monotonously as the viscosity of the reaction medium is increased and this ratio is larger by more than one order of magnitude as the solvent is changed from C_2Mim to C_{10}Mim (Table 3.2). This possibly suggests some specific kind of organization of the solvent molecules to larger extent as the alkyl chain length of the RTIL molecule is increased.

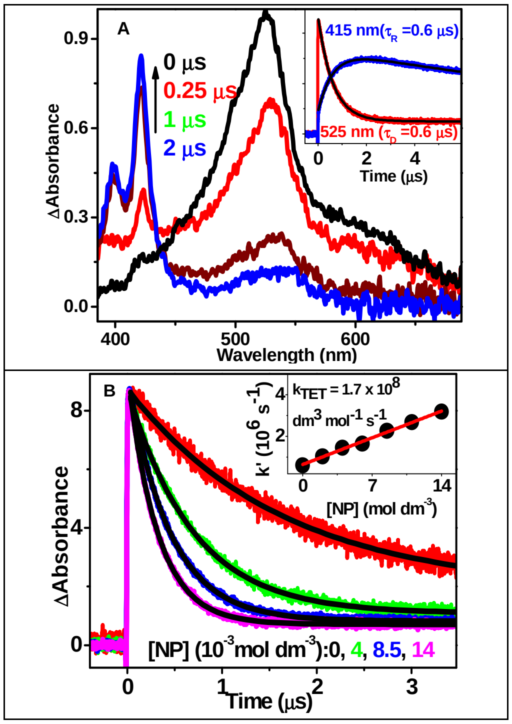

Figure 3.6: (A) Time resolved transient absorption spectra recorded at different delay times following photoexcitation of a solution of 6 x 10^{-3} mol dm^{-3} of BP and 4.8 x 10^{-3} mol dm^{-3} of NP

in C_4Mim. Inset: Temporal profiles recorded at 525 nm (τ_{decay}~ 0.6 μs) and 415 nm (τ_{growth}~ 0.6 μs). (B) Temporal profiles recorded at 525 nm following photoexcitation of a solution of 6 x 10^{-3} mol dm^{-3} of BP and different concentrations of the quencher (NP). The inset represents the plot of k' vs. quencher concentrations and the rate constant (K_{TET}) for TET process is given in the inset.

Rate constants of the TET process for the BP – NP and BP - BIP chemical systems have also been estimated in SDS micelle and those have been given in Table 3.2. Viscosity of the nonpolar core of the SDS micelle has earlier been estimated to be about 24 cP by using electronic spin resonance technique and the diffusion controlled rate to be ~3.2 x 10^8 dm^3 mol^{-1} s^{-1}, adopting ET reactions using PY - $RuBPY^{2+}$ chemical system as the probe. [56-58] De Schryver and coworkers explained that this value of diffusion- controlled quenching rate constant is typical for the micellar interior.[58]

Table 3.2: Viscosities of the solutions, values of k_{TET} determined experimentally, k_{Diff} values calculated using equation 2 and k_{TET}/k_{Diff} for BP – NP and BP - BIP pairs in two conventional solvents, SDS micelle and four RTIL solvents.#

Solvent	**η (cP)**	**k_{TET} (10^8 $dm^3 mol^{-1} s^{-1}$)**	**k_{Diff} (10^8 $dm^3 mol^{-1} s^{-1}$)^a**	**k_{TET} /k_{Diff}**
Acetonitrile (ACN)	0.35 (0.35)	113 (160)	186	0.61 (0.6)
Ethylene Glycol (EG)	15.6 (15.6)	4.3 (5.4)	4.24	1.01 (1.5)
SDS micelle (SDS)	24 (24)^b	2.5 (3.3)	3.2^c	0.78 (1.03)
C_2Mim	44.2 (44.6)^d	1.9 (2.2)	1.5 (1.49)	1.3 (1.5)
C_4Mim	91.2 (92.1)^d	1.7 (1.2)	0.73 (0.72)	2.3 (1.7)
C_6Mim	205.1 (207.2)^d	1.4 (1.6)	0.33 (0.32)	4.3 (5.0)
C_{10}Mim	493.2 (501.4)^d	2.3 (2.2)	0.14 (0.13)	16.9 (16.9)

#Results for the BP – BIP pair has been given inside the first bracket. **a**Calculated using equation 2; **b**ref 57; **c**ref 58; dViscosities of the solutions of RTILs have been determined experimentally. Viscosities of the solutions have been found to vary marginally in the presence of different concentrations of the solutes and hence the average value of those of the solutions has been given here.

TET Process in RuBPY^{2+} – AN system: RuBPY^{2+} – AN pair has been chosen as another one for the TET studies in RTILs considering the fact that the most probable location of RuBPY^{2+} should be near the ionic head group region of the SDS micelle or RTIL solvents, if the latter really possess a micelle-like microscopic structure, whereas that of AN should reside in the nonpolar core (alkyl group) region.[59] Higher energy of the T_1 state of RuBPY^{2+} (E_T ~2 eV) than that of AN (E_T ~ 1.8 eV) make the TET process from the T_1 state of RuBPY^{2+} to AN molecule possible.[60]

Time resolved transient absorption spectrum of the T_1 state of RuBPY^{2+} in C_4Mim shows several distinct features, namely, the ground state bleaching band in the 400 - 530 nm region, the stimulated emission band originating from the T_1 state in the 580 - 700 nm region with the maximum at ca 620 nm and the excited state absorption (ESA) band due to T-T absorption in the 360 - 390 nm region with the maximum at ca 375 nm (S3.2 in SD section). Since RTIL solvents absorb in the wavelength region below 380 nm, monitoring the ESA band in the 360 - 390 nm region is not expected to provide accurate results regarding the triplet lifetime of RuBPY^{2+} in RTIL. However, monitoring the decay of the stimulated emission intensity at 620 nm may provide useful information regarding the dynamics of the T_1 state of RuBPY^{2+} in RTIL. In addition, the T - T absorption spectrum of AN appears in the 380 – 450 nm region with the maximum at 403 nm and hence rise in population of the T_1 state of AN could also be followed at this wavelength.[61] The lifetime of the triplet state of RuBPY^{2+} thus determined in RTIL is 0.93 μs, which is quite long to make it a suitable system for our purpose (S3.2 in SD section).

Laser flash photolysis technique has been used to study the interaction of the T_1 state of RuBPY^{2+} with AN in different kinds of solvent media following photoexcitation of the donor at 532 nm. The time resolved absorption spectra recorded following photoexcitation of a solution containing 1 x 10^{-3} mol dm^{-3} of RuBPY^{2+} and 4.25 x 10^{-3} mol dm^{-3} of AN in C_4Mim are shown in Figure 3.7. Decay of the stimulated emission from the T_1 state of RuBPY^{2+} in the 580 – 750 nm region or recovery of the bleach band in the 450 – 520 nm region is accompanied by a concomitant rise of the AN triplet absorption signal in the 400 – 450 nm region. This observation establishes the TET process from the T_1 state of RuBPY^{2+} to AN molecule. Rates of pseudo first order decay (k') of stimulated emission monitored at 620 nm or bleach recovery at 575 nm or growth of the AN triplet at 403 nm have been determined in the presence of different concentrations of the quencher and hence the bimolecular rate constant for the TET process in C_4Mim has been obtained from the slope of the linear fit to the data in the plot of k' vs. concentrations of the quencher. The rate constants of the TET process have been estimated in all other solvent media and given in Table 3.3.

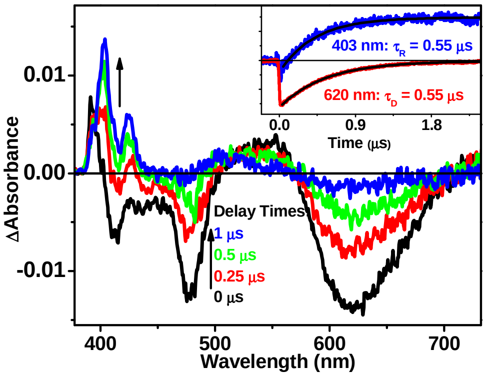

Figure 3.7: Time resolved absorption spectra recorded following photoexcitation of 1 x 10^{-3} mol dm^{-3} of $RuBPY^{2+}$ and 4.3 x 10^{-3} mol dm^{-3} of AN in C_4Mim. **Inset:** Temporal profiles recorded at 620 nm and 403 nm, showing the decay of stimulated emission from the T_1 state of RuBPY and rise of absorption due to increase in population of the T_1 state of AN, respectively.

Table 3.3: Viscosities of the solutions, values of k_{TET} determined experimentally, k_{Diff} values calculated using equation 2 and k_{TET}/k_{Diff} for $RuBPY^{2+}$ – AN pair in two conventional solvents, SDS micelle and four RTILs.

Solvent	η (cP)	K_{TET} (10^8 dm^3 $mol^{-1}s^{-1}$)	k_{Diff} (10^8 $dm^3mol^{-1}s^{-1}$)	K_{TET} /k_{Diff}
CAN	0.35	120	186	0.65
EG	15.7	4.8	4.21	1.14
SDS	24	5.9	3.2	1.84
C_2Mim	44.6	3.3	1.49	2.2
C_4Mim	92.1	1.3	0.72	1.81
C_6Mim	207.2	0.7	0.32	2.19
C_{10}Mim	501.4	0.4	0.13	3.1

We calculated the values of k_{Diff} and also the values of k_{TET}/k_{Diff} for the TET process for the $RuBPY^{2+}$ – AN pair in all those solvents used here. These values are also given in Table 3.3. We find that k_{TET}/k_{Diff} values follow a different trend as compared to those observed for the other two donor – acceptor pairs discussed in the earlier section. For the present triplet energy donor – acceptor pair, the k_{TET}/k_{Diff} values increase only marginally as the viscosity of the solvent increases but remain more or less similar as the solvent is changed from C_4Mim to C_{10}Mim. So, in the present case, the rate of the TET process follows a similar trend as the bulk viscosity of the RTIL solutions and the rate of the TET process is significantly slower as compared to those observed in the cases of BP –NP and BP – BIP chemical systems.

3.2.2.2. ET Studies using Nanosecond Electron Pulse Radiolysis Technique: We studied the ET processes from the PY radical anion ($PY^{\cdot-}$), which was generated using electron beam irradiation, to BP or MV^{2+}. Use of PY concentration, which was larger by more than about ten times as that of the acceptor, ensured that PY molecules in solution captured electrons to generate $PY^{\cdot-}$ preferentially. Both PY and BP molecules are expected to reside in the neutral alkyl group region, whereas MV^{2+} should preferentially be located near the ionic head group region of RTIL. $PY^{\cdot-}$ has the lifetime of about 5 μs in C_4Mim, which is quite long to achieve the stationary state condition in the RTIL media (vide infra). Therefore, the ET studies in the PY – BP and PY – MV^{2+} systems are expected to complement the results of the TET studies discussed in the earlier sections to enable us to provide a generalized concept about the micro-heterogeneous structure of the RTIL solvents.

ET Process from $PY^{\cdot-}$ to BP: The $PY^{\cdot-}$ has an absorption maximum at ca. 490 nm and the BP radical anion ($BP^{\cdot-}$) has an absorption band in the 600 - 740 nm region with the absorption maximum at ca. 680 nm. Distinct absorption bands of the donor and the acceptor anion radicals make the observation of the ET process unambiguous. Time resolved absorption spectra recorded following electron pulse radiolysis of a solution containing 4 x 10^{-2} mol dm^{-3} of PY and 2.2 x 10^{-3} mol dm^{-3} of BP in C_4Mim (Figure. 3.8A) and the temporal profiles recorded at 490 and 680 nm (inset of Figure 3.8A) clearly revealed the features of the ET process from $PY^{\cdot-}$ to BP. We have also recorded the temporal profiles for the decay of $PY^{\cdot-}$ at 490 nm with varying concentrations of BP in the range of 0 - 5 x 10^{-3} mol dm^{-3} (Figure 3.8B). They have been fitted single exponentially and the plot of the pseudo first order rate constants vs. acceptor concentration has been used to determine the rate constant of the ET process (k_{ET}). k_{ET} has also been estimated for this reaction in other RTILs and has been compared with the theoretically calculated diffusion rate constants (using equation 3.8) in Table 3.4 .Quality of fits to the temporal profiles and residual distributions in the case of ET process for PY-BP pair in four RTIL solvents are shown in S3.4 in the SD section. We find that, like in the case of the TET studies in BP - NP (or BP - BIP) systems, the ratio of the experimentally determined rates of ET in the PY$^{\cdot -}$ -BP system to the diffusion controlled rate in RTIL solutions calculated using equation 3.8 gradually increases as the alkyl chain length of the RTIL solvent molecule is increased. We find that, in the case of C_{10}Mim, the experimentally determined rate, k_{ET}, is about ten times faster as compared to the diffusion controlled rate, k_{Diff}, calculated using the bulk viscosity of the solution.

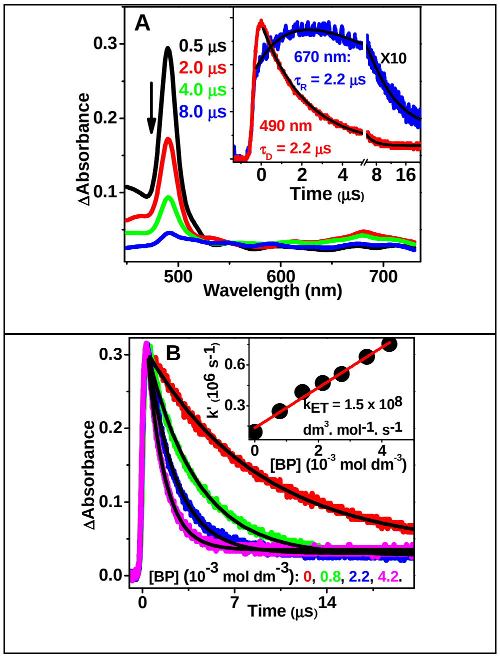

Figure 3.8: (A) Time resolved absorption spectra recorded at different delay times following electron pulse radiolysis of 4 x 10^{-2} mol dm^{-3} of PY and 2.2 x 10^{-3} mol dm^{-3} of BP in C_4Mim. **Inset:** The kinetic traces recorded at 490 nm and 680 nm along with the best-fit functions and the associated decay (D) and rise (R) lifetimes for the PY$^{\bullet -}$and the BP$^{\bullet -}$, respectively.(B) Temporal profiles recorded at 490 nm for different quencher concentrations along with the best fit functions. The inset represents the k' vs. quencher concentration plot. The bimolecular ET rate constant is also given in the inset.

Table 3.4: Viscosities of the solutions, values of k_{ET} determined experimentally, k_{Diff} values calculated using equation 3.8 and k_{ET}/k_{Diff} for PY – BP system in two conventional solvents, SDS micelle and RTILs.

Solvent	**η (cP)**	**k_{ET} (10^8 dm^3 mol^{-1}s^{-1})**	**k_{Diff} (10^8 dm^{3}mol^{-1}s^{-1})**	**k_{ET} /k_{Diff}**
can	0.35	180	186	0.96
EG	15.7	4.7	4.21	1.12
SDS	24	2.7	3.2	0.84
C_2Mim	44	2.6	1.94	1.32
C_4Mim	93	1.5	0.7	2.1
C_6Mim	185	1.4	0.37	3.8
C_{10}Mim	490	1.5	0.14	10.4

ET Process in $PY^{\cdot -}$– MV^{2+} System: Time resolved absorption spectra recorded following pulse radiolysis of a solution containing 4 x 10^{-2} mol dm^{-3} of pyrene and 2 x 10^{-3} mol dm^{-3} of MV^{2+} in C_4Mim is shown in Figure 3.9A and the temporal profiles recorded at 490 and 610 nm in the inset of Figure 3.9A. Knowing the fact that reduced [$MV^{\cdot +}$] radical is well-characterized by a strong absorption band in the 550 - 700 nm region with the absorption maximum at ca. 610 nm (S3.5 in SD section),[62] these data clearly reveal the occurrence of the ET process from $PY^{\cdot -}$ to MV^{2+}. ET rate constants have been estimated using varying concentrations of MV^{2+} and the values of k_{ET} /k_{Diff} thus calculated are given in Table 3.5. We find that the results presented in this table resembles nearly to those observed in the case of the TET process for the $RuBPY^{2+}$ – AN system.

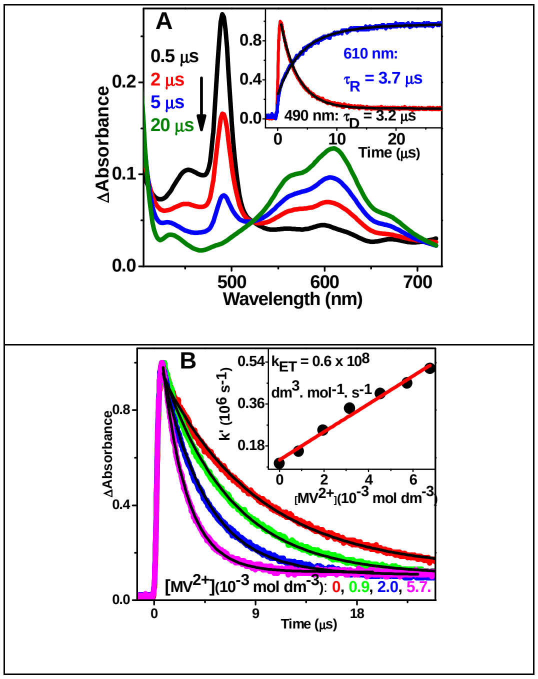

Figure 3.9: (A) Time resolved absorption spectra recorded at different delay times following electron pulse radiolysis of 4 x 10^{-2} mol dm^{-3} of PY and 2 x 10^{-3}mol dm^{-3} of MV^{2+} in C_4Mim. **Inset:** The kinetic traces recorded at 490 nm and 610 nm along with the best-fit functions and the associated decay (D) and rise (R) lifetimes of the donor and acceptor respectively. (B) Temporal profiles recorded at 490 nm for different acceptor concentrations and the inset graph represents the k' vs. acceptor concentration plot. The bimolecular ET rate constant thus determined is also given in the inset.

Table 3.5: Viscosities of the solutions, values of k_{ET} determined experimentally, k_{Diff} values calculated using equation 3.9 and k_{ET}/k_{Diff} forpyrene-MV^{2+} pair in four RTILs and two conventional solvents.

Solvent	**η (cP)**	**k_{ET} (10^8 dm^{3}mol^{-1}s^{-1})**	**k_{Diff} (10^8 dm^{3}mol^{-1}s^{-1})**	**k_{ET} /k_{Diff}**
ACN	0.35	140	186	0.75
EG	15.7	4.2	4.2	1
C_2Mim	36	1.5	1.8	0.83
C_4Mim	95.6	0.6	0.7	0.86
C_6Mim	192	0.17	0.34	0.5
C_{10}Mim	480	0.14	0.14	1

3.2.3. Correlation of the Rate Constants of the TET and ET Processes with Viscosities of the Media: In the above discussion, we assumed about occurrence of the TET and ET processes investigated here in the stationary regime of the diffusional quenching and hence the pseudo-first-order rate constants of the quenching reactions were determined using single-exponential fits to the temporal decay profiles of the donor triplet or radical anion. The single exponential fitting approach can be adopted if the long-time asymptotic behaviour of the decay is fitted only after the transient effect has ceased to contribute to the decay dynamics. The time-dependence of the bimolecular reaction rate constant, k(t), can be calculated using the Smoluchowski formulation modified by Collins and Kimball (equation 3.9),[63, 64]

$$k(t) = k_d \left[1 + \frac{R_{DQ}}{\sqrt{\pi D_{DQ} t}} \right] \qquad (3.9)$$

Where k_d ($=4\pi R_{DQ} D_{DQ}$) is the Smoluchowski limit for the diffusion controlled rate, and R_{DQ} and D_{DQ} are the reactions radius (or may be considered as contact radius) and mutual diffusion coefficient (given by equation 3.10), respectively, for the donor (D) and quencher (Q). The second term in the bracket in equation 3.9 represents the contribution of the transient quenching process.

$$D_{DQ} = \frac{k_B T}{6\pi\eta} \left(\frac{1}{r_D} + \frac{1}{r_Q} \right) \qquad (3.10)$$

Where r_D and r_Q are the van der Waals radii calculated using the atomic volume addition method as proposed by Edward.[65]

In a much simplified approach, a rough estimation of the time domain, within which the effect of transient quenching is prevalent and beyond which the quenching process may be considered as mainly dominated by diffusion controlled process, can be made by assuming that the contribution of the transient effect should be smaller than 50% of k_d or the value of the factor $R/(\sqrt{\pi D_{DQ} t}) \leq 0.5$. Adopting the values of R_{DQ} for the BP-NP and Py-BP pairs calculated by the volume addition method of Edward (6.5 and 7.3 Å, respectively) and D_{DQ} values calculated using equation 3.10, we estimate the time-domain, within which the transient quenching effect should be dominant and the results of these calculations are given in the TABLE S3.6 in SD section.

Table S3.6 reveals that, in the case of TET process for the BP-NP pair, the diffusion controlled process is dominant beyond 40 ns time domain in C_4Mim. Following this information, the pseudo-first order fittings to different decay profiles recorded in this solvent have been performed for the time domain longer than 40 ns (Figur 3.6). However, in the case of C_{10}Mim, the regime of transient quenching is extended up to about 200 ns and hence the quenching data were fitted by pseudo-first order kinetics only beyond this time domain to ensure determination of the reaction rate occurring in diffusion controlled regime (see S3.3 in SD section). To ensure good fitting of the data, the single exponential fit function and the residuals have been plotted in S3.3 in SD section. Similar approach of data fitting was adopted in other cases too. To cite the other example, table S3.6 reveals that in the case of ET process for the Py-BP pair, the diffusion controlled regime is ensured beyond 280 ns time domain for the solvent of highest viscosity. In addition, Figure 3.8B as well as Figure S3.4 in SD section show the pseudo-first order kinetic fittings along with the residual distribution analysis to the decay profiles representing quenching of $PY^{\bullet-}$ by BP recorded using pulse radiolysis technique. In all these cases the decay profiles have been fitted in longer than 300 ns time domain, which ensures that we report here the diffusion controlled rates free from the effect of transient quenching even in the case of solvent of the highest viscosity. In addition, perfect linear plots of k′ vs quencher concentration (which may be considered as Stern-Volmer kind of plots) through the entire range of concentration of the quencher also dictates occurrence of the quenching processes in the diffusion controlled regime without any significant contribution of transient quenching.

Since diffusion of the reactants, which brings two reactants in contact to interact with each other is the only factor controlling the rates of these barrierless TET and ET processes investigated here, we have made an attempt to correlate the rate constants of these processes with the inverse of viscosity (i.e. $1/\eta$) as revealed by equation 3.8 (Figure 3.10). Features of this figure lead us to make an interesting inference that, in the cases of both the TET and ET processes involving either the ionic donor or the ionic acceptor, the bimolecular rates of these reactions follow a linear relationship with $1/\eta$ and slopes of the best-fit lines agree reasonably well with that calculated using equation 3.8 (6.6×10^9 dm^3 $mol^{-1}s^{-1}cP^{-1}$). This suggests that diffusion of these reactants is controlled by the macroscopic or bulk viscosity of the solutions of RTIL as measured experimentally. However, in the case of donor - acceptor pairs, in which both the molecules are nonionic, rates of both the TET and ET reactions in RTIL solvents do not follow a linear relationship, but become faster than the calculated rate of a diffusion controlled process in the corresponding solvent as the length of the alkyl chain in the RTIL solvent molecule increases. Further, the ratio, k_{TET}/k_{Diff} or k_{ET}/k_{Diff} (Tables 3.2 and 3.4) increases by about 10 times in the cases of nonionic donor - acceptor molecule pairs, while this value is near to unity in the cases of donor – acceptor pairs, in which one of them is an ionic species (Tables 3.3 and 3.5). These observations obviously suggest the microheterogeneous structutre of RTIL liquids, which have sites or pockets of different microviscosities and a particular reactant is solvated in a region of like nature, say, nonpolar or polar.

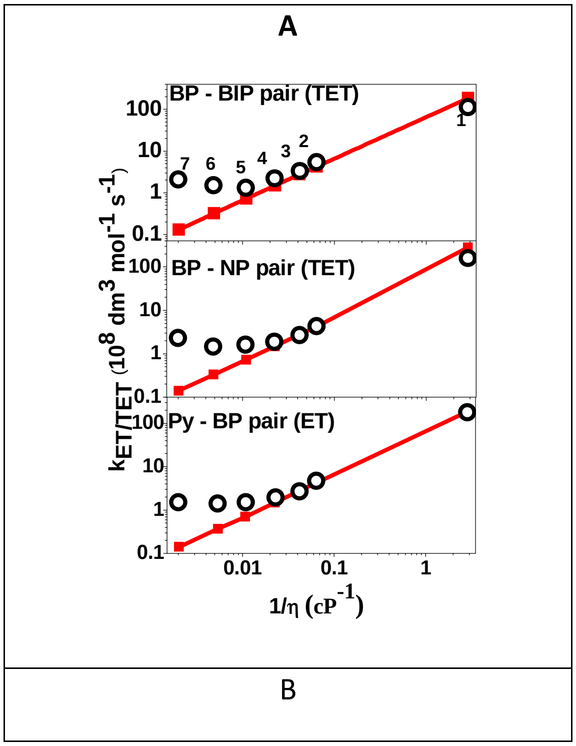

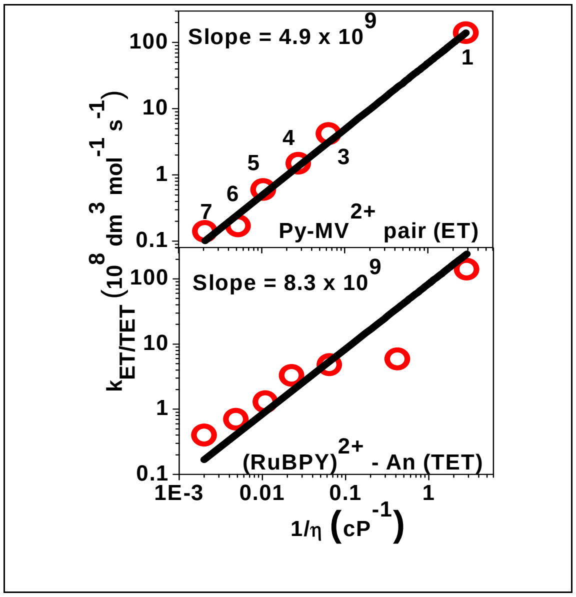

Figure 3.10: Variation of bimolecular rate constants of the TET and ET processes as a function of the inverse of viscosity (1/η) (equation 3.8) in the case of (A) nonionic donor – acceptor pairs (open circles) and (B) nonionic molecule (or cationic) donor – cationic (or nonionic molecule) acceptor (open circles). Filled squares represent values of k_{Diff} calculated using viscosity of solutions determined experimentally. Solvent media: (1) Acetonitrile, (2) ethylene glycol, (3) SDS Micelle, (4) C_2Mim, (5) C_4Mim, (6) C_6Mim, (7) C_{10}Mim.

3.2.4. Heterogeneous Structure of RTIL Solvents: As discussed in section 3.3.1, both Maroncelli and co-workers as well as Vauthey and coworkers predicted that diffusion controlled processes can be observed in viscous solvents, like RTIL, only by using long lived transient donors, which survive for more than a few microsecond enabling one to monitor the reactions occurring in the stationary regime.[66, 67] Experimentally we have also established this prediction In the second part of this work, we have chosen a few long-lived (lifetime of about a few microsecond) triplet states as energy donors, spectroscopic properties of which are well known, as well as radical anions as electron donors, to determine the rates of the energy and electron transfer reactions, respectively, in a series of RTIL solvents, SDS micelle as well as in two conventional solvents. However, considering the fact that RTIL solvents consist of a polar head group as well as a non polar tail of long chain alkyl group, we have selected both the neutral and ionic solutes as the donor or acceptor to explore how the different kinds of interactions between the solute and the solvent influences the rate of reactions. Complementing our expectations, our experimental results revealed two interesting facts. Rate of the energy or electron transfer reaction, for which one of the reactants is an ionic species, is controlled by the bulk or macroscopic viscosity of the solvent, including in all those RTIL solvents used here. However, in those cases, for which both the donor and the acceptor molecules are nonionic, the reaction rate becomes faster as compared to the diffusion controlled rate as the length of the alkyl chain of the RTIL solvent molecule becomes longer.

Considering the fact that both the TET and ET processes investigated here are barrierless, the rate of the reactions should be determined by the rate of diffusion of the reactant species bringing them together in contact. Therefore, observations made in this work suggest significant role of the microscopic structure of the solvent determining the rates of diffusion of the reactant species. Faster TET and ET rates as compared to that calculated for the diffusion controlled process, as observed in the cases of the neutral donor - acceptor pairs in RTILs with longer nonpolar alkyl chain, may be interpreted as that the effective frictional force exerted by the solvent to the solute diffusion, for which the microviscosity of the solution at the location of the solute should be a good measure, is less as compared to the bulk viscosity of the solution. In other words, motions of both the neutral reactants occur through a region, where the local viscosity is less as compared to the bulk viscosity of the solution. Significant increase of TET or ET rate between the neutral reactants, which is revealed by gradual increase in the value of k_{ET}/k_{Diff} or k_{TET}/k_{Diff}, with increase in the length of the alkyl chain of the RTIL solvent molecule, suggests that the nonpolar alkyl chain plays an important role in creating heterogeneity in the solution. van der Waals interaction between these alkyl chains of RTILs, creates a nonionic alkyl pocket in RTIL solution. Both the donor and the acceptor molecules prefer to stay inside the nonionic pockets. The TET or ET process takes place between the donor and acceptor molecules residing inside the same pocket and the diffusive motion of the reactants experiences much lower microscopic viscosity as compared to the bulk viscosity of the solution. This is the reason why the TET or ET rates in the cases of donor – acceptor pairs consisting of neutral molecules become faster than the diffusion controlled rate.

Results of our molecular dynamic simulations reveal that self-organization of the RTIL molecules becomes more significant as the alkyl chain length increases and nearly a micelle-like structure may be predicted in the case of C_{10}Mim. RTILs containing long alkyl chain have been shown to exhibit surface active properties, designated as surface active ionic liquids (SAILs) which are capable to form supramolecular aggregates.[68, 69] Considering this fact, we thought of determining the rate constants for the TET process for the BP - NP and BP – BIP pairs in SDS micelles (Table 3.2). Since the SDS miceller molecule also contain an alkyl chain of twelve carbon atoms, we may assume that the microviscosity of the nonpolar alkyl chain region, at which the neutral molecules reside in C_{10}Mim, may be comparable to that in the case of SDS micelle. To our pleasant surprise, we find that the rates of the TET process for these two chemical systems determined in C_{10}Mim and SDS micelle are comparable (Table 3.2). Viscosity of the nonpolar core of the SDS micelle has earlier been estimated to be about 24 cP,[56] and this leads us to predict that the microviscosity of the nonpolar alkyl chain region of the C_{10}Mim also is very similar.

Further to substantiate the conclusion that the microenvironment observed by the apolar solutes in C_{10}Mim is very similar to that in SDS micelles, we probed the polarity of the microenvironment of the pyrene molecule in all those RTILs used here by adopting the method of Acree et al.[70] This method compares the ratios of intensities of the vibronic bands at 373 and 385 nm (i.e. I_{373}/I_{385}) in the fluorescence spectra of pyrene to compare the polarity of the media in which the probe resides. Our results shown in Figure S 3.7 in SD section shows that the polarity of the microenvironment in which the pyrene molecule resides in C_{10}Mim liquid is very similar to that of SDS or TX-100 micelles.[71] Therefore, comparable rates of the TET reactions in SDS and C_{10}Mim are not merely a coincidence but conclusion about similar viscosities and polarities of the microenvironment of an apolar probe in these two media is quite reasonable.

On the other hand, in the case of $RuBPY^{2+}$- AN and Py – MV^{2+} pairs, in which one of the reactants is a cationic species, the rates of the TET and ET processes, respectively, are nearly equal to the diffusion controlled rates, which are calculated using the bulk viscosity of the solutions. In these cases, AN and PY, being neutral molecules, are more likely to be located in the nonpolar alkyl chain region. Whereas $RuBPY^{2+}$ and MV^{2+} preferably reside in the ionic pocket of the RTIL solvent and diffusive motion of these ionic species may be slowed down due to columbic interaction between the ionic solute and the ionic head groups of the RTIL solvent molecules. This suggests that the motion of the reactants for these two pairs of reactants, occur through different regions of the RTIL solution, which is inherently heterogeneous. Therefore, the reaction rates are expected to experience the macroscopic viscosity of the solution.

In support of our experimental findings being reported here, we find a large number of reports, which have already provided considerable insight into the nature of interaction between the solute and ionic constituents of various RTIL solvents, thus shedding light on the microenvironments of these promising, but complex media. [58, 72-88] Guo et. al used fluorescence correlation spectroscopy (FCS) to study the diffusion dynamics of rhodamine 6G dye to provide experimental evidence for chain length dependent self-aggregation in RTIL solvents of a homologous series of N-alkyl-N-methylpyrrolidinium-bis-(trifluoromethylsulfonyl) imide, [C_nMPy][Tf_2N] with varying alkyl chain length (n = 3, 4, 6, 8, and 10).[86] They observed biphasic diffusion dynamics of the solute. However, both the fast and slow diffusion coefficients decreased with increasing alkyl chain length, with the relative contribution from slower diffusion increasing for longer-chain [C_nMPy][Tf_2N]. This led them to propose that the biphasic diffusion dynamics originated from self-aggregation of the nonpolar alkyl chains in the cationic [C_nMPy]$^+$. Later, Patra and Samanta, as well as Bhattacharyya and co-workers, also reported about the biphasic dynamics in RTILs with long alkyl chains.[87,88]

MD simulations and early SAXS results only identified self-aggregation for alkyl chain lengths longer than n = 4 in C_nMIM systems. More recent SAXS results for the C_nMIM series from n = 2 to 9 suggested the existence of self-aggregation domains for n > 3.[72, 73] These works demonstrated that the liquid structure of a neat RTIL was largely determined by a combination of intermediate and long range Coulombic and hydrogen-bonding interactions as well as packing factors. The translational diffusion rate of a solute was shown to differ depending upon which spatial region of the RTIL, the probe molecule was experiencing.

Samanta and coworkers investigated the rotational dynamics of dipolar and nonpolar solutes in a series of N-alkyl-N-methylmorpholinium (alkyl = ethyl, butyl, hexyl, and octyl) bis(trifluoromethansulfonyl)-imide (Tf_2N) ionic liquids to reveal their location in distinct environments of these media using fluorescence anisotropy decay measurement method.[50] They revealed that the dipolar solute, 4-aminophthalimide was located in a polar environment because of its H-bonding interaction with the constituent ions of the ionic liquids, whereas the location of the nonpolar solute, AN, was in the nonpolar region of the ionic liquids formed largely by the alkyl group of the cation. On the other hand, the dipolar solute, PRODAN, was to be distributed in both the regions. These results revealed the microheterogeneous structure of the ionic liquids, formed by the segregation of the alkyl chains on one hand and the charged components on the other and hence emphasized the importance of selection of reactants.

Considering variation of the rate constants of TET and ET reactions between neutral molecules or molecular ions conducted in RTIL solvents with increasing length of the alkyl chain as well as the results of MD simulations, we predict preferential organizations of the RTIL molecules with long alkyl chain length to form nearly a micelle-like structure creating distinct regions with nonpolar and polar pockets. Reactant species is preferentially solubilized in a particular region depending on its polarity and its diffusional motion is dependent on the microviscosity of the region, in which it is solubilized. These facts may be depicted in a schematic diagram represented in Figure 3.11.

3.3. CONCLUSIONS

This work presented in this chapter first experimentally verified whether we can observe diffusion controlled reaction in viscous RTIL media with long lived transients. In the second part the studies extended for observation of TET and ET reactions involving long lived triplet states and radical anions, respectively, in conventional solvents, SDS micelle and RTIL solvents, namely, 1-alkyl-3-methyl-imidazoliumtetrafluoroborate, in which the chain length of the alkyl group is varied up to ten carbon atoms. These diffusion controlled reactions occur in the stationary quenching regime. Strong dependence of the reaction rates on the non-ionic or ionic nature of the reactants elucidates the microscopic heterogeneity of the RTIL solvents, which becomes more significant as the alkyl chain length of the RTIL solvent becomes longer. Results of our MD simulations predict preferential organizations of the RTIL molecules, specifically with long alkyl chain length, to form nearly a micelle-like structure creating distinct regions with nonpolar and polar pockets. Reactant species is preferentially solubilized in a particular region depending on its polarity and its diffusional motion is dependent on the microviscosity of the region, in which it is solubilized.

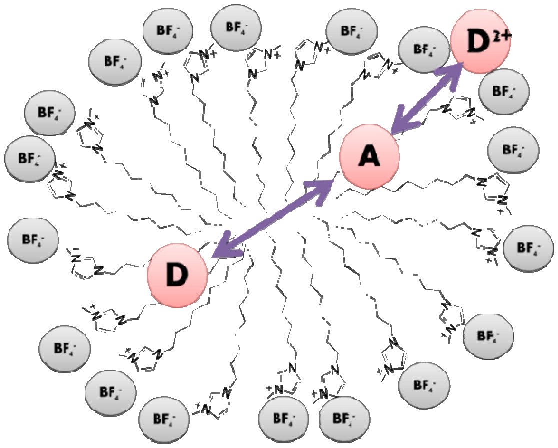

Figure 3.11: The RTIL solvent molecules with long alkyl chain undergo self-organization to form micelle-like structures creating distinct regions with nonpolar and polar pockets. Neutral donor and neutral acceptor molecules mainly remain in the nonionic alkyl pocket and diffusion occurs through low viscosity nonionic pocket. On the other hand, ionic donor molecules preferred to be solvated in the ionic region. The reactants need to diffuse through both ionic and nonionic pockets to take part in the energy transfer or electron transfer process.

Rates of TET and ET processes estimated for the neutral donor – neutral acceptor pairs, which prefer to remain solubilized in the nonpolar pocket, are faster than those calculated using the Smoluchowski equation (equation 3.8) and the bulk or macroscopic viscosity (η) of the solutions, determined experimentally. This suggests that the microscopic viscosity experienced by these solutes is lower as compared to the bulk viscosity of the solutions. Comparable values of TET and ET rate constants for these neutral donor – neutral acceptor pairs in the C_{10}Mim and in SDS micelle suggest that the viscosity of the nonionic pocket of the C_{10}Mim is nearly similar to that of the core region of SDS micelle, which has been reported to be about 24 cP.[59] However, when one of the reactant species of the donor - acceptor pair is ionic, the rate of the TET or ET process is slower and is nearly equal to that calculated using Smoluchowski equation and the bulk viscosity, possibly because of electrostatic interaction between the ionic head groups and the ionic reactant as well as diffusion of the reactants through different kinds of regions of the heterogeneous RTIL solutions. Thus this work truly establishes the microheterogeneous structure of the imidazolium cation based ionic liquids consisting of regions of different polarities as well as different microviscosities.

3.4. REFERENCES

1. Samanta. A. *J. Phys. Chem. B.* **2006,** *110*, 13704**.**
2. Welton, T. *Chem. Rev.* **1999**, *99,* 2071.
3. Wasserscheid, P.; Keim, W. *Angew. Chem., Int. Ed.***2000**, *39*, 3772**.**
4. Dupont, J.; de Suza, R. F.; Suarez, P. A. Z. *Chem. Rev.* **2002**, *102,* 3667**.**
5. Buzzeo, M. C.; Evans, R. G.; Compton. R. G. *Chem. Phys. Chem.* **2004**, *5*, 1106.
6. Chiappe, C.; Pieraccini, D. *J. Phys. Org. Chem.* **2005**, *18*, 275.
7. Rogers, R.D.; Seddon, K. R. *Science* **2003**, *302*, 792.
8. Seddon, K. R. *Nature Mater.* **2003,** *2***,** 363.
9. Castner, E. W.; Wishart, J. F. *J. Chem. Phys.* **2010**, *132*, 120901.
10. Castner, E. W.; Margulis, C. J.; Maroncelli, M.; Wishart, J. F. *Annu. Rev. Phys. Chem.* **2011**, *62*, 85.
11. Plechkova, N. V.; Seddon, K. R. *Chem. Soc. Rev*. **2008**, 123.
12. Wishart, J. F. *Energy Environ. Sci.* **2009**, 956.
13. Hallett, J. P.; Welton, T. *Chem. Rev.* **2011**, *111*, 3508.
14. Berthon, L.; Nikitenko, S. I.; Bisel, I.; Berthon, C.; Faucon, M.; Saucerotte, B.; Zorz, N.; Moisy. P. *Dalton Trans.* **2006**, 2526**.**
15. Bai, Y.; Cao, Y.; Zhang, J.; Wang, M.; Li, R.; Wang, P.; Zakeeruddin, S. M.; Grätzel, M. *Nat. Mater.* **2008**, *7*, 626.
16. Bai, Y.; Zhang, J.; Wang, Y.; Zhang, M.; Wang, P. *Langmuir* **2011**, *27*, 4749.
17. Hardin, B. E.; Sellinger, A.; Moehl, T.; Humphry-Baker, R.; Moser, J. E.; Wang, P.; Zakeeruddin, S. M.; Grätzel, M.; McGehee, M. D. *J. Am. Chem. Soc.* **2011**, *133*, 10662.
18. Thied, R. C.; Etter, J. E. Ha.; Seddon, K. R.; Pitner, W. R.; Rooney, D. W.; Hebditoh, D. *World Pat*., WO01/13379A1, 18 August **1999**
19. Dietz, M. L.; Dzielawa, J. A. *Chem. Commun*, **2001**, 2124.
20. Grodkowski, J.; Neta, P.; Wishart, J. F. *J. Phys. Chem. A.* **2003**, *107*, 9794**.**
21. Skrzypczak, A.; Neta, P. *J. Phys. Chem. A.* **2003**, *107*, 7800**.**
22. Paul, A.; Samanta, A. *J. Phys. Chem. B.* **2007**, *111*, 1957**.**
23. Sarkar, S.; Pramanik, R.; Seth, D.; Setua, P.; Sarkar, N. *Chem*.Phys. Lett. **2009**, *477*, 102.
24. Sarkar, S.; Pramanik, R.; Ghatak, C.; Rao, V. G.; Sarkar, N. *J. Chem. Phys.* **2011**, *134*, 74507.
25. Vieira, R. C.; Falvey, D. E. *J. Am. Chem. Soc.* **2008**, *130,* 1552.
26. Vieira, R. C.; Falvey, D. E. *J. Phys. Chem. B* **2007**, *111*, 5023.
27. Wishart, J. F.; Neta, P. *J. Phys. Chem. B.* **2003**, *107,* 7261**.**
28. Behar, D.; Neta, P.; Schultheisz, C. *J. Phys. Chem. A* **2002**, *106*, 3139.

29. Lee, C.; Winston, T.; Unni, A.; Pagni, R. M.; Mamanto, G. *J. Am. Chem. Soc.* **1996**, *118*, 4919.
30. Liang, M.; Kaintz, A.; Baker, G. A.; Maroncelli, M. *J. Phys. Chem. B.* **2012**, *116*, 1370.
31. Koch, M.; Rosspeintner, A.; Angulo, G.; Vauthey, E. *J. Am. Chem. Soc.***2012**, *134*, 3729.
32. Gordon, C. M.; McLean, A. J. *Chem. Commun.* **2000,** 1395.
33. Gangamallaiah V.; Dutt, G. B. *J. Phys. Chem. B* **2013**, 117, 12261.
34. Behar, D.; Gongalez, C.; Neta, P. *J. Phys. Chem. A* **2001**, *105*, 7607.
35. Growdkoski, J.; Neta, P. *J. Phys. Chem A*, **2002**, *106*, 5468.
36. Growdkoski, J.; Neta, P. *J. Phys. Chem A*, **2002**, *106*, 9030.
37. Growdkoski, J.; Neta, P. *J. Phys. Chem A*, **2002**, *106*, 11130.
38. Asano, A.; Yang, J.; Kondoh, T.; Norizawa, K.; Nagaishi, R.; Takahashi, K.; Yoshida, Y. *Rad. Phys. Chem.* **2008,** *77*, 1244.
39. Takahashi, K.; Sato, T.; Katsumura, Y.; Yang, J.; Kondoh, T.; Yoshida, Y.; Katoh, R. *Rad. Phys. Chem.* **2008**, *77*, 1239.
40. Kimura, A.; Taguchi, M.; Kondoh, T.; Yang, J.; Yoshida, Y.; Hirota, K. *Rad. Phys. Chem.* **2008**, *77*, 1253.
41. Shirota, H.; Funston, A. M.; Wishart, J. F.; Castner, E. W. *J. Chem. Phys.* **2005,** *122*, 184512.
42. Yang, J.; Kondoh, T.; Norizawa, K.; Nagaishi, R.; Taguchi, M.; Takahashi, K.; Katoh, R.; Anishchik, S. V.; Yoshida, Y.; Tagawa, S. *Rad. Phys. Chem.* **2008,** *77*, 1233.
43. Wishart, J. F.; Funston, A. M.; Szreder, T.; Cook, A. R.; Gohdo, M. *Faraday Discuss.*, **2012,** *154*, 353.
44. Wishart,J. F. *J. Phys. Chem. Lett.* **2010**, *1*, 3225.
45. Getoff, N.; Solar, S.; Richter, U. B.; Haenel, M. W. *Rad. Phys. Chem.* **2003**, *66*, 207.
46. Samanta, V.; Singh, A. K.; Mukherjee, T.; Palit, D. K. *Res. Chem.. Intermed.* **2006**, *32*, 767.
47. Hayon, E.; Ibata, T.; Lichtin, N. N.; Simic, M. *J. Phys. Chem.* **1972**, *76*, 2072.
48. Laidler, K. *Chemical Kinetics*; Harper Collins: New York, **1987**.
49. Smoluchowski, M. V. *Z. Phys. Chem. Leipzig* **1917**, *92***,** 129.
50. Murov, S. L.; Carmichael, I.; Hug, G. L. *Handbook of Photochemistry*, Marcel Dekker, New York, **1993.**
51. Carmichael I.; Hug, G. L. *J. Phys. Chem. Ref. Data.***1986**, *15***,** *1.*
52. Takahashi, K.; Tezuka, H.; Kitamura, S.; Satoh, T.; Katoh, R. *Phys. Chem. Chem. Phys.***2010**, *12*, 1963.
53. Muldoon, M. J.; McLean, A. J.; Gordon C. M.; Dunkin, I. R. *Chem. Commun.***2001**, 2364.
54. Smoluchowski, M. V. *Z. Phys. Chem. Leipzig* **1917**, *92***,** 129.
55. Steinfeld, J. I.; Francisco, J. S.; Hase, W. L. *Chemical Kinetics and Dynamics*; Plenum Press: Englewood Cliffs, NJ, **1989.**
56. Bahri, M. A.; Hoebeke, M.; Grammenos, A.; Delanaye, L.; Vandewalle N.; Seret, A. *Colloids Surf. A* **2006**, *290***,** 206.

57. Silva, A. F.; Fiedler, H. D.; Nome, F. *J. Phys. Chem.A* **2011**, *115*, 2509.

58. Soboleva, I. V.; van Stam, J.; Dutt, G. B.; Kuzmin, M. G.; De Schryver, F. C. *Langmuir* **1999**, *15*, 6201.

59. Khara, D. C.; Kumar, J. P.; Mondal, N.; Samanta, A. *J. Phys. Chem. B* **2013**, *117,* 5156.

60. Wrighton M.; Markham, J. *J. Phys. Chem.* **1973**, **77**, 3042.

61. Hess, B.; Bekker, H.; Berendsen, B. J. C.; Fraaije, J. G. E. M. *J. Comp. Chem.***1997**, *18*, 1463.

62. Watanabe, T.; Honda, K. *J. Phys. Chem*. **1982**, *86*, 2617.

63. Castanho, M. A. R. B.; Prieto, M. J. E. *Biochim. Biophys.Acta,* **1998**, *1373***,** 1.

64. Eftink, M. R.; Lakowicz, J. R. (Ed.), *Topics in Fluorescence Spectroscopy*, Vol. 2, Plenum Press, New York, **1991**.

65. Edward, J. T. *J. Chem. Educ.*, **1970**, *47***,** 261.

66. Berndsen, H. J. C.; Spoel, D. V. D.; Drunem, R. V. *Comp. Phys. Comm.* **1995**, *91*, 43.

67. Spoel, D. V. D.; Lindahl, E.; Hess, B.; Groenhot, G.; Mark, A. E.; Berendsen, B. J. C. *J. Comp. Chem.***2005**, *26*, 1701.

68. Gu, Y.; Shi, L.; Cheng, X.; Lu, F.; Zheng, L. *Langmuir* **2013**, *29*, 6213.

69. Galgano, P. D.; El Seoud, O. A. *J. Colloid Interface Sci.* **2010**, *345*, 1.

70. Acree, W. E.; Zvaigzn, A. I.; Fetzer, J. C. *Applied Spectroscopy*, **1990,** *44*, 1193.

71. Piñeiro, L.; Novo, M.; Al-Soufi, W.; *Advances in Colloid and Interface Science*, **2015**, *215*, 1

72. Li, S.; Bañuelos, J. L.; Guo, J.; Anovitz, L.; Rother, G.; Shaw, R. W.; Hillesheim, P. C.; Dai, S.; Baker, G. A.; Cummings, P. T. *J. Phys. Chem. Lett.* **2012**, *3*, 125.

73. Hardacre, C.; Holbrey, J. D.; McMath, S. E. J.; Nieuwenhuyzen, M. *ACS Symposium Series* **2009**, *818* (Chapter-31), 400.

74. Russina, O.; Triolo, A.; Gontrani, L.; Caminiti, R. *J. Phys. Chem. Lett.* **2012**, *3*, 27.

75. Aoun, B.; Goldbach, A.; González, M. A.; Kohara, S.; Price, D. L.; Saboungi, M. L. *J. Chem. Phys.* **2011**, *134*, 104509.

76. Urahata, S. M.; Ribeiro, M. C. C. *J. Phys. Chem. Lett.* **2010**, *1*, 1738.

77. Russina, O.; Gontrani, L.; Fazio, B.; Lombardo, D.; Triolo, A. Caminiti, R. *Chem. Phys. Lett.* **2010**, *493*, 259.

78. Hardacre, C.; Holbrey, J. D.; Mullan, C. L.; Youngs, T. G. A.; Bowron, D. T. *J. Chem. Phys.* **2010**, *133*, 074510.

79. Bodo, E.; Gontrani, L.; Caminiti, R.; Plechkova, N. V.; Seddon, K. R.; Triolo, A. *J. Phys. Chem. B* **2010**, *114*, 16398.

80. Annapureddy, H. V. R.; Kashyap, H. K.; Biase, P. M. D.; Margulis, C. J. *J. Phys. Chem. B* **2010**, *114*, 16838.

81. Habasaki, J.; Ngai, K. L. *J. Chem. Phys.* **2008**, *129*, 194501.

82. Wang, Y.; Jiang, W.; Yan, T.; Voth, G. *Acc. Chem. Res.* **2007**, *40*, 1193.

83. Triolo, A.; Russina, O.; Bleif, H. J.; Cola, E. D. *J. Phys. Chem. B* **2007**, *111*, 4641.

84. Xiao, D.; Rajian, J. R.; Li, S.; Bartsch, R. A.; Quitevis, E. L. *J. Phys. Chem. B* **2006**, *110*, 16174.

85. Wang, Y.; Voth, G. A. *J. Phys. Chem. B* **2006**, *110*, 18601.

86. Guo, J.; G. Baker, G. A.; Patrick, C.; Hillesheim, P. C.; Dai, S.; Shaw, R. W.; Mahurin, S. M. *Phys. Chem. Chem. Phys.*, **2011**, *13*, 12395.

87. Patra, S.; Samanta, A. *J. Phys. Chem. B* **2012**, *116*, 12275.

88. Sasmal, D. K.; Mandal, A. K.; Mondal, T.; Bhattacharyya, K.; *J. Phys. Chem. B* **2011**, *115***,** 7781.

CHAPTER 4

EXCITON DYNAMICS IN ANTHRACENE NANOAGGREGATES

4.1. INTRODUCTION

During the last two decades, nanoscience has become a fascinating field of research for the scientists from different disciplines. Preparation and properties of the nanomaterials have received huge attention due to their wide scale applications in multiple fields.[1-7] Among them, nanomaterials prepared using organic molecules have shown immense potentiality due to their low cost, ease of syntheses and excellent optical properties. The quantum confinement effect is less pronounced for organic nanoaggregates, but it has an additional advantage because of the possibility of producing different monomers by substitution,[8,9] which helps tuning the properties of the nanoaggregates in desired manner. Organic nanocomposites are found to be useful for application in OLEDs,[10] field effect transistors,[11] organic solar cells,[12] wave guides,[13] etc.

Different kinds of interactions, e.g. hydrophobic, π-π interaction, H-bonding, etc lead to formation of nanoaggregates and these interactions are weak in nature. Therefore, the thermodynamic stability is, of course, a point of concern for these materials. Materials consisting of polycyclic aromatic hydrocarbons are known to be good organic semiconductors (OSC), having excellent optical and electronic properties. They form crystals due to π-π intermolecular interactions.[14] These molecules are extremely hydrophobic and form nanoaggregates, which are quite stable in ambient condition.[15-17] It is important to understand the properties of these materials for their applications in preparing devices. Methods of synthesis of the nanoaggregates of the polyacene compounds have been reported earlier by several groups and their basic photophysical properties have also been explored in recent years.[15-17] Exciton dynamics in bulk crystal form and in thin films for a few of these polycyclic aromatic compounds have also been reported earlier.[18-21] However, to the best of our knowledge, no information about the exciton dynamics in the nanoaggregates of these compounds is available in the literature.

Anthracene, in its crystalline form, has been found to display many attractive optoelectronic properties, such as high charge carrier mobility,[22] anisotropy,[23, 24] aromagnetism,[25] etc. Moderate band gap of 3.1 eV,[26] and high emission quantum yield,[27] make anthracene a potential material for application in OLED,[26] organic photovoltics,[28] optoelectronic devices,[29] etc. Knowledge about the photophysical and diffusion properties of excitons populated in various kinds of materials is important in designing the optoelectronic devices with improved performance. Although exciton dynamics in the crystalline phase and in thin films of anthracene have been extensively studied by several groups,[30 - 33] to the best of our knowledge, these properties have not been discussed in nanoaggregates. Preparation of anthracene nanoaggregate by reprecipitation technique has been reported recently and these particles have been shown to be quite stable in ambient condition.[16, 17, 34-38]

Herein, we have investigated the basic photophysical properties and exciton dynamics in anthracene nanoaggregates using steady state and time-resolved absorption and fluorescence spectroscopic techniques. We have determined the excitation intensity dependence of the exciton – exciton annihilation rates to estimate the diffusion constants and diffusion lengths for both the singlet and triplet excitons.

4.2. RESULTS AND DISCUSSION

4.2.1. Morphological characterization: Morphological analysis is considered as the primary step in characterization of the nanomaterials. Herein, DLS and AFM techniques have been used to determine the size distribution of the nanoaggregates. Size distribution of the nanoaggregates determined using DLS technique has been shown in Figure 4.1A. It is observed that the average size of the nanoaggregates is about 260 ± 25 nm. AFM image of the nanoaggregates is also shown in Figure 4.1B. We find that the average height of the nanoaggregates is about 50 ± 10 nm and the diameter of the nanoaggregates varies in the 50 - 400 nm range. AFM analysis also indicates that the particles of these nanoaggregates are not spherical in shape but the aspect ratio varies in the range 0.05 - 0.1. Therefore, they may be better described as nanodiscs.

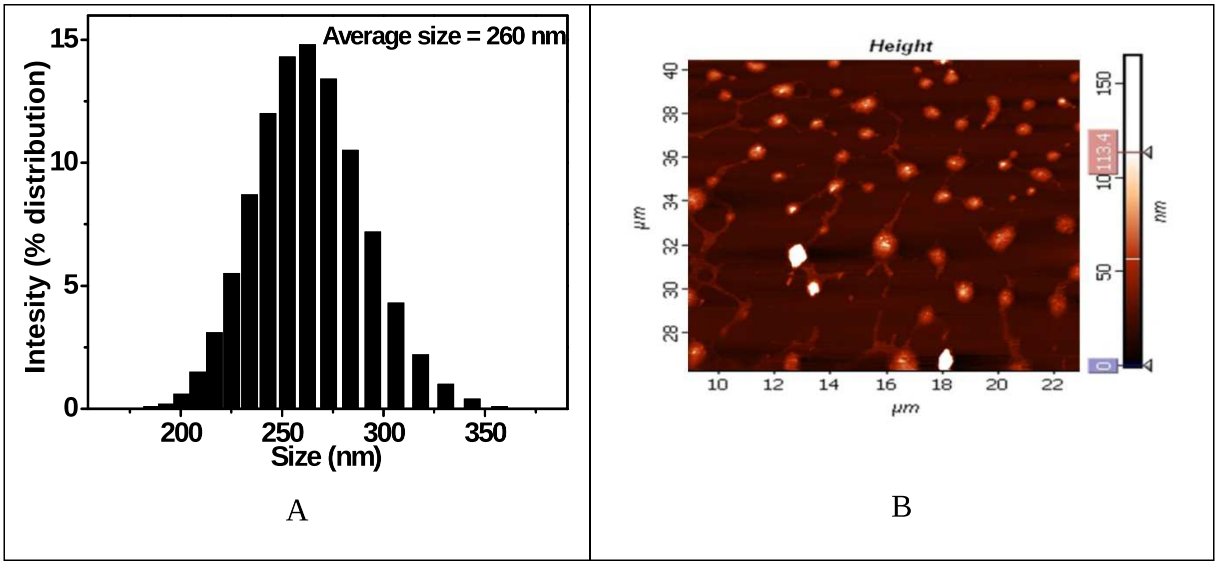

Figure 4.1:.Size distribution of the anthracene nanoaggregates determined using DLS (A) and AFM (B) techniques.

Arrangement of the anthracene molecules in the nanoaggregates has been understood from the X-ray diffraction analysis. After vacuum drying of the nanoaggregate sample, it was brought to powder form and XRD measurement was performed. The XRD pattern has been compared with those of the crystalline forms reported earlier.[39, 40] In the case of the nanoaggregate sample; we observe a weak but broad featureless XRD band in the range of 15 - 35 degree of the diffraction angle with a few intense lines superimposed on it (Figure 4.2). Those sharp lines are perfectly coincident with those observed in the XRD pattern of the crystalline state. This observation leads us to describe the nanoaggregated form of anthracene as a crystalline substance with the presence of a large number of defect sites, providing it partial amorphous nature. The defect sites may have remarkable effect on the photophysical properties of the excitons populated in the nanoaggregate as compared to those in anthracene crystal or thin film.

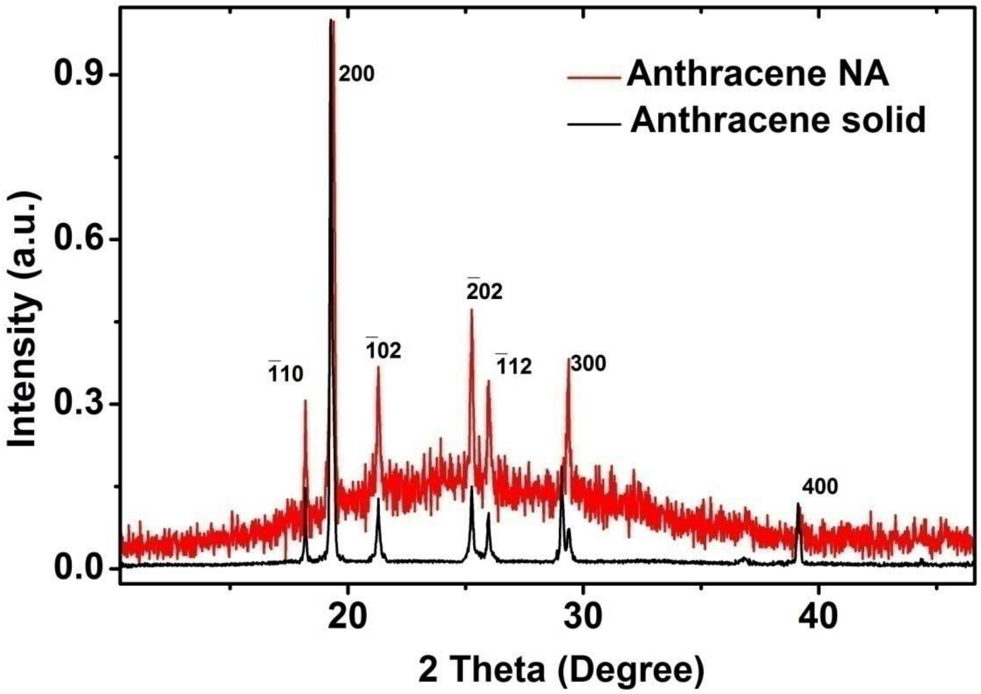

Figure 4.2: XRD pattern recorded for anthracene nanoaggregate and bulk solid.

4.2.2. Steady state absorption and emission spectra: In Figure 4.3, we have compared the steady state absorption spectrum of anthracene dissolved in acetonitrile with that of the aqueous dispersion of the nanoaggregate. It is well known that the absorption spectrum of anthracene in organic solvents shows distinct and sharp vibrational progressions. Similar vibrational progressions have also been found in the absorption spectrum of the nanoaggregate sample. However, the positions of each of these progressions is nearly the same as that observed in the case of the molecule in solution, the lowest energy one (corresponding to the 0 - 0 transition) appears at a position, which is red-shifted by about 20 nm as compared to that in solution. In addition, the relative heights of the individual vibronic bands are significantly changed and the widths of these bands arising due to Devydov splitting are also increased.[41] The long tail in the red region of the absorption spectrum of the nanoaggregate sample is assigned to Mie scattering. Absence of this extended absorption in the red region of the fluorescence excitation spectrum (inset of Figure 4.4) confirms its assignment to Mie scattering. All these new features observed in the absorption spectrum of the nanoaggregate as compared to that of the molecule in solution may be attributed to strong intermolecular interaction between the different monomeric anthracene units in the closely packed nanoaggregated state.

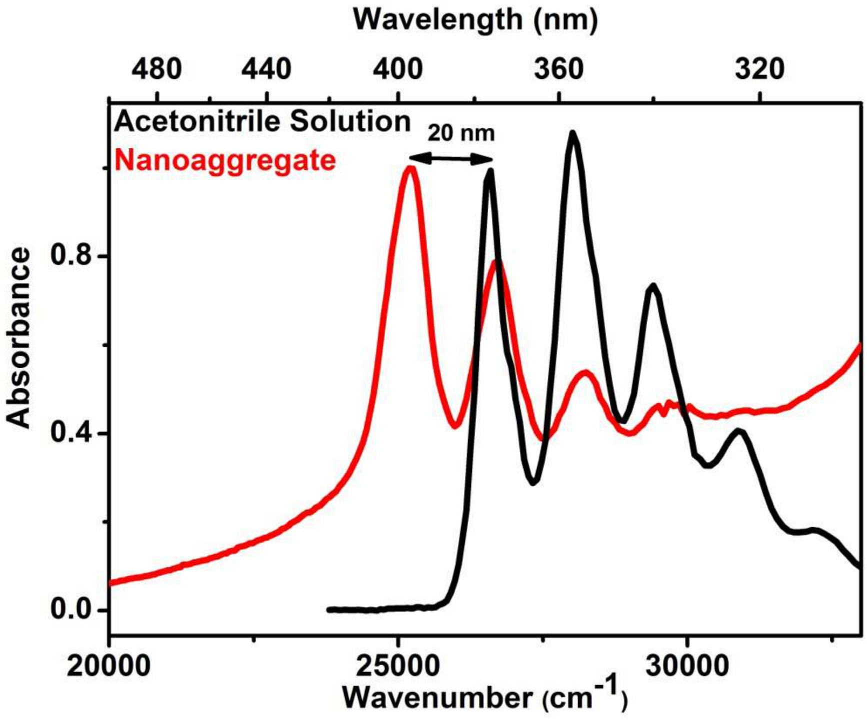

Figure 4.3: UV-visible absorption spectra of anthracene dissolved in acetonitrile and anthracene nanoaggregate dispersed in water.

Room temperature PL spectra recorded for the anthracene molecule in acetonitrile solution as well as for the aqueous dispersion of the nanoaggregate sample are presented in Figure 4.4. We find that the emission spectrum of the nanoaggregate also consists of the features of sharp vibrational progressions. However, like in the case of the absorption spectrum of the nanoaggregate, the largest energy vibronic band in the emission spectrum is also found to be red-shifted by about 20 nm as compared to the 0 – 0 vibronic band of the monomer in acetonitrile solution appearing at 380 nm. Absence of this vibronic band in the emission spectrum of the nanoaggregate sample, ensures the absence of any isolated monomer molecule in aqueous dispersion of the nanoaggregate sample.

We have determined the emission quantum yield (ϕ_F) of the nanoaggregate sample relative to that of the monomer in acetonitrile and the former is found to be reduced by about one half as compared to the later. Increased rate of the intersystem crossing (ISC) process may be one of the possible reasons for the reduced ϕ_F in the nanaoaggregate sample. However, in the crystalline form of anthracene, the rate of the intersystem crossing (ISC) process has been found to decrease significantly as compared to that of the monomer in solution.[42, 43] The reason has been explained as follows: In the case of anthracene molecule in solution, the energy level of the T_2 state lies just below the S_1 energy level. This leads to efficient coupling between these two states and hence the rate of the ISC process is very fast. In solid crystalline form, due to stronger intermolecular interactions, the relative positions of these energy levels are changed and the energy level of the T_2 state is lifted up with respect to that of the S_1 excitonic state by about 73 meV. In addition, the S_1-T_1 energy gap being large (1.3 eV), coupling between these two states are poor.[42,43] Hence in the crystalline solid form, the rate of the ISC process is likely to decrease as compared to that of the molecule in solution.

In the case of anthracene nanoaggregates, the absorption spectrum possesses good similarities with that of the anthracene crystal. In addition, our XRD analysis has revealed that the nanoaggregate also possesses good crystalline character. Therefore, these characteristics of the nanoaggregate sample suggest that the energy levels associated with these two kinds of materials may be quite similar.[44] We have also discussed earlier that, quantum confinement effect in the nanoaggregate is small and hence similarities in the energy levels in the nanoaggregate and in crystalline solid are a good possibility. Therefore, we may assume that the rate of the ISC process in the nanoaggregate is not larger than that of the monomer molecule in solution and hence the ISC process can not be a responsible factor for smaller ϕ_F in the nanoaggregate. We predict that one or both of other two photophysical processes, namely, faster rate of the internal conversion process and trapping of excitons in the defect sites, are responsible for lower ϕ_F in the nanoaggregate (vide infra).

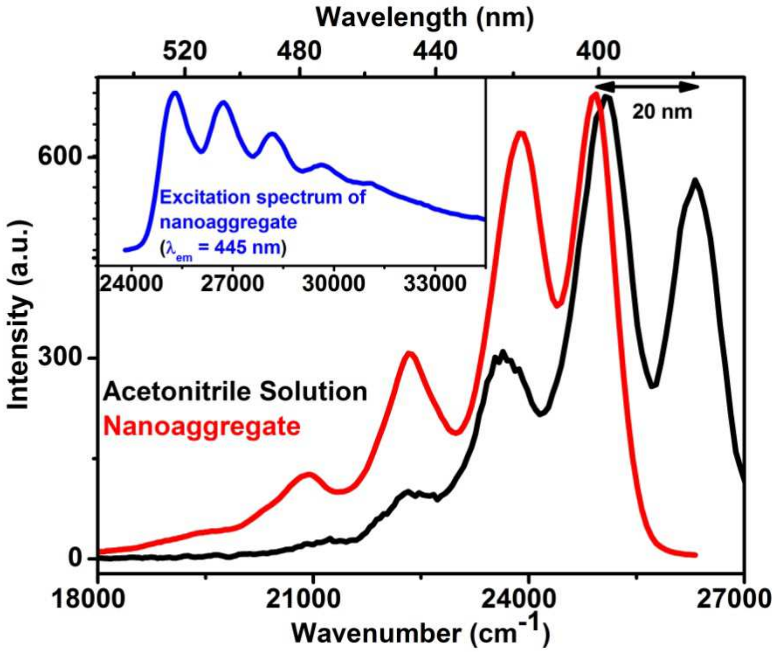

Figure 4.4: Steady state fluorescence spectra of anthracene in acetonitrile solution and anthracene nanoaggregate dispersed in water. Inset: Excitation spectrum recorded for anthracene nanoaggregate for 445 nm emission.

4.2.3. Time-resolved studies using TCSPC technique: To resolve the deactivation pathways for the excitonic states of the nanoaggregate populated following photoexcitation, time-resolved fluorescence experiments have been performed by using TCSPC technique. Temporal emission profiles have been recorded at regular intervals of 10 nm in the 400 – 650 nm region with a time resolution of about 200 ps following photoexcitation of the aqueous dispersions of the nanoaggregate sample at 374 nm. Each of these decay profiles could be fitted with a multi-exponential function consisting of two or three components by using iterative deconvolution method. Three of them, along with the best-fit functions, are shown in Figure 4.5 and the lifetimes (τ) as well as the relative amplitudes (a) thus estimated are presented in Table 4.1.

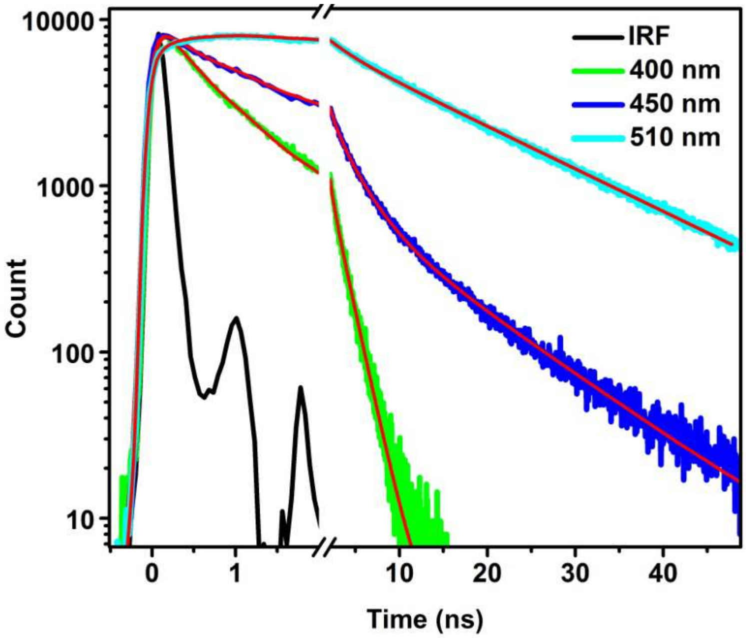

Figure 4.5*:* Temporal florescence profiles recorded at three different wavelengths along with the multi-exponential best-fit functions for the anthracene nanoaggregate sample. The lifetimes (τ) and the relative amplitudes (a) associated with the best-fit functions are given in Table 4.1.

Table 4.1: Lifetimes (τ) and relative amplitudes (a) associated with the best-fit functions for the temporal fluorescence profiles recorded following photoexcitation of the nanoaggregate dispersed in water.

Wavelength (nm)	Lifetime (ns) (Relative amplitude)		
	τ_1 (a_1)	τ_2 (a_2)	τ_3 (a_3)
400	0.52 ± 0.06 (0.47 ± 0.05)	1.8 ± 0.4 (0.53 ± 0.05)	-
450	0.72 ± 0.08 (0.17 ± 0.04)	2.89 ± 0.3 (0.40 ± 0.05)	11.72 ± 1.5 (0.43 ± 0.05)
510	0.44 ± 0.05 (-0.01 ± 0.01)	2.78 ± 0.3 (0.04 ± 0.01)	16.7 ± 2 (0.97 ± 0.05)

Multi-exponential decay of the excitonic emission suggests population of multiple excitonic states following photoexcitation of the nanoaggregate sample. The temporal profile recorded at 400 nm could be fitted by using a biexponential decay function with the lifetimes of 0.52 and 1.8 ns. However, each of the temporal profiles recorded at longer wavelengths (say, at $\lambda \geq 450$ nm) could only be fitted by using a three exponential function. For example, the temporal profile recorded at 450 nm, has been fitted with a three-exponential decay function with the lifetimes of 0.72, 2.8, and 12 ns. We find that the amplitude associated with the longest lived component (i.e. a_3) increases, but those of the two shorter lived components (i.e. a_1 and a_2) decrease, as the monitoring wavelength is tuned towards the longer wavelength region. Temporal profiles recorded at wavelengths longer than 500 nm show an initial rise of fluorescence intensity with the lifetime of 0.44 ns followed by a biexponential decay with the lifetimes of about 2.8 and 16 ns. Similarities in the lifetimes of the fastest decay component associated with the temporal profiles recorded at <450 nm and that of the rising component observed at >500 nm possibly suggest a complementary relationship between them. We attribute the former one to the decay of the excitonic state populated following photoexcitation of the nanoaggregate and the later to the population of an excimeric state of anthracene.

Seko *et al* have reported that excimer formation takes place predominantly in the surface region of anthracene microcrystal.[17] In nanoaggregates, the surface area to volume ratio is large and the regular arrangement of the molecules in the crystal is interrupted at the surface. Therefore, possibility of the presence of surface defects is very large in the nanoaggregate sample. In this report, we have not been able to define the specific role of surface defects on the exciton dynamics, instead we observe the overall effect of the defects present both in the bulk and at the surface. However, we can predict that, due to the large surface area to volume ratio in the nanoaggregate, surface defects play a major role in exciton trapping. It may be noted that the lifetimes and the relative amplitudes associated with the best fit-functions for the temporal fluorescence profiles show significant wavelength dependence. This possibly can be attributed to several factors. Firstly, because of different size distribution of the particles in the nanoaggregate assembly, lifetimes of the excitonic states in different particles may vary to some extent. According to the exciton - polariton model, lifetimes of the excitonic states depend upon the size of the nanoaggregates.[45] In addition, wavelength dependence may also arise due to the heterogeneities of the defect sites because of differences in orientations of the monomers, and hence, populating excimeric states of different geometries (vide infra).[46, 47]

Most importantly, wavelength dependence of the temporal profiles may also arise due to reabsorption effect. Exciton diffusion and reabsorption of exciton emission have been extensively studied in anthrecene crystal earlier both experimentally as well as by MD simulation.[48 - 52] Reabsorption of exciton emission has been reported to be significant only in the case of thick crystals (thickness of a few tens of μm).[49] However, in our case, the average size of the nanoaggregates prepared by us is only about 0.26 μm. Negligible effect of reabsorption on exciton dynamics in the nanoaggregates has been evident from two observations. Firstly, the absorption or excitation spectrum and the emission spectrum of the exciton populated in the nanoaggregate maintain a perfect mirror image relationship. Further, the exciton lifetime is extraordinarily short (0.5 ± 0.2 ns) as compared to that reported in crystals. Usually, thin crystals show a fairly short decay time of the exciton luminescence, while thick crystals show long decay time due to reabsorption effect. The short decay time in thin crystals has rather been explained by the trapping of the excitons at the crystal defects at the surface, the number of which is rather larger in thinner crystals.[49] The short decay time has been commonly considered to be intrinsic. Therefore, we assign the component having lifetime of 0.5 ± 0.2 ns to the free S_1 excitonic state, which is shorter than that of the singlet exciton populated in anthracene crystal.[20] Trapping of excitons at the defect sites and more surface encounter due to smaller size of the nanoaggregates are the major factors responsible for this short exciton lifetime in the nanoaggregate.[53]

While τ_3 may be assigned to the lifetime of the excimeric state, the assignment of τ_2 is not unanonymous. The later may have contribution from the quasi-free excitonic state, which is populated in the anthracene crystal because of strong exciton – phonon interaction.[54] Population of quasi-free excitonic state becomes significant if the coupling constant is greater than unity, a condition which may arise at high pressure (say 5-18 kbar). However, in anthracene crystal at an ambient condition, the exciton – phonon coupling constant has a value of 0.85, and hence population of the quasi-free excitonic state in the crystal at ambient condition as well as in the nanoaggregate is quite unlikely.[54] Therefore, both the fluorescence decay components, τ_2 and τ_3, represent the components of a biexponential fit to the nonexponential decay of the self-trapped excitonic and / or excimeric emissions. Population of the excimeric states is generally not observed in the case of anthracene in solution phase at ambient condition. In solution phase, anthracene molecules, on photoexcitation using uv light, prefer to form photodimers.[55] Excimer emission has been reported by different research groups in bulk crystals having defect sites as well as at high pressure condition.[56 - 61] Shapes of the excimer emission spectra have been shown to depend on the experimental conditions thus populating the excimeric states having different kinds of geometries or configurations.

Temporal fluorescence profiles recorded at different wavelengths have been used to construct the '*time resolved area normalized emission spectra*' (TRANES) of anthracene nanoaggregate.[63, 64] These have been shown in Figure 4.6, which reveals that distinctly different kinds of excitonic and / or excimeric states are populated at different delay times and they emit in different wavelength regions. The time-resolved emission spectrum recorded at 0.2 ns delay time is mainly dominated by the contributions from free excitons. As the delay time increases up to 4 ns, contribution from the free excitons decreases leading to decay of emission intensity of the vibrational progression appearing in the 380 – 410 nm region. This is accompanied by the concomitant rise of intensities of the vibration progressions appearing in the 410 – 440 nm region, which may be assigned to population of the self-trapped excitons. With further increase in delay time, we observe the development and evolution of a new broad emission band in the 450 – 600 nm region in expense of the one with the well-resolved vibrational bands in the 380 - 440 nm. We assign the emission band appearing in the 440 – 600 nm region to the excimeric state. However, the shape of this new emission band changes significantly as the delay time increases. This may be attributed to the reorientation of the anthracene molecules in the defect sites stabilizing the excimeric state. This also explains the wavelength dependence of τ_2 and τ_3 (Table 4.1) and time evolution of the transient fluorescence spectra in the 450 – 600 nm region (Figure 4.6).

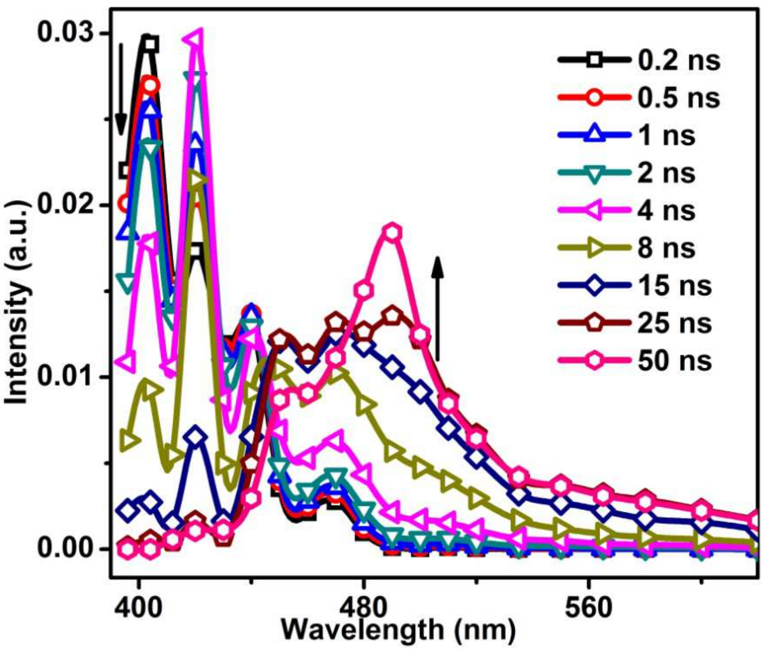

Figure 4.6: Time-resolved area normalized emission spectra (TRANES) of anthracene nanoaggregate.

4.2.4. Sub-picosecond transient absorption studies: Transient absorption (TA) spectroscopic technique has been employed to obtain information regarding the ultrafast dynamics of the excitonic state populated in the anthracene nanoaggregate. Time-resolved TA spectra recorded following photoexcitation of the anthracene nanoaggregate sample at 400 nm are shown in Figure 4.7. The spectrum recorded at 0.3 ps delay time consists of a broad excited state absorption (ESA) band in the 460 – 750 nm region with a maximum at ca 580 nm. With increase in delay time, the entire ESA band decays leading to the development of a weak negative absorption band in the 450 – 650 nm region. The entire ESA band is assigned to the excitonic state populated upon photoexcitation. Considering its signature in the TRANES, the negative absorption band appeared after 30 ps delay time is assigned to stimulated emission from the excimeric state. However, because of limitation of our femtosecond spectrometer (having provision of delay time up to about 1 ns), we could not measure complete evolution of the SE band.

Figure 4.7B shows the temporal evolution of the transient species recorded at three selective wavelengths. Each of them reveals instrument response time limited rise of ESA followed by a non-exponential decay. We also observe that the temporal profiles show dependence on excitation intensity and this suggests that the non-exponential decay of the excitonic state in sub-ps time domain is the result of exciton-exciton annihilation reaction (vide infra).[20, 35, 64] In addition, since the ESA band is overlapped with the stimulated emission spectrum of the excimeric state, the temporal profiles should also be associated with a component representing the rise of stimulated emission (negative absorbance). Therefore, we adopt the following kinetic model to analyse the temporal profiles recorded in the transient absorption experiments.

4.2.4.1. Singlet - singlet exciton annihilation: The S_1 excitonic state populated following photoexcitation of the anthracene nanoaggregate sample undergoes the following processes:

$$S_1 \xrightarrow{k_1} S_0 \qquad (4.1)$$

$$S_1 + S_1 \xrightarrow{k_2} S_n + S_0 \qquad (4.2)$$

$$S_1 + D \xrightarrow{k_3} E \qquad (4.3)$$

Equation 4.1 represents the natural decay of the free S_1 excitonic state to the ground state, S_0, whereas Equation 4.2 represents the second order decay of the S_1 excitonic state due to exciton – exciton annihilation process, which populates S_n ($n > 1$) excitonic state and the S_0 state. S_n excitonic state undergoes ultrafast vibrational relaxation and internal conversion process and produces back the S_1 excitonic state. Equation 4.3 represents the trapping of the S_1 excitonic states at defect sites (D) leading to population of the excimeric state (E).

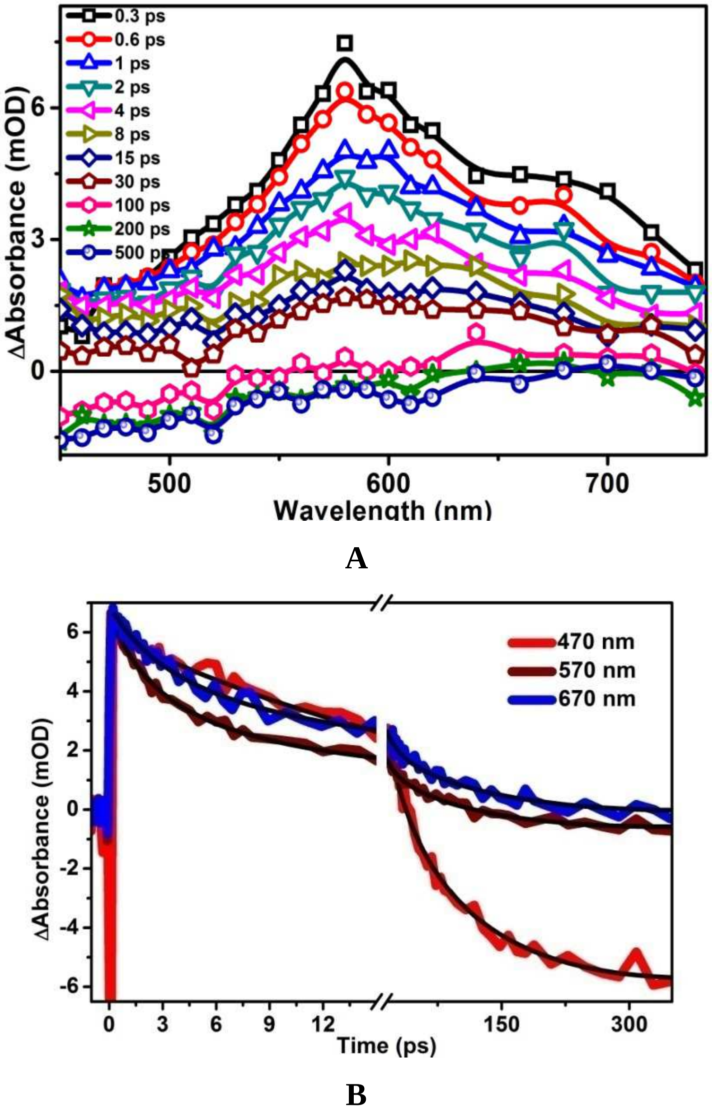

Figure 4.7: (A) Time-resolved transient absorption spectra recorded at different delay times following photoexcitation of the nanoaggregate sample by using 400 nm laser pulses. **(B)** Temporal profiles recorded at three different wavelengths, along with the best fit functions (they have been normalized at the maximum ESA value).

We write the rate equation for the S_1 excitonic state,

$$\frac{d[S_1]}{dt} = -k_1'[S_1] - \frac{k_2[S_1]^2}{2} \qquad (4.4)$$

k_1' represents the annihilation-free decay of the S_1 excitonic state, i.e. combination of natural decay (Equation 4.1) and decay due to excimer formation (Equation 4.3) i.e. k_1' = $k_1 + k_3[D]$.

Here, we assume that the defect concentration is fixed for a particular sample of the nanoaggregate prepared for the experiment. k_2 represents the exciton - exciton annihilation decay rate constant. Solution of Equation 4.4 gives us the concentration of the S_1 excitonic state at time ‘t’ (Equation 4.5 solution shown in S4.1 in SD section).

$$[S_1] = [S_1]_0 \, X \, \frac{[exp(-k_1' t)]}{(1+k_2' t)} \qquad (4.5)$$

Here, $k_2' = \frac{k_2[S_1]_0}{2}$ (4.6)

Decay of the ESA band represents the decay of the S_1 excitonic state. Therefore, we write,

$$[\Delta\mathrm{OD}]_{ESA} = [\Delta\mathrm{OD}]_0 \, X \, \frac{[exp(-k_1' t)]}{(1+k_2' t)} \qquad (4.7)$$

Population of the excimeric state is associated with the rise of stimulated emission or negative absorption signal. Following Equation 4.3, the rate equation for evolution of the stimulated emission signal can be written as,

$$\frac{dE}{dt} = k_3 [D] [S_1] \qquad (4.8)$$

Using the value of $[S_1]$ estimated in Equation 4.5 and making an assumption that [D] is constant for the particular sample of nanoaggregate investigated, we can solve the above equation to obtain the expression for [E],

$$[E] = [S_1]_0 k_3 [D] t [\exp(-k_1 t)]] \qquad (4.9)$$

Since stimulated emission from the excimeric state contributes as a negative signal to the decay of the transient absorption signal, we write,

$$[\Delta\mathrm{OD}]_{SE} = -[\Delta\mathrm{OD}]_0 \, k_3' t [\exp(-k_1 t)]] \qquad (4.10)$$

Here k_3' = $k_3[D]\alpha$ (4.11)

Where, α is a constant, which is the ratio of the stimulated absorption cross section of the S_1 state and the stimulated emission cross section of the excimeric state at a particular wavelength and hence is wavelength dependent.

The excimeric state has a very long lifetime (>15 ns) and hence the negative absorption signal due to this state, following its rise, will remain constant as a residual emission signal (R). Therefore, the transient absorption signal has three major contributions, which may be represented as,

$$[\Delta OD]_{Total} = [\Delta \mathrm{OD}]_{ESA} + [\Delta \mathrm{OD}]_{SE} + R \qquad (4.12)$$

$$[\Delta OD]_{Total} = [\Delta \mathrm{OD}]_0 X \frac{[exp(-k_1' t)]}{(1+k_2' t)} - [\Delta \mathrm{OD}]_0 k_3' t[\exp(-k_1' t)]] + R \qquad (4.13)$$

We find that all the experimentally recorded decay profiles could be fitted well with the Equation 4.13 (Figure 4.7B) and Table 4.2 presents the parameters best-fitting the temporal profiles recorded at 470, 570 and 670 nm using the excitation pulse energy of 6 μJ/pulse. The inverse of k'$_1$[$\tau = (k_1')^{-1}$= 0.35 ns], which is close to the lifetime τ_1 (Table 4.1) estimated from the TCSPC measurements, represents the lifetime of the free S_1 excitonic state. The value of k_2' has been observed to be dependent on the monitoring wavelength, and it also depends upon the value of $[\Delta \mathrm{OD}]_0$. We have performed the intensity dependent measurements of the temporal profiles to find out the annihilation rate constant and other exciton diffusion parameters for the nanoaggregate.

Table 4.2: Parameters best-fitting the temporal profiles recorded at 470, 570 and 670 nm using the excitation pulse energy of 6 μJ/pulse.

Parameters	**470 nm**	**570 nm**	**670 nm**
$[\Delta \mathrm{OD}]_0$ (mOD)	11.1 ± 1	6.46 ± 0.7	6.31 ± 0.06
k'_1 (10^9 s^{-1})	2.9 ± 0.3	3.1 ± 0.3	2.9 ± 0.4
k'_2 (10^{11} s^{-1})	2.17 ± 0.1	1.52 ± 0.08	7.55 ± 0.08
k'_3 (10^8 s^{-1})	8.0 ± 1	2 .0 ± 0.5	1.0 ± 0.2
R (10^{-3})	- 5.1 ± 1	- 0.2 ± 0.05	- 0.1 ± 0.02

At high excitation intensities, exciton - exciton annihilation process is considered to be a dominating decay process. Rate of this process is directly dependent on the rates of the diffusive motion of the excitons in the nanoaggregate and hence has been rightly used for estimation of the exciton diffusion parameters.[20, 35, 64] We have recorded the temporal profiles at 590 nm by varying the excitation pulse energies in the range of 3 - 12.5 μJ/pulse. These temporal profiles have been fitted using Equation 4.13 (Figure 4.8) and best-fit parameters are provided in Table S4.2 in SD section.

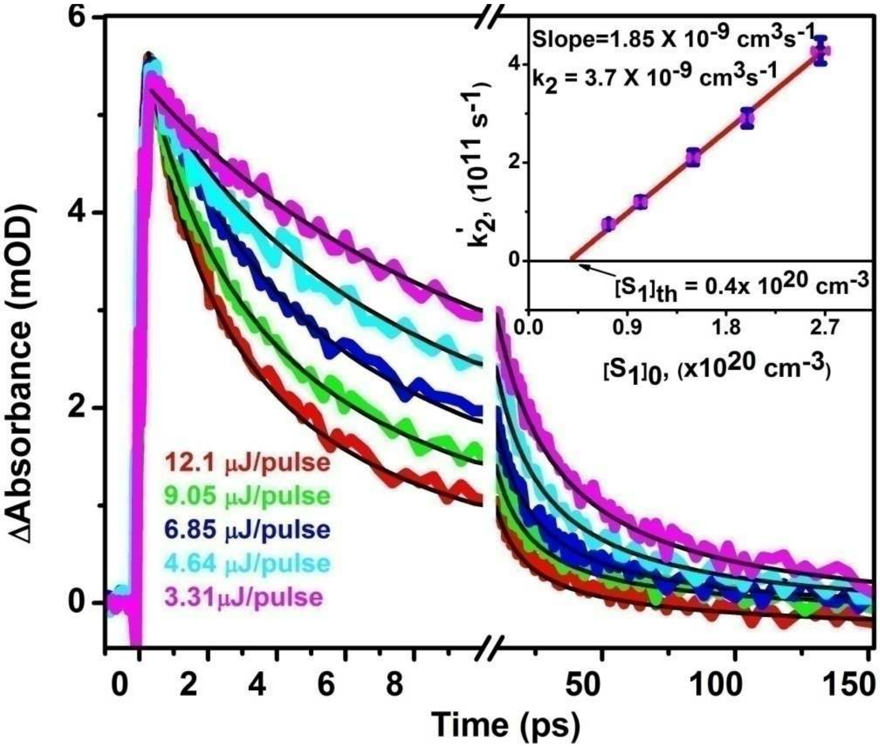

Figure 4.8: Temporal TA profiles recorded at 590 nm following photoexcitation of anthracene nanoaggregate using 400 nm light of different pump intensities, along with the best-fit functions following equation 13. Inset: plot of k_2 vs. $[S_1]_0$.

In this analysis, we have only considered the contribution from the singlet excitons. Population of the triplet excitons occurs at relatively longer time domain and therefore we neglect the contribution of the triplet excitons to the temporal profiles of the transients recorded in the sub-ps time domain (vide infra).

We mentioned earlier that exciton - exciton annihilation is a diffusion controlled process. Therefore, the rate constant of the exciton – exciton annihilation process has been frequently used to calculate the exciton diffusion coefficient as well as the exciton diffusion length. Exciton diffusion length is one of the important parameters, which need to be known in the case of applications of the material in photovoltaic and other optoelectronic devices. The exciton diffusion constant, D, is related to the annihilation rate constant, k_2, by equation (4.14)

$$k_2 = 8\pi R_a D \qquad (4.14)$$

Where, R_a is the annihilation radius. The value of R_a can be estimated by determining the threshold value of the exciton density or $[S_1]_{th}$ for on-setting the exciton - exciton annihilation process. $[S_1]_{th}$ has been estimated from the plot of k_2' vs the exciton density at zero delay time or $[S_1]_0$. In turn, $[S_1]_0$ has been calculated for a given excitation intensity using the percent absorption of light by the sample (S4.3. in SD section), the excitation volume and the average number of anthracene molecules per aggregate. k_2' Should have a nonzero value, if the excitation intensity is large enough to create a population density of exciton, which is larger than the threshold exciton density. In the case of anthracene nanoaggregate studied here, we estimate the value of $[S_1]_{th}$ as 0.4 x 10^{20} cm^{-3}, which represents the fact that for this value of exciton density, there is only one exciton within a sphere of volume of about 25 nm^3. The approximate value of the radius of this sphere is about 1.8 nm, which may be considered as the annihilation radius for the singlet exciton in the anthracene nanoaggregates. We could also determine the value of k_2 (3.7x 10^{-9} cm^3 s^{-1}) from the slope of the plot of k_2' vs $[S_1]_0$ (inset of Figure 4.8 and Table 4.3).

Table 4.3: Estimation of k_2 from the excitation energy dependence of $[S_1]_0$ (see inset of Figure 4.8)

Excitation energy (µJ / pulse)	**$[S_1]_0$, (x 10^{20} cm^{-3})**	**k'_2 (x 10^{11} s^{-1})**	**k_2 (cm^{-3} s^{-1})**
12.1 ± 0.3	2.66 ± 0.07	4.28 ± 0.26	3.7±1.6 x 10^{-9}
9.05 ± 0.2	1.99 ± 0.04	2.95 ± 0.17	
6.85 ± 0.2	1.5 ± 0.04	2.105 ± 0.14	
4.64 ± 0.2	1.02 ± 0.04	1.2 ± 0.09	
3.31 ± 0.1	0.73 ± 0.02	0.748 ± 0.06	

Using these values of k_2 and R_a in Equation (4.14), we determine the value of exciton diffusion coefficient, D, as 0.83 $\times 10^{-3}$ $cm^2\ s^{-1}$. It has been observed that, for anthracene crystal the reported exciton diffusion constant has wide range of values and exciton diffusion process is anisotropic in nature. In this present work, we have assumed that the diffusion process is isotropic in the nanoaggregate samples. The value of the diffusion coefficient thus determined for the anthracene nanoaggregate is nearly similar to those determined in the solid crystals (Table 4.4).[65, 66] We estimate the exciton diffusion length, L_D, in the nanoaggregate using Equation (4.15),

$$L_D = (6D\tau)^{1/2} \qquad (4.15)$$

Using the value of the lifetime of the exciton ($\tau = 0.35$ ps), the diffusion length has been calculated to be ~13 nm, which is also nearly similar to that in crystalline anthracene (Table 4.4). However, shorter S_1 exciton lifetime results to a slight decrease in the exciton diffusion length in the nanoaggregate sample.[66] Comparison of these values in the anthracene crystal and nanaoaggregate further ensures that the matrices or molecular packings in these two kinds of materials are not very much different.

Table 4.4: Comparison of the annihilation rate constants, exciton diffusion coefficients and diffusion lengths for singlet exciton in anthracene crystal and nanoaggregate.

System	**k_2 ($cm^3\ s^{-1}$)**	**D ($cm^2 s^{-1}$)**	**L_d (nm)**
Crystal	5-20 x 10^{-9}	1-10 x 10^{-3}	25 - 100
Nanoaggregate	3.7 ± 1.6 x 10^{-9}	0.83 ± 0.3 x 10^{-3}	13.2 ± 4

[a] refs. 20, 65 - 70

The effect of the defect sites on the exciton diffusion length has already been reported by Cohen et. al. They have estimated the diffusion length in smooth and rough crystal regions of anthracene.[69] For the smooth crystal region, where the proper molecular packing is expected, the exciton diffusion length determined is about 49 nm. On the other hand, for the rough region with a lot of defect sites, the exciton diffusion length has been found to be shorter by about 10 - 15 nm.[69] It has also been known that crystals formed by different methods possess different exciton diffusion lengths. According to the reports available in the literature, the exciton diffusion length in a crystal grown from the molecular vapour is about 105 nm. Whereas this value is shortened to about 40 - 50 nm in a crystal grown from solution and to about 25 nm in that grown from melt.[69] This means that exciton diffusion length varies in crystals grown under different conditions. Therefore, the marginal reduction in exciton diffusion length as compared to that of the crystals, is predicted considering the presence of partial amorphous nature in the nanoaggregates. The effect of small size and surface defects on the exciton diffusion length, need to be discussed in short.

4.2.4.2. Triplet-triplet exciton annihilation: The yield of the intersystem crossing (ISC) process originating from the S_1 state of anthracene in hexane has been reported to be about 0.55.[71] However, in solid thin films or in crystalline forms, the energy level of the T_2 state lies above than that of the S_1 state. As a consequence of this, the yield of the triplet state is reduced by about two orders of magnitude.[43, 44] Yield of the triplet exciton in the nanoaggregates is also a point of interest to us. In Figure 4.9, we have presented the time-resolved transient absorption spectra recorded following photoexcitation of anthracene nanoaggregate using laser pulses of 355 nm wavelength and 10 ns duration.

The absorption spectrum of the triplet exciton is very broad extending through the 300 – 750 nm region on which the fine structures superimposed may have arisen due to ground state bleaching. Triplet absorption spectrum of anthracene in acetonitrile solution reported earlier also shows the presence of a broad band in the 450 – 650 nm region; although the shape of the spectrum recorded in the nanoaggregate is much more broad, possible because of strong interactions between the triplet and the lattice.[72 - 74] Long-lived triplet exciton in anthracene crystal have been detected by simultaneous observation of both their weak red phosphorescence as well as delayed blue fluorescence due to exciton-exciton annihilation.[73] While the free-free interaction, which follows bimolecular kinetic equations, is dominant at room temperature, interaction between free and shallowly trapped excitons is much more efficient in yielding delayed blue fluorescence at low temperature.[74] We have estimated the triplet exciton yield in the anthracene nanoaggregate to be about 0.14 ± 0.03 by using a method reported by Bachilo and Weisman (S4.4 in SD section).[75]

To understand the dynamics of the triplet exciton, we recorded the temporal profiles at 540 nm using different excitation intensities. Like in the case of the singlet exciton, we found strong intensity dependence of the temporal absorption profiles suggesting triplet – triplet exciton annihilation. These temporal profiles have also been analyzed following the mixed order decay scheme. Decay of the triplet excitonic state follows mainly two parallel processes: (1) natural radiative and / or nonradiative decay (Equation 4.16) and (2) triplet-triplet exciton annihilation reaction (Equation 4.17).

$$T_1 \xrightarrow{k_1(T)} S_0 \qquad (4.16)$$

$$T_1 + T_1 \xrightarrow{k_2(T)} S_n + S_0 \qquad (4.17)$$

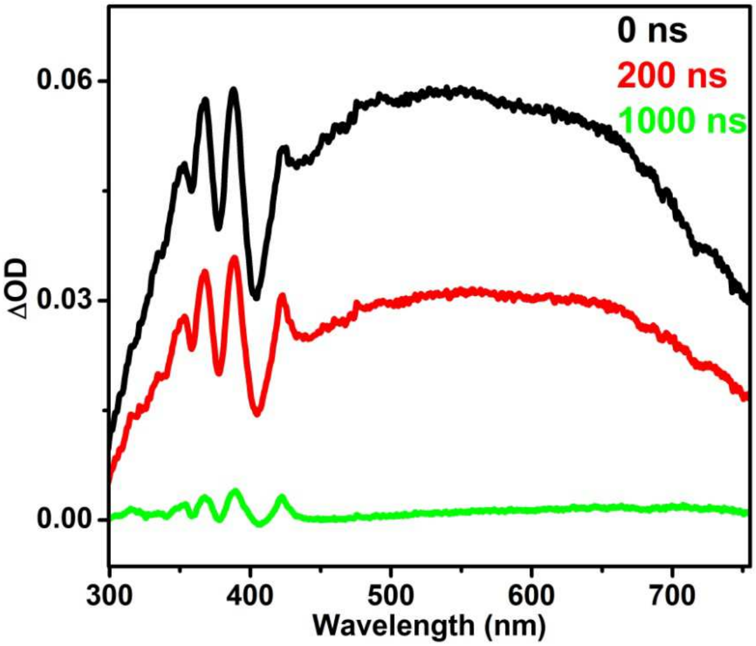

Figure 4.9: Time-resolved transient absorption spectra recorded at differrent delay times following photoexcitation of the anthracene nanoaggregate sample using 355 nm laser light of 10 ns duration.

Solving the kinetic equations corresponding to these two processes, we derive Equation 18, which represents the decay of the triplet excitons,

$$[\Delta \mathrm{OD}]_{ESA} = [\Delta \mathrm{OD}]_0 \, X \, \frac{[exp(-k_1'(T)t)]}{[1+k_2'(T)t]} \qquad (4.18)$$

Temporal profiles along with the best-fit functions following Equation 4.18 are shown in Figure 4.10 and the inset of this figure shows the plot of k_2' (T) vs. density of triplet exciton, $[T_1]_0$. Triplet – triplet exciton annihilation rate constant, k_2(T), thus estimated is 2.22 x 10^{-13} cm^3 s^{-1}. This value is smaller by nearly two orders of magnitude as compared to that estimated for the triplet exciton populated in anthracene crystal.[76, 77] The values of the annihilation radius and the diffusion coefficient for the triplet exciton could be estimated as 1.26 nm and 7.0 x 10^{-8} cm^2s^{-1}, respectively. The diffusion coefficient of the triplet exciton in the nanoaggreagte is thus smaller by two orders of magnitude as compared to that reported for the crystal (Table 4.5).[78] Smaller diffusion coefficient and shorter triplet exciton lifetime are the responsible factors for reduction of the diffusion length of the triplet exciton by about three orders of magnitude.[79]

Table 4.5: Comparison of the triplet - triplet exciton annihilation rate constant, k_2(T), diffusion coefficient and diffusion length of the triplet exciton in the solid crystal and the nanoaggregate.

System	**τ(T_1-exciton)**	**k_2(T) (cm^3 s^{-1})**	**D (cm^2 s^{-1})**	**L_d (nm)**
Solid Crystal[b]	40 ms	0.5-5 x 10^{-11}	5 – 50 x 10^{-6}	10000 - 20000
Nanoaggregate	1± 0.1 μs	2.2 ± 0.8 x 10^{-13}	7.0 ± 2 x10^{-8}	6.5 ± 2

[b] ref. 75 - 82

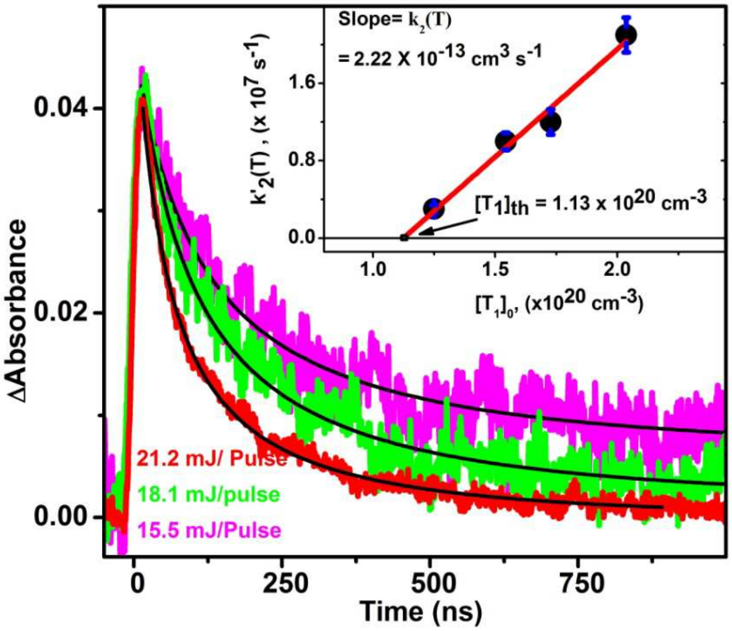

Figure 4.10: Temporal TA profiles, along with the best-fit functions, recorded at 544 nm following photoexcitation of the anthracene nanoaggregate by using different pump intensities. Inset diagram represents the estimated $k'_2(T)$ vs. $[T_1]_0$ plot.

In fact, similar to the singlet exciton, triplet exciton also may be trapped in defect sites and form the triplet excimeric state. There are a few reports available in the literature about the triplet exciton trapping in anthracene crystal.[83, 84] Arnold et. al. have artificially created crystal dislocation sites in anthracene crystal and trapped triplet excitons.[83] In another report, Goode et.al. reported population of the triplet excimeric state at imperfect crystal sites.[84] In nanoaggregates, due to imperfect molecular packing, presence of defect sites makes trapping of the triplet excitons highly probable and reduce the triplet exciton lifetime and exciton diffusion length. The broad excited absorption observe in the time resolved spectra for early time scale expected to have contribution from the excimer state also. Our nanosecond flash photolysis system has time resolution of 10 ns which may be considered quite long for the triplet exciton trapping process and therefore in the excited absorption band excimer state absorption is also quite expected.

More significant effect on the triplet exciton diffusion, as compared to that of the singlet exciton, can be explained on the basis of the mechanism associated with the triplet exciton diffusion. The triplet exciton diffusion occurs through electronic spin exchange mechanism, which is a slow process.[85]

4.3. CONCLUSION

The present work provides us a clear picture regarding the bulk solid like crystal structure of the anthracene nanoaggregate having significantly large concentration of defect sites. Anthracene nanoaggregates (NA) have been synthesized using well known reprecipitation method in the presence of PVA stabilizer. The DLS and AFM analyses reveal that the particles have shapes of nanodiscs with the average diameter and height of about 260 nm and 50 nm, respectively. Maxima of the 0 - 0 vibronic bands in the absorption and emission spectra of the NA are red-shifted by about 20 nm as compared to the corresponding one in the monomeric absorption and emission bands. Time-resolved emission study shows wavelength dependent dynamics, which originates from the distribution of particle size as well as the orientational heterogeneities in the aggregate leading to different types of defect sites and hence the excimeric states of different conformations. Transient absorption studies reveal nonexponential dynamics of both the singlet and triplet excitonic state due to exciton - exciton annihilation reaction at high excitation intensities. Exciton annihilation rate constants of the singlet and the triplet excitons have been determined as 3.7×10^{-9} cm^3 s^{-1} and 2.2×10^{-13} cm^3 s^{-1}, respectively and exciton diffusion lengths to be about 13.2 and 6.5 nm, respectively. The singlet exciton diffusion length is comparable to that of the anthracene crystal and this suggests that the nanoaggreagates may also be considered as materials for efficient optoelectronic and photovoltaic devices. However, drastic reduction in triplet exciton diffusion coefficient in the nanoaggregate form is explained considering slower triplet energy transfer mechanism via spin exchange.

4.4. REFERENCES

1. Liu, H.; Xu, J.; Li, Y. *Acc. Chem. Res*. **2010,** *43*, 1496
2. Cui, S.; Liu, H.; Gan, L.; Li, Y.; Zhu, D. *Adv. Mater* **2008,** *20*, 2918.
3. Palmer, L. C.; Stupp, S. I. *Acc. Chem. Res*. **2008,** *41*, 1674.
4. Bhongle, C. J.; Chang, C. W.; Lee, C. S.; Diau, E. W. G.; Shu, C. *J. Phys. Chem. B* **2005,** *109*, 13472.
5. Yao, H.; Yamashita, M.; Kimura, K. *Langmuir* **2009,** *25*, 1131.

6. Xiao, J.; Yang, H.; Yin, Z.; Guo, J.; Boey, F.; Zhang, H.; Zhang, Q. *J. Mater. Chem.* **201**1, *21*, 1423.
7. Xiao, D.; Xi, L.; Yang, W.; Fu, H.; Shuai, Z.; Fang, Y.; Yao, J. *J. Am. Chem. Soc.* **2003**, *125*, 6740.
8. Meng, H.; Sun, F.; Goldfinger, M. B.; Jaycox, G. D.; Li, Z.; Marshall, W. J.; Blackman, G. S. *J. Am. Chem. Soc***.** **2005,** *127*, 2406.
9. Meng, H.; Sun, F.; Goldfinger, M. B.; Gao, F.; Londono, D. J.; Marshall, W. J.; Blackman, G. S.; Dobbs, K. D.; Key, D. E. *J. Am. Chem. Soc*. **2006,** *128*, 9304.
10. Yu, J. Y.; Chen, I. W. P.; Chun-hsien Chen, C. H.; Lee, S. J.; Chen, I. C.; Lin, C. S.; Cheng, C. H. *J. Phys. Chem. C* **2008**, *112,* 3097.
11. Chao, Y. C.; Chung, C. H.; Zan, H. W.; Meng, H. F.; Ku, M. C. *Appl. Phys. Lett.* **2011,** *99*, 233308.
12. Liang, W. W.;Chang,C. Y.; Lai, Y. Y.; Cheng, S. W.; Chang, H. H.; Yin-Yu Lai, Y. Y.; Cheng, Y. J.; Wang, C. L.; Hsu, C. S. *Macromolecules* **2013**, *46,* 4781.
13. Zhao, Y. S.; Zhan, P.; Kim, J.; Sun, C.; Huang, J. *Acs Nano* **2010**, *4,* 1630.
14. Hinoue, T.; Shigenoi, Y.; Sugino, M.; Mizobe, Y.; Hisaki, I.; Miyata, M.; Tohnai, N. *Chem. Eur. J.* **2012**, *18,* 4634.
15. Latterini, L.; Roscini, C.; Carlotti, B.; Aloisi, G. G.; Elisei, F. *Phys. Stat. Sol.* ***A*** **2006**, *203*, 1470.
16. Chung, H. R.; Kwon, E.; Oikawa, H.; Kasai, H.; Nakanishi, H. *J. Crystal growth* **2006**, *294*, 459.
17. Seko, T.; Ogura, K.; Kawakami, Y.; Sugino, H.; Tanaka, J. *Chem. Phys. Lett.* 1998, *291*, 438.
18. Fujino, T.; Tahara, T. *J. Phys. Chem. B* **2003,** *107*, 5120.
19. Furube, A.; Murai, M.; Tamaki, Y.; Watanabe, S.; Katoh, R. *J. Phys. Chem. A* **2006,** *110*, 6465.
20. Yago, T.; Tamaki, Y.; Furube, A.; Katoh, R. *Phys. Chem. Chem. Phys*. **2008,** *10*, 4435.
21. Burdett, J. J.; Müller, A. M.; Gosztola, D.; Bardeen, C. J. *J. Chem. Phys.* 2010, *133*, 144506.
22. Briseno, A. L.; Aizenber, J.; Han, Y. J.; Penkada, R. A.; Moon, H.; Lovinger, A. J.; Kloc, C.; Bao, Z. *J. Am. Chem. Soc*. **2005,** *127*, 12164.

23. Dutta, A. K. *Langmuir* **1997,** *13*, 5678.

24. Clark, L. B.; Philpott, M. R. *J. Chem. Phys* **1970,** *53*, 3790.

25. Fedotov, V. A.; Marinov, K.; Boardman, A. D.; Zheludev, N. I. *New Journal of Phys*. **2007,** *9*, 95.

26. Meyer, Y. H.; Astier, R.; Leclerq, J. M. *J. Chem. Phys*. **1972,** *56*, 801.

27. Katoh, R.; Susuki, K.; Furube, A.; Kotani, M.; Tokumaru, K. *J. Phys. Chem. C.* **2009,** *113*, 2961.

28. Garnett, E.; Yang, P. *Nano. Lett*. **2010,** *10*, 1082.

29. Gabor, N. M.; Zhong, Z.; Bosnick, K.; Park, J.; Mceuen, P. L. *Science* **2009**, *325*, 1367.

30. Takahasi, Y.; Tomura, M. *J. Phys. Soc. Jpn*. **1971,** *31*, 1100.

31. Seefeld, K. P.; Muller, H.; Bassler, H. *J. Lumin.* **1978**, *16*, 395.

32. Galanin, M. D.; Khan-Magometova, S. D.; Chizhikova, Z. A.; Demchuk, M. I.; Chernyavskii, A. F. *J. Lumin*. **1975**, *9*, 459.

33. Horiguchi, R.; Iwasaki, N.; Maruyama. Y. *J. Phys. Chem.***1987,** *91*, 5135.

34. Oliveira, D.; Baba, K.; Teizer, W.; Kasai, H.; Oikawa, H.; Nakanishi, H. *Nanocrystal, Intech*, **2011.**

35. Kakade, S.; Ghosh, R.; Palit, D. K. *J. Phys. Chem. C* **2012**, *116*, 15155.

36. Wu, J. H.; Xu, T. Z.; Ang, S. G.; Xu, G. Q. *Nanoscale* **2011**, *3*, 1855.

37. Liu, H.; Li, Y.; Xiao, S.; Gan, H.; Jiu, T.; Li, H.; Lei, J.; Zhu, D.; Yu, D.; Xiang, B.; Chen, Y. *J. Am. Chem. Soc***.** **200**3, *125*, 10794.

38. Zhao, M.; Wang, S.; Bao, Q.; Wang, Y.; Aug, P. K.; Loh, K. P. *Chem. Commun.* **2011,** 47, 4153.

39. Madhurambal, G.; Srinivasan, P. A. *Cryst. Res. Technol* **2006**, *41*, 231.

40. DeHaven, S.; Wincheski, R.; Albin, S. *Materials* **2014,** *7*, 6291.

41. Philpott, M. R. *J. Chem. Phys.* **1969**, *50*, 5117.

42. Köhler, A.; Bässler, H. *Material Science and Engineering R*. **2009**, *66*, 71.

43. Kellogg, R. E. *J. Chem. Phys.***1966**, *44*, 411.

44. Mulder, B. J. *J. Phys. Chem. Sol.* **1968**, *29*, 182.

45. Nishimura, H.; Yamaoka, T.; Hattori, K.; Matsui, A. Mizuno, K. *J. Phys. Soc. Jpn*. **1985**, *54*, 4370.

46. Kalinowski, J. *Materials Science-Poland.* **2009,** *27*, 735.

47. Kalinowski, J.; Giro, G.; Cocchi, M.; Fattori, V.; Zamboni, R. *Chem. Phys.* **2002**, *277*, 387.
48. Bateman, R. J.; Chance, R. R.; Hornig, J. F. *Chem. Phys.* **1974**, *4*, 402.
49. Nishimura, H. *J. Phys. Colloq.* **1985**, *46(C7)*, C7-55.
50. Nozue, Y.; Goto, T. *J. Phys. Soc. Jpn.* **1989**, *58*, 1831.
51. Shimura, H.; Ohba, Y. Jpn. *J. Appl. Phys.* **1981**, *20*, 1683.
52. Birks, J. B. *Mol. Cryst. Liq. Cryst.* **1973**, *28*, 117.
53. Nozue, Y. *J. Phys. Soc. Jpn.* **1988**, *57*, 3204.
54. Kobayaschi, M.; Mizuno, K.; Matsui, A. *J. Phys. Soc. Jpn.***1989**, *58*, 809.
55. Breton, G. W.; Vang, X. *J. Chem. Educ*. **1998**, *75*, 81.
56. Jones, P. F.; Nicol, M. *J. Chem. Phys.* **1968,** *48*, 5440.
57. Dreger, Z. A.; Balasubramaniam, E.; Gupta, Y. M.; Joly, A. G. *J. Phys. Chem. A.* **2009,** *113*, 1489.
58. Hofmann, J.; Seefeld, K. P.; Hofberger, W.; Bässler, H. *Molecular Physics*. **1979**, *3*7, 973.
59. Fielding, P. E.; Jarnagin, R. C. *J. Chem. Phys.* **1967**, *47*, 247.
60. Mataga, N.; Torihashi, Y.; Ota, Y. *Chem. Phys. Lett.* **1967,** *1*, 385.
61. Dreger, Z. A.; Lucas, H.; Gupta, Y. M. *J. Phys. Chem. B* **2003,***107*, 9268.
62. Koti, A. S. R.; Krishna, M. M. G.; Periasamy, N. *J. Phys. Chem. A* **2001**, *105*, 1767.
63. Koti, A. S. R.: Periasamy, N. *Res. Chem. Intermed.* **2002**, *28*, 831.
64. Paillotin, G.; Swenberg, C. E.; Breton, J.; Geacintov, N. E. *Biophys. J.* **1979,** *25*, 513.
65. Katoh, R.; Kotani, M. *J. Chem. Phys.* **1991,** *94*, 5954.
66. Pope, M.; Swenberg, C. E. Electronic Processes in Organic Crystals and Polymers, Oxford University Press, New York, 2ndedn, **1999**.
67. Schwoerer, M.; Wolf, H. C. Organic Molecular Solids, Wiley-VCH Verlag Gmbh & Co. KGaA, Weinheim, **2007**.
68. Jasny, J.; Sepiol, J. *J. Phys. E: Sci. Instrum.*, *1981*, *14*, 493.
69. Cohen, M. D.; Klein, E.; Ludmer, Z. *Chem. Phys. Lett.***1976**, *37*, 611.
70. Meth, J. S.; Marshall, C. D.; Fayer, M. D. *Solid State Comm.* **1990,** *74*, 281.
71. Donati, D.; Williams, J. O. *Mol. Cryst. Liq. Cryst.* **1978**, *44*, 23.

72. Windsor, M. W.; Dawson, W. R. *Molecular Crystal*. **1968**, *4*, *253.*

73. Smith, G. C. *Phys. Rev.* **1968**, *166*, 839.

74. Babenko, S. D.; Benderskii, V. A.; Goldanskii, V. I.; Lavrushko, A. G. Tychinskii, V. P. *Physica Status Solidi (b)* **1971**, *45*, 91.

75. Bachilo, *S.* M**.**; *We*isman, R. B. *J. Phys. Chem. A* **2000**, *104*, 7111.

76. Kostin, A. K.; Vannikov, A. V. *Radial. Phys. Chem*. **1980**, *15*, 613.

77. Avakian, P.; Merrifield, R. E. *Molecular Crystal*. **1968**, *5*, 37.

78. Swenberg, C. E. *J. Chem. Phys.* **1969**. *51*, 1753.

79. Drew, M.; Williams, D. F. *J. Chem. Phys.***1971**, *54*, 1844.

80. Avakian, P.; Merrifield, R. E. *Phys. Rev. Lett.***1964**, *13*, 541.

81. Moore, G. F. *Nature* **1966**, *211*, 1170.

82. Schwoerer, M.; Wolf, H. C. Organic Molecular Solids, Wiley-VCH Verlay GmbH & Co. KGaA, Weinheim, **2007**.

83. Arnold, S.; Whitten, W. B.; Damask, A. C. *J. Chem. Phys.* **1970**, *53*, 2878.

84. Goode, D.; Lupien, Y.; Siebrand, W.; Williams, D. F.; Thomas, J. M. and Williams, J. O. *Chem. Phys. Lett.* **1974**, *25*, 308.

85. Yost, S. R.; Hontz, E.; Yeganeh, S. and Voorhis, T. V. *J. Phys. Chem. C*. **2012**, *116*, 17369

CHAPTER 5

DIFFUSION CONTROLLED ENERGY TRANSFER PROCESS IN DOPED ANTHRACENE NANOAGGREGATES: MULTIPLE DOPING LEADS TO EFFICIENT WHITE LIGHT EMISSION

5.1. INTRODUCTION

Organic electronic materials have become great competitor for the inorganic counterpart in recent years. Organic molecules showing potential applications in display devices, sensors, organic solar cells and many other optoelectronic devices, have been widely studied.[1-5] This large range of applications need understanding of the fundamental processes associated with the operation of organic electronic devices as well as the basic photophysical properties of the materials. Organic materials are normally used in the form of thin layers (or films) having thickness in the nanometer range. Nanoaggregates (NA) of a large number of organic molecules have also been synthesized in the last few decades[6-20] and potentiality of their applications in electronic devices has been explored.[18-21] Polycyclic aromatic hydrocarbons are π-electron conjugated systems and possess low energy gap between HOMO and LUMO levels, which correspond to the near UV and visible region. Therefore, they are suitable for optoelectronic applications. High emission quantum yield of these materials make them also suitable for display and LED applications.[1]

Doped organic and inorganic nanomaterials have been well known for differently colour-tuned emission.[22 - 24] Following transfer of excitation energy from the host molecule to the guest molecule, emission of light takes place from the guest molecule. Since these two molecules emit different colours, it is possible to tune the colour of the emitted light just by varying the doping percentage as well as the guest molecule. Excited singlet state of anthracene molecule (see Scheme 5.1 for the molecular structure) emits in the blue region (i.e. in the 370 - 480 nm region) in solution phase. However, in nanoparticle form, the entire emission band is red-shifted by about 20 nm and the singlet anthracene exciton emits in the blue-violet region.[14, 25, 26] Easy synthesis route and possibilities of generation of multiple colours with better emission yields through doping in nanoaggregates, motivated us to take up the present work. However, while the emission yield of anthracene in solution phase is around 0.36, it reduces to 0.17 ± 0.02 in the case of nanoaggregates.[26-28]

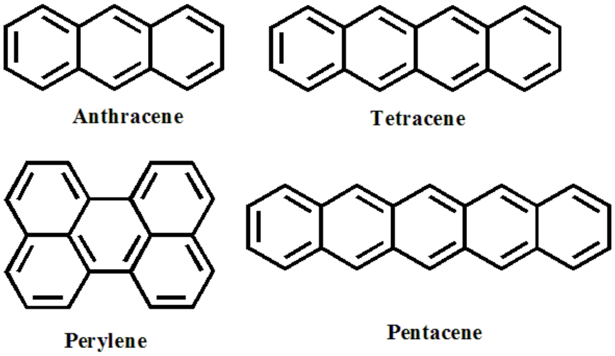

Scheme 5.1: Molecular structures of the aromatic hydrocarbons used in this work.

Perylene is a well known polycyclic compound having high emission yield in solution phase (~0.9).[27] The absorption band of perylene appears in the 380 - 430 nm region, which makes it a suitable material for fluorescence resonance energy transfer (FRET) from anthracene. Therefore we have chosen perylene as one of our dopants. Tetracene is chosen as another dopant, which is also a polycyclic compound having one extra conjugated benzene ring as compared to the anthracene molecule. The structural similarities between them help us to accommodate tetracene molecule easily in the anthracene nanoaggregate. It also absorbs light in the 400 to 470 nm region and acts as a highly efficient acceptor in the FRET from anthracene.[29] Pentacene consists of five conjugated benzene rings with the linear arrangement and has absorption band extended in the region of 400 to 500 nm.[29] Therefore, it also promises to be a suitable material for FRET from anthracene in the nanoaggregate. Although pentacene undergoes photo-oxidation in solution posing a limitation for its application in solution phase,[30] in solid form, pentacene is quite stable to photo-oxidation and hence expected to be a suitable dopant for the FRET process while embedded in the anthracene nanoaggregate matrix.[31] Since the host and three dopant molecules emit at different wavelength regions of the visible spectrum, multiple or combined doping of these three materials and proper tuning of concentration ratio may provide the potentiality to generate white light emission from the nanoaggregate samples. White light emitting materials have wide scale applications in display systems and LEDs and hence these materials have drawn huge research interest in recent years.[32-36] The low cost and easy availability of the above-mentioned host and dopant materials may make these nanoaggregates useful material for OLEDs and display systems. Herein, we report syntheses of doped anthracene nanoaggregates, and energy transfer (ET) processes from the anthracene excitonic state to the acceptor molecules, namely, perylene, tetracene and pentacene. Efficient ET processes in the anthracene nanoaggregate doped with all three acceptor molecules in proper proportion ensure the possibility of development of a strong white light source with pumping by using near UV light.

5.2. RESULTS AND DISCUSSION

5.2.1. Morphological Characterization: Size and shape of the nanomaterials have always been of primary concern prior to their use in any application. We have used DLS and AFM techniques as a part of the morphological analysis of the nanoaggregates. DLS measurements reveal that the average sizes of the undoped and doped nanoaggregates are comparable and they are distributed in the range of 260 - 320 nm. Figure 5.1A presents the DLS data collected for perylene doped anthracene (PeAn) nanoaggregates. AFM imaging data also supports that the diameter of these nanoaggregates are distributed in the 200 - 400 nm range. However, the shapes of these nanoaggregates are not completely spherical and the average height of the nanoaggregates is around 35 ± 10 nm. Results of the measurements with anthracene nanoaggregate doped with tetracene, pentacene or all three dopants simultaneously (we describe them as TeAn, PnAn or MAn, respectively) are given in the SD section (Figure S5.1). Table 5.1 reveals that the average diameter of anthracene nanoaggregate decreases with decrease in the size of the dopant, i.e. the order of the average diameter is: An < TeAn < PnAn < PeAn. This possibly can be explained by the better compatibility of the sizes of the host and the dopant molecules.

Table 5.1: Average diameters and heights of the nanoaggregate samples used in this study.

Nanoaggregate System	Average Diameter (nm)	Average Height (nm)
An	260 ± 25	50 ± 10
PeAn	285 ± 25	35 ± 10
TeAn	265 ± 25	28 ± 10
PnAn	280 ± 25	40 ± 10
Man	330 ± 25	40 ± 10

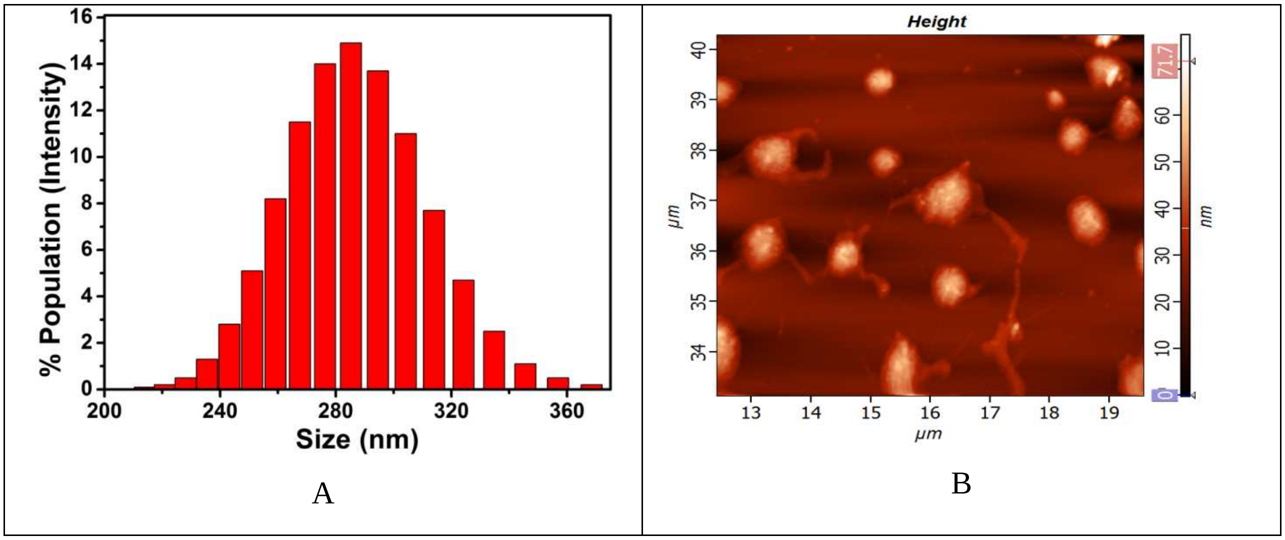

A

B

Figure 5.1: (A) Size distribution estimated using DLS technique and (B) AFM image of PeAn.

5.2.2. Steady State Absorption Measurements: Steady state UV-visible absorption spectrum provides us direct information about the band gap of the nanomaterials. Absorption spectrum of anthracene nanoaggregate is found to consist of vibrational progressions, which are similar to those known to be the prominent features of the absorption spectrum of the molecule in solution (Figure 5.2).[26] However, the maximum of the vibronic band corresponding to the 0 – 0 transition is red-shifted by about 20 nm in the nanoaggregate as compared to that of anthracene molecule in solution. In the case of PeAn nanoaggregate, no significant change in the absorption spectra of the nanoaggregates with varying concentration of the dopant up to about 1% (which corresponds to the dopant concentration of 4.8×10^{-2} mol. dm^{-3}), could be observed (Figure 5.2). Method of calculation of the dopant concentration in anthracene nanoaggregate is given in the SD section (S5.2). When the doping percentage is increased beyond 1%, the absorption due to the dopant material gradually becomes evident. In our study, we have used less than 1% doping concentration in most of the experiments and hence we may consider that the major amount of the incident light is absorbed by the host molecule (i.e. anthracene). In Figure 5.2, we have also compared the absorption spectra of perylene in THF and nanoaggregate of perylene only. The absorption spectrum of perylene nanoaggregate is, however, broader with the loss of fine structures of the vibronic bands, which are the characteristics of the spectrum recorded in solution. The maximum of the absorption spectrum of perylene nanoaggregate is also shifted to higher energy region. These are typical characteristics of H-aggregates (vide infra). Absorption spectra of the anthracene nanoaggregates doped with varying concentrations of tetracene and pentacene are also monitored and the absorption spectra found to show the absorption features of the host only (i.e. anthracene) (S5.3 in SD section).

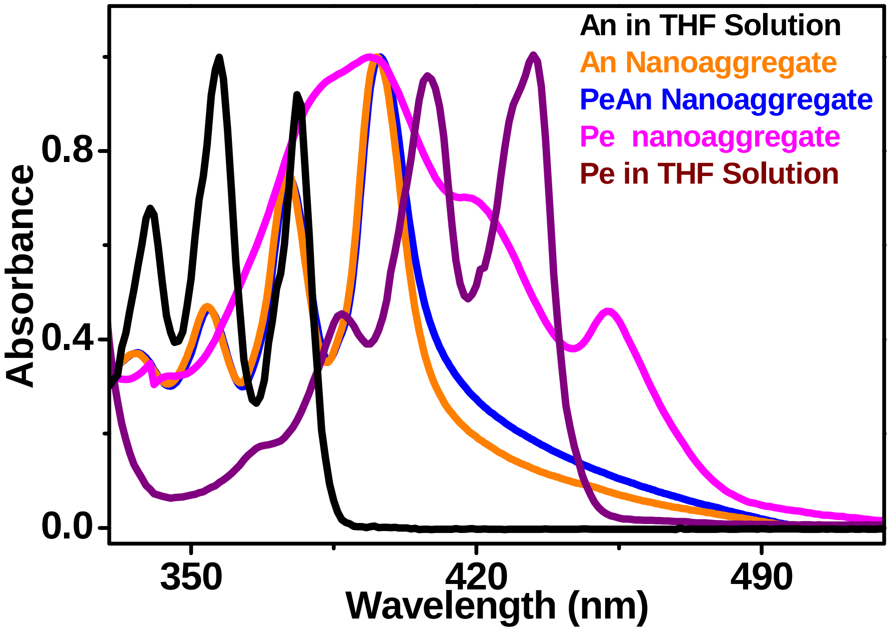

Figure 5.2: Normalized steady state absorption spectra of anthracene (An) in THF solution, An nanoaggregate, Perylene (Pe) doped An nanoaggregate with doping concentration of 4.8 x 10^{-3} mol dm^{-3}, Pe in THF solution and Pe nanoaggregate.

5.2.3. Steady State Emission Measurements: Following photoexcitation by using 355 nm light, we have recorded the emission spectra of anthracene and perylene in THF solutions as well as undoped or pure anthracene and perylene nanoaggregates (Figure 5.3). We observe that, in the emission spectrum of the undoped anthracene nanoaggregate, the vibronic band corresponding to the 0 - 0 transition occurring in the emission spectra of anthracene molecule in solution is missing.[26] In the case of pure perylene nanoaggregate, we observe an emission band, although very week, in the 500 – 700 nm region with the maximum at ca 580 nm (Figure 5.3C). This weak but broad emission band of perylene nanoaggregate may be assigned to perylene excimer. Very weak perylene excimer emission in solution has been reported earlier.[37] In the case of anthracene nanoaggregate, excimer band is extremely week and appears only as a long tail in the lower energy region of the emission spectrum.[26] In perylene nanoaggregates, the arrangement of the molecules is possibly quite similar to that in the α-crystalline form of perylene. Here the perylene molecules form dimers, in which the relative distance between the molecular planes is <0.4 nm, because of which excimer formation becomes facile. H-aggregate kind of association of perylene molecules has been evident in the absorption spectrum of perylene nanoaggregate (Figure 5.2). On the other hand, anthracene molecules exist mainly in β form. In this arrangement, the relative distances between molecular planes are > 0.4 nm, because of which interaction between two adjacent molecules are not so strong to form the excimeric state. In anthracene nanoaggregates, the dimeric forms may exist only at defect sites and hence only weak emission from the excimeric state is observed.[26]

In Figure 5.3, we have also shown the emission spectrum of the PeAn nanoaggrgate with 0.01% doping of perylene. We observe that intensity of emission from perylene exciton in the PeAn nanoaggregate is quite significant even with 0.01% doping because of very efficient ET from the singlet excitonic state of anthracene to perylene molecule to populate the perylene excitonic state (vide infra for quantitative measurements of efficiency of ET process). It is also important to observe that each of the vibrational progressions in the emission spectrum of perylene exciton in the nanoaggregate is also red-shifted by about 9 nm as compared to those in solution.

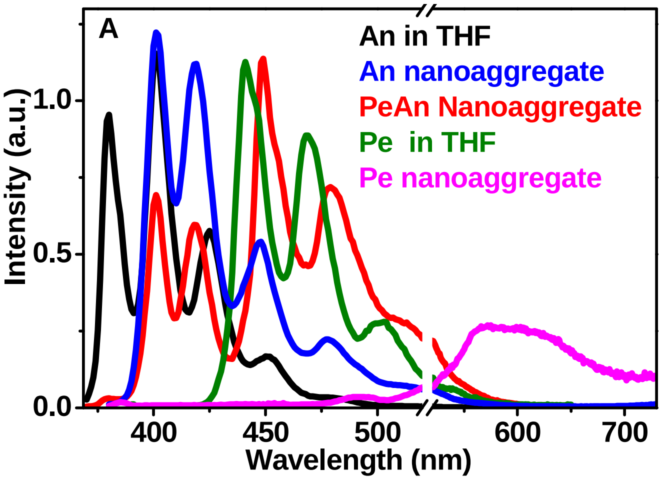

Figure 5.3: Steady state fluorescence spectra of anthracene (An) (2 x 10^{-6} mol dm^{-3}) and perylene (Pe) (1 x 10^{-6} mol dm^{-3}) in THF as well as undoped An and Pe nanoaggregate samples dispersed in water. In addition, this figure also shows the emission spectrum of PeAn nanoaggregate with 0.01% doping (concentration 4.8 x 10^{-4} mol dm^{-3}) of Pe. Excitation wavelength is 355 nm.

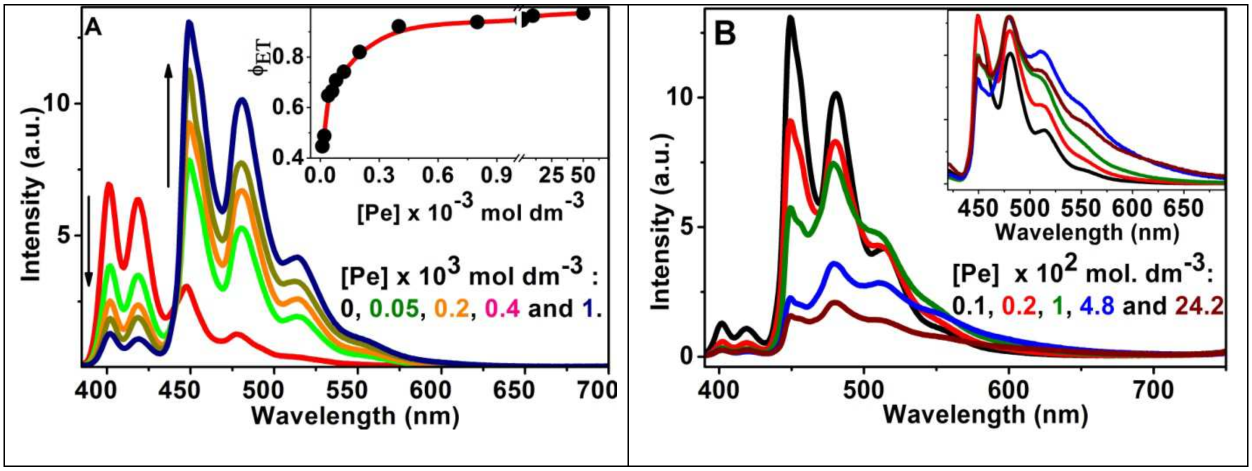

Figure 5.4: **(A)** Fluorescence spectra for An nanoaggregate and PeAn nanoaggregate samples having dopant concentrations up to 1 x 10^{-3} mol. dm^{-3} and **(B)** the samples with dopant concentrations varying from 0.1 to 24.2 x 10^{-2} mol. dm^{-3}. **Inset of A**: Plot of energy transfer efficiency (ϕ_{ET}) vs. dopant concentration. **Inset of B**: Emission spectra normalized at the maximum intensity.

Figures 5.4 (A and B) show the emission spectra of both the undoped and differently doped PeAn nanoaggregates. We observe that intensity of emission in the 390 - 430 nm region, which is assigned to the singlet excitonic state of anthracene, decreases and that due to the singlet excitonic state of perylene increases concomitantly in the 440 - 640 nm region with increase in concentration of the dopant (Figure 5.4A). However, on further increase in concentration of the dopant beyond 1 x 10^{-3} mol. dm^{-3}, the emission intensity starts decreasing (Figure 5.4B). Further, at this range of dopant concentration, we observe a gradual increase in emission intensity in the 500 - 700 nm region with increase in dopant concentration. Evolution of the emission spectra at higher concentrations of the dopant (>1 x 10^{-3} mol. dm^{-3}) in PeAN nanoaggregate may be assigned to formation of perylene excimer and / or anthracene - perylene exciplex.[38, 39] We expect a significant contribution of anthracene – perylene exciplex state to the emission enhancement observed in the wavelength region above 500 nm (inset of Figure 5.4B).

Efficiency of ET, $\Phi_{ET}(SS)$, from the singlet excitonic state of anthracene to perylene molecule has been estimated using equation 5.1.

$$\Phi_{ET}(SS) = 1 - \left(\frac{I_{DA}}{I_D}\right) \qquad (5.1)$$

Here I_D and I_{DA} are the steady state (SS) emission intensities measured for the undoped and doped nanoaggregates, respectively, at a particular wavelength. We have measured these parameters at 400 nm, since contribution of acceptor emission at this wavelength is nearly negligible (Figure 5.4A). The plot of Φ_{ET}(SS) vs. dopant concentration has been shown in the inset of this figure. We observe that the Φ_{ET}(SS) value increases sharply with increase in dopant concentration up to about 2 x 10^{-3} mol. dm^{-3}, but with further increase in dopant concentration, Φ_{ET}(SS) value increases only marginally. We estimated that in PeAn nanoaggregate, transfer of about 97% of the excitation energy of the donor to the acceptor could be achieved with perylene concentration larger than 5 x 10^{-3} mol dm^{-3}.

Table 5.2: Maximum quantum yield of emission, ϕ_F(max), the corresponding dopant concentration and maximum ET efficiency, ϕ_{ET}(max), achieved for undoped and doped nanoaggregate samples and the rates of ET process, i.e. k_{ET} (SS) and k_{ET}(TR), determined using steady state and time resolved emission techniques, respectively. k_{ET} (Förster) is the rate of ET process calculated assuming Förster mechanism.

NA	ϕ_F(max)	[Dopant] (10^{-3} mol dm^{-3})	ϕ_{ET}(max)	k_{ET} (10^{11} dm^3 $mol^{-1}s^{-1}$)		
				k_{ET}(SS)	k_{ET} (TR)	k_{ET} (Förster)[c]
An	0.17	-	-			
PeAn	0.36	1	98	6.21	6.22[a] (5.3)[b]	3.8
TeAn	0.29	48	99	3.80	4.01 [a] (4.91) [b]	0.98
PnAn	0.17	0	92	3.38	2.0[a] (4.38) [b]	0.55
MAn[d]	0.46	-	-		-	

[a]Results from TCSPC measurements; [b]Results from fluorescence upconversion measurements; [c]See section 5.3.6; [d]Quartenary nanoaggregate (i.e. anththracene nanoaggregate doped with Pe, Te and Pn), see section 5.3.7 for optimum composition.

Steady state emission studies have also been carried out for TeAn and PnAn nanoaggregate samples. Results of these experiments are provided in the SD section (Figures S5.4). In each of these cases, reduction of emission intensity of the donor and concomitant increase in the emission intensity of the acceptor with increase in dopant concentration ensures occurrence of the ET process. In the case of TeAn nanoaggregate, emission of the excitonic state of tetracene occurs in the 500 - 580 nm region. On the other hand, for PnAn nanoaggregate, acceptor emission appears in the 590 - 680 nm region. Like in the case of PeAn nanoaggregate, positions of the emission bands of the excitonic states of tetracene and pentacene in doped anthracene nanoaggregates are red shifted as compared to those in the emission spectra of these molecules in solution phase. These observations justify the prediction about strong intermolecular interaction leading to modulation of the HOMO - LUMO energy levels of both the donor and acceptor molecules in the nanoaggregate matrix.

Like in the case of PeAn nanoaggregate, ET efficiencies in other two cases too are large and show similar kind of dependence on concentration of the dopant, i.e. efficiency increases sharply with increase in concentration of the dopant up to about 2 x 10^{-2} mol. dm^{-3} and attains a limiting value for the dopant concentration larger than this (Figures S5.4). In TeAn nanoaggregate, ET efficiency of about 98% is achievable. However, in the case of pentacene, due to extended π conjugation, the absorption band is further red shifted and the overlap between the donor emission and acceptor absorption spectra is poorer. In this case, maximum ET efficiency could be achieved is about 92% with the dopant concentration of about 1 x 10^{-2} mol dm^{-3}, which is limited by the solubility of pentacene in THF (the good solvent).

We have determined the dependence of the emission yield on the concentrations of the dopant in the binary nanoaggregates (Figure S5.5 in SD section) and the maximum quantum yield and the dopant concentration(s), at which the emission yield is maximum, in the case of each of the binary (or quarternary) nanoaggregates, are given in Table 5.2. In the case of PeAn nanoaggregate, the emission yield increases up to the dopant concentration of about 1 x 10^{-3} mol dm^{-3}, above which the emission yield decreases sharply with increase in concentration of the dopant. Considering that the value of fluorescence quantum yield of perylene in cyclohexane and Pe nanoaggregate are 0.94 and 0.03, it becomes obvious that initial increase of emission intensity with increase in dopant concentration up to 1 x 10^{-3} mol dm^{-3} may be assigned to larger yield of emission of Pe exciton but increasing Pe concentration leads to formation of excimer or exciplex resulting reduction of overall emission yield. The fluorescence yields of tetracene and pentacene in THF have been measured here are 0.31 ± 0.04 and 0.03 ± 0.01, respectively, and those for tetracene and pentacene nanoaggregates are 0.005 and 0.003, respectively. Very low emission yield in these nanoaggregates may be explained due to occurrence of singlet fission process.[40-43] In the case of TeAn, the emission yield continues to increase up to 0.29 corresponding to the dopant concentration of about 4.8 x 10^{-2} mol dm^{-3}, beyond which the emission yield decreases due to the possibility of decay of singlet excitonic state of tetracene through singlet exciton fission process.

However, in the case of PnAn, the emission quantum yield decreases monotonously with increase in concentration of the dopant because the emission yields of both the excited state of the monomeric form as well as the excitonic state populated in the nanoaggrgate form are lower than that of the excitonic state of anthracene in the nanoaggregate.

In order to understand the mechanism of the ET processes, we determined the rates of these processes using both steady state and time-resolved quenching experiments. Steady state Stern-Volmer (S-V) plot (equation 5.2) for quenching of anthracene exciton emission by perylene molecule in PeAn nanoggregate has been shown in Figure 5.5A.[44] The S-V plots for other two cases have been provided in the SD section (Figure S5.6). In all these cases, we find that the S-V plot for the steady state quenching of anthracene exciton emission by the dopant (acceptor) molecules (equation 5.2, in which [A] is the concentration of the acceptor) is linear only in the low concentration range (e.g. in the case of PeAn nanoaggregate, up to about 2×10^{-3} mol. dm^{-3} of perylene). Rate constants, k_{ET}(SS), for the ET processes have been determined from the slope of the best fit line (taking care of the points in the region of low acceptor concentration only) and the values are given in Table 5.2. In equation 5.2, we have used the average lifetime of anthracene exciton emission ($<\tau_D> \sim 3.4$ ns) estimated from the time resolved fluorescence study (Table 5.3) to estimate the values of k_{ET}(SS). Figure 5.5A and Figure S5.6 in SD section reveal that, at higher concentrations of the dopants, S-V plots show negative deviation from the linearity. This observation has been explained in section 5.3.5.

$$\left(\frac{I_D}{I_{DA}}\right) = 1 + k_{SV}(SS)\,[A] = 1 + k_{ET}(SS) < \tau_D > [A] \qquad (5.2)$$

5.2.4. Time Resolved Emission Measurements: Measurements of the decay of the donor exciton emission intensity and concomitant rise of that of the acceptor provide us the direct evidence for the energy transfer process. In Figure 5.6, we have presented the results of the TCSPC measurements in the case of undoped and perylene - doped anthracene nanoaggregate samples following photo-excitation at 374 nm. We have measured the time evolution of anthracene exciton emission at 400 nm and that of the acceptor at 480 nm. We observe that both decay of anthracene exciton emission and rise of perylene exciton emission signals become faster with increase in dopant concentration. This ensures the bimolecular energy transfer process from the donor to the acceptor. The temporal profiles could only be fitted using multi-exponential functions and the results of the analyses have been provided in Table S5.7 in SD section. Multi-exponential nature of the decay of exciton emission in undoped anthracene nanoaggregate can be explained by assuming different kinds of environments around excitons as well as exciton – exciton annihilation process (vide infra).[26] In addition, multi-exponentiality of the decay profile of the anthracene exciton and also the time evolution of the perylene exciton emission may arise due to the same reason. Results of time resolved emission measurements for TeAn and PnAn nanoaggregates are also analysed in the same procedure (S5.8 in SD section).

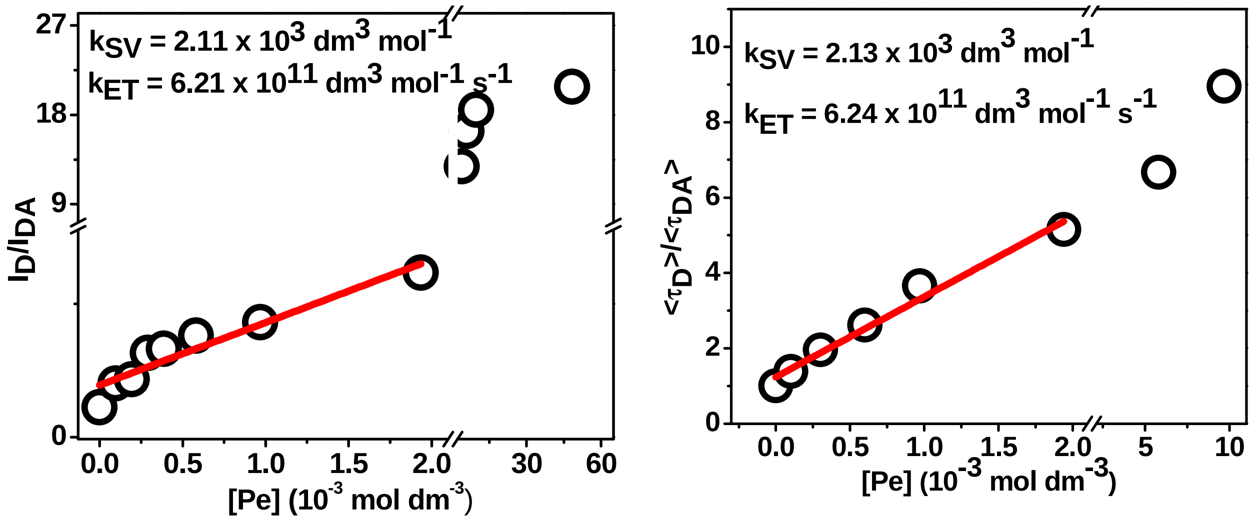

Figure 5.5: Stern-Volmer plots for perylene doped anthracene nanoaggregates using (A) steady state and (B) time resolved emission measurements.

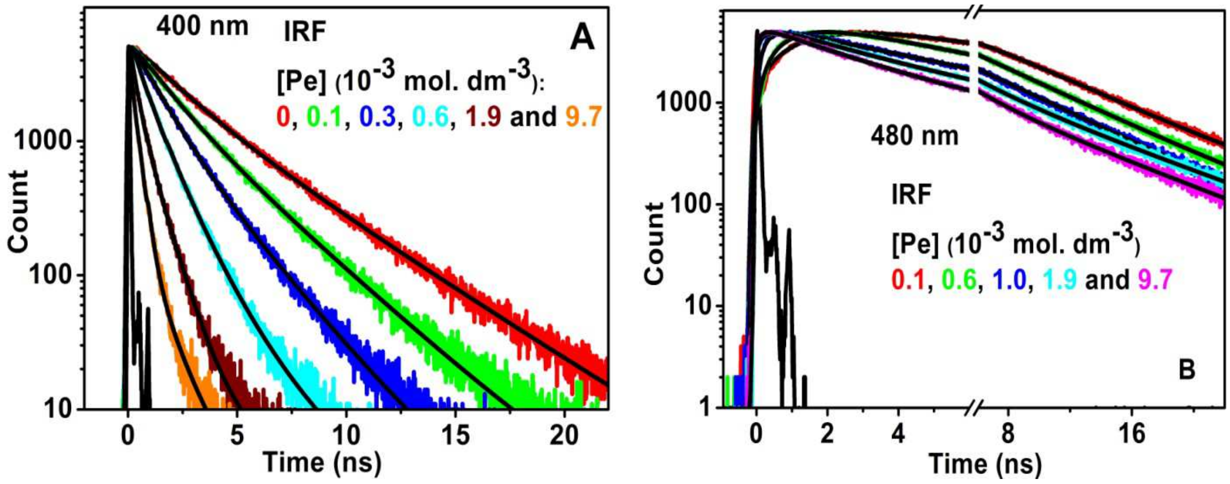

Figure 5.6: Temporal profiles recorded following photoexcitation of the undoped anthracene and differently doped PeAn nanoaggregate samples at 374 nm.

The average lifetimes have been used to estimate the rate constant of the ET process, k_{ET}(TR), using the S-V equation (equation 5.3), in which $<\tau_D>$ and $<\tau_{DA}>$ are the average lifetimes of the donor exciton in undoped and doped samples, respectively. The average lifetimes estimated from the fitting of the temporal profiles recorded at 400 nm in Table S5.9 in SD section. S-V plot for the PeAn nanoaggregate using time-resolved emission data is given in Figure 5.5B and those for TeAn and PnAn nanoaggregates in Figure S5.10 in SD section.

$$\left(\frac{<\tau_D>}{<\tau_{DA}>}\right) = 1 + k_{SV}(TR)\,[A] = 1 + k_{ET}(TR) < \tau_D > [A] \qquad (5.3)$$

Values of k_{ET}(TR) thus determined for three doped nanoaggregates have been provided in Table 5.2 and we find that the k_{ET}(TR) and k_{ET}(SS) values are comparable. Like in the case of steady state emission data, the S-V plot constructed from the time-resolved data also deviate from the liner relationship at the higher concentration range of the dopant. Good agreement between the values of k_{ET}(TR) and k_{ET}(SS) determined in the lower concentration regime (<1 x 10^{-2} mol dm^{-3}) also suggest that the excitonic interaction via the ET process is really the dynamic one.

ET efficiencies, ϕ_{ET}(TR), have also been estimated by using equation 5.4. The fluorescence quenching efficiencies of the donor emission or ϕ_{ET}(TR) for PeAn, TeAn and PnAn nanoaggregates are given in Table S5.9 (SD section). We find a similar trend of ϕ_{ET}(TR) values as those estimated from the steady state analysis .

$$\Phi_{ET}(TR) = 1 - \left(\frac{<\tau_{DA}>}{<\tau_D>}\right) \qquad (5.4)$$

We also made attempts to study the ET processes from the S_1 state of anthracene to three aromatic molecules, which have been used here as dopants in anthracene nanoaggregates, in the solution phase. However, since the absorption bands of anthracene and the acceptors are overlapping in the 320 – 420 nm, the steady state quenching experiments did not yield any meaningful results. In quenching experiments, increase in fluorescence intensity of the acceptor could be observed with increasing concentration of the acceptor due to direct excitation of the acceptor and hence quantitative estimation of the efficiency of the ET process was not possible. Therefore, we adopted the time resolved emission technique to investigate the ET processes in solution phase. The lifetimes of anthracene fluorescence in THF were measured in absence and presence of different concentrations of the quencher and the rate of quenching due to ET process was determined using S-V method. In the case of anthracene – perylene pair in THF, the S-V plot was linear through the entire range of concentration of perylene used in the experiment and the ET rate thus determined (1.6 x 10^{10} dm^3 mol^{-1} s^{-1}) was seen to be diffusion controlled in THF (Figure S5.11 in SD section). However, in the cases of other two donor – acceptor pairs, namely anthracene – tetracene and anthracene – pentacene, in THF solution, quenching of the lifetime of anthracene fluorescence was observed to be nearly negligible even up to the highest concentration of the acceptor, which could be achieved within the limit of solubility of the acceptor in this solvent (Figure S5.12 in SD section). k_{ET} values thus determined are 8.4 x 10^9 s^{-1} and 2.5 x 10^9 s^{-1} for the anthracene – tetracene and anthracene – pentacene pairs, respectively. These rates are slower by about two orders of magnitude as compared to those in doped anthracene nanoaggrgates and by about an order of magnitude as compared to that for the anthracene – perylene pair in THF.

These observations suggest that nanoaggregates provide some unique advantages for efficient ET process as compared to those in solutions and this can be rationalized considering several factors. Firstly, due to stronger intermolecular interactions in the nanoaggregate, the energy gap between the HOMO and LUMO of the anthracene molecule reduces and it causes a red shift of the emission band by about 20 nm. This results a larger overlap of donor emission with the absorption spectrum of the acceptor, leading to more efficient energy transfer. Secondly, in the nanoaggregates, donor and acceptor molecules are closely packed and hence the effective concentration of the acceptor is three to four orders of magnitude higher in the nanoaggregates as compared to that in solution and the probability of finding the acceptor molecule in the close proximity of the donor is very large. Discussion in the following sections may help us to understand the mechanism of larger energy transfer rate and efficiency in nanoaggregates more precisely and quantitatively.

5.2.5. Fluorescence Upconversion Experiments: Time resolved fluorescence measurements performed with the quencher concentrations in the range >1 x 10^{-2} mol. dm^{-3} using TCSPC technique (time resolution is about 200 ps) indicated the presence of short lived lifetime components, which could not be well resolved by using this technique. We have used fluorescence up-conversion technique (time resolution is about 150 fs) to record the temporal emission profiles at 430 nm to monitor the decay of anthracene exciton emission in doped anthracene nanoaggregates having dopant concentrations larger than 1 x 10^{-2} mol dm^{-3}. Each of these temporal emission profiles follows nonexponential decay behaviour and decay of the excited state population of anthracene exciton is found to be faster at larger excitation energy (Figure 5.7A). These observations suggest significant contribution by the exciton – exciton annihilation process towards the decay of the donor excitonic state, S_1 (equation 5.5).[26] These temporal profiles thus consist of two distinct components, namely, exciton – exciton annihilation process, which should follow second order kinetics with the rate constant k_2 and annihilation free exciton decay process (equation 5.6), which should follow first order kinetics with the rate constant k_1. In addition to these two decay channels, another process contributing to the decay of the excitonic emission in undoped anthracene nanoaggregate is population of the excimric state following trapping of excitons at the defect site (D) (equation 5.7). This may be considered as a pseudo-first order process with the rate constant k_3. However, excimeric emission is long-lived and contributes as a long-lived residual emission. Considering these aspects, we derive the kinetic equation 5.8 for the decay of excitonic emission intensity, I_t, following photoexcitation of undoped anthracene nanoaggregate.[26] In this equation, $k'_2 = (½)k_2[S_1]_0$ where $[S_1]_0$ is the initial concentration of the excitonic state of anthracene populated by the excitation pulse and $\tau = (k_1 + k_3)^{-1}$. The terms I_0 and R in equation 5.8 represent the maximum emission intensity and a minor contribution of the excimeric state to the residual long-lived emission intensity, respectively. However, in the case of doped anthracene nanoaggregates, we need to consider contribution of another process contributing to the decay of the excitonic state, namely, ET process (equation 5.9) and the expression of $<\tau>$ needs to be revised in the case of doped nanoaggregates as, $<\tau> = (k_1 + k_3 + k_{ET}[A])^{-1}$.

$$S_1 + S_1 \xrightarrow{k_2} S_n + S_0 \qquad (5.5)$$

$$S_1 \xrightarrow{k_1} S_0 \qquad (5.6)$$

$$S_1 + D \xrightarrow{k_3} E \qquad (5.7)$$

$$I_t = \left(\frac{I_O}{1 + k_{an}t}\right) e^{\frac{-t}{\tau}} + R \qquad (5.8)$$

$$S_1 + A \xrightarrow{k_{ET}} S_0 + A^* \tag{5.9}$$

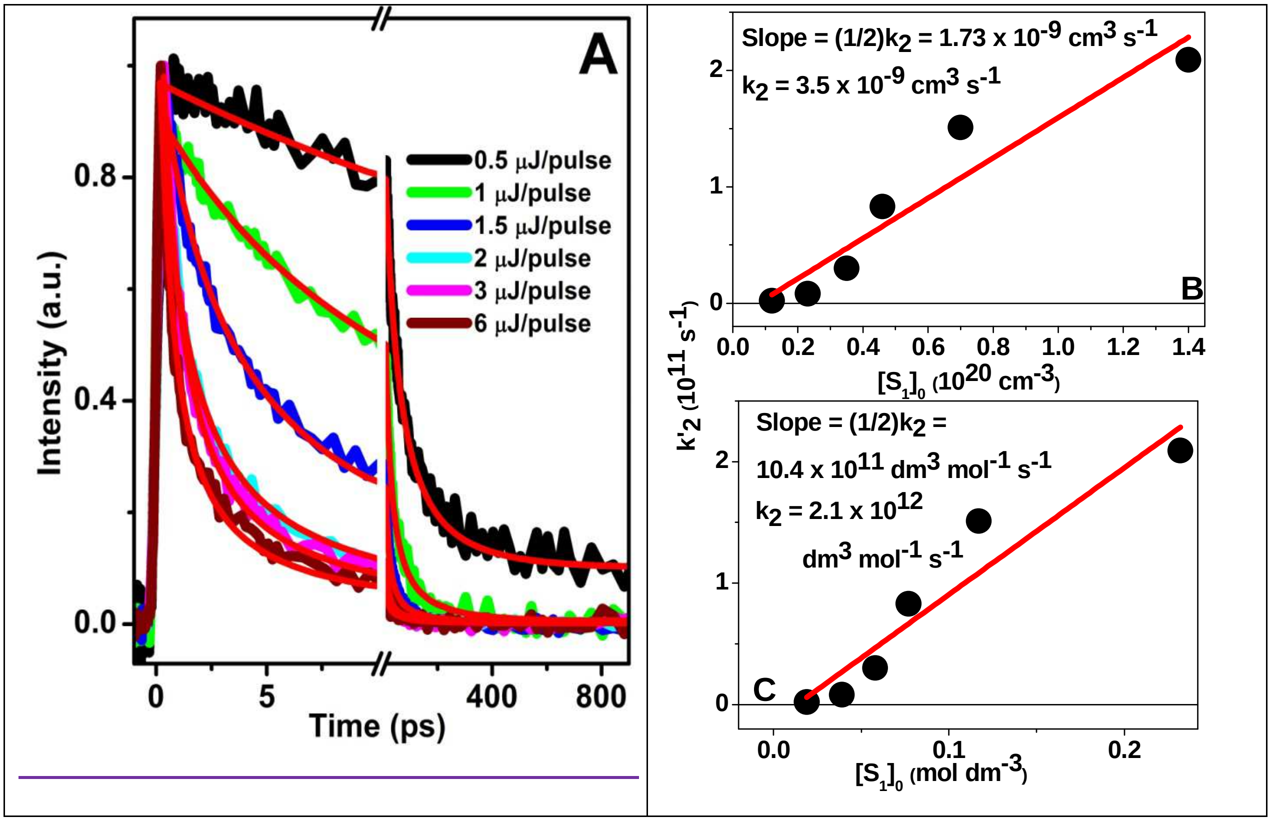

Figure 5.7: (A) Temporal emission profiles recorded at 430 nm following photoexcitation of the undoped anthracene nanoaggregate samples using different excitation energies, along with the best-fit functions generated using equation 5.8. (B) and (C): Plots of k'$_2$ vs. $[S_1]_0$ (exciton concentration at zero delay time). Insets provide the values of k_2 determined from the slopes of the best-fit lines.

Table 5.3: Parameters fitting the temporal emission profiles recorded at 430 nm using different excitation energies, following equation 5.8.

Energy/pulse (μJ)	$[S_1]_0$ (10^{20} cm^{-3})[a]	$[S_1]_0$ (mol dm^{-3})[a]	I_0	k'_2 (10^{11} s^{-1})	τ (ns)	R
0.5	0.12	0.019	0.872	0.02	0.33	0.1
1	0.23	0.039	0.918	0.08	0.33	0.004
1.5	0.35	0.058	1.03	0.3	0.32	0.002
2	0.46	0.077	1.099	0.83	0.29	0.003
3	0.7	0.117	1.483	1.51	0.26	0.002
6	1.4	0.232	1.4	2.09	0.25	0.006

[a] Method of calculation is shown in S5.13 in SD section.

Therefore, each of the temporal emission profiles recorded at 430 nm using fluorescence upconversion technique has been fitted using equation 5.8, which represents mixed (first and second) order kinetics. The temporal profiles recorded using different excitation energies along with the fitting functions are shown in Figure 5.7A and the fitting parameters are provided in Table 5.3. We calculated the exciton density at zero delay time, $[S_1]_0$, (in units of both cm^{-3} and mol dm^{-3}) and plotted k'_2 vs $[S_1]_0$ to determine the values of k_2 from the slope of the best fit line (Figures 5.7B and 5.C). Value of k_2 thus obtained is 3.5 x 10^{-9} cm^3 s^{-1} or 2.1 x 10^{12} dm^3 mol^{-1} s^{-1}. This value agrees well with that determined by us using transient absorption spectroscopic technique and reported earlier (3.7 x 10^{-9} cm^3 s^{-1}).[26] In addition, the values of the annihilation radius (R_a = 2.4 nm) and the diffusion coefficient (D = 5.8 x $10^{-4}$$cm^2$ .s^{-1}) have also been determined (Text 5.13 in SD).

Temporal emission profiles recorded at 430 nm following photoexcitation of differently doped PeAn nanoaggregates using excitation energy of about 3 μJ/pulse are shown in Figure 5.8 and the parameters obtained by fitting these curves using equation 8 are provided in Table 5.4. We observe that the exciton – exciton annihilation rate constant, as expected, has similar values (k'_2 = (1.55 ± 0.10) x 10^{11} s^{-1}) in PeAn nanoaggregates with different dopant concentrations. However, the value of τ is found to decrease with increase in dopant concentration. Since the values of k_1 and k_3 may be assumed to remain constants in the cases of both undoped and doped anthracene nanoaggregates, decrease of the value of τ with increase in concentration of the dopant may be assigned to increase in ET rate, k_{ET}. Like in the cases of the steady state and TCSPC experimental data, S-V plot constructed using the fluorescence upconversion data shows linear behaviour only in the lower concentration region (<0.01 mol dm^{-3}) of perylene used as dopant (Figure S5.14 in SD section). The ET rate, k_{ET}(FS), thus determined for PeAn nanoaggregate using the linear part of the S-V plot, is 5.3 x 10^{11} dm^3 mol^{-1} s^{-1} .

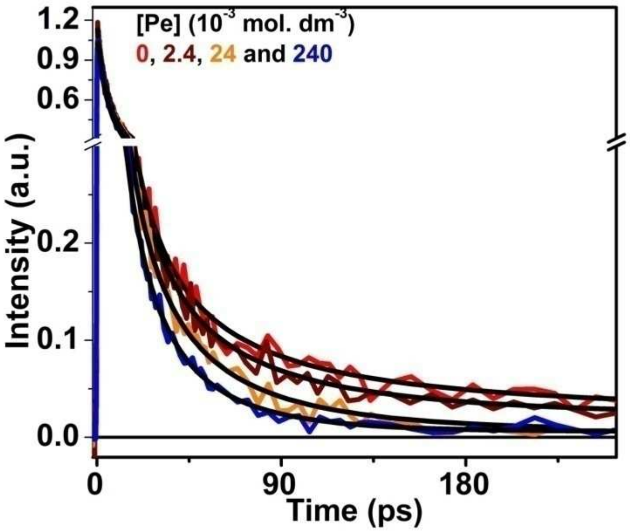

Figure 5.8: Temporal profiles recorded at 430 nm for differently doped PeAn nanoaggregates using excitation energy of 3 μJ/pulse, along with the best-fit functions generated using equation 5.8 (The best fit parameters are given in Table 5.4).

Table 5.4: Parameters associated with the best fit functions for the temporal profiles (see Figure 5.8), which were recorded at 430 nm using different dopant concentrations, generated using equation 5.8.

[Perylene] (10^{-3} mol dm^{-3})	I_0	k'_2 (10^{11} s^{-1})	τ (10^{-9} s^{-1})	R
0[a]	1.12	1.58	0.36	0.026
2.4	1.21	1.64	0.18	0.022
4.8	1.22	1.52	0.13	0.01
24	1.17	1.50	0.11	0.006
48	1.08	1.56	0.08	0.014
240	1.12	1.44	0.06	0.006

[a] Undoped anthracene nanoaggregate.

Because of overlapping of the emission bands of anthracene and perylene excitons in the 450 – 500 nm region (Figure 5.3), we could not record the rise of the emission signal corresponding to population of the perylene excitonic state. Therefore, it has not been possible to correlate the ultrafast decay of excitonic emission of anthracene recorded in sub-200 ps time domain with the ET process. However, in the case of TeAn nanoaggregate, since the excitonic emission bands of anthracene and tetracene are well separated, we could record the rising emission signal corresponding to excitonic emission of tetracene (Figure 5.9).

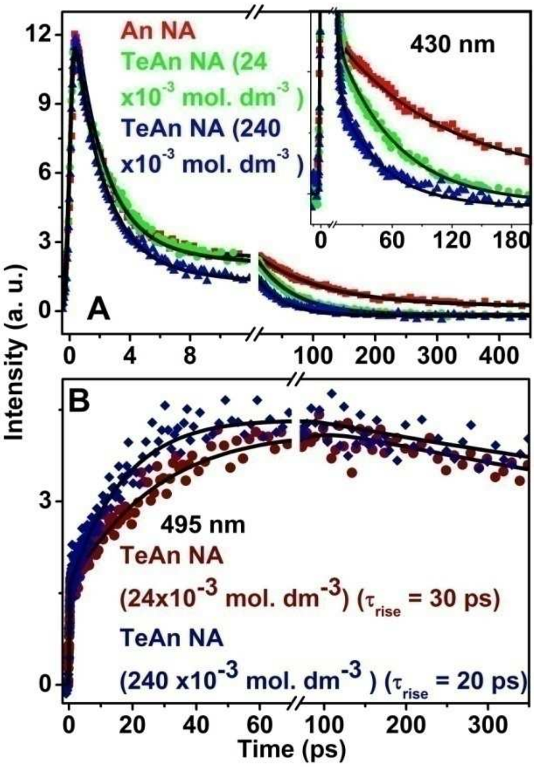

Figure 5.9: (A) Temporal profiles recorded at 430 nm for anthracene nanoaggregate (An NA) and TeAn nanoaggregates with 0.5 and 5% doping using excitation energy of 3 μJ/pulse, along with the best-fit functions generated using equation 5.8. Inset of A shows the temporal profiles at different time and intensity scales. (B) Rise of tetracene excitonic emission intensity monitored at 495 nm. Rise times are given in the insets of B.

Decay of excitonic emission of anthracene (Inset of Figure 5.9A) and rise of the excitonic emission of tetracene (Figure 5.9B) occurring in the same time scale confirms the ET process from anthracene excitonic state to that of tetracene. Parameters fitting the temporal profiles, recorded at 430 nm using different excitation energies, using equation 8 are given in Table S5.16 in SD section. Figure S5.15 and Table S5.17 in SD section provides the results of fluorescence upconversion measurements for PnAn nanoaggregate. Like in the case of PeAn nanoaggregate, S-V plots constructed using the fluorescence upconversion data for TeAn and PeAn nanoaggregates show linear behaviour only in the lower concentration region (<0.01 mol dm^{-3}) of the dopant (Figures S.14 in SD section). The ET rates, k_{ET}(FS), were thus determined using the linear part of the S-V plot. The k_{ET}(FS) values for all three doped nanoaggregates are given in Table 5.2 and these values are quite in good agreement with those determined using steady state and TCSPC techniques considering the experimental errors associated with the methods or techniques applied for determining these values. In all three cases, S-V plots show negative deviations at higher concentrations of the dopant.

5.2.6. Energy Transfer Mechanism: Here the dopants in the anthracene nanoaggregates have been chosen to ensure significant overlap between the excitonic emission band of anthracene and the absorption bands of the dopant, which lead to efficient energy transfer from anthracene singlet excitonic state to the dopant to populate the excitonic state of the latter. According to Förster's theory, resonance energy transfer between a donor - acceptor pair separated by a distance of 'R' occurs through dipole-dipole interaction and the rate constant, k_{ET}, associated with the ET process can be estimated using equation 5.10,[36, 45]

$$k_{ET} = \frac{1}{<\tau_D>}\left(\frac{R_0}{R}\right)^6 \qquad (5.10)$$

Here, $<\tau_D>$ represents the lifetime of the excited or the excitonic state of the donor in absence of the acceptor and R_o represents the Förster radius, which can be estimated using equation 5.11.

$$R_0^6 = \frac{9000\Phi_D k^2(\ln 10)}{128\pi^5 N_A \eta^4}\int_0^\infty F_D(\lambda)\varepsilon_A(\lambda)\lambda^4 d\lambda \qquad (5.11)$$

Here, Φ_D represents the emission quantum yield of the donor, n is the refractive index of the medium, N_A is the Avogadro number and κ^2 is a factor describing the relative orientations of the transition dipoles of the donor and acceptor. $F_D(\lambda)$ is the intensity of excitonic emission at wavelength λ corresponding to a normalized emission spectrum of the donor and $\varepsilon_A(\lambda)$ is the absorption coefficient of the acceptor at λ. Therefore, the integrand in equation 5.11 represents the overlap integral, the value of which describes the extent of overlap between the normalized emission spectrum of the donor exciton and the absorption spectrum of the acceptor doped in anthracene nanoaggregate.

We have calculated the values of Förster radii for three donor-acceptor pairs in doped anthracene nanoaggregates using 'Photochem CAD' software module.[46, 47] For all these calculations, we have assumed condition of static isotropic average in a rigid matrix and used the value of κ^2 as 0.476.[45] The values of Förster radii thus obtained are 2.91, 2.35 and 2.05 nm, for PeAn, TeAn and PnAn nanoaggregates, respectively (S5.18 in SD section). This is also the order of decreasing the values of the overlap integrals.

Herein, we try to correlate the efficiency of the ET process, which has been estimated experimentally by using, say, the time resolved TCSPC technique with that, which can be theoretically calculated assuming that the process follows the Förster's mechanism.[22,23] Förster's theory of resonance energy transfer is best described by considering a particular pair of donor and acceptor. We calculate that the average number of anthracene molecules in a single nanoaggregate particle may be excited by the excitation light source (energy 28 pJ/pulse) used in our TCSPC experiments is less than 0.5, i.e. on an average not more than one exciton is populated in individual nanoaggregate particles (see S.5.19 in SD section). We have also shown the variation of the ET rate constant against the donor-acceptor distance (see Figure S5.20 in SD section). Further, we assume that the dopant molecules are randomly distributed in doped anthracene nanoaggregate and N_P is the number of nanoaggregate particles present in the irradiated volume of the sample. We write equation 5.12 to estimate the average value of the rate constant for the ET process, k'_{ET}, assuming that only the Förster's mechanism of ET is operative.

$$k'_{ET} = \frac{1}{N_p}\sum_{j}^{N_p} k_{ET} = \frac{1}{N_p}\sum_{j}^{N_p} \frac{1}{<\tau_D>}\left(\frac{R_0}{R_j}\right)^6 \qquad (5.12)$$

Here R_j is the distance between the only exciton created following photoexcitation and the nearest dopant molecule in the j^{th} nanoparticle. The quenching efficiency then is estimated using equation 5.13.

$$\Phi_{ET} = \frac{k'_{ET}}{\frac{1}{<\tau_D>} + k'_{ET}} \qquad (5.13)$$

Details of the procedure followed to calculate the values of k'_{ET} (in s^{-1}) for the differently doped anthracene nanoaggregates with varying concentrations of the dopant assuming Förster's mechanism are given in SI section (see S5.21 in SD section). We also calculated second order ET rates, k_{ET}(Förster), by plotting k'_{ET} vs dopant concentrations (Figures 5.10 A, C and E and Table 5.2) and we find that the Förster's ET rates are significantly slower than the energy transfer rates determined experimentally and this difference is obviously becomes more significant for TeAn and PnAn nanoaggregates because of smaller values of the overlap integral (equation 5.11). This supports the fact that Forster's ET mechanism may not be the only mechanism responsible for the process of ET from the anthracene excitonic state to that of the dopant, but the ET via exciton diffusion, the rate of which is faster by two – six times depending on the kind of dopant than that of Förster's ET rate, may also have significant contribution.

We note that if the rate of exciton diffusion determines the rate of the ET process, the latter is given by $k_{ET} = 4\pi DR_{ET}$. On the other hand, exciton - exciton annihilation rate constant, k_2 is given by $k_2 = 8\pi R_a D$, where D is the diffusion coefficient for anthracene exciton in the nanoaggregate matrix, and R_a and R_{ET} are the exciton – exciton annihilation radius and exciton – dopant interaction radius, respectively.[48] Considering that values of R_a and R_{ET} are comparable, we find that $k_{ET} = k_2/2$. Following this argument, the rate of the ET process, which is controlled by exciton diffusion, is 1 x 10^{12} dm^3 mol^{-1} s^{-1}. We find that the average value of the rate constant of the ET process determined in PeAn nanoaggregate using three different techniques is about 6 ± 0.05 x 10^{11} dm^3 mol^{-1} s^{-1} (Table 5.2). This value is larger than that calculated assuming that only Forster's ET mechanism is operative (3.9 x 10^{11} dm^3 mol^{-1} s^{-1}; Table 5.1). But the latter is a bit slower than the rate of exciton diffusion. In addition, Table 5.2 reveals that Forster's ET rates calculated for other two nanoaggregates, namely TeAn and PnAn (11 x 10^{10} and 5.6 x 10^{10}, dm^3 mol^{-1} s^{-1}, respectively) are also significantly slower than the average values of the ET rates, which have been determined experimentally (~4.24 ± 0.7 x 10^{11} dm^3 mol^{-1} s^{-1} and 3.25 ± 0.8 x 10^{11} dm^3 mol^{-1} s^{-1} for TeAn and PnAn, respectively). The latter values, like in the case of PeAn nanoaggregate, are also a bit slower than the exciton diffusion rate. Therefore, we infer that ultrafast exciton diffusion may possibly be the factor responsible for more rapid and more efficient quenching of exciton emission in doped anthracene nanaoaggregates than that achievable via Förster's mechanism.

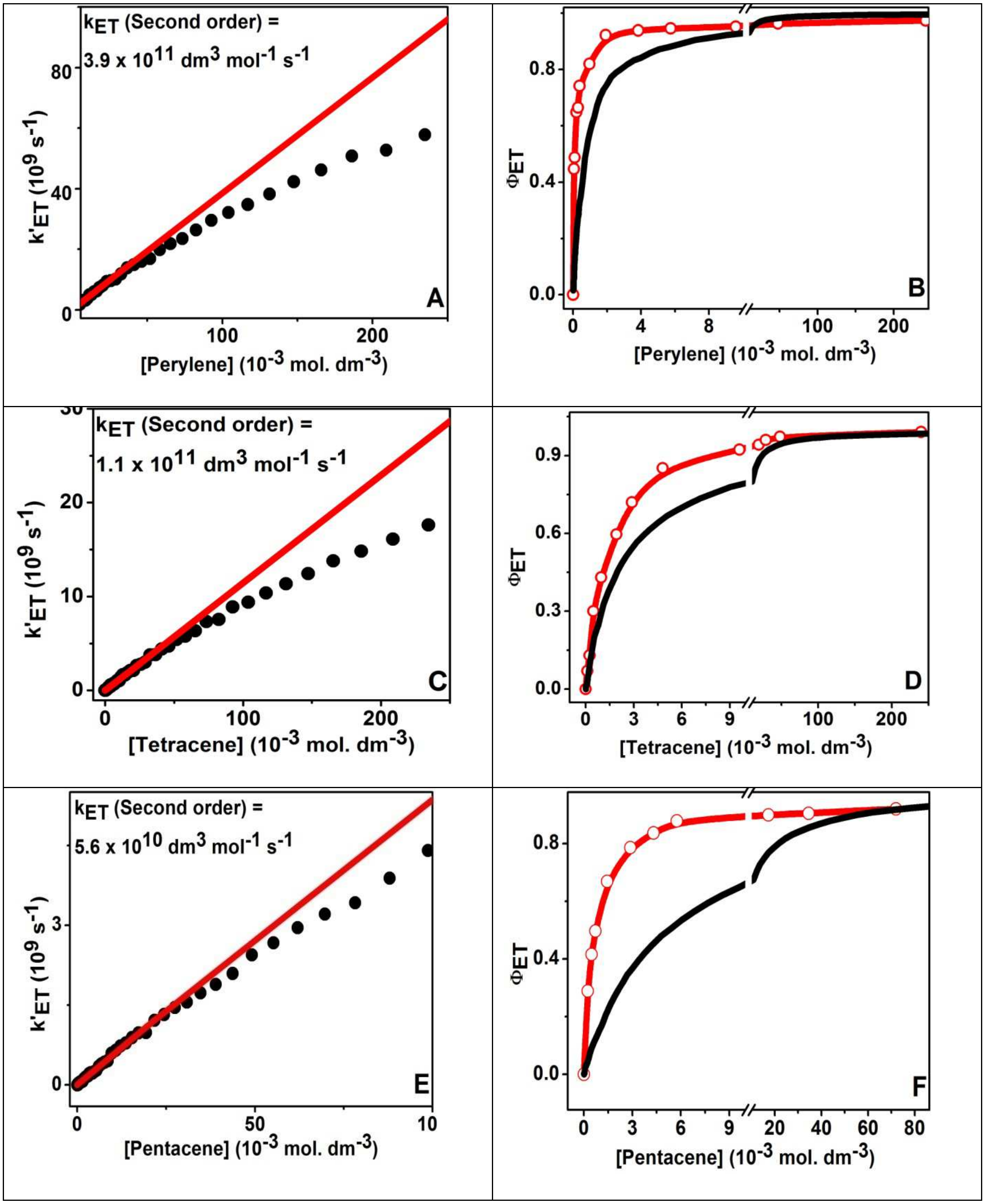

Figure 5.10: (A), (C) and (E) represent the plots of ET rate constants, calculated following Förster's FRET model, vs. the concentration of perylene, tetracene and pentacene respectively. (B), (D) and (F) Show the comparison between experimental data (red line with open circles) and simulation data (black line) for quenching efficiency study for all those three systems.

In Figure 10, we have also compared the ET efficiencies determined experimentally using the steady state emission experiment with those calculated using equation 5.13. We find that in each of these cases, experimentally determined values of the ET efficiencies (ϕ_{ET}) are significantly larger than those calculated assuming Förster mechanism for the dopant concentrations up to about 1 x 10^{-2} mol dm^{-3}. Beyond this concentration range of the dopant, the experimentally determined and the calculated values of the ET rates tend to become nearly comparable. It is now important to note that the S-V plots constructed using the data obtained from each of three kinds of experiments as well as in the cases of all three kinds of nanoaggregates studied here show negative deviations from linearity (Figures 5.5). In addition, even in the lower concentration range of the dopant (up to about 1 x 10^{-2} mol dm^{-3}), the average values of the rates of the ET process from the excitonic state to the dopant (k_{ET}) is much larger than that calculated assuming that only Förster's mechanism is operative. Therefore, it becomes obvious that in all three nanoaggregate systems studied here, Förster's model for the ET process is not adequate enough to explain the ultrafast ET rates determined experimentally.

McNeill et. al. also made similar observations regarding more rapid and efficient energy transfer in dye-doped conjugated polymer nanoparticles as compared to that calculated by considering only Förster's mechanism.[22] They explained this observation by predicting the exciton diffusion assisted energy transfer mechanism, which results faster energy transfer than that of Förster. Mitsui et. al. also have shown for tetracene doped p-terphenyl nanoparticle, that the ET process is more efficient than FRET process.[23] They assumed rapid exciton diffusion model to fit the quenching data. In this work, we have experimentally determined the rate of diffusion of the anthracene exciton, which is the energy donor and directly correlated the ET rate with that of exciton diffusion. Therefore this work provides direct experimental evidence for the exciton diffusion assisted energy transfer processes in organic nanoaggregates.

However, when the acceptor concentration increases beyond 2 x 10^{-2} mol dm^{-3}, the average distance between the photo-generated exciton and the acceptor molecules in a nanoparticle becomes comparable to or smaller than the reaction radius, R_{ET} ($R_a = R_{ET}$ ~2.4 nm), which is also comparable to Förster radius (R_0 = 2.91, 2.35 or 2.05 nm for PeAn, TnAn or PnTn nanoaggregates, respectively). We also calculated the Förster ET rate using a simulation method at various concentrations of perylene in PeAn nanoaggregate and found that the ET rate really becomes independent of dopant concentration beyond 2 x 10^{-2} mol dm^{-3} (Table S5.22 in SD section) to attain a limiting value, which agrees well with that experimentally determined. Therefore, we infer that at large doping concentration, both the rate and efficiency of the ET process in the doped nanoaggregate attain a limiting value and the ET process may be considered to be occurring in the static quenching regime and the quenching reaction does not need diffusion of excitons.

5.2.7. White Light Emission from Ternary Doped Anthracene Nanoaggregate: Materials undergoing efficient fluorescence emission with large spectral width covering the entire visible region are important because of their wide scale applications in LED and display devices. Researches towards preparation and characterization of low cost and more energy efficient materials for the above applications have been of immense interest in recent years.[49, 50] Aromatic hydrocarbons used for the present study are quite cheap and method of preparation of energy efficient doped nanoaggregates is quite easy. We have shown in the earlier sections that even with a minor amount of doping of perylene, tetracene or pentacene in anthtracene nanoaggregate, fluorescence emission in a wide wavelength region extending in the 400 – 700 nm could be achieved with high efficiency.

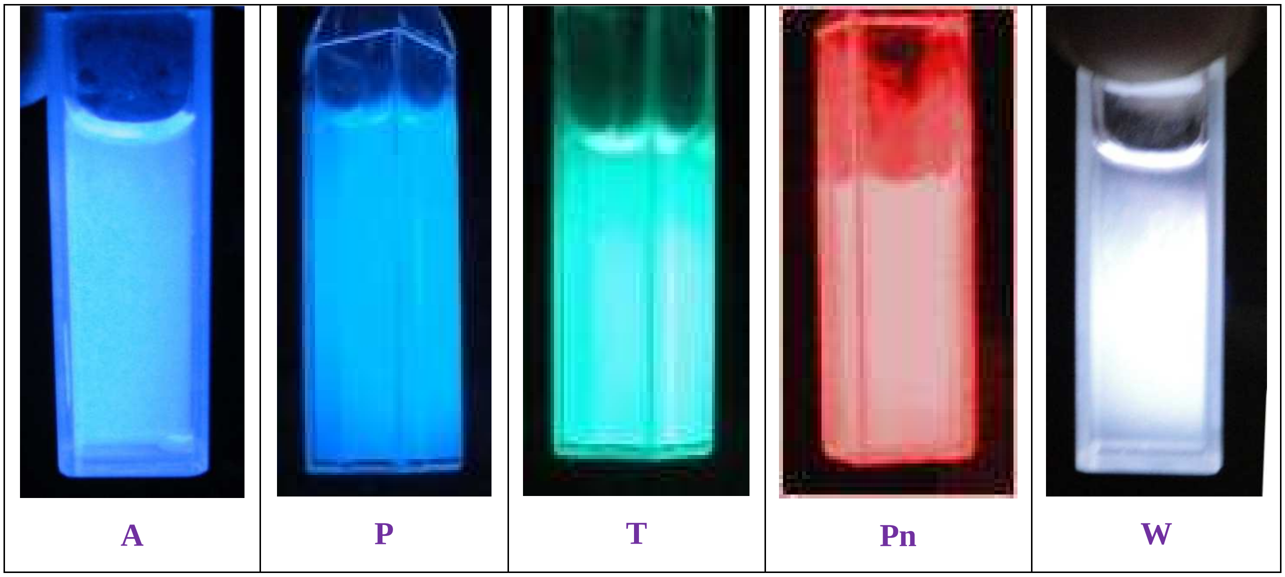

Figure 5.11: Photographs of emissions observed from anthracene nanoaggregates: undoped anthracene [A], perylene doped anthracene [P], tetracene doped anthracene [T], pentacene doped anthracene [Pn] and teranery doped anthracene [W] nanoaggregates dispersed aqueous solution under UV excitation (355 nm).

We observed that following photoexcitation of undoped anthracene nanoaggregate using 355 nm (UV) light generates fluorescence emission of deep blue colour and the emission yield is around 0.16 (Figure 11 and Figure S5.23 in SD section). With perylene doping into the anthracene nanoaggregate matrix, the emission of sky blue colour is generated and the emission yield enhances to about 0.36 ± 0.02 at the perylene concentration of ~ 1 x 10^{-3} mol dm^{-3}. Hence, doping of perylene in anthracene nanoaggregate not only changes the colour of emission but also makes the material more efficient fluorescence emitter. Nanoaggregate material doped with tetracene molecules produces bright green emission with the emission yield is around 0.29 at the tetracene concentration of ~48 x 10^{-3} mol dm^{-3}. Pentacene doping produces pink red colour with the emission yield of about 0.12 at the perylene concentration of~ 0.72 x 10^{-3} mol dm^{-3} but total emission yield decreases with the increase in pentacene concentration (discussed earlier in section 5.3.3). Therefore, we find that doping of these three compounds individually into the anthracene nanoaggregate matrix produces light in different regions of the visible spectrum (Figure 5.11A). We explored the possibility of generating the colours covering the entire range of the visible spectrum using ternary doped anthracene nanoaggregate material. We show the emission spectrum of the ternary doped anthracene nanoaggregate material with perylene and tetracene, each of them having concentration of 1.44 ± 0.2 x 10^{-3} mol. dm^{-3} and pentacene with concentration of 1.5 ± 0.3 x 10^{-2} mol dm^{-3}, recorded following photoexcitation at 355 nm (Figure S5.23 in SD section). The positional coordinates corresponding to the emission spectra of differently doped nanoaggregate samples are shown in 1931 CIE plot (Figure 5.12), which reveals the white light character of the emission from the ternary doped anthracene nanoaggregate.

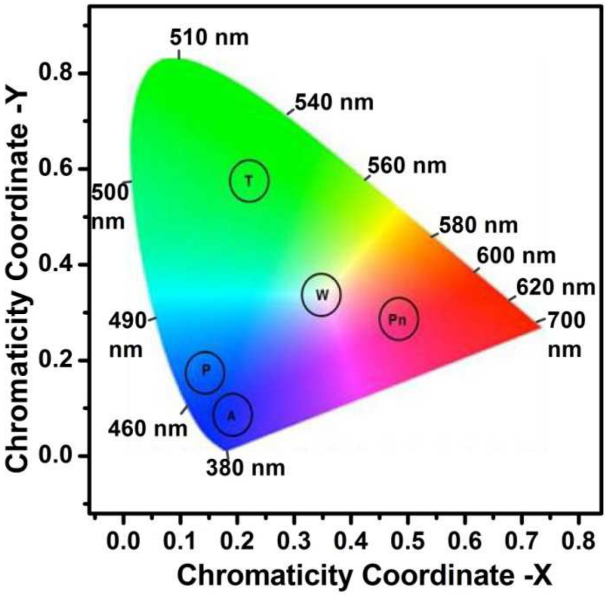

Figure 5.12: The position coordinate in CIE 1931 plot for the above samples.

5.3. CONCLUSION

Reprecipitation method could be successfully used to synthesize singly or multiple doped nanoaggregates of anthracene without significant change in the size of the particle. In the case of nanoaggregates with suitable donor - acceptor combinations, efficient resonance energy transfer from the excitonic state of the host molecule to that of the guest or dopant molecule has been observed. At low concentration of the dopant molecules, say <1 x 10^{-2} mol dm^{-3}, the efficiency of the energy transfer processes is much larger and the rate is much faster than those calculated assuming Förster's resonance energy transfer mechanism. However, the rate of diffusion of anthracene exciton in the nanoaggregate matrix measured using fluorescence spectroscopic method has been seen to be much faster than the ET rate. Thus, exciton diffusion assisted Förster resonance energy transfer model is proposed. In this concentration regime, the average distance of the donor and the acceptor species is much longer than the Förster radius and the energy transfer rate is mainly governed by the exciton diffusion process in the host matrix. However, at higher concentration of the dopant, say >1 x 10^{-2} mol dm^{-3}, the average donor – acceptor distance becomes comparable to or shorter than the Förster radius and hence the Forster ET rate to the rate of exciton diffusion. At the high concentration regime of the quencher, both the energy transfer rate and efficiency attains a limiting value and the ET rate is determined mainly by Förster mechanism. Multiple doping of anthracene nanoaggregate by perylene, tetracene and pentacene in proper proportion have been shown to emit of white light with large efficiency. This material may have potential applications in display and OLED systems.

5.4. REFERENCES

1. Anthony, J. E. *Chem. Rev.***2006**, *106*, 5028.
2. Murphy, A. R.; Fréchet, J. M. J. *Chem. Rev.***2007**, *107*, 1066.
3. Figueira-Duarte, T. M.; Müllen, K. *Chem. Rev.* **2011**, *111*, 7260.
4. Chops, K.; Rand, B. P.; Cheyns, D.; Verreet, B.; Empl, M. A.; Heremans, P. *Nature Comm.* **2014**, *5*, 3406.
5. Samuel, I. D. W.; Turnbull, G. A. *Chem. Rev.* **2007**, *107*, 1272.
6. Liu, H.; Xu, J.; Li, Y. *Acc. Chem. Res*. **2010,** *43*, 1496
7. Cui, S.; Liu, H.; Gan, L.; Li, Y., Zhu, D. *Adv. Mater* **2008,** *20*, 2918.
8. Palmer, L. C.; Stupp, S. I. *Acc. Chem. Res*. **2008,** *41*, 1674.
9. Bhongle, C. J.; Chang, C. W.; Lee, C. S.; Diau, E. W. G.; Shu, C. *J. Phys. Chem. B.***2005,** *109*, 13472.
10. Yao, H.; Yamashita, M.; Kimura, K. *Langmuir* **2009**, *25*, 1131.
11. Xiao, J.; Yang, *H.;* Yin, Z.; Guo, J.; Boey, F.; Zhang, H.; Zhang, Q. *J. Mater. Chem.* **2011**, *21*, 1423.
12. Xiao, D.; Xi, L.; Yang, W.; Fu, H.; Shuai, Z.; Fang, Y.; Yao, J. *J. Am. Chem. Soc.* **2003,** *125*, 6740.
13. Meng, H.; Sun, F.; Goldfinger, M. B.; Jaycox, G. D.; Li, Z.; Marshall, W. J.; Blackman, G. S. *J. Am. Chem. Soc***.** **2005,** *127*, 2406.
14. Meng, H.; Sun, F.; Goldfinger, M. B.; Gao, F.; Londono, D. J.; Marshall, W. J.; Blackman, G. S.; Dobbs, K. D.; Key, D. E. *J. Am. Chem. Soc*. **2006,** *128*, 9304.
15. Latterini, L.; Roscini, C.; Carlotti, B.; Aloisi, G. G.; Elisei, F. *Phys. Stat. Sol. A* **2006**, *203*, 1470.
16. Chung, H. R.; Kwon, E.; Oikawa, H.; Kasai, H.; Nakanishi, H. *J. Crystal growth* **2006**, *294*, 459.

17. Seko, T.; Ogura, K.; Kawakami, Y.; Sugino, H.; Tanaka, J. *Chem. Phys. Lett.* **1998**, *291*, 438.
18. Yu, J. Y.; Chen, I. W. P.; Chun-Hsien Chen, C. H.; Lee, S. J.; Chen, I. C.; Lin, C. S.; Cheng, C. H. *J. Phys. Chem. C* **2008**, *112*, 3097.
19. Chao, Y. C.; Chung, C. H.; Zan, H. W.; Meng, H. F.; Ku, M. C. *Appl. Phys. Lett.* ***20*11,** *99*, 233308
20. Liang, W. W.; Chang,C. Y.; Lai, Y. Y.; Cheng, S. W.; Chang, H. H.; Yin-Yu Lai, Y. Y.; Cheng, Y. J.; Wang, C. L.; Hsu, C. S. *Macromolecules* **2013**, *46*, 4781.
21. Zhao, Y. S.; Zhan, P.; Kim, J.; Sun, C.; Huang, J. *Acs Nano* **2010,** *4*, 1630.
22. Wu, C.; Zheng, Y.; Szymanski, C.; McNeill, J. *J. Phys. Chem. C* **2008**, *112*, 1772.
23. Mitsui, M.; Kawano, Y. *Chem. Phys.* **2013**, *419*, 30.
24. Gartzia-Rivero, L.; Cerdán, L.; Banuelos, Enciso, E.; Arbeloa, Í. L.; Costela, Á. Garcia-Moreno, I. *J. Phy***s.** *Chem. C* **2014**, *118*, 13107.
25. Oliveira, D.; Baba, K.; Teizer, W.; Kasai, H.; Oikawa, H.; Nakanishi, H. *Nanocrystal, Intech*, **2011**.
26. Manna, B; Ghosh, R.; Palit, D. K. *J. Phys. Chem. C.* **2015**, *119*, 10641.
27. Berlman, I. B. “Handbook of Fluorescence Spectra of Aromatic Molecules,” Academic Press, N.Y. **1971**
28. Dawson, W. R.; Windsor, M. W. *J. Phys. Chem.* **1968**, *72*, 3251.
29. Burdett, J. J.; Müller, A. M.; Gosztola, D.; Bardeen, C. J. *J. Chem. Phys.* **2010**, *133*, 144506.
30. Northrop, B. H.; Houk, K. N.; Maliakal, A. *Photochem. Photobiol. Sci.* **2008**, *7*, 1463.
31. Maliakal, A.; Raghavachari, K.; Katz, H.; Chandross, E.; Siegrist, T. *Chem. Mater*. **2004**, *16*, 4980.
32. Reineke, S.; Thomschke, M.; Lūssem, B.; Leo, K. *Rev. Mod. Phys*. **2013**, *85*, 1246.
33. Praveen, V. K.; Ranjith, C.; Armaroli, N. *Angew. Chem. Int. Ed.* **2014**, *53*, 365.
34. Shunmugam, R.; Tew, G. N. *Polym. Adv. Technol.* **2008**, *19*, 592.
35. Sun, C. Y.; Wang, X. L.; Zhang, X.; Qin, C.; Li, P.; Su, Z. M.; Zhu, D. X.; Shan, G. G.; Shao, K. Z.; Wu, H.; Li, J. *Nature Comm.* **2013**, *4*, 2717.

36. Kwon, J. E.; Park, S.; Park, S. Y. *J. Am. Chem. Soc.***2013**, *135*, 11239.
37. Johnson, P. C.; Offen, H. W. *Chem. Phys. Lett.* **1973**, *18*, 258.
38. Gharge, M. N.; Bhattar, S. L.; Kolekar, G. B.; Patil, S. R. *Indian J. Chem.* **2008**, *47A*, 1642.
39. R. Katoh, S. Sinha, S. Murata.; M. Tachiya. *J. Photochem. Photobiol. A: Chem.* **2001**, *145*, 23.
40. Merrifield, R. E.; Avakian, P.; Groff, R. P. *Chem. Phys. Lett.* **1969**, *3*, 155.
41. Wilson, M. W. B.; Rao, A.; Johnson, K.; Gélinas, S.; Pietro, R. D.; Clark, J.; Friend, R. H. *J. Am. Chem. Soc.* **2013**, *135*, 16680.
42. Zimmerman, P. M.; Bell, F.; Casanova, D.; Gordon, M. H. *J. Am. Chem. Soc.* **2011**, *133*, 19944.
43. Wilson, M. W. B.; Rao, A.; Ehrler, B.; Friend, R. H. *Acc. Chem. Res.* **2013**, *46*, 1330.
44. Stern, O.; Volmer, M. *Physik. Zeitschr.* **1919**, *20***,** 183.
45. Lakowicz, J. R. Principles of Fluorescence Spectroscopy, Kluwer Academic/Plenum Publishers, New York, **1999**.
46. Du, H.; Fuh, R. C. A.; Li, J.; Corkan, L. A.; Lindsey, J. S*Photochem. Photobiol.* **1998**, *68*, 141.
47. Dixon, J. M.; Taniguchi, M.; Lindsey, J. S. *Photochem. Photobiol.* **2005**, *81*, 212.
48. Kenkre, V. M.; Schmid, D... *Phys. Lett.* **1983**, *94*, 603.
49. Farinola, G. M.; Ragni, R. *Chem. Soc. Rev.* **2011**, *40*, 3467.
50. Mukherjee, S.; Thilagar, P. *Dyes and Pigments* **2014**, *110*, 2.

CHAPTER 6

EXCITON DYNAMICS IN PYRENE AND PERYLENE NANOAGGREGATES

6.1. INTRODUCTION

Investigations of the fundamental physical and chemical properties of the particles having sizes in the nanometer range have found importance because of their several unique properties and wide scale applications in various fields of science and technology.[1-11] Properties of inorganic nanoparticles have been well investigated and they have been found suitable for wide scale applications because of their excellent stability, better control over size and morphology as well as significant quantum size effect.[4-7] However, properties of the organic nanoaggregates are less explored due to their limitations with respect to stability, less control over size and morphology as well as less pronounced quantum confinement effect. Although organic polymers and surfactants have been successfully used as stabilizers to improve the stability and to control the size of the particles quite precisely, very weak intermolecular interactions, such as ππ stacking, hydrogen bonding, etc, which are responsible for self aggregation of the molecules, are, however, the inherent limitations in preparing organic nanoparticles of good stability. In general, sizes of the organic nanoaggregates (normally a few hundred nanometers) are much larger than their corresponding excitonic Bohr radius. As a result, energy levels of the excitonic states generated in the organic nanoaggregate are not dependent on the sizes of the particles prepared in laboratory. In spite of those limitations, fundamental research investigating the properties of organic nanoaggregates find importance because of several reasons. For example, band gap of the nanoparticle may be tuned by incorporating various substituents on the main molecular moity.[14, 15] Large extinction coefficients and high emission quantum yields of the nanoaggregates of some organic compounds may have potential applications in various kinds of optoelectronic devices.[8, 9, 12, 16-22] Organic nanoaggregates are used as photocatalysts and drug delivery agents, for living cell imaging, etc.[23, 24, 25] Above all, preparation of the organic nanoaggregates due to self-assembling of the monomer molecules in aqueous - organic solvents is a low cost facile route.

Dilute solution (concentrations in the range of a few µM) of pyrene or perylene in conventional organic solvents is strongly fluorescent upon photoexcitation using UV light. However, in concentrated solutions, excited states of these molecules form excimer and the fluorescence emission from the excited state of the monomer is strongly quenched. Excimer emission of pyrene is even much stronger than the monomer emission. However, transition corresponding to emission from the excimeric state of perylene is symmetry forbidden and hence perylene excimer emission is very weak.[26] In the case of polyacene molecules, since the intermolecular π-π interactions as well as hydrophobic interactions are quite strong, these molecules in aqueous - organic solvents self-assemble to form aggregates.

Synthesis and properties of the nanoaggregates of polyacene molecules e.g. anthracene, tetracene, coronene, have already been reported.[12, 13, 23, 27-35] Latterni et.al. have synthesized perylene nanoparticle using reprecipitation method.[33] Kang et. al. have used colloidal chemical reaction route to synthesize perylene nanoaggregates.[34] Syntheses of nanoaggregates of both pyrene and perylene molecules have already been achieved through various routes. Here, we have used reprecipitation method due to its simplicity and facileness for syntheses of nanoaggregates. Steady state absorption and emission properties of the nanoaggregates of these materials have also been reported earlier.[33,23] Although exciton dynamics and exciton migration in different crystalline forms of pyrene and perylene have already been reported by different groups,[36-39] dynamics of excitons in the nanoaggregates of these materials are yet to be explored. Knowledge about the exciton dynamics, exciton diffusion coefficient and diffusion length in the nanoaggregate are essential to decide about the suitability of a material in its applications in optoelectronic or photovoltaic devices. Here we have described the exciton dynamics and estimated those physical parameters related to exciton diffusion in nanoaggregate matrices.

6.2. RESULTS AND DISCUSSION

6.2.1. Morphological Characterization: Morphological analyses of the nanoaggregates were performed using DLS and AFM techniques after synthesis following reprecipitation method.[40] Particle size distributions in the nanoaggregates of pyrene and perylene as measured by the DLS technique, are shown in Figures 6.1A and 6.1C, respectively. Both the histograms indicate quite large polydispersities in the sizes of the particles in the nanoaggregates and the particle size distribution is in the range of 10 -1000 nm. The most probable diameter of the particles is about 120 nm with FWHM is about 200 nm.

AFM images of the nanoaggregate samples are shown in Figures 6.1B and 6.1D. It has been found that heights of the nanoaggregates are distributed in the range of 40 - 80 nm and the diameter is distributed in the 100 - 500 nm range for both the nanoaggregates. This means that the average diameters of these aggregates are about 2 - 5 times larger as compared to their heights and hence the particles are of disc shaped. It is important to mention here that the exciton Bohr radii of organic nanoaggregate particles are of the same order as the diameter of the molecule and hence a few nanometer. Therefore, the quantum size effect is not expected to be effective in altering the dynamics of exciton populated in particles of different sizes.

To elucidate the features of molecular packing in the nanoaggregates, XRD patterns for the powdered nanoaggregate samples have been recorded and those have been shown in Figure 6.2. XRD pattern for each of these nanoaggregates shows a few sharp lines superimposed on a broad envelope in the two theta range of 10 - 40^0. Positions of these lines exactly matches with those observed in the case of the ‘α’ form of perylene or pyrene crystal (hand book of nanostructured materials and nanotechnology).[41-44] This suggests that the nanoaggregates prepared in the present work mainly possess the ‘α’ crystalline phase for both the nanoaggregates. The broad scattering background associated with the XRD patterns, suggests partial amorphous nature of this material because of improper or disordered packing of molecules. It is obvious that this disordered molecular arrangement may have a significant role on the dynamics of exciton and its diffusion properties.

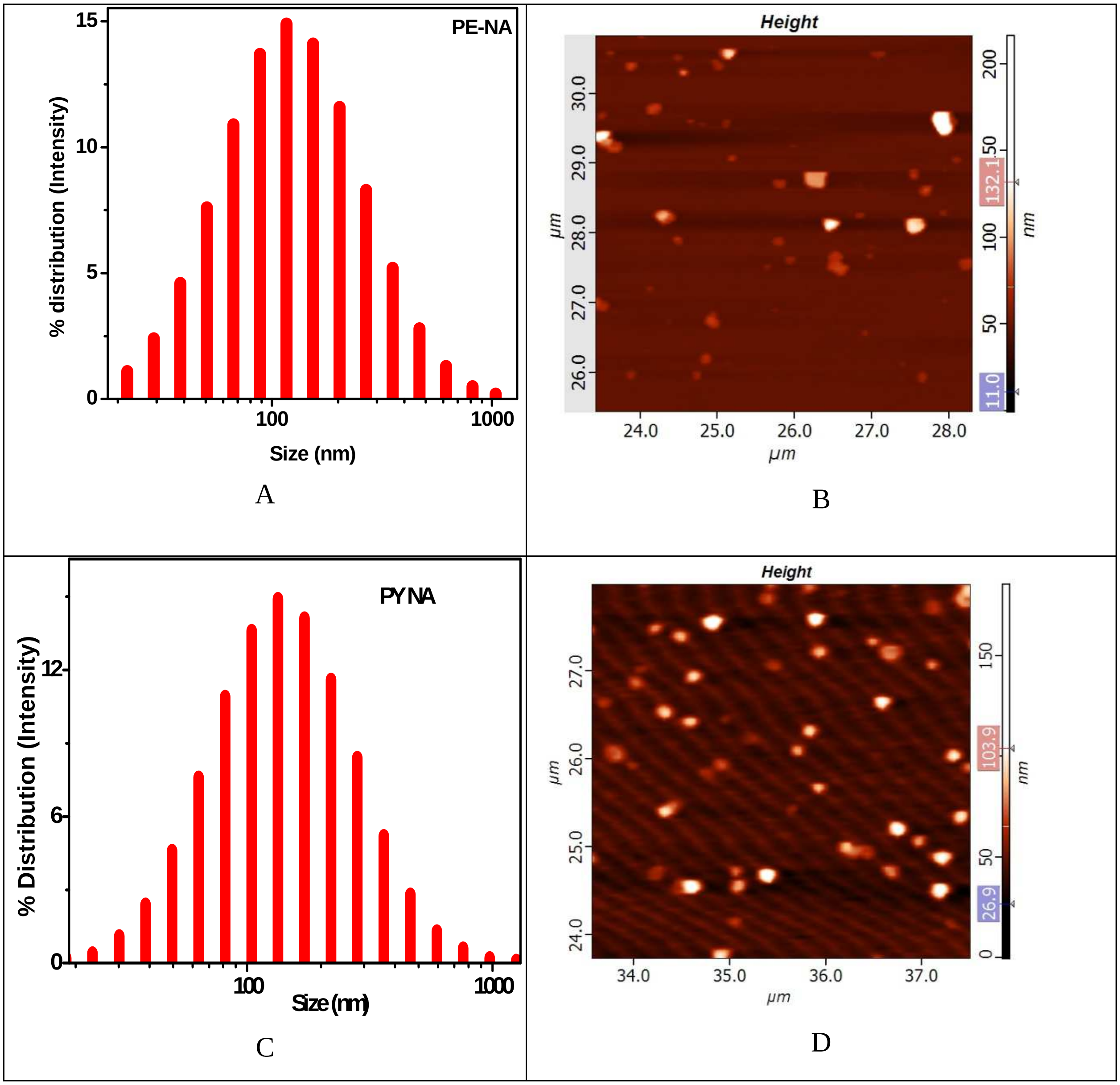

A

B

C

D

Figure 1: Size distributions estimated from DLS measurements (A and C) and the AFM images (B and D) of the perylene (A and B) and pyrene (C and D) nanoaggregates.

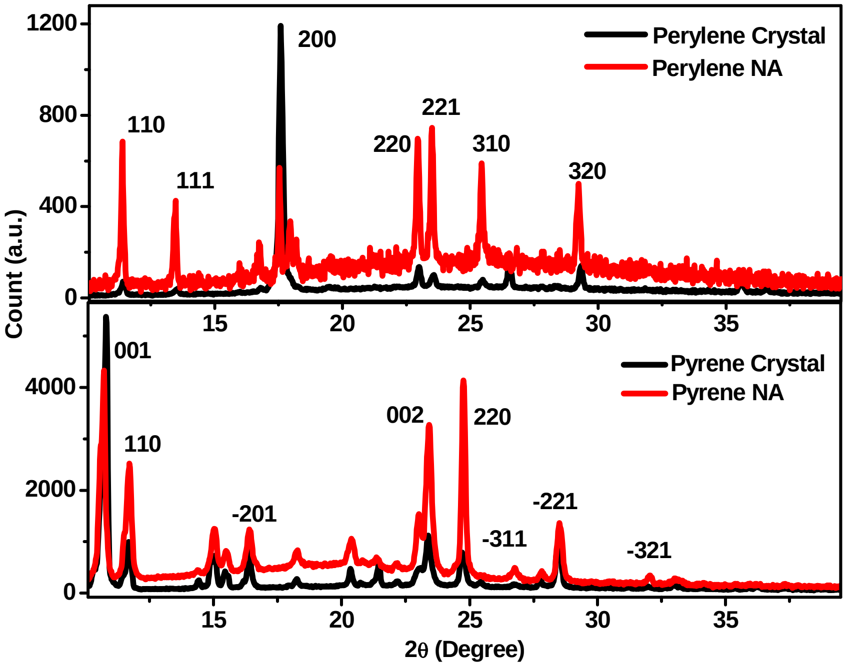

Figure 6.2: XRD patterns for and pyrene and perylene nanoaggregate samples (red curves), which have been compared with those of pyrene and perylene crystals, respectively.

6.2.2. Steady State Absorption and Emission Spectra: Steady state absorption and photoluminescence spectra of perylene nanoaggregates have already been reported in the literature and here we report the same as a part of characterization of the nanoaggregates.[33] Monomers of both these molecules in DMSO show the features of sharp vibronic bands, which are the characteristics of aromatic hydrocarbons. In the cases of the steady state absorption spectra of both the nanoaggregates, the characteristic features of the vibronic transitions are nearly lost but the presence of the weak vibronic transitions, which are superimposed on a broad band, are quite evident. However, the maximum of each of these vibronic bands is shifted towards lower energy with respect to the most intense vibronic band of the monomer. This possibly suggests reduction in the energy gap between the HOMO and LUMO levels in the nanoaggregate. The absorption spectrum is overlapped with strong Mie scattering, which appears as a long tail in the 380-600 nm region (see Figure 6.3). In the case of perylene nanoaggregates, however, the presence of a broad absorption band with the maximum at ca 381 nm possibly suggests formation of H-aggregate. This feature is not very evident in the case of pyrene nanoaggregate.

Monomer molecules of both pyrene and perylene in dilute solutions of organic solvents are strongly fluorescent following photoexcitation using UV light and the fluorescence spectra are characterized by the sharp vibronic bands.[45] However, with increasing concentration of the solutes (for example in cyclohexane solution), shapes of the emission spectra change and emission efficiencies are decreased. In the case of pyrene, a red shifted broad emission band has been characterized as the excimer emission of pyrene.[46] Excimer formation has been demonstrated in the crystalline (α phase) as well as in molten state of perylene.[46,47] Mataga et al. also reported about excimeric fluorescence in the case of perylene in frozen cyclohexane at 77K.[48] In Figure 6.3, we have shown the photoluminescence spectra of pyrene and perylene nanoaggregates. Broad (but possibly consisting of multiple bands) spectra, which appear at the lower energy side of the monomer fluorescence spectra, resemble to the emission spectra of excimers (vide infra).

Both pyrene and perylene may exist in two crystalline forms, namely α and β phase and α phase is thermodynamically more stable than the β phase. These two phases possess $P2_1/a$ space group symmetry. α Phase is suitable for excimer formation, because, in this kind of crystal structure, two molecules reside at sufficiently close distance to interact. In both the cases, the solid crystals consist of mainly α phase and excimer emission is observed following excitation with UV light. Existence of β phase has been observed in crystal defect sites or crystals obtained with special preparation conditions.[10, 49, 50] α-Perylene crystalline form, which is suitable for excimer formation, generally shows orange emission and β-perylene crystal, which is comparably less stable, show mainly green emission.[10,51,52] In nanoaggregates, we observe a broad spectral envelop extended in the wavelength region from 480 to 750 nm. The emission spectra covering both the green and orange region and consisting of multiple bands possibly suggests existence of both the crystalline phases in nanoaggregates. However, orange emission seems to be more dominating.

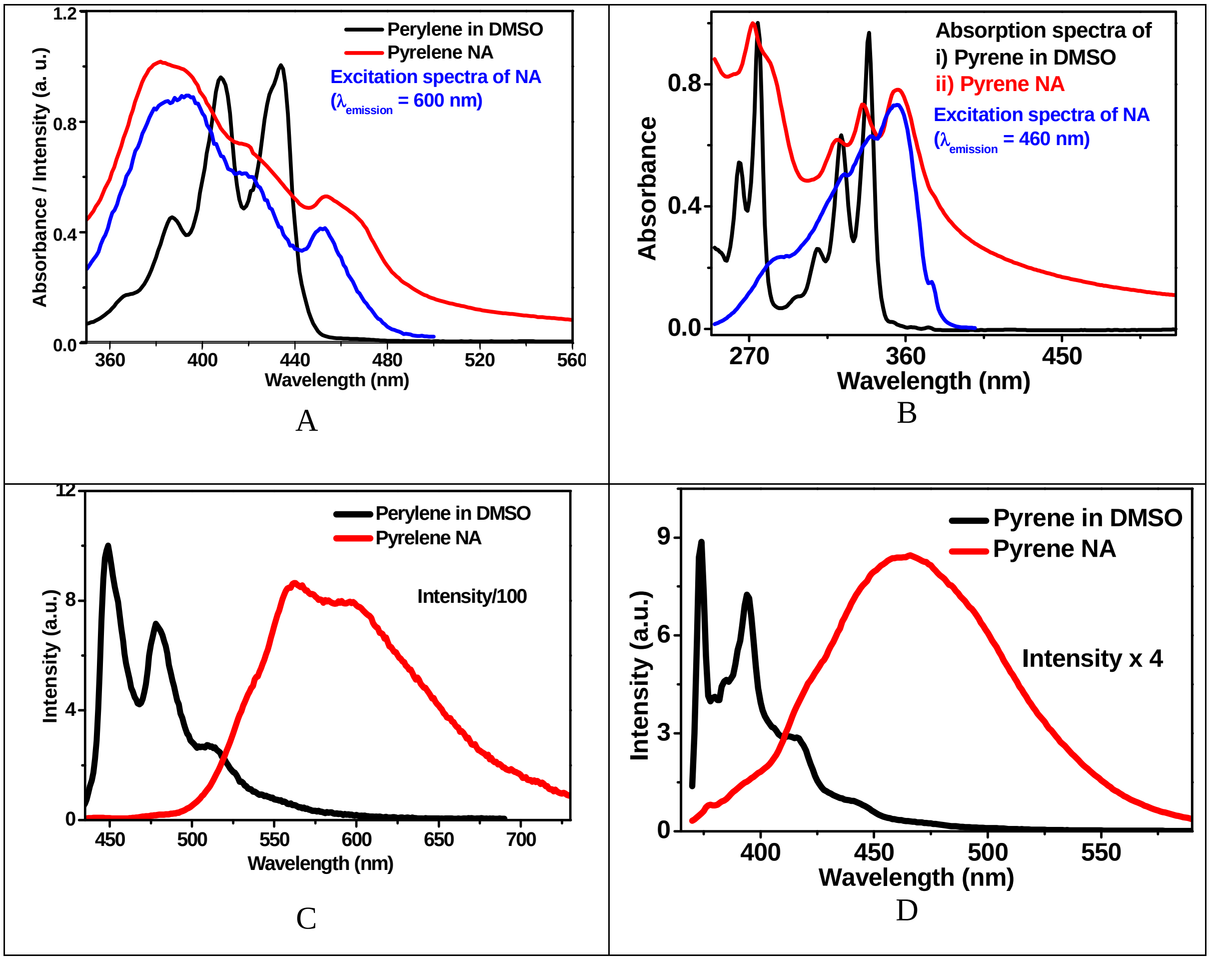

Figure 6.3: UV-Visible absorption and excitation spectra (A and C) and fluorescence spectra (B and D) of perylene and pyrene in dilute DMSO solutions and in nanoaggregates.

6.2.3. Time Resolved Fluorescence Study: Excitons, which are generated following absorption of light by the nanoaggregates, follow some distinct routes to populate back the ground state. Detailed knowledge about the dynamics of those processes is essential prior to using these materials in optoelectronic devices. Herein we have used time resolved emission and transient absorption spectroscopic techniques to understand the dynamics of excitons in the nanoaggregate matrices in nanosecond to sub-picosecond time domain. TCSPC technique has been used to understand the dynamics in the excimeic states, which occurs in nanosecond time domain.

Temporal profiles for perylene nanoaggregate emission have been recorded in the 440 – 750 nm region at 10 or 20 nm intervals using TCSPC technique and those recorded at a few selective wavelengths along with the corresponding multiexponential best-fit functions are shown in Figure 6.4. Each of them could be fitted well using a three exponential function with very similar lifetimes, although the relative amplitudes (both magnitude and sign) associated with the best fit functions are wavelength dependent. That is why the shapes of the temporal profiles recorded at different wavelengths are distinctly different. Values of the parameters associated with the best-fit functions are provided in Table 6.1. We find three major processes associated with the lifetimes of 0.18 ± 0.02, 0.81 ± 0.01 and 8.5 ± 1 ns, responsible for the dynamics of excitons in nanosecond time domain. We tentatively assign these lifetimes to free exciton and excitons in shallow traps and deep traps, respectively (vide infra).

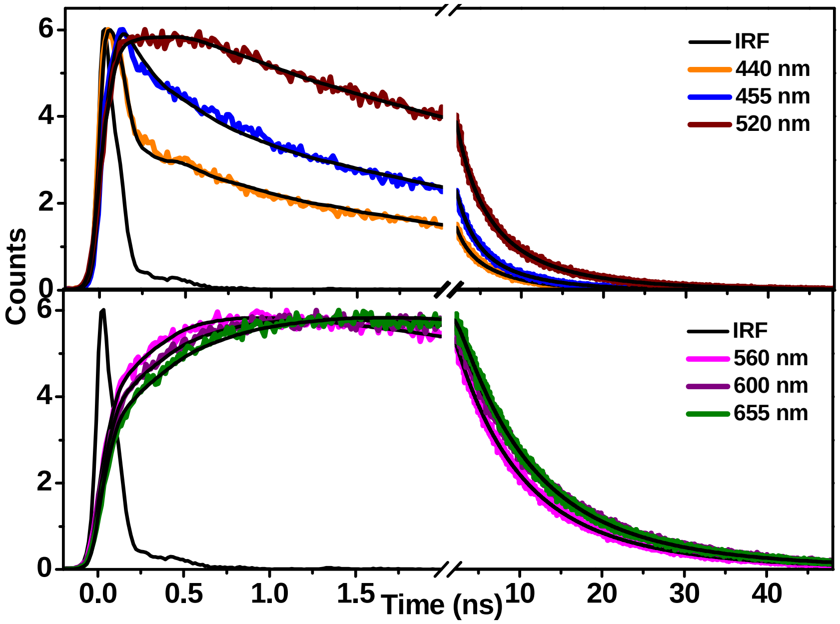

Figure 6.4: Temporal profiles recorded at a few selective wavelengths following photoexcitation of perylene nanoaggregate at 374 nm. Black lines represent the best-fit functions.

Table 6.1: Lifetimes (relative amplitudes)* estimated from the three-exponential fit to the temporal profiles recorded at three selective wavelengths following photoexcitation of perylene nanoaggregate.

Wavelength (nm)	τ_1 (a_1)	τ_2 (a_2)	τ_3 (a_3)
440	0.15 ns (35.3)	0.80 ns (41.6)	7.6 ns (23.1)
520	0.19 ns (-248.5)	0.81 ns (197.2)	7.7 ns (151.2)
600	0.20 ns (-186.4)	0.82 ns (-160)	9.8 ns (443.4)

*Positive and negative amplitudes are associated with the decay and rise lifetimes of the components, respectively.

Best-fit functions to the decay profiles have been used to construct the time resolved emission spectra (TRES) and time resolved area normalized emission spectra (TRANES), which have been shown in Figure 6.5.[53,54] Time evolutions of the TRES clearly support the inferences made in the previous paragraph regarding the dynamics of the S_1 excitonic state of perylene. Lifetime of the free excitonic state, which emits in the blue region of the TRES (440 – 480 nm), is comparable to the instrument response time (about 200 ps) or shorter because of very efficient trapping of the excitonic state in defect sites during its migration in the nanoaggregate matrix. This leads to formation of the excimeric states, which have strong emissions in the 490 – 750 nm region.

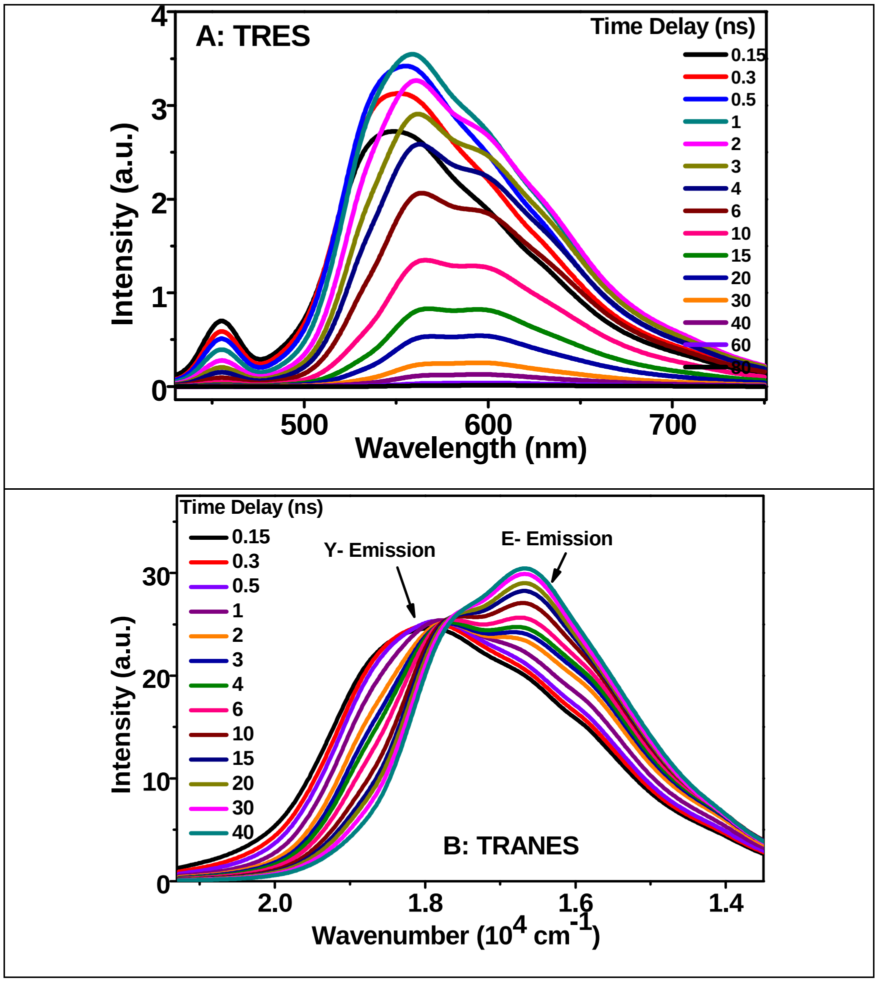

Figure 6.5: (A) Time-resolved emission spectra (TRES) of perylene nanoaggregate dispersed in water in nanosecond time domain.

(B) Time-resolved area normalized emission spectra (TRANES) of the excimeric emission of perylene nanoaggregate. The Y emission comes from an excitonic state in a shallow trap and the E emission comes from the self-trapped excitonic state in a deep trap or excimeric state.

On the other hand, the TRANES presented in Figure 6.5B provide us the information about the dynamics of the excimeric state, which may be described by a merely two-step process, as suggested by the appearance of a nearly isoemissive point at ca 17700 cm^{-1} or 565 nm. Initially, the free S_1 exciton while migrating in the nanoaggregate matrix relaxes to a swallow trap leading to an excitonic emission with the maximum at ca 17927 cm^{-1} or 557 nm. This emission has the lifetime of about 0.81 ns. Subsequently, this exciton further relaxes into a deep trap. The exciton in a deep trap may be considered as the excimeric state, which has the emission maximum at ca 16670 cm^{-1} or 600 nm (vide infra for energy level diagram) and the emission lifetime of about 8.5 ns. These two kinds of emission bands have been well characterized in the case of perylene crystals in earlier studies and they have been assigned to Y-emission and E-emission, respectively.[55-56] Well defined bands of the Y- and E-emissions and the presence of the isoemissive point suggest occurrence of two consecutive trapping processes and that the probability of the S_1 excitons being directly trapped in a deep trap is quite small (vide infra).

In the case of pyrene nanoaggregates, temporal profiles recorded at three selective wavelengths, along with the three exponential best-fit functions, are shown in Figure 6.6 and the estimated lifetimes and the relative amplitudes associated with the best-fit functions are provided in Table 6.2. Like in the case of perylene nanoaggregate, the dynamics of the S_1 excitonic state of pyrene generated in the nanoaggregate matrix also can be described by a three exponential process with the lifetimes of about 1.1 ± 0.1, 4 ± 1 and 27 ± 2 ns.

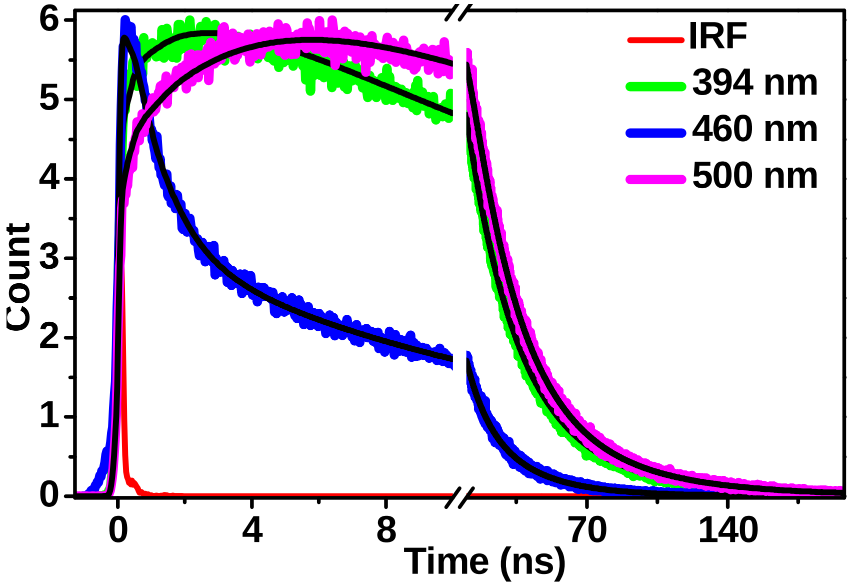

Figure 6.6: Temporal profiles for exctonic emission of pyrene in the nanoaggregate recorded at three selective wavelengths and the associated three exponential best-fit function. The best-fit parameters are provided in Table 6.2.

Table 6.2: Lifetimes (relative amplitudes)* estimated from the three exponential fit to the temporal profiles recorded at three selective wavelengths following photoexcitation of pyrene nanoaggregate.

Wavelength (nm)	τ_1 (a_1)	τ_2 (a_2)	τ_3 (a_3)
440	0.96 ns (40.4)	3.9 ns (25.5)	25.1 ns (33.5)
455	1.1 ns (-56.0)	4 ns (-8.7)	27.9 ns (162.9)
520	1.1 ns (-41.8)	4 ns (-159.9)	29 ns (383.7)

We also constructed the TRES and TRNES for the emission of pyrene nanoaggregate using the best fit functions to the decay profiles recorded in the 380 – 600 nm region (Figure 6.7). TRES shows the presence of dual emission bands at 0.15 ns delay time, which is the earliest time window for our TCSPC measurement. The sharp band in the 380 – 400 nm region with the maximum at 394 nm may be assigned to the emission from free S_1 excitonic state of pyrene nanoaggregate and the broad band in the 400 – 600 nm region with a flat top maximum at ca 450 nm is to the trapped exciton. As the delay time is increased up to about 4 ns delay time, time evolution of the TRES reveals quick decay of the excitonic band at 394 nm and a concomitant rise of intensity of the trapped exciton emission band accompanied by a dynamic shift of the mission band maximum to ca 465 nm and narrowing of the emission band width. On further increase in delay time, the emission band of the trapped exciton decay without any significant change in the shape of the emission spectrum.

TRANES (Figure 6.7B) provide a clearer picture about the dynamics of pyrene exciton in the nanoaggregate. The spectrum recorded at 0.15 ns delay time in the TRANES could really be resolved into three Lorenrzian bands with the maximum at 25360 cm^{-1} (394 nm), 22950 cm^{-1} (436 nm) and 21710 cm^{-1} (461 nm), which are assigned to free exciton, and excitons trapped at shallow traps (V-state) and deep traps (E-state), respectively.[58] However, time evolution of the TRANES reveals that, while emission intensity of both the free excitons and excitons at shallow traps decay with increase in delay time, intensity of the emission band due to the excitons in the deep trap or the excimeric species increases. In addition, time evolution of the excimeric emission is accompanied by a dynamic red shift of the emission maximum to 21070 cm^{-1} (475 nm) within 150 ns delay time. This dynamic red shift suggests energy stabilization of the excimeric species due to some kind of intra-excimeric geometrical relaxation process occurring inside the trap.

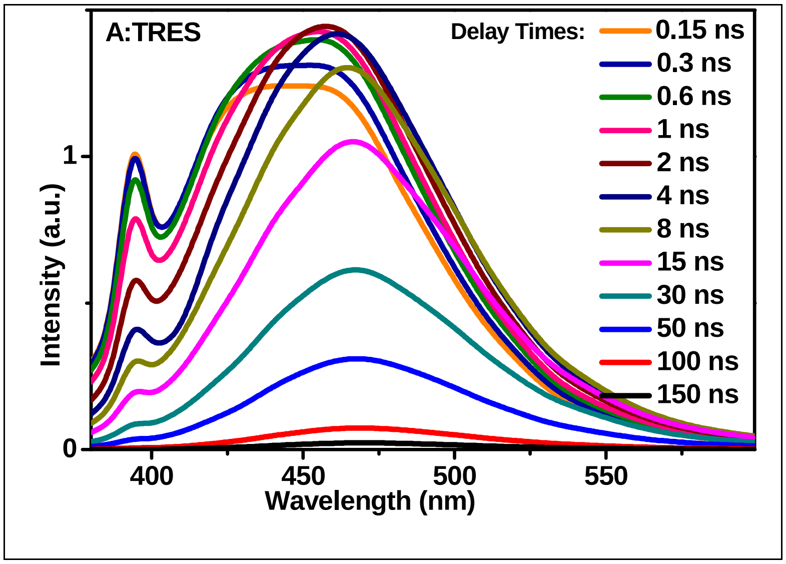

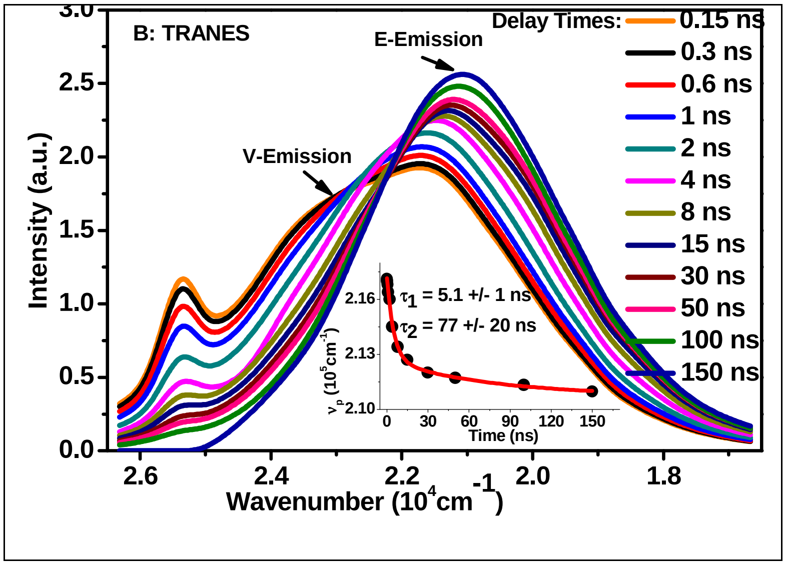

Figure 6.7: TRES and TRANES of pyrene nanoaggregate measured using TCSPC technique. The inset shows the peak frequency shift due to geometric relaxation of the excimer in deep trap.

We observed that for both the nanoaggregates, like in the cases of the crystalline states, the process of excimer formation from the free S_1 excitonic state occurs in two steps.[59, 60] To explore the possibility whether the excimer formation process is associated with any energy barrier, temperature dependence of the dynamics of the excimeric state has been investigated using the TCSPC technique. Temperature of the samples has been varied in the range of 15^0C to 75^0C and the temporal profiles have been recorded at 560 nm and 600 nm for pyrene and perylene nanoaggregates, respectively (Figure 6.8). In both the cases, we observed significant temperature dependence of the temporal profiles and the lifetimes associated with the best fit functions are given in Table 6.3.

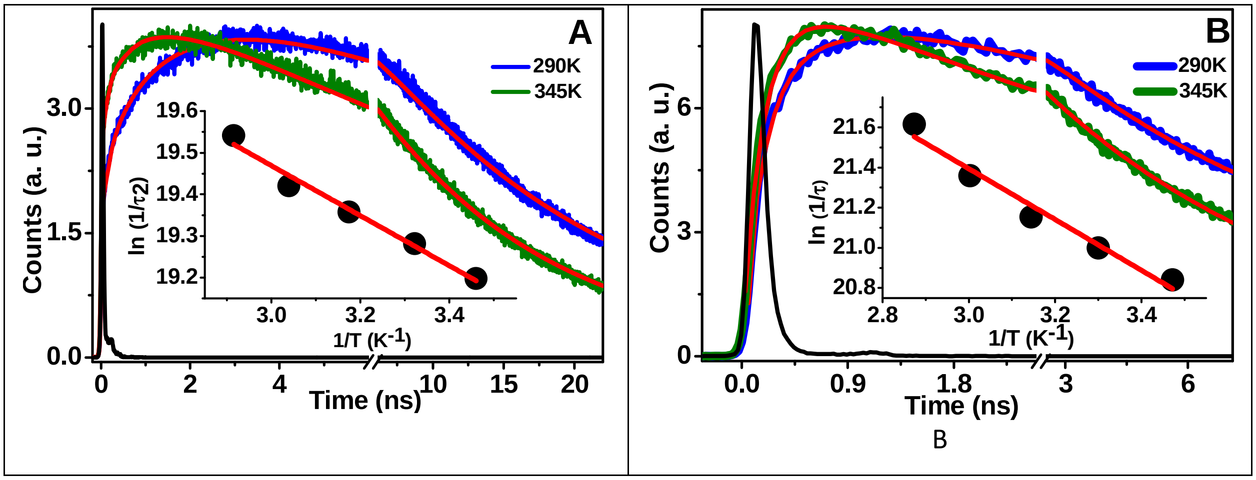

Figure 6.8: Temporal profiles recorded at 560 nm and 600 nm for pyrene (A) and perylene (B) nanoaggregates, respectively, at 290 and 345 K. Black curve is the instrument response function. Insets show the plot of ln(k) vs. 1/T for the respective nanoaggregates.

Table 6.3: Temperature dependence of the lifetimes of three components obtained by multiexponential fitting of the emission profiles recorded for pyrene and perylene nanoaggregates.

(A) Pyrene Nanoaggregate:

Temperature (K)	τ_1	τ_2	τ_3
289	1.01 ns	4.61 ns	32.3 ns
301	1.03 ns	4.23 ns	30.4 ns
315	0.98 ns	3.92 ns	28.5 ns
329	0.97 ns	3.68 ns	28.2 ns
343	0.95 ns	3.26 ns	27.1 ns

(B) Perylene nanoaggregate:

Temperature (K)	τ_1 (a_1)	τ_2 (a_2)	τ_3 (a_3)
288	0.18 ns (42.5)	0.89 ns (32.7)	8.04 ns (-86.1)
303	0.17 ns (63.5)	0.76 ns (33.3)	8.1 ns (-86.0)
318	0.17 ns (67.2)	0.65 ns (29.7)	7.8 ns (-89.4)
333	0.17 ns (71.9)	0.53 ns (23.6)	7.4 ns (-92.8)
348	0.16 ns (107.8)	0.41 ns (18.5)	7.1 ns (-95.3)

We observe significant temperature dependence of the lifetime component τ_2, which is associated with the excimer formation process or trapping of the exciton in deep traps. The rate constants of excimer formation (inverse of the lifetimes of the S_1 excitonic states in shallow trap, i.e. $(\tau_2)^{-1}$ in Tables 6.1 and 6.2) for perylene and pyrene estimated at different temperatures could be used to determine the energy barrier associated with the relaxation from the shallow trap to the deep trap from the Arrhenius plot (ln(k) vs. 1/T plot, insets of Figure 6.8). The energy barrier associated with excimer formation of pyrene is around 52 meV. On the other hand, the energy barrier associated in case of perylene nanoaggregates is around 107 meV.

Results of the time resolved fluorescence spectroscopic studies, which have been described here, lead us to propose the schematic diagrams of the excited state processes in these two nanoaggregate systems as shown in Figure 6.9. In the case of pyrene nanoaggregate, free excitons may directly be trapped in deep traps in addition to their trapping in swallow traps. The energy barrier for conversion of the excitons in the shallow traps to the excimeric states is small and hence the yield of the excimeric state is quite large in pyrene nanoaggregate. In the case of perylene, direct self trapping of free excitons to populate the excimeric state is less probable and hence the free excitons are initially trapped in a shallow trap and subsequent population of the excimeric state is associated with a relatively larger energy barrier. Dynamics of trapping of excitons generated in these nanoaggregate systems are very similar to those reported earlier in corresponding crystals.

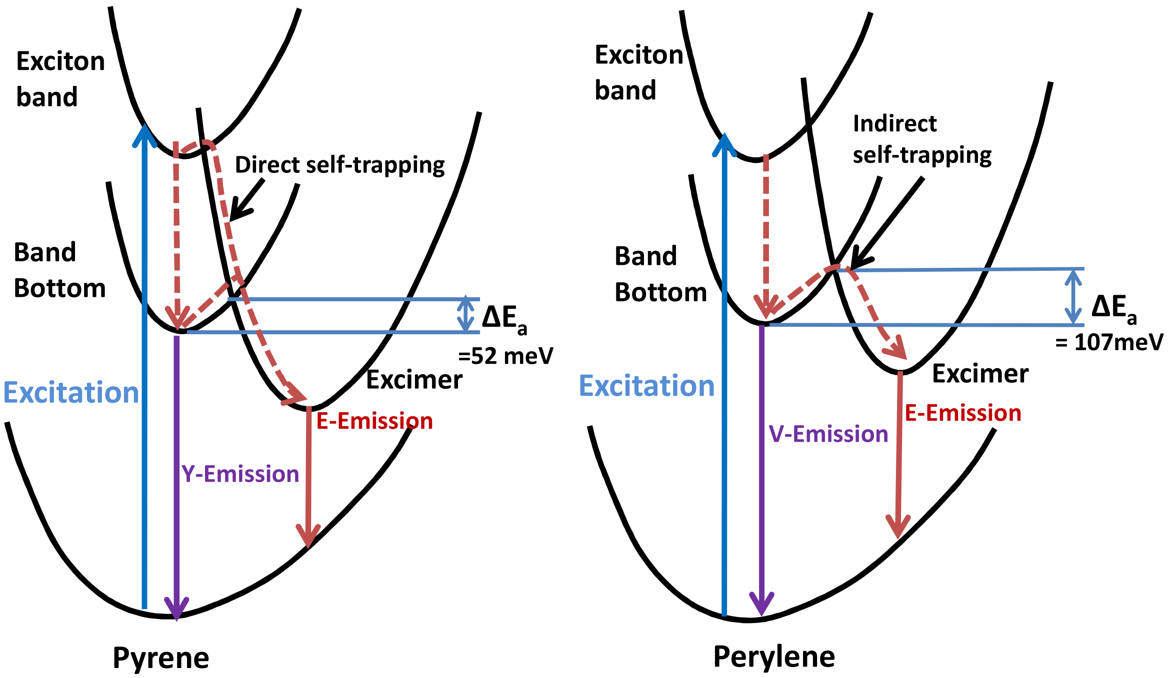

Figure 6.9: The schematic diagram depicting the processes for trapping of excitons in pyrene and perylene nanoaggregates.

6.2.4. Ultrafast Transient Absorption Study: Ultrafast transient absorption experiments have been carried out for both the samples to resolve the dynamics of excitons in sub-picosecond time domain. Following photoexcitation of perylene nanoaggregate dispersed in aqueous solution using 390 nm pump pulse, time resolved transient absorption spectra have been recorded in the 430 - 750 nm region and temporal dynamics have been analysed at a few selective wavelengths to reveal the exction decay processes. Transient spectrum recorded at 0.25 ps delay time shows a broad excited state absorption (ESA) band in the 480 – 750 nm region overlapped with a bleaching band with the maximum at ca 460 nm (Figure 6.10). With increase in delay time, the ESA band decays within 1 ns, but without significant recovery of the bleaching band. In addition we observe the development of a stimulated emission (SE) band in the 500 – 700 nm region with the maximum at 580 nm after 200 ps delay time. Comparison between this SE spectrum and the spectrum in the TRES recorded at similar delay times, provides an evidence for the presence of excitons in both shallow and deep traps.

Within the broad envelop of the ESA band of the differential absorption spectrum of the S_1 excitonic state recorded at 0.25 ps delay time, we identify two ESA bands with the maxima at

500 nm and 650 nm,. Analyses of the temporal profiles at a few selective wavelengths (Figure 6.11) reveal that these two bands decay with very similar lifetimes. We assign these two bands to perylene radical cation ($Pe^{2+\bullet}$) and deloclalized electron (e_{matrix}) in the nanoaggregate matrix, which are the constituent parts of the perylene excitonic species created following photoexcitation of the nanoaggregate.[61]

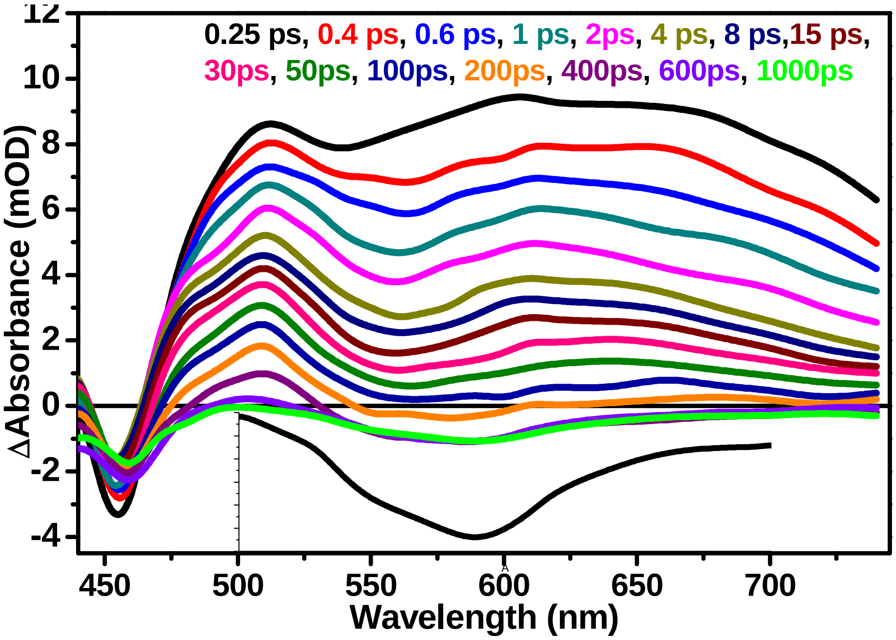

Figure 6.10: Time resolved transient absorption spectra recorded following photoexcitation of perylene nanoaggregate dispersed in water. Inset shows one portion of the transient absorption spectra recorded at 1000 ps delay time on the magnified scale to show the stimulated emission band.

Temporal profiles, recorded at three selective wavelengths, at which the effect of negative absorption bands, namely the bleaching and stimulated emission bands, are minimum, are shown in Figure 6.11. Each of these profiles could be fitted well using a three exponential function with the lifetimes of 0.5 ± 0.1, 5.8 ± 0.3 and 185 ± 5 ps. We will discuss in the following section that the decay process of the free exciton really follows a nonexponential dynamics and assignment of the first two of the three components can be made from the intensity dependent dynamics of exciton. However, the third component with the lifetime of about 185 ps may be assigned to the intrinsic decay lifetime of free exciton created in the nanoaggregate matrix and this agrees quite well with that predicted from the results of TCSPC measurements (see the values of τ_1 in Table 6.1).

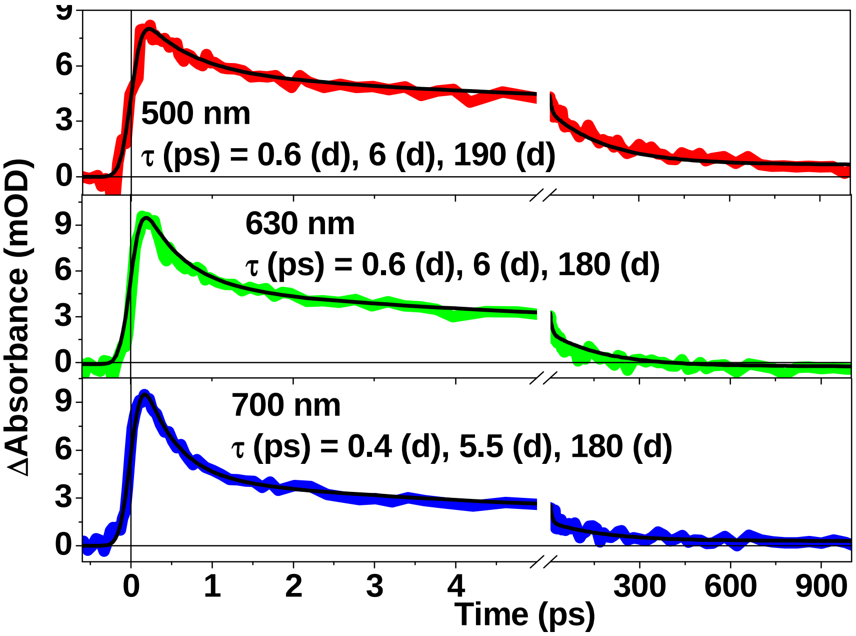

Figure 6.11: Temporal dynamics of free excitons in perylene nanoaggregate recorded at three selective wavelengths. Nonexponential dynamics of the exciton has been fitted with a three exponential function and the lifetimes estimated at different probe wavelengths are very similar.

In Figure 6.12, we have shown the time resolved transient absorption spectra of pyrene nanoaggregate dispersed in water, recorded following photoexcitation using 260 nm pump. Spectroscopic characteristics and dynamics of the transient species associated with the time evolution of the transient spectra are very similar to those described in the case of perylene nanoaggregate. In this case, the absorption of the pyrene radical cation ($Py^{2+\bullet}$) appears as a shoulder at 450 nm to the very broad ESA band of the delocalized electron in the 470 – 700 nm region.[62, 63] In addition, features of the broad and flat-top SE band with the centre of maximum at ca 450 nm recorded at 600 ps delay time are very similar to those associated with the emission spectra recorded in the sub 1 ns time domain of the TCSPC experiment (see Figure 6.7A).

Analysis of each of the temporal profiles recorded at three selective wavelengths in the region of the ESA band of the S_1 excitonic state of pyrene nanoaggregate reveals nonexponential dynamics, which could be fitted well with a three exponential function with the lifetimes of 0.6 ±

0.1, 48 ± 3 and >500 ps (Figure 6.13). Like in the case of perylene, assignment of the first two components will be made only from the intensity dependence of exciton dynamics, while the third component is related to the intrinsic decay lifetime of the free excitonic state. Considering the maximum range of the delay time could be used in our transient absorption experiments (up to about 1.2 ns), estimation of the lifetimes longer than 500 ps has not been possible. However, our TCSPC measurements revealed that this value is about 1 ns (see the value of τ_1 in Table 6.2).

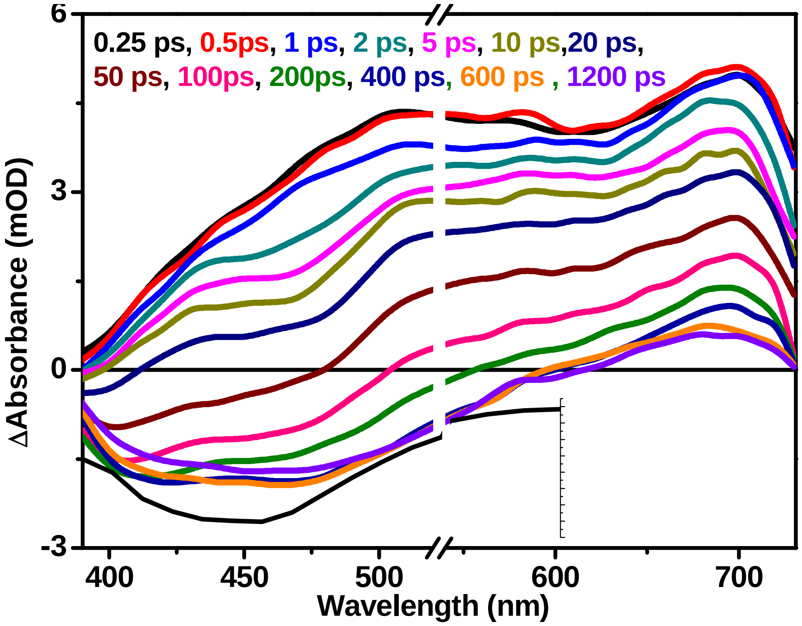

Figure 6.12: Time resolved transient absorption spectra recorded following photoexcitation of pyrene nanoaggregate dispersed in water. Inset shows time resolved emission spectrum recorded at 0.6 ns delay after photoexcitation at 374 nm using TCSPC technique.

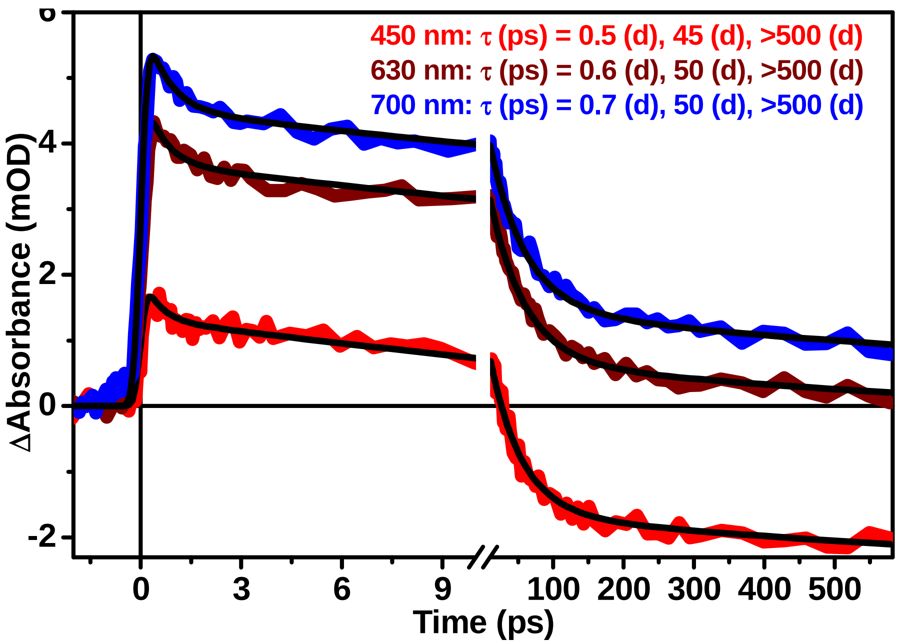

Figure 6.13: Temporal dynamics of free excitons in pyrene nanoaggregate at three selective wavelengths. Non exponential dynamics of the exciton has been fitted with a three exponential function and the lifetimes estimated at different probe wavelengths are very similar.

6.2.4.1. Excitation intensity dependent study: In Figure 6.14, we show the intensity dependence of the temporal dynamics of the S_1 excitonic state in perylene nanaoaggregate recorded at 630 nm. If they are fitted using a three exponential function, the lifetimes of two shorter lived components become faster as the intensity of the pump light increases (see table S6.1 in SD section). But that of the third component, which has been assigned to the intrinsic decay lifetime of the free excitonic state, remains more or less independent of intensity of the pump pulse used for excitation. Intensity dependence of the lifetimes of two ultrafast components suggests occurrence of a second order process because of creation of higher concentrations of free excitons at larger pump intensities. Exciton - exciton annihilation reaction is a well-known process when the exciton density is sufficiently large.[64-68] Therefore, we expect the temporal dynamics to follow a mixed order kinetics: the first order component represents the natural decay of the free excitonic state, while the exciton – exciton annihilation process follows the second order decay process. Following our earlier approach applied to investigation of exciton dynamics in anthracene nanoaggregates, we analyse the exciton dynamics in perylene and pyrene nanoaggregates using the following reaction scheme (eqs. 6.1 -6.3).[60] Free S_1 excitonic state undergoes the following photophysical processes.

$$S_1 \xrightarrow{k_1} S_0 \qquad (6.1)$$

$$S_1 + S_1 \xrightarrow{k_2} S_n + S_0 \qquad (6.2)$$

$$S_1 + S_0 \xrightarrow{k_3} E \qquad (6.3)$$

Expression for the rate of change of concentration of the S_1 excitonic state may be written as,

$$\frac{d[S_1]}{dt} = -k_1'[S_1] - \frac{k_2[S_1]^2}{2} \qquad (6.4)$$

Here k_1' represents the annihilation free decay of the excitonic state, i.e. k_1' = k_1 + k_a. $[S_0]$, the concentration of the host molecules in the ground state, has been assumed to be very large and a constant. k_2 is the rate constant for the exciton – exciton annihilation reaction. Solution of equation 6.4 gives us the concentration of the S_1 excitonic state at a particular time t after photoexcitation, $[S_1]_t$.[63]

$$[S_1]_t = [S_1]_0 \ \frac{\exp(-k_1' t)}{(1+k_2')} \qquad (6.5)$$

Here k_2' = $k_2 [S_1]_0 / 2$

Excited state absorption due to the S_1 excitonic state may be assumed to be proportional to $[S_1]_t$.

Hence equation 6.5 may be written as,

$$\Delta OD(t) = \Delta OD(t=0) \ \frac{\exp(-k_1' t)}{(1+k_2' t)} \qquad (6.6)$$

Excimer formation also contributes to the total differential absorption signal, and its contribution is proportional to the concentration of the excimeric state, [E]. According to eq. 6.3, concentration of the excimeric state at time t may be evaluated by solving the differential eq. 6.7.

$$\frac{d[E]}{dt} = k_3\,[S_0]\,[S_1] \qquad (6.7)$$

Using the value of $[S_1]_t$ estimated in eq. 6.7 and taking the assumption that $[S_0]$ is a constant, we may solve the above equation to get the final form,

$$[E] = [S_1]_0 k_3 [S_0] t [\exp(-k_1 t)] \qquad (6.8)$$

Here stimulated emission from the excimeric state will contribute to differential absorption as a negative signal and it may be represented as,

$$[\Delta\mathrm{OD}]_{SE} = -[\Delta\mathrm{OD}]_0\, k_3' t [\exp(-k_1 t)] \qquad (6.9)$$

Here k_3' = $k_3[S_0]\alpha$ and α is introduced as the proportionality constant for concentration to absorption signal conversion.

The total differential transient absorption signal in this ultrafast time scale has major contributions from three components and may be represented in the following form,

$$[\Delta OD]_{Total} = [\Delta\mathrm{OD}]_{ESA} + [\Delta\mathrm{OD}]_{SE} + R \qquad (6.10)$$

$$[\Delta OD]_{Total} = [\Delta\mathrm{OD}]_0\, X \frac{[exp(-k_1' t)]}{(1+k_2' t)} - [\Delta\mathrm{OD}]_0\, k_3' t [\exp(-k_1' t)] + R \qquad (6.11)$$

R is the residual differential absorption signal for the long-lived excimeric state. The temporal profiles recorded at different wavelengths could be fitted using Equation 6.11.

As we mentioned earlier that decrease in excitation energy density leads to lowering the rate of exciton - exciton annihilation, study of dependence of the excition decay rates on excitation energy density not only helps us to identify the process but also helps us to estimate the exciton diffusion coefficient and exciton diffusion length in the nanomaterials because the exciton – exciton annihilation reaction is well known to be a process controlled by the rate of exciton diffusion. There are numerous report, which describe the methods of estimation of the exciton diffusion parameters by varying the intensity of pump light.[38, 43-46] Exciton diffusion length in perylene crystal having β phase has been estimated using the same method.[38] However for perylene nanoaggregates no such reports are available and hence here we estimate those parameters in perylene and pyrene nanoaggregates to compare them with those estimated in the crystals.

In the case of perylene nanoaggregate, energy of the excitation pulse of 390 nm has been varied in the range of 11 μJ/pulse to 3 μJ/pulse and the temporal profiles have been recorded at 630 nm. Each of these temporal profiles have been fitted following equation 6.11 and the fitting parameters are provided in Table 6.4. We have also recorded the temporal profiles at 500 nm and 700 nm and analysed (See S6.2 in SD section) and the results are found to be similar to those obtained with the analysis of the profile recorded at 630 nm. The k_2' value thus obtained has been used for determination of exciton – exciton annihilation rate constant, k_2, from the slope of the linear plot of k_2' vs. initial exciton density, $[S_1]_0$. Values of the exciton density for different excitation energies could be estimated following the procedure described in SD section (S6.3). Value of the exciton - exciton annihilation rate constant (k_2) for perylene nanoaggregates thus determined is 1.72 x 10^{-9} cm^3 s^{-1}. Results for the pyrene nanoaggregates have been discussed in supporting Information section.

$$k_2 = 8\pi D R_a \qquad (6.12)$$

$$L_D = (6D\tau)^{1/2} \qquad (6.13)$$

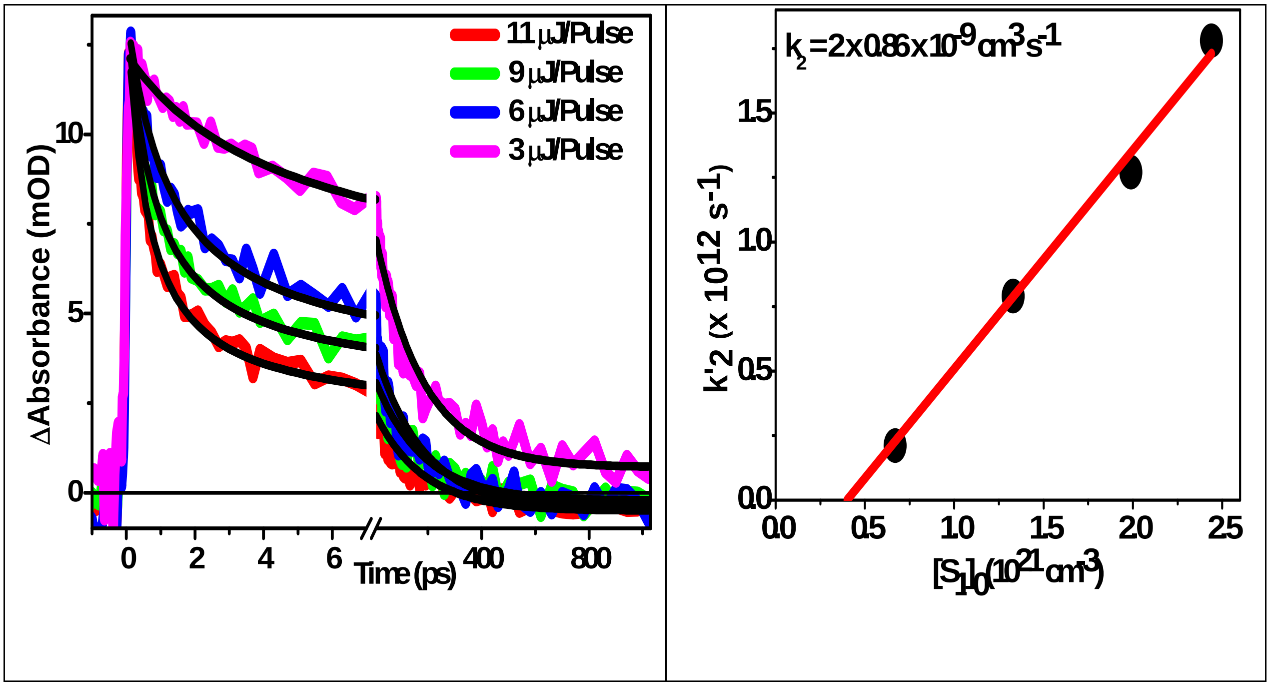

Figure 6.14: (A) Temporal profiles recorded at 630 nm for different excitation pulse energies for perylene nanoaggregates and (B) k'_2 vs. initial exciton density, $[S_1]_0$ plot.

Table 6.4: Fitting parameters of the temporal profiles using equation 6.11 recorded at 650 nm for perylene nanoaggregates after exciting the sample 390 nm light with different energy/pulse.

Pulse energy	**$[S_1]_0$ (10^{21} cm^{-3})**	**$[OD]_0$ (10^{-3})**	**k_1 (10^9 s^{-1})**	**k'_2 (10^{12} s^{-1})**	**k'_3 (10^9 s^{-1})**
11 µJ/pulse	2.44	11.65	5.2	1.78	1.25
9 µJ/pulse	1.99	10.5	5	1.27	1.37
6 µJ/pulse	1.33	9.84	5.2	0.79	1.15
3 µJ/pulse	0.67	6.6	5.2	0.21	1.29

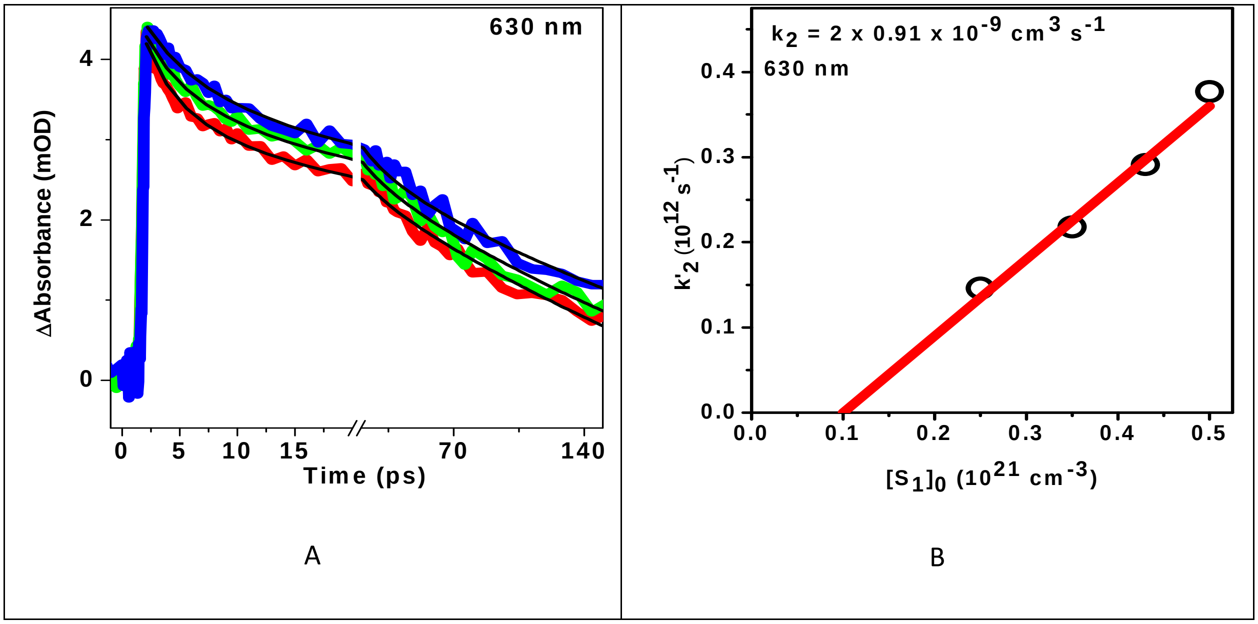

A

B

Figure 6.15:(A) Temporal profiles recorded at 630 nm for different excitation pulse energies for pyrene nanoaggregates and (B) k'_2 vs. initial exciton density, $[S_1]_0$ plot.

Table 6.5: Fitting parameters of the temporal profiles using equation 6.11 recorded at 630 nm for pyrene nanoaggregates after exciting the sample 266 nm light with different energy/pulse.

Pulse energy	**$[S_1]_0$ (10^{21} cm^{-3})**	**$[OD]_0$ (10^{-3})**	**k_1 (10^9 s^{-1})**	**k'_2 (10^{12} s^{-1})**	**k'_3 (10^9 s^{-1})**
20 µJ/pulse	0.50	3.18	1	0.377	4.5
17 µJ/pulse	0.43	2.81	1	0.291	4.9
14 µJ/pulse	0.35	2.57	1	0.218	5.1
10 µJ/pulse	0.25	2.48	1	0.146	4.7

Since the exciton – exciton annihilation process follows second order reaction kinetics and controlled by the rate of exciton diffusion, the later is related to the diffusion coefficient (D) of the exciton by equation 6.12. In this equation, R_a represent exciton annihilation radius for that material. Exciton annihilation radius has been evaluated from the number of photons absorbed at the condition of onset of annihilation. The onset of annihilation may be defined as the exciton density above which exciton annihilation rate constant posses non-zero value. In the case of perylene nanoaggregate, we determine the value of exciton density for the threshold of annihilation reaction, $[S_1]_0$, to be about 0.4 x 10^{21} cm^{-3}. This value could be used to estimate the value of the exciton annihilation radius, R_a, to be about 0.84 nm. Introduction of this value of R_a in the equation 6.12, helps us to get the value of the diffusion coefficient of excitons, D, in perylene nanoaggregate to about 9.1×10^{-4} $cm^2. s^{-1}$.

The three dimensional exciton diffusion length, L_D, in a material may be estimated using equation 6.13. Here τ represents the life time of the excitonic state. In the present cases, we are mainly observing the annihilation process of free excitons, produced immediately after photo excitation. These free excitons undergo natural decay with the exciton lifetime of 190 ps. The free excitons in perylene nanoaggregate found to have exciton diffusion length of 10.2 nm.

It has been observed that in the case of nanoaggregates the free exciton lifetime increases significantly as compared to that of the free exciton lifetime in the α crystalline phase.[69] Due to very short lifetimes of the free excitonic states of the α form, one may expect that the exciton diffusion lengths should also be smaller by an order of magnitude and hence efficiencies of these materials are expected to be reduced significantly in the cases of their applications in photovoltaic and other optoelectronic applications.[36] However, considering the isotropic diffusion nature in the case of perylene nanoaggregate (equation 6.13), we estimate the value of the exciton diffusion length of 10.2 nm. Therefore, the nanaoaggregates having α-crystalline phase are expected to be better materials for the above applications as compared to that of the crystals.

We also estimated those photophysical parameters of the excitonic states in the case of pyrene nanaoaggregates from the excitation pulse energy dependence of the dynamics of the excitonic state upon photoexcitaion at 260 nm using excitation energies in the range of 10 - 20 μJ/Pulse. The temporal profiles recorded at 630 and 700 nm are fitted using equation 6.11. The temporal profiles recorded at 630 nm using different pump intensities are provided in Figure 6.15 and the corresponding fitting parameters are provided in table 6.5. Following the similar methodologies as employed for perylene nanoaggregates, the diffusion parameters are estimated. The photophysical parameters of the excitonic states generated in pyrene nanoaggregate have been compared with those of perylene nanoaggregate in Table 6.6. Like in the case of perylene nanoaggregate, the free exciton lifetime in pyrene nanoaggregates are also observed to be enhanced and exciton diffusion length (L_D ~ 20 ± 4 nm) is also significantly longer.

Table 6.6: Exciton annihilation rate constant, annihilation radius, diffusion coefficient, lifetime, diffusion length estimated for pyrene and perylene nanoaggregates in the present work.

NA System	**Wavelength**	**k_2 (10^{-9} cm^3 s^{-1})**	**R_a (nm)**	**D (x 10^{-4} cm^{-2} s^{-1})**	**τ (ns)**	**L_D (nm)**
Pyrene	630 nm	1.82	1.36	5.34	1	17.8
	700 nm	2.64	1.06	9.91	1	24.4
Perylene	500 nm	1.26	1.06	4.7	190	7.3
	630 nm	1.72	0.84	9.1	190	10.2
	700 nm	3.74	1.33	11.2	190	11.3

6.3. CONCLUSION

The present work indicates that both of the pyrene and perylene nanoaggregates can be prepared using reprecipitaion method having most probable size of 120 nm and these nanoaggregates are mostly dominated by the α-phase of molecular packing. The emission spectra also show broad excimer emission in both the cases and confirm the presence of α-phase. The pyrene excimer emission is highly efficient and comparable with the emission yield of its monomeric form. On the other hand the perylene excimer emission is weak and it shows almost two order decrease in the emission yield than that of the monomeric form. The time resolved fluorescence measurement leads us to the confirmation of presence of emission from free excitonc state, shallow and deep trap excitonic states in these two nanoaggregates. The temperature dependent time resolved study of the growth of excimeric states in these to NAs is employed to estimate the associated energy barrier in this process. The shallow trap to deep trap state transition found to possess the energy barriers of 57 meV and 102 meV for pyrene and perylene nanoaggregate, respectively.

In nanoaggregate form the free exciton lifetime found to be enhanced as compared to the corresponding α-crystalline form. It causes enhancement in the exciton diffusion length of free excitons in the nanoaggrgate form. The exciton diffusion lengths are 10 ± 2 nm and 20 ± 4 nm for perylene and pyrene nanoaggregates, respectively.

6.4. REFERENCES

1. Liu, H.; Xu, J.; Li, Y. *Acc. Chem. Res*. **2010,** *43*, 1496.
2. Cui, S.; Liu, H.; Gan, L.; Li, Y., Zhu, D. *Mater* **2008,** *20*, 2918.
3. Palmer, L. C.; Stupp, S. I. *Acc. Chem. Res*. **2008,** *41*, 1674.
4. Rao, C. N. R.; Kulkarni, G. U.; Thomas, P. J.; Edwards, P. P. *Chem. Soc. Rev.* **2000**, *29*, 27.
5. Devenish, R. W.; Goulding, T.; Heaton, B. T.; Whyman, R. *J. Chem. Soc., Dalton Trans.* **1996**, 673.
6. Tenne, R.; Redlich, M. *Chem. Soc. Rev*. **2010**, *39*, 1423.
7. Yildiz, I.; E. Deniz, E.; Raymo, F. M. *Chem. Soc. Rev*. **2009**, *38*, 1859.
8. Bhongle, C. J.; Chang, C. W.; Lee, C. S.; Diau, E. W. G.; Shu, C. *J. Phys. Chem. B.* **2005**, *109*, 13472.
9. Yao, H.; Yamashita, M.; Kimura, K. *Langmuir* **2009,** *25*, 1131.
10. Xiao, J.; Yang, H.; Yin, Z.; Guo, J.; Boey, F.; Zhang, H.; Zhang, Q. *J. Mater. Chem.* **2011**, *21*, 1423.
11. Gesquiere, A. J.; Uwada, T.; Asahi, T.; Masuhara, H.; Barbara, P. F. *Nano Lett.* **2005**, *5*, 1321.
12. Lei, Y.; Liao, Q.; Fu, H.; Yao, J. *J. Phys. Chem. C*. 2009, *113*, 10038.
13. Zhang, X.; Zhang, X.; Shi, W.; Meng, X.; Lee, C.; Lee, S. *J. Phys. Chem. B* **2005**, *109***,** 18777.
14. Xiao, D.; Xi, L.; Yang, W.; Fu, H.; Shuai, Z.; Fang, Y.; Yao, J. *J. Am. Chem. Soc.* **2003,** *125,* 6740-6745.

15. Meng, H.; Sun, F.; Goldfinger, M. B.; Jaycox, G. D.; Li, Z.; Marshall, W. J.; Blackman, G. S. *J. Am. Chem. Soc***. 2005,** *127*, 2406.

16. Zhang, C.; Zhang, J. Y.; Zhao, Y. S.; Yao, J. *Chem. Comm*. 2010, *46*, 4959.

17. Garnett, E.; Yang, P. *Nano. Lett.* **2010**, ***10,*** 1082.

18. Gabor, N. M.; Zhong, Z.; Bosnick, K.; Park, J.; Mceuen, P. L. *Science* 2009, *325*, 1367.

19. Zhao, Y. S.; Zhan, P.; Kim, J.; Sun, C.; Huang, J. *Acs Nano* **2010,** *4*, 1630.

20. Yu, J. Y.; Chen, I. W. P.; Chun-hsien Chen, C. H.; Lee, S. J.; Chen, I. C.; Lin, C. S.; Cheng, C. H. *J. Phys. Chem. C* **2008**, *112,* 3097.

21. Chao, Y. C.; Chung, C. H.; Zan, H. W.; Meng, H. F.; Ku, M. C. *Appl. Phys. Lett.* **2011,** *99*, 233308.

22. Liang, W. W.; Chang,C. Y.; Lai, Y. Y.; Cheng, S. W.; Chang, H. H.; Yin-Yu Lai, Y. Y.; Cheng, Y. J.; Wang, C. L.; Hsu, C. S. *Macromolecules* **2013**, *46*, 4781.

23. Kim, H. Y.; Bjorklund, T. G.; Lim, S. H.; Bardeen, C. J. *Langmuir* **2003**, *19*, 3941**.**

24. Jana, A.; Devi, K. S. P., Maiti, T. K.; Singh, N. D. P. *J. Am. Chem. Soc.* **2012**, *134,* 7656.

25. Zhu, L.; Wu, W.; Zhu, M. Q.; Han, J. J.; Hurst, J. K.; A. D. Q. Li, A. D. Q. *J. Am. Chem. Soc.* **2007**, *129***,** 3524.

26. Katoh, R.; Sinha, S.; Murata, S.; Tachiya, M. *J. Photochem. Photobiol. A: Chem.* **2001**, *145*, 23.

27. Chung, H. R.; Kwon, E.; Oikawa, H.; Kasai, H.; Nakanishi, H. *J. Crystal growth*. **2006**, *294,* 459.

28. Seko, T.; Ogura, K.; Kawakami, Y.; Sugino, H.; Tanaka, J. *Chem. Phys. Lett.* **1998**, *291*, 438.

29. Oliveira, D.; Baba, K.; Teizer, W.; Kasai, H.; Oikawa, H.; Nakanishi, H. *Nanocrystal, Intech*, **2011.**

30. Wu, J. H.; Xu, T. Z.; Ang, S. G.;. Xu, G. Q. *Nanoscale* **2011**, *3*, 1855.

31. Liu, H.; Li, Y.; Xiao, S.; H. Gan, H.; Jiu, T.; Li, H.; Lei, J.; Zhu, D.; Yu, D.; B. Xiang, B.; Chen, Y. *J. Am. Chem. Soc.* 2003, *125*, 10794.

32. Zhao, M.; Wang, S.; Bao, Q.; Wang, Y.; P. K. Aug, P. K.; Loh, K. P. *Chem. Commun.* **2011**, *47*, 4153.

33. Latterini, L.; Roscini, C.; Carlotti, B.; Aloisi, G. G.; Elisei, F. *Phys. Stat. Sol. A* **2006**, *203*, 1470.

34. Kang, L.; Wang, Z.; Cao, Z.; Ma, Y.; Fu H.; Yao, J. *J. Am. Chem. Soc.* **2007**, *129*, 7305.

35. Tachikawa, T.; Chung, H. R.; Masuhara, A.; Kasai, H.; Oikawa, H.; Nakanishi, H.; Fujitsuka M.; Majima, T. *J. Am. Chem. Soc.* **2006,** *128***,** 15944.

36. Fujino, T.; Tahara, T. *J. Phys. Chem. B* **2003,** *107*, 5120.

37. Furube, A.; Murai, M.; Tamaki, Y**.;** Watanabe, S.; Katoh, R. *J. Phys. Chem. A* **2006,** *110*, 6465.

38. Fujino, T.; Fujima, T.; Tahara, T. *J. Phys. Chem. B* 2005, *109*, 15327.

39. Yago, T.; Tamaki, Y.; Furube, A.; Katoh, R. *Phys. Chem. Chem. Phys*. **2008,** *10*, 4435.

40. Kakade, S.; Ghosh, R.; Palit, D. K. *J. Phys. Chem. C*. **2012**, *116***,** 15155.

41. Ibe, S.; Ise, R.; Oaki, Y.; Imai, H. *Cryst. Eng. Comm.* **2012**, *14*, 7444.

42. Lei, Y.; Liao, Q.; Fu,h.; Yao, J. *J. Phys. Chem. C* **2009**, *113*, 10038.

43. Ishii, A.; Miyasaka, T. A. *Chem. Phys. Chem.* **2014**, *15*, 1028.

44. Jiang, H.; Zhang, K. K.; Ye, J.; Wei, F.; Hu, P.; Guo, J.; Liang, C.; Chen, X.; Zhao, Y. McNell, L. E.; Hu, W.; Kloc, C. *Small* **2013**, *9*, 990.

45. Berlman, I. B. "Handbook of Fluorescence Spectra of Aromatic Molecules," Academic Press,N. Y. **1965**.

46. Barks, J. B. Wiley-Interscience, New York, **1970**.

47. Mataga, M.; Kupota, T. Molecular Interactions and Electronic Spectra, Dekkcr, New York, **1970**.

48. Mataga, M.; Torihashi, Y.; Ota, Y. *Chem. Phys. Lett.* **1967**, *1*, 385.

49. Vrbelis, J. H.; Swift, J. A. *Cryst. Growth. Des*. **2014**, *14,* 5244.

50. Yago, T.; Tamaki, Y.; Furube, A.; Katoh, R. *Chem. Lett.* **2007**, *36*, 370.

51. Ito. F.; Kogasaka, Y.; Yamamoto, K. *J. Phys. Chem. B* **2013**, *117*, 3675.

52. Pick, A.; Kluest, M.; Rinn, A.; Harms, K.; Witte, G. *Cryst. Growth. Des.* **2015**, *15*, 5495.

53. Koti, A. S. R.; Krishna, M. M. G.; Periasamy, N. *J. Phys. Chem. A* **2001**, *105*, 1767.

54. Koti, A. S. R.: Periasamy, N. *Res. Chem. Intermed.* **2002**, *28*, 831.

55. Mahrt,J.; Willig, F.; Storck, W.; Weiss, D.; Kietzmann, R.; Schwarzburg, K.; Tufts, B.; Trösken, B. *J. Phys. Chem.* **1994**, *98*, 1888.

56. Tange, M.; Okazaki, T.; Liu, Z.; Suenaga, K.; Iijima, S.; *Nanoscale*, **2016**, *8*, 7834.

57. Weiss, D.; Kietzmann, R.; Mahrt, J.;Tufts, B.; Storck, W.; Willig, F. *J. Phys. Chem.* **1992**, *96*, 5320-5325.

58. Mizuno, K.; Matsui, A. *J. Luminescence* **1987**, *38*, 323.

59. Walker, B.; Port, H.; Wolf, H. C. *Chem. Phys.* **1985**, *92*, 177.

60. Seyfang, R.; Port, H.; Wolf, H. C. *J. Luminescence*. 1988, *42*, 127.

61. Tamai, N.; Porter, C. F.; Masuhara, H. *Chem. Phys. Lett.* **1993**, *211*, 364.

62. Manna, B.; Ghosh, R.; Palit, D. K. *J. Phys. Chem. B* **2013**, *113*, 5113.

63. Foggi, P.; Pettini, L.; Sànta, I.; Righini, R.; Califano, S. *J. Phys. Chem.* **1995**, *99*, 7439.

64. Manna, B.; Ghosh, R.; Palit, D. K. *J. Phys. Chem. C*. **2015**, *119*, 10641-.

65. Paillotin, G.; Swenberg, C. E.; Breton, J.; Geacintov, N. E. *Biophys. J.* **1979,** *25*, 513.

66. Sundstrom, V.; Gillbro, T.; Gadonas, R. A.; Piskarskas, A. *J. Chem. Phys.* **1988**, *89*,2754.

67. Valkunas, L.; Akesson, E.; Pullerits, T.; Sundstrom, V. *J.* **1996**, *70*, 2373-2379.

68. Manna, B.; Ghosh, R.; Palit, D. K. *J. Phys. Chem. C.* **2016**, *120*, 10641.

69. Inoue, A.; Yoshihara, K.; Kasuya, T.; Nagakura, S. *Bull. Chem. Soc. Japan.* **1972**, *45*, 720.

CHAPTER 7

PHOTOPHYSICS AND EXCITON DYNAMICS IN NANOAGGREGATES OF PHTHALOCYANINES AND THEIR ZINC DERIVATIVES

7.1 INTRODUCTION

Organic semiconductors provide emerging technology for consumer electronics. Organic light emitting diodes (OLEDs) have already entered into the market as they offer more vibrant colours when compared to conventional liquid crystalline screens.[1] Organic photovoltaics (OPV) promise flexible and inexpensive solar cells, which will find niche applications for smart power generation in portable devices of daily usage.[2] These devices convert electricity to light or light to electrical current using excited state species called excitons. Dynamics of excitons determine key device performance characteristics such as power conversion efficiency of solar cells and brightness of OLEDs.[3]

Exciton diffusion length (L_D) is the characteristic distance that excitons are able to diffuse during their lifetime in a given material. Organic materials having a long exciton diffusion length are desirable for improving the efficiency of the device and hence understanding the factors that limit exciton diffusion length is important.[4, 5] Organic crystals show a large spread of L_D ranging from 1 to 100 nanometers for singlets and up to several micrometers for triplet excitons.[6 - 17] The majority of amorphous materials show singlet exciton diffusion length of 5–10 nm despite large variability in chemical structure.[3] It has been suggested that singlet exciton diffusion length is limited by excitonic traps, which are present in every solution-processed organic semiconductor. However, the nature of these traps still has to be identified in order to reduce or eliminate their impact on exciton diffusion. The inherent disorder present in organic semiconductors to large extent determines physical processes related to exciton diffusion. Controlling exciton diffusion length remains an interesting topic of research.

Exciton diffusion has been studied in large number of small molecules and conjugated polymers in crystalline as well as amorphous matrices.[3, 18 - 21] However, it remains challenging to understand the relationship between the chemical structure and the exciton diffusion length. There are only a few works which investigate exciton diffusion length as a function of molecular structure.[4, 22 - 25] In particular the effect of conjugation length on the exciton diffusion has not been addressed. It is not really clear why the exciton diffusion length is so similar in such a broad selection of materials and what factors really influence the exciton diffusion length. To answer these questions systematic measurements of exciton diffusion lengths are needed in materials with various molecular structures, morphologies and molecular packing effeciencies.[4, 26 - 28]

Bioinspired molecular materials such as derivatives of phthalocyanine and porphyrin offer promising prospects for the realization of efficient exciton diffusion.[29] The molecular structure of these molecules is found to strongly affect the molecular organization in thin films and in turn the efficiency of exciton diffusion.[30 - 35] High singlet exciton diffusion coefficients exceeding 10^{-6} m^2 s^{-1} have been reported.

Phthalocyanines (PC) have been established to be important classes of compounds because of their very special electronic properties and high thermal and chemical stability, which promise potential applications in photovoltaic devices[36], nonlinear optics,[37] and many others. Optical properties of phthalocyanines can be controlled and manipulated through binding with different metal ions with different axial ligands as well as covalent attachments with various peripheral substituents. Extensive use of phthalocynines in many areas is possible due to their intense absorption of visible and near infrared (NIR) light, long chemical and optical stability, and tunability in optical characteristics by substitutions in the peripheral groups. Further expansion of the conjugated π-electron system of the PC skeleton in naphthalocyanine (NPC) results in a red-shifted Q-band absorption, which widens the opportunity to harvest NIR region of solar energy spectrum for efficient photovoltaic applications .[38]

One of the important aspects of the chemistry of phthalocyanines is their strong tendency to form aggregates involving stacking of molecules by π- π interactions.[13] It is reported earlier about the excited state dynamics of monomeric {Zinc 2,9,16, 23-tetra-tert-butyl-29H, 31H-phthalocyanine} (Zn-tBuPC) in aprotic solvents and also of nanoaggregates in non-aqueous hydrogen bonding solvents, in which formation of ZnPC nanoaggregates was spontaneous.[13] Zn-tBuPC exists as monomeric species in DMSO, but forms nanoaggregates in hexafluoroisopropanol (HFIP), a strong hydrogen bonding solvent, via hydrogen bonding interactions. This property has been found to be unique for Zn-tBuPC but not with other phthalocyanine derivatives being investigated here. However, all those phthalocyanines form nanoaggregates in water because of hydrophobic interactions. Understanding the excitonic properties of these molecules in aggregated state has very important implication in photovoltaic and other optoelectronic applications. Herein, we have explored the excited state dynamics of the monomers and exciton dynamics in nanoaggregates of terta-t-butyl phthalocyanine (tBuPC), terta-t-butyl naphthalocyanine (tBuNPC) and their Zn Complexes, namely, Zn-tBuPC and Zn-tBuNPC and compare them with those of well-studied Zn complex of basic phthalocyanine (ZnPC) (Scheme I).[4, 31, 39] Comparison of the excitonic properties in these nanoaggregate matrices will provide an understanding about the effect of extended π-conjugation, substitution of bulkier functional groups on the aromatic ring and Zn complexation on the exciton diffusion properties.

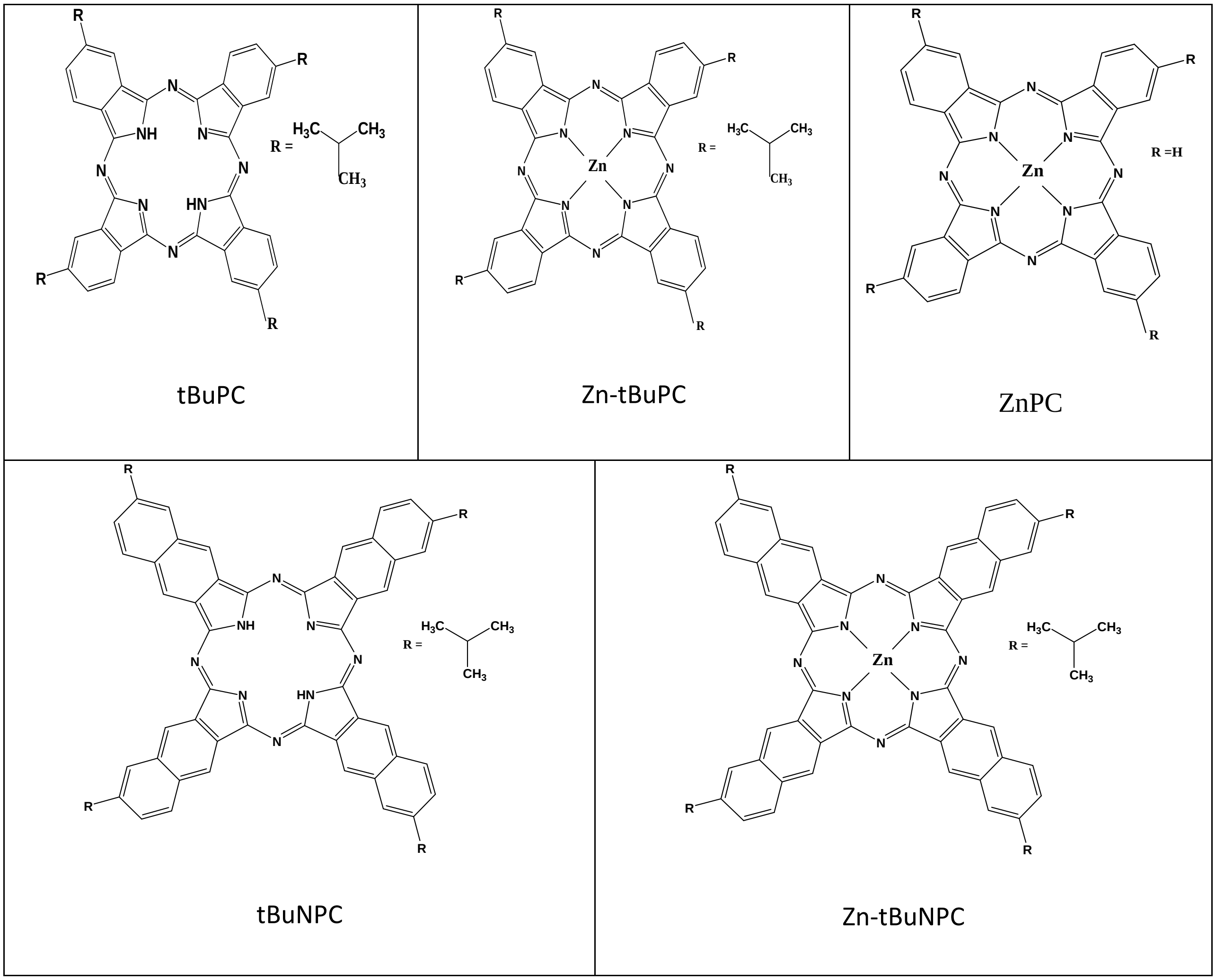

Scheme 7.1: Molecular structure of ,9,16,23-Tetra-tert-butyl-29H,31H-phthalocyanine (tBuPC), Zinc 2,9,16,23-tetra-tert-butyl-29H,31H-phthalocyanine (Zn-tBuPC), Zinc phthalocyanine (ZnPC), 2,11,20,29-Tetra-tert-butyl-2,3-naphthalocyanine (tBuNPC), Zinc 2,11,20,29-tetra-tert-butyl-2,3-naphthalocyanine (Zn-tBuNPC)

Several methods have been used to measure exciton diffusion length; however, it is unclear which methods are more reliable for a given situation.[13,22,40-43] Reported techniques to measure exciton diffusion length include photoluminescence (PL) surface quenching, time-resolved PL bulk quenching modeled with a Monte Carlo simulation, exciton–exciton annihilation (EEA), modeling of solar cell photocurrent spectrum, time-resolved microwave conductance, spectrally resolved PL quenching, and Förster resonance energy transfer theory.[13,22,40-43] Currently, there is little known about how the value of the measured exciton diffusion length of the same material can vary depending on the technique employed. EEA technique based on time-resolved PL at different excitation densities have been shown to be better suited for organic amorphous semiconductor materials.[13,22, 44-46] Ultrafast time resolved exciton-exciton annihilation technique has been extensively studied in molecular crystals, molecular J-aggregates, thin films, photosynthetic light harvesting antennae and light harvesting complexes and conjugated polymers.[13,22, 44-46] We have adopted here EEA technique based on time resolved absorption spectroscopy considering that the phthalocyanine nanoaggregates are nearly nonfluorescent. We have shown earlier that this technique may provide very reliable results on estimation of diffusion length.[13]

7.2. RESULTS AND DISCUSSION

7.2.1. Morphological Characterization of Phthalocyanine Nanoaggregates: Morphology of the nanoaggregates of those phthalocyanine derivatives have been characterized using DLS and AFM techniques. For DLS measurements, the aqueous dispersion of the nanoaggregates were diluted enough to minimize the absorption at 632.7 nm (output of He-Ne laser) and scattering was monitored at an angle of 130^o at 25 ºC. The photon correlation spectra as a function of time were analyzed for particle size distribution using the CONTIN algorithm (assuming spherical polydisperse particles). The corresponding size intensity weighted size distributions for all four nanaoaggregates dispersed in aqueous solutions are shown in Figure S7.1 in SD section. The most probable diameter and the FWHM of the size distribution function are given in Table 7.1.

The most probable diameter is relatively smaller in the cases of the aggregates of the basic phthalocyanines (about 200 and 250 nm for tBuPC and tBuNPC, respectively) as compared to those of their Zinc derivatives (about 300 and 378 nm for Zn-tBuPC and Zn-tBuNPC, respectively). However, the average diameter of nanoaggregates of ZnPC is the smallest. Size distribution follows symmetric Gaussian distribution function in all cases.

Table 7.1: Morphological parameters of phthalocyanine nanoaggregates dispersed in aqueous solutions.

NA	DLS Analysis (Gaussian size distribution)		AFM Analysis		V_{AG} (10^5 nm^3)	Molecular volume (nm^3)[a]	N_{AG}, 10^6
	Average size (nm)	FWHM (nm)	Average Diameter (nm)	Average Height (nm)			
tBuPC	196	47.0	200 ± 20	40 ± 5	0.99	1.27	12.56
tBuNPC	224	44.7	250 ± 30	50 ± 5	1.12	3.15	35.25
ZnPC	108	45.0	115 ± 20	40 ± 5	0.85	1.10	22.2
Zn-tBuPC	300	86.8	320 ± 40	40 ± 5	0.99	3.24	32.10
Zn-tBuNPC	378	39.8	380 ± 50	40 ± 5	1.12	4.04	45.30

[a] Calculated using Edward’s volume addition method (ref. 47).

Figure S7.2 in SD section presents the AFM images for nanaoaggregate samples. Using the AFM technique, average diameters and the average heights have been determined and these values are given in Table 7.1. Average volume of the nanoaggregate (V_{Ag}) has been calculated using the dimensions of the particles determined from the AFM measurements by the following equation.

$$V_{AG} = \pi b a^2 \qquad (7.1)$$

Where, ‘*b*’ is the height of the particle and ‘*a*’ is the half of the diameter (or radius). The values of V_{Ag} thus determined have also been given in Table 7.1. Using volume addition method proposed by Edward,[47] volumes of monomer molecules (V_M) have been calculated and hence the average number of molecules ($N_{AG} = V_{AG}/V_M$) in each particle of the nanoaggregate have been calculated and are given in Table 7.1.

The molecular packing and orientations are also one key factor to affects the exciton dynamics in the nanoaggregates. Therefore XRD technique has been employed for dry powder samples of nanoaggregates to obtain information regarding the molecular pickings (Figure 7.1).

It has been observed that for the nanoaggregates where the phthalocyanine moieties possess bulky tBu group at the four peripheral postions the back ground scaterring is highly prominent and some minor crystalline peake can be observed. This indicates inefficient molecular packing and presence of amorphous nature in these nanoaggregates. On the other hand, the nanoaggregate of the molecule having no bulky substituent provides crystalline peakes in their XRD data. This indicates presence of much better packing in this nanoaggregate as compared to other phthalocyanines. The bulky tBu substituents present in the four peripheral positions of the phthalocyanine causes more intermolecular separation and weak inter molecular interactions. As a result the molecular packing gets randomized inside the aggregates.

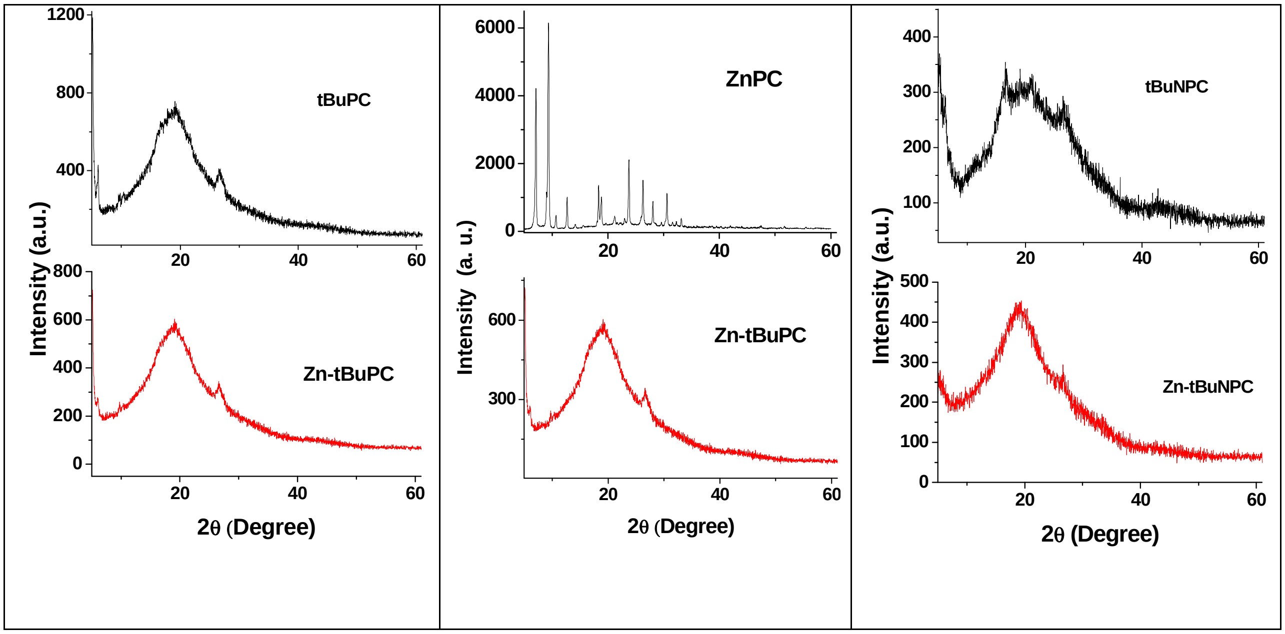

Figure 7.1: XRD pattern obtained for pthalocyanine nanoaggregates (A) tBuPC and Zn-tBuPC, (B) ZnPC and Zn-tBuPC (C) tBuNPC and Zn-tBuNPC

7.2.2. Steady state absorption and emission and time resolved emission studies:

tBuNPC and Zn-tBuNPC : Figure 7.2A shows steady state absorption and emission spectra of tBuNPC (2.5 x 10^{-5} mol dm^{-3}) in toluene. At low concentration, tBuNPC exists mainly as monomer in toluene and the absorption spectrum consists of two bands. Soret band or B-band in the 300 - 450 nm region and Q-band in the 700 - 800 nm region. Latter consists of a very sharp and intense band with the maximum at 780 nm as well as two other relatively weaker vibronic bands at 694 and 740 nm, which are the typical characteristics shown by the monomeric form of a phthalocyanine derivative. Absorption spectrum of tBuNPC nanoaggregate dispersed in aqueous solution is shown in Figure 7.2A. Since the absorption band assigned to nanoaggregate appears at the higher energy side of that of the Q-band of the monomer, H-type of aggregation, i.e. parallel stacking arrangements of the molecules, may be predicted.[12] Absorption spectrum of nanoaggregate is also associated with shoulder bands on the lower energy side of the Q-band of the monomer. This suggests that arrangement of the molecules in the aggregates may possibly not be perfectly in the parallel stacking but other kind, for example, oblique arrangement of the molecular planes is also possible.[6]

Monomer of tBuNPC shows dual emission bands following photoexcitation at 355 nm (Figure 7.2A). One is in the UV region with the maximum at ca 400 nm and another is in the NIR region with the maximum at ca 791 nm. They may be assigned to the fluorescence emission originating from the S_2 and S_1 states, respectively. However, emission quantum yield of tBuNPC nanoaggregate is very low and can be considered as nearly nonfluorescent.

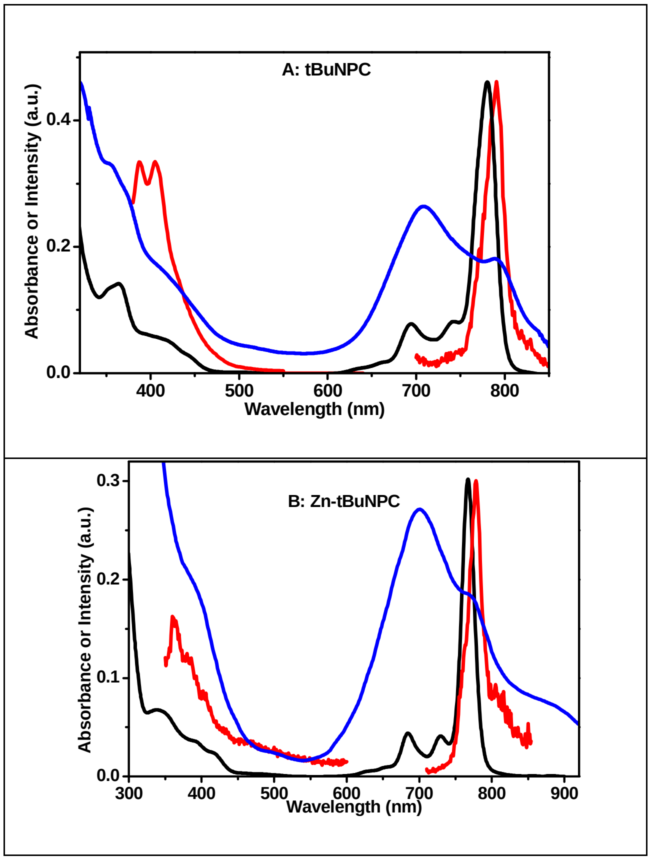

Figure 7.2: Absorption (black) and emission (red) spectra of tBuNPC (2.5 x 10^{-5} mol dm^{-3}) and Zn-tBuNPC (5 x 10^{-5} mol dm^{-3}) in toluene and absorption spectra of tBuNPC and Zn-

tBuNPC nanoaggregates dispersed in water (blue curves). Emission spectra are recorded following photoexcitation at 355 nm.

Figure 7.2B shows the absorption and emission spectra of Zn-tBuNPC in toluene as well as the absorption spectrum of Zn-tBuNPC nanoaggregate dispersed in water. Maximum of the Q-band, which represents the $S_1 \leftarrow S_0$ transition, appears at ca 760 nm. The Q-band also consists of two vibronic bands of very low intensity in the 650 – 750 nm region. A broad Soret band or B-band in the 300 - 450 nm region with the maximum at ca 350 nm arises due to the $S_2 \leftarrow S_0$ transition. It is important to mention here that, unlike in the case of tBuNPC, Zn-tBuNPC does not form nanoaggregate in non-aqueous solvents of even very high polarity, like DMSO but in aqueous solution. Absorption band of the Zn-tBuNPC nanoaggregate in aqueous dispersion is significantly broadened covering the 550 - 1000 nm region. Maximum of the absorption spectrum is blue-shifted to 700 nm with respect to that of the monomer and reveals the presence of two shoulders at ca 760 and 900 nm. Intensity of the B-band also increases significantly.

Fluorescence spectrum of the monomeric Zn-tBuNPC recorded in toluene has also been presented in Figure 7.2B and the extremely narrow band of the fluorescence spectrum shows a maximum at 773 nm. While monomeric Zn-tBuNPC in toluene is highly emissive (quantum yield is about 0.13), Zn-tBuNPC nanoaggregate dispersed in water is nearly nonfluorescent. Fluorescence lifetime of the excited singlet (S_1) state of Zn-tBuNPC in toluene has been determined using TCSPC technique to be 2.5 ns (Figure S7.3 in SD section).

tBuPC, Zn-tBuPC and ZnPC: Preparation and characterization of nanoaggregate of Zn-tBuPC have already been discussed earlier in a paper published by Kakade et. al.[13] Although Zn-tBuPC forms nanoaggregates in hydrogen bonding solvents, it exists as monomer in aprotic solvents even of large polarity like DMSO (Figure S7.4 in SD section). Lifetime of the S_1 state of Zn-tBuPC in DMSO is about 3.4 ns.[13] Absorption spectrum of Zn-tBuPC nanoaggregate dispersed in aqueous solution has also been shown in this figure.

However, tBuPC partially aggregates in polar aprotic solvents and hence the absorption spectrum of the monomer molecule of tBuPC has been recorded in toluene (Figure 7.3) in which only monomers exist. Fluorescence lifetime of tBuPC in toluene is about 6 ns (Figure S7.3 in SD section). Figure 7.2 also shows the absorption spectrum of its nanoaggregate dispersed in water. We find that, like in the cases of naphthalocyanines, phthalocynaines also form H-aggregates.

While in the case of Zn-tBuPC, some kind of stacking arrangements different from perfectly parallel kind of stacking of molecules is quite evident, nanoaggregate of tBuPC prepared here may be predicted to have nearly perfect H-type stacking. Nanoaggregates of tBuPC and Zn-PC are also found to be nearly nonfluorescent like Zn-tBuPC.

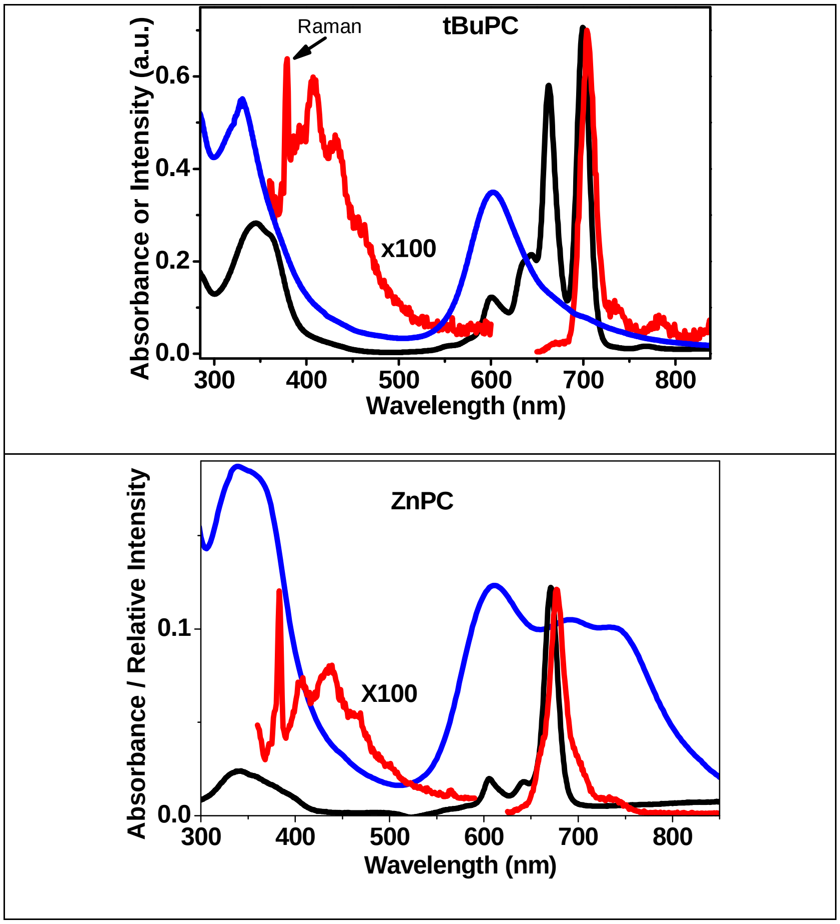

Figure 7.3: Absorption spectra of monomer (black) and nanoaggregate dispersed in aqueous solution (blue) and fluorescence spectrum of monomer (red) of tBuPC and ZnPC.

On the contrary, the absorption spectrum of ZnPC nanoaggregate is quite broad with the bands appearing both in the lower and higher energy sides of the monomer band. This suggests presence of stacking arrangements in the nanoaggregates in combination of both H- and J-type.

7.2.3. Excited State Dynamics: We adopted UV (390 nm) pump – visible probe (400 – 1000 nm) transient absorption spectroscopic technique for investigation of the dynamics of the excited states of phthalocyanines in solution and the excitons in nanoaggregates. This study has also been useful for estimating the diffusion coefficient and the diffusion length of the excitons in the nanoaggregate matrices.

tBuNPC : Figure 7.4A presents the time resolved transient absorption (TA) spectra recorded following photoexcitation of tBuNPC in toluene, in which tBuNPC exists as monomer at the specified concentration (2.5 x 10^{-5} mol dm^{-3}), using 390 nm light pulses. The transient spectrum recorded immediately after photoexcitation, i.e. at 0.2 ps delay time, shows two excited state absorption (ESA) bands, one in the 500 - 700 nm region and another in the lower energy region beyond 820 nm, in addition to a bleaching band in the 700 – 820 nm region with the maximum at 770 nm. Comparison of the shape of this transient spectrum with that of the steady state absorption spectrum (Figure 7.2) clearly reveals significant overlapping of the ESA and bleaching bands. Time evolution of the transient spectra shows a marginal decay of ESA bands in sub-1 ps time domain followed by a rise up to about 50 ps. ESA bands decay at much longer time scale. On the other hand, the bleaching band shows a small rise up to about 1 ps delay time accompanied by a small red shift of the maximum from 770 to 780 nm. Following this, the bleach band recovers slowly.

Temporal dynamics of the transient species have been analyzed at a few selective wavelengths and the results are shown in Figure 7.4B. Each of these temporal profiles could be best-fitted using multiexponential functions and the lifetimes associated with the best-fit functions along with the information whether the particular component is associated with the rise or decay of absorption using the assignment ‘r’ or ‘d’, respectively, are given in the insets. The ultrafast component with the lifetime of about 0.45 ± 0.02 ps may be assigned to the lifetime of the S_2 state, which is populated following photoexcitation using 390 nm light. The intermediate component with the lifetime of 18 ± 3 ps may be assigned to vibrational relaxation following population of the vibrationally hot S_1 state via intersystem crossing process from the S_2 state.[13] The component with the long lifetime is assigned to the decay of the S_1 state considering that the lifetime of the S_1 state is 3.5 ns as determined using the TCSPC technique. Time evolution of the bleaching band as described in the earlier paragraph is now easily understood considering overlapping of the bleaching band (maximum at ca 780 nm) and the stimulated emission band (maximum at ca 800 nm). The latter band rises with increase in population of the lowest energy vibrational level (v =0) following the $S_2 \rightarrow S_1$ internal conversion process and vibrational relaxation in the S_1 state.

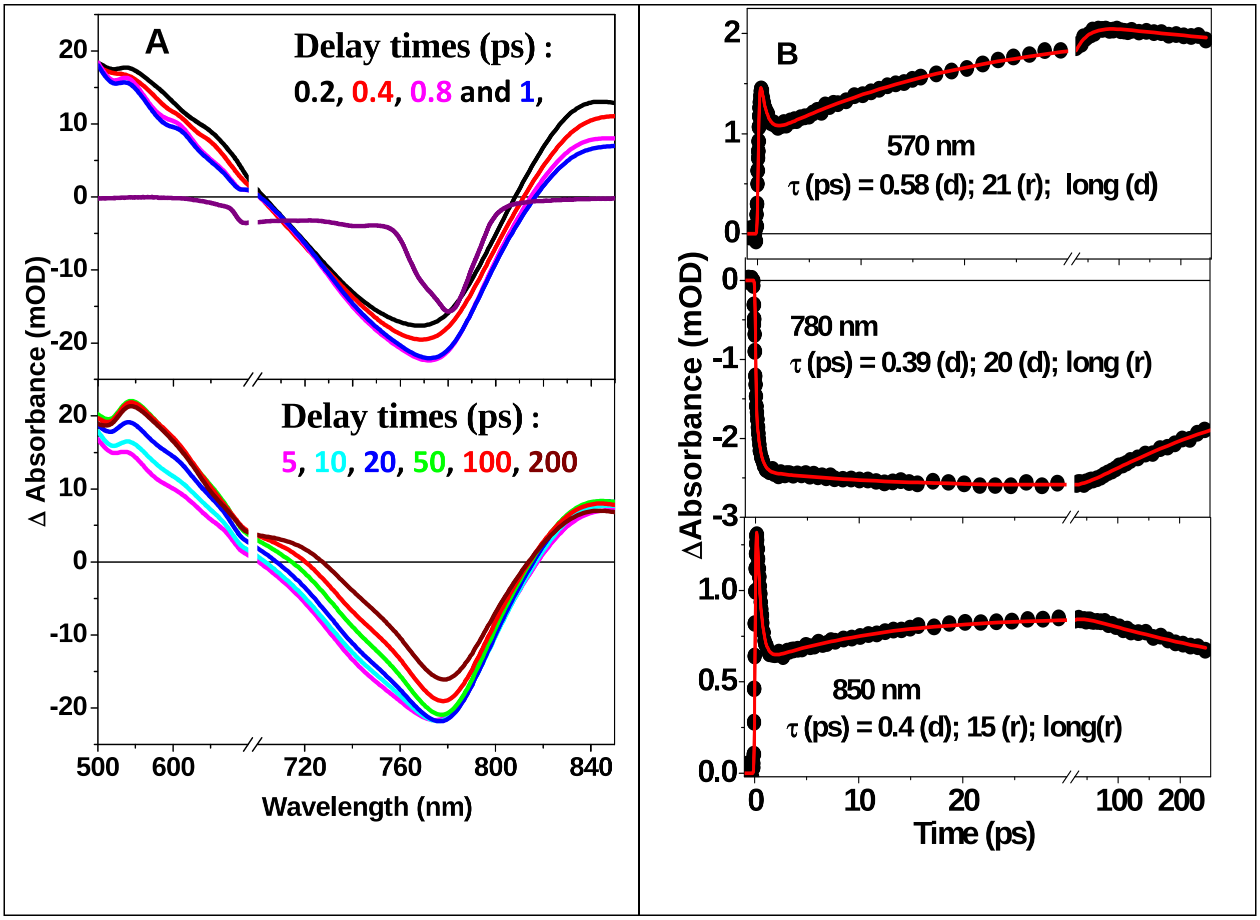

Figure 7.4: (A) Time resolved TA spectra of tBuNPC (2.5 x 10^{-5} mol dm^{-3}) in toluene following photoexcitation using 400 nm laser pulses. Purple colored curve represents the shape of the steady state absorption spectrum of tBuNPC in toluene. (B) Temporal dynamics of the transient species recorded following photoexcitation of NPC in toluene.

Figure 7.5 shows the time resolved TA spectra recorded following photoexcitation of tBuNPC nanoaggregate dispersed in aqueous solution. TA spectra are characterized by a strong excitonic absorption band in the 500 – 650 nm region and a bleaching band in the 650 – 760 nm region. Presence of the near isosbestic point at 665 nm during the course of decay of the excitonic band and recovery of the bleaching band suggests that no other process than the excitonic decay is involved in the time evolution of the transient spectra shown in Figure 7.5.

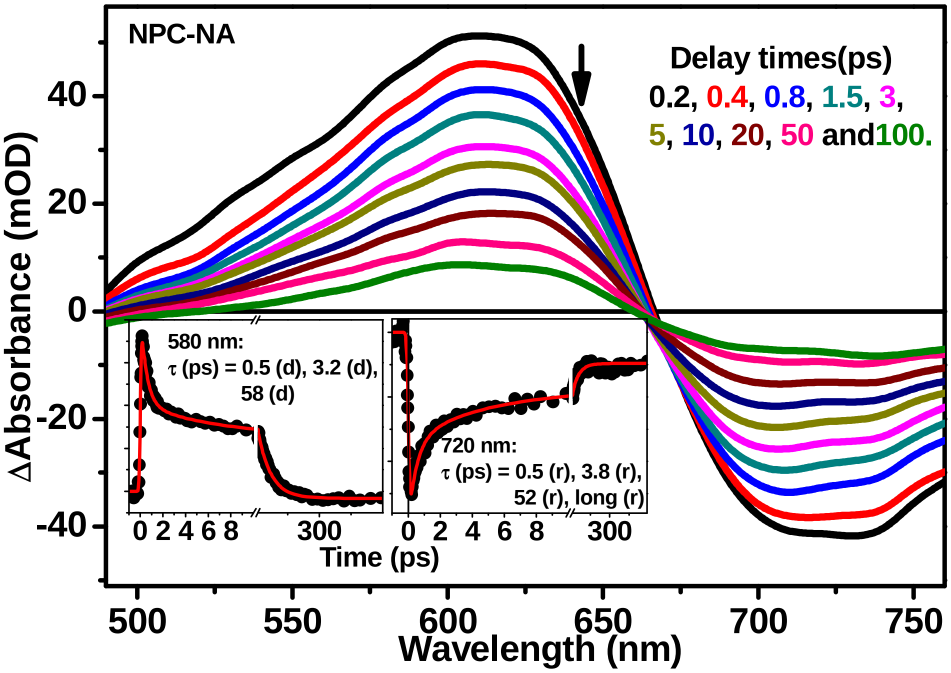

Figure 7.5: Time resolved TA spectra of tBuNPC nanoaggregate dispersed in water recorded following photoexcitation at 390 nm. Insets show the temporal dynamics of excitonic decay and bleach recovery monitored at 580 and 720 nm respectively, along with the best fit functions and the lifetimes associated with the best-fit multiexponential functions.

In the insets of Figure 7.5, we have shown the temporal profiles recorded at 580 and 720 nm to analyze the dynamics of the excitonic state generated in the tBuNPC nanoaggregate and the bleach recovery, respectively. Temporal profile of the excitonic state could be fitted well using a three exponential function with the decay lifetimes of 0.5, 3.2 and 58 ps. We assign the longest lived component with 58 ps lifetime to the excitonic state and find significant shortening of the lifetime of the excitonic state generated in the nanoaggregate as compared to that of the S_1 state of the monomer, which has been measured to be about 3.5 ns in toluene. Assignment of other two ultrafast components with the lifetimes of 0.5 and 3.2 ps could be made only after examining the dependence of the lifetimes on the power density of the excitation light and this aspect will be discussed in the section 3.2.4.

The bleach recovery dynamics also could be fitted using three exponentially rising components with the lifetimes of 0.5, 3.8 and 52 ps, which nearly complement the excitonic absorption dynamics. However, the bleach recovery signal also consists of an additional component representing a long-lived residual bleach. This suggests population of the long-lived triplet excitonic state with a small yield. This feature has been observed in all four cases of the nanoaggregates investigated here but we will not discuss this aspect further.

Similar dynamics observed through the entire bleach band as well as the ESA band suggests that the broad steady state absorption band of tBuNPC nanoaggregate appearing in the 600 – 850 nm region (Figure 7.2A) may be assigned to the same kind of aggregated species.

Zn-tBuNPC: Time evolution of the TA spectra of Zn-tBuNPC monomer in toluene following photoexcitation using 390 nm light is shown in Figure 7.6A. Photoexcitation of Zn-tBuNPC using 390 nm laser pulses populates the S_2 electronic state of the molecule. TA spectrum recorded at 0.2 ps delay time consists of a broad ESA band in the 480 - 650 nm region with maxima at 500 and 600 nm and a structured bleaching band in the 650 – 770 nm region. The vibronic structure of the bleaching band replicates those observed in the steady state absorption spectrum of Zn-tBuNPC in the same solvent (Figure 7.2B). Time evolution of the TA spectra shows marginal decrease in absorbance of the ESA band up increasing delay time, but do not show complete decay even after the delay time is increased up to 800 ps.

Figure 7.6B presents the temporal profiles recorded at two selective wavelengths following photoexcitation of Zn-tBuNPC in toluene along with the best multi-exponential fit functions. Temporal profile recorded at 630 nm is associated with an initial decay of ESA with the lifetime of about 0.28 ps, followed by another component of slower decay of ESA with the lifetime of 13 ps and subsequent decay of ESA with a long (longer than 500 ps) lifetime. That at 760 nm is associated with a strong negative absorption signal appearing with the instrument response time limited rise followed by further biexponential rise with the lifetimes of 0.25 ps and 11 ps. Complete recovery of the bleach signal takes place in a much longer time scale. Therefore, in each case, the temporal profile is associated with residual positive or negative absorption representing a long-lived component. Following the arguments put in the case of the photophysics of tBuNPC in toluene, the component with the average lifetime of 0.28 ± 0.05 ps is assigned to the S_2 to S_1 internal conversion (IC) process leading to population of the higher vibrational levels of the S_1 state and that with the average lifetime of 12 ± 1 ps to the vibrational cooling in the S_1 state due to dissipation of excess vibrational energy to the solvent modes. The component associated with the residual absorption or bleach signal, is obviously assigned to the long decay time of the S_1 state. This assignment is supported by the results of TCSPC measurements providing the value of the fluorescence lifetime of 2.5 ns (Figure S7.3 in SD section).

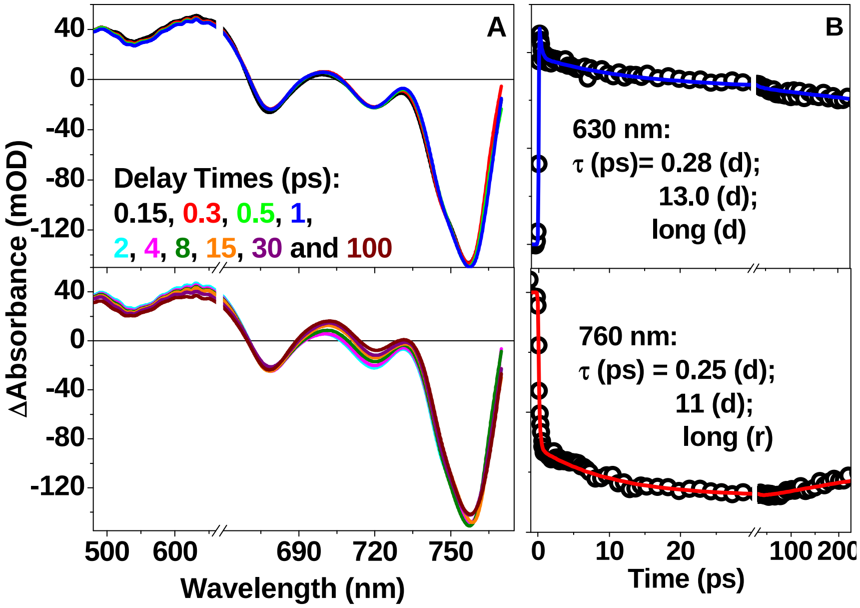

Figure 7.6: (A) Time resolved TA spectra of Zn-tBuNPC (1 x 10^{-5} mol dm^{-3}) in toluene following photoexcitation using 400 nm laser pulses. (B) Temporal profiles recorded at two selective wavelengths along with the best fit functions. The lifetimes associated with the multi-exponential fit functions are given in the insets.

Figure 7.7A presents time resolved TA spectra of exciton generated in Zn-tBuNPC nanoaggregate dispersed in aqueous solution following photoexcitation using 390 nm light. TA spectrum recorded at 0.2 ps delay time consists of a broad bleaching band in the 650 – 900 nm region with the maximum at ca 700 nm (and a shoulder at 740 nm) and a strong ESA band in the 500 - 650 nm region with a maximum at ca 550 nm. Occurrence of the isosbestic point at ca 650 nm between the ESA and the bleaching bands of the TA spectra during the course of its time evolution again suggests that both these bands represent the same transient species. Unlike in the case of Zn-tBuNPC monomer (Figure 7.6), the decay of both the bands in the TA spectra of the exciton in ZnNPC nanoaggregate is complete within about 150 ps leaving a little residual absorption or bleach signal (insets of Figure 7.7).

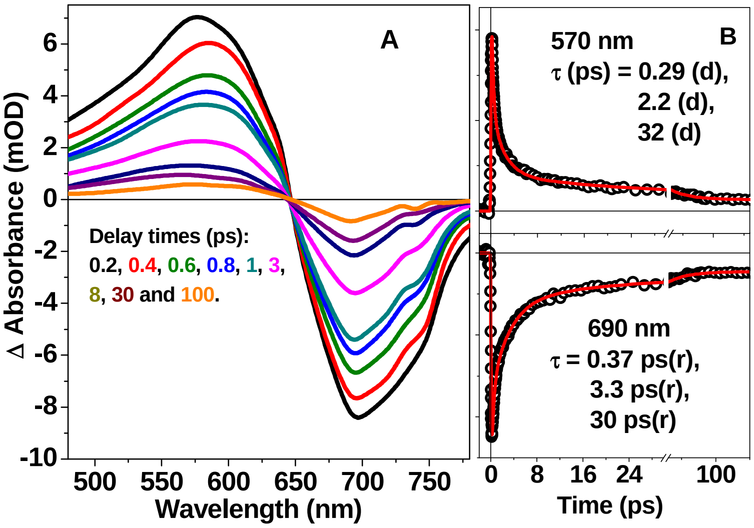

Figure 7.7: (A) Time-resolved TA spectra of Zn-tBuNPC nanoaggregate dispersed in aqueous solution following photoexcitation using 390 nm laser pulses. (B) Temporal profiles recorded at two selective wavelengths along with their best fit functions. The lifetimes associated with the multi-exponential fit functions are given in the insets.

Each of the temporal profiles recorded at 570 and 690 nm could be fitted well with a three exponential function with nearly similar time constants (Figure 7.7B). Average lifetimes of these three components associated with the dynamics of the excitonic state are 0.32 ± 0.05, 2.8 ± 0.5, and 31 ± 1 ps. Photophysical parameters related to exciton dynamics have been estimated from the intensity dependence of the lifetimes of those three components and have been discussed in section 7.2.3.5.

tBuPC and Zn-tBuPC : Figure 7.8 shows the time resolved TA spectra recorded following photoexcitation of tBuPC in toluene. Features of time evolution of the transient spectra are very similar to those we observed in the cases of monomers of tBuNPC and Zn-tBuNPC (Figures 7.4 and 7.6). Analyses of the temporal profiles recorded at 580 nm and 700 nm (insets of Figure 7.8) reveal complimentary dynamics of the excited state and bleach recovery, respectively. Following the arguments put in the earlier two cases, we assign the lifetimes of 18 ± 2 ps vibrational cooling process. In this case, possibly the lifetime of the internal conversion process is shorter than the instrument response time limit (~ 120 fs).

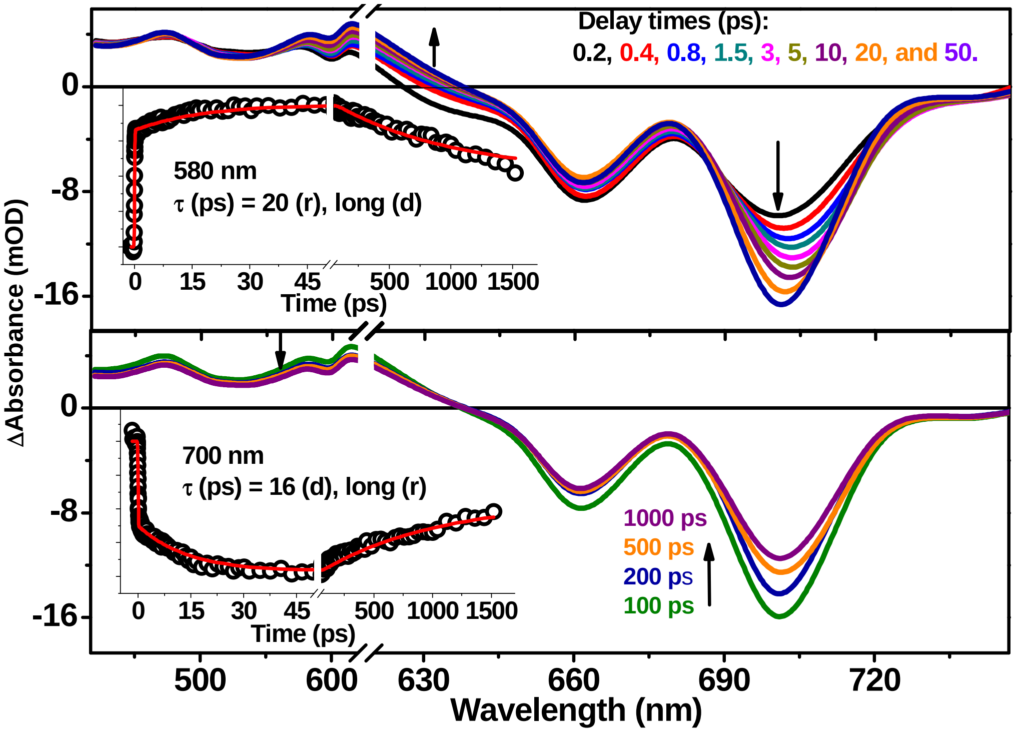

Figure 7.8: Time-resolved TA spectra of tBuPC in toluene solution following photoexcitation using 390 nm laser pulses. Inset: Temporal profiles recorded at two selective wavelengths 580 and 700 nm along with their best fit functions. The lifetimes associated with the multi-exponential fit functions are given in the insets.

Time evolution of the transient spectra of the excitonic state created in nanoaggregate of tBuPC is shown in Figure 7.9A. In this case too, presence of the isosbestic point between the excitonic absorption and bleaching bands clearly reveals dynamics involving only two states, namely, the excitonic state and the ground state. Temporal profiles presented in Figure 7.9B also reveal the complimentary dynamics of the excitonic absorption and bleach recovery and hence support the inference regarding two state dynamics. Lifetime of the excitonic state is about 35 ps and two ultrafast components with the lifetimes of 0.5 and 5 ps are related to the dynamics of the excitonic state, which will be unraveled from its excitation intensity dependence.

Photophysics of monomeric species of Zn-tBuPC in DMSO and exciton dynamics in the nanoaggregates formed in hydrogen bond donating solvent (HFIP) and also that dispersed in aqueous solution have been already reported in an earlier publication by Kakade et. al.

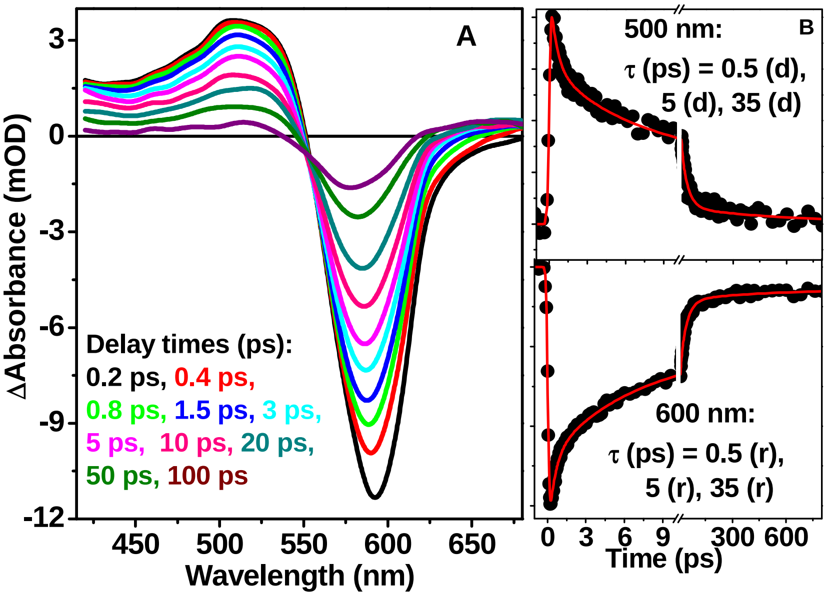

Figure 7.9: (A) Time resolved transient spectra recorded following photoexcitation of nanoaggregates of tBuPC dispersed in aqueous solution. (B) Temporal dynamics at 500 and 600 nm along with the best fit functions and the associated lifetimes of three components.

ZnPC: The time resolved TA spectra of the monomeric ZnPC molecules in toluene and temporal profiles are shown in Figure 7.10. The excited state dynamics have similar features as those observed in the cases of other phthalocynaines. We estimate the S_2 lifetime and vibrational cooling time are 0.4 and 15 ps. The S_1 state has lifetime of a few ns.

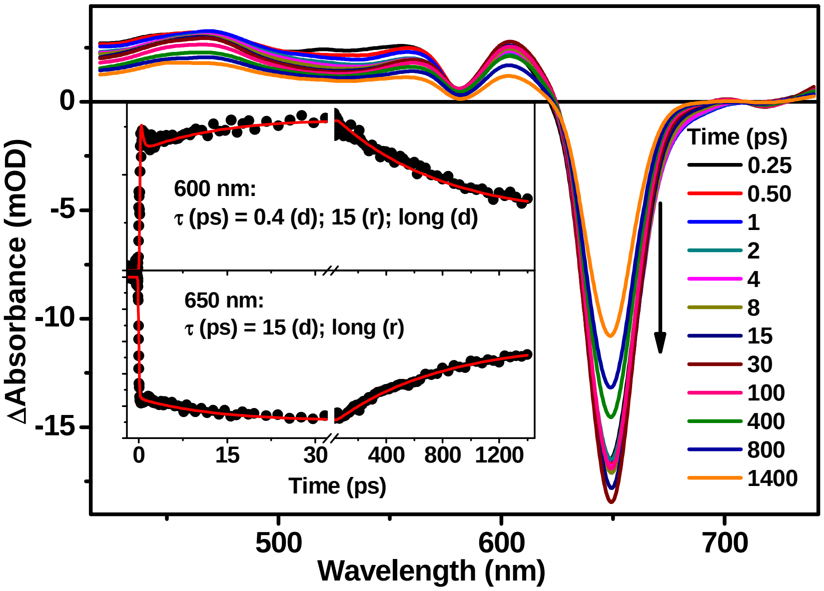

Figure 7.10: Time-resolved TA spectra of ZnPC in toluene solution following photoexcitation using 390 nm laser pulses. Inset: Temporal profiles recorded at two selective

wavelengths 600 and 650 nm along with their best fit functions. The lifetimes associated with the multi-exponential fit functions are given in the insets.

In Figure 7.11, we show the time resolved spectra of ZnPC nanoaggregates dispersed in aqueous solution following photoexcitation at 390 nm. Exciton absorption shows a broad ESA band in the 420 - 550 nm region and bleaching bands in the 550 – 750 nm region. Significant mismatch between shapes of the bleaching bands and the steady state absorption spectrum in the 550 – 730 nm region suggests strong overlapping between the ESA and bleaching bands in this region. Therefore, the exciton dynamics has been investigated by monitoring the temporal profiles at 520 nm and 670 nm at which the overlapping between these two bands are minimum.

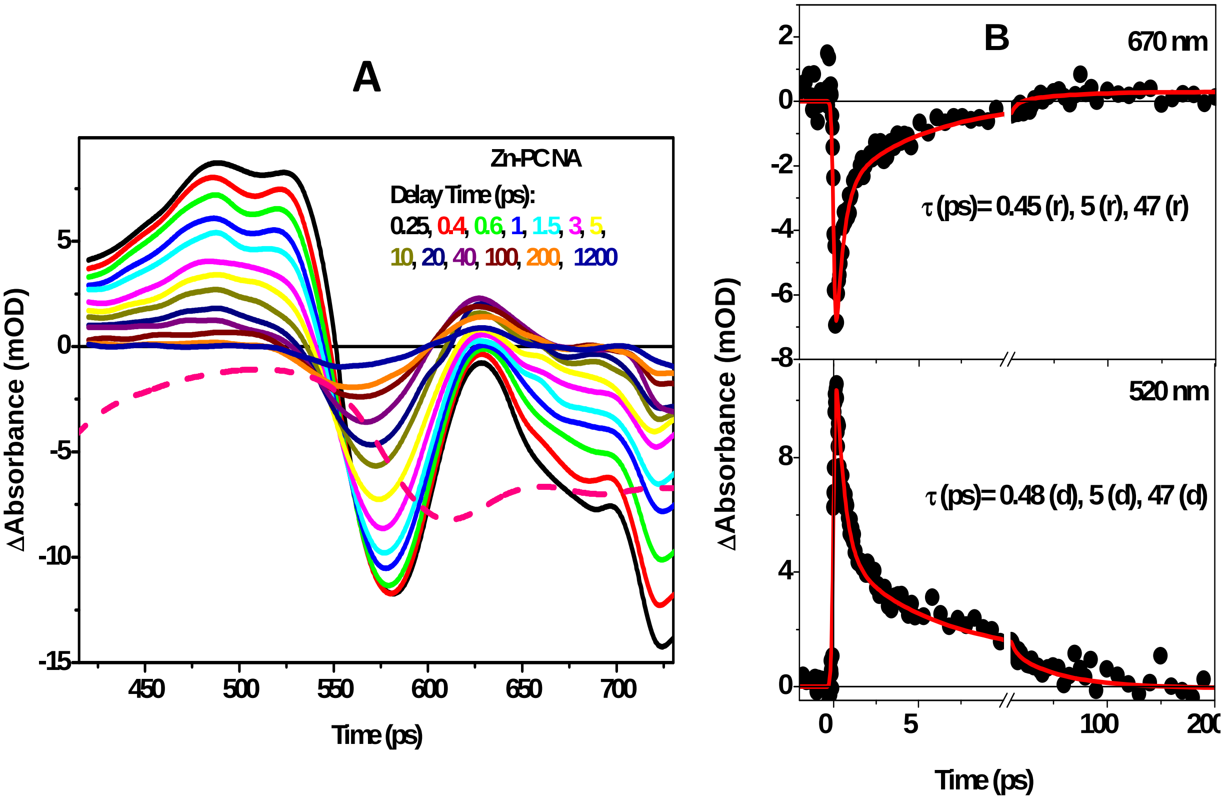

Figure 7.11: **(A)** Time resolved transient spectra recorded following photoexcitation of nanoaggregates of ZnPC dispersed in aqueous solution. Dashed pink line represents the steady state absorption spectrum of ZnPC nanoaggregate. (B) Temporal dynamics at 520 and 670 nm along with the best fit functions and the associated lifetimes of three components.

Excitation Intensity Dependence of Exciton Dynamics in Nanoaggregates: In the S_1 excitonic state of the nanoaggregate, the most important process is the exciton - exciton annihilation reaction, in which two excitons diffuse towards each other to react promoting an additional nonradiative depopulation channel for the excitonic state and one of these two excitons are destroyed to populate back the ground state (vide infra). This is a second order process. Rate of this process is controlled by the rate of diffusion of the excitons and dependent on the concentration of the S_1 exciton populated following photoexcitation of nanoaggregate and hence intensity of the pump pulse. Therefore, the rate of exciton - exciton annihilation reaction provides information regarding diffusion coefficient and diffusion length of exciton migration in the nanoaggregate matrix and these parameters are directly related to the efficiency of a photonic device prepared using this nanomaterial.

We have recorded the temporal profiles at two selective wavelengths following photoexcitation of the nanoaggregates by varying intensities of the pump pulse in the range of 3 to 12 µJ/Pulse (Figure 7.12). We followed the changes in the dynamics of the S_1 excitonic state by monitoring the decay of the ESA band as well as bleach recovery. In Figure 7.12, we present a typical result for excitation intensity dependence of the dynamics of ESA decay and bleach recovery in the case of tBuNPC nanoaggregate. Similar type of observation also observed for other four nanoaggregates.

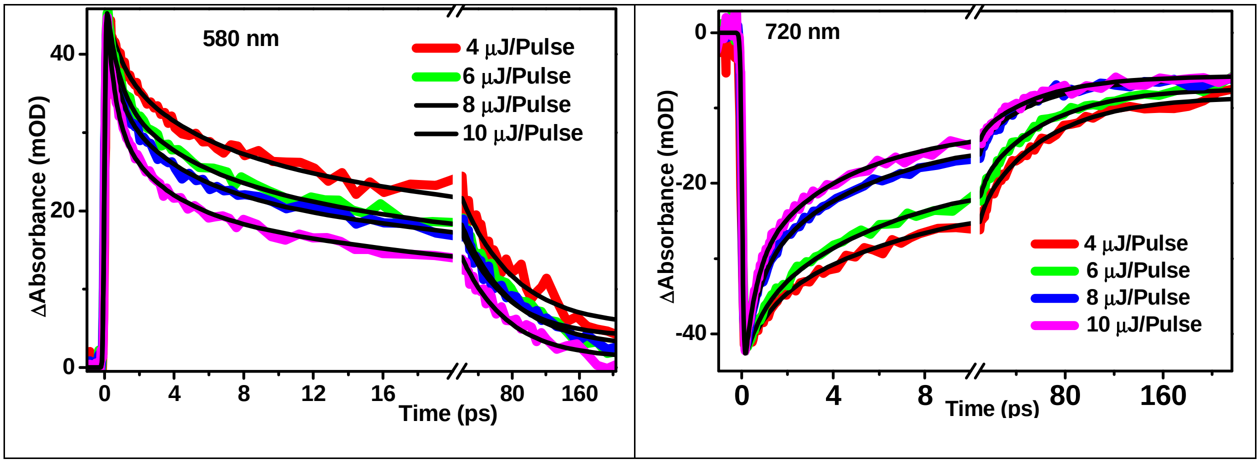

Figure 7.12: Excitation energy (in µJ/pulse) dependence of the dynamics of ESA and bleach recovery monitored at 580 and 720 nm, respectively, in the case of tBuNPC nanoaggregate dispersed in aqueous solution.

Each of the temporal profiles presented in Figure 7.12 has been fitted using a three or four exponential function. The associated lifetimes and the relative amplitudes of the signals are given in Table 7.2. We observe that variation of the lifetimes of two ultrafast components, τ_1 and τ_2, are very similar in both the ESA absorption and bleach recovery dynamics and become longer on decreasing the intensity of the pump pulse. But the third component with the lifetime τ_3 remains nearly independent of excitation intensity. Therefore, it is evident that they represent different kinds of processes. Since lifetimes of both τ_1 and τ_2, increase by decreasing the intensity of the pump pulse, they really represent the non-exponential decay dynamics of the S_1-exciton and not the decay of the S_2-state by internal conversion and vibrational relaxation processes, respectively, as explained in the case of the excited states of the monomers. Therefore, we explain that following photoexcitation of the nanoaggregates to the S_2 excitonic state using 390 nm light, the S_2 state undergoes ultrafast relaxation to the S_1 excitonic state with a lifetime shorter than 120 fs. Observed nonexponential decay of the excitonic state could be assigned to the time-dependent decay of the S_1 exciton due to exciton - exciton annihilation reaction, the rate of which is controlled by the rate of diffusive migration of the excitons. The intensity independent component, τ_3, represents the lifetime of the unimolecular decay of the S_1 exciton in absence of exciton - exciton annihilation reaction. The long – lived component (lifetime τ_4) with a small amplitude associated with the bleach recovery dynamics may probably be assigned to the triplet exciton populated with very small yield.

Table 7.2: Excitation energy dependence of the dynamics of ESA decay and bleach recovery in the case of tBuNPC nanoaggregate following photoexcitation using 400 nm laser pulses of 100 fs duration.

Excitation Energy	Wavelength (nm)	τ_1 (ps) (a_1)	τ_2 (ps) (a_2)	τ_3 (ps) (a_3)	τ_4 (ps) (a_4)
10 μJ/Pulse	580	0.50 (-28)	3.2 (-19)	55 (-29.2)	--
	720	0.52 (26)	3.8 (25.6)	50 (14.5)	long
8 μJ/Pulse	580	0.60 (-19)	3.8 (-19)	55 (-30)	--
	720	0.64 (20)	4.5 (26)	50 (16)	long
6 μJ/Pulse	580	0.70 (-19.8)	4.6 (-18)	62 (-33)	--
	720	0.75 (10.6)	5.2 (24.5)	55 (23.5)	long
4 μJ/Pulse	580	0.90 (-12)	5.0 (-18)	65 (-35)	--
	720	1.0 (10)	5.6 (18)	55 (27.8)	long

Exciton - Exciton Annihilation: In our earlier work on the exciton dynamics of Zn-tBuPC we adopted the Pilotin's approach to estimate the diffusion coefficient and diffusion length of the excitons generated in the nanoaggregates. However, comparing these values with those reported earlier we find that Pilotin's method overestimate these values.[13, 44] Therefore, we adopt an approach based on mixed order kinetic analysis to estimate the diffusion parameters of the excitons. This method of analysis has already been used in the cases of anthracene nanoaggregate.[22, 23]

Based on the above discussion on intensity dependence of the decay dynamics of the S_1 excitonic states, we write the following reaction scheme for the creation and decay of the S_1 excitonic state (which will be represented as $S_1(X)$ in the following equations) in phthalocyanine nanoaggregates:

$$S_0 \xrightarrow{390\,nm} S_2(X) \xrightarrow{<120\,fs} S_1(X) \qquad (7.2)$$

$$S_1(X) \xrightarrow{k_1} S_0 \qquad (7.3)$$

$$S_1(X) + S_1\,(X) \xrightarrow{k_2} S_0 + S_n(X) \rightarrow S_0 + S_1(X) \qquad (7.4)$$

We write the expression for the rate of change of concentration of the S_1 excitonic state as,

$$\frac{d[S_1(X)]}{dt} = -k_1\,[S_1(X)] - \frac{k_2\,[S_1(X)]^2}{2} \qquad (7.5)$$

Here k_1 and k_2 represent the annihilation free or natural decay of the excitonic state and the rate constant of the annihilation process, which follows a second order rate equation, respectively. Solution of equation 7.5 gives us the concentration of the S_1excitonic state at time 't'.

$$[S_1(X)]\,(t) = [S_1(X)]_0\,\frac{\exp\,(-k_1\,t)}{(1 + k_2^{'}\,t)} \qquad (7.6)$$

Here, $k_2^{'} = \frac{k_2\,[S_1(X)]_0}{2}$ (7.7)

Here, $[S_1(X)]_0$ is the concentration of the S_1 excitonic state created immediately after photoexcitation. Considering that absorbance of the S_1 excitonic state at time 't' is proportional to its concentration at that time, we write,

$$OD\,(t) = OD\,(t = 0)\,\frac{\exp\,(-k_1\;t)}{(1 + k_2^{'}\;t)} \qquad (7.8)$$

Since the temporal profiles have been monitored at those two wavelengths, at which the ESA and bleach bands have nearly no overlap, we assume that we measure absolute absorbance and not the differential absorbance, to write equation 7.8. Since the bleaching signal is associated with a long-lived residual negative absorbance (R), equation 7.8 is revised as,

$$OD\,(t) = OD\,(t = 0)\,\frac{\exp\,(-k_1\;t)}{(1 + k_2^{'}\;t)} + R \qquad (7.9)$$

Temporal profiles recorded at 580 and 720 nm have been fitted using equation 7.9 (Figure 13) and the fitting parameters are given in Table 7.3. Method of calculation for exciton density at t = 0 (i.e. the value of $[S_1(X)]_0$) is given in SD section (S7.5). Insets of Figure 13 shows the linear relationship between k_2' and $[S_1(X)]_0$ and the annihilation rate constant, k_2 could be estimated from the slope of the best fit line. Method of estimation of the annihilation radius, R_a, using the threshold value of $[S_1(X)]_0$ obtained from the intercept of the X-axis of the k_2' vs $[S_1(X)]_0$ plot, is also shown in SD section (S7.6). Values of k_2 and R_a estimated for tBuNPC nanoaggregate are given in Table 7.3.

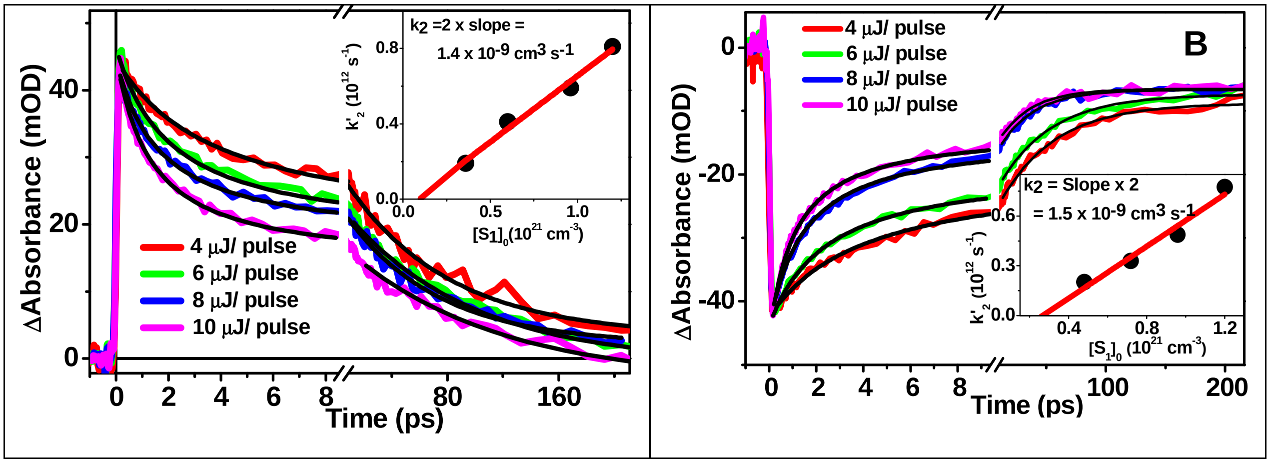

Figure 7.13: Excitation energy (in μJ/pulse) dependence of the dynamics of ESA and bleach recovery monitored at 580 and 720 nm, respectively, in the case of tBuNPC nanoaggregate dispersed in aqueous solution. Each of the temporal profiles has been fitted using equation 7.9. Values of k_1 and k_2' associated with the fit function are given in Table 7.3.

Table 7.3: Parameters obtained from fitting the excitation intensity dependent dynamics of ESA and bleach recovery dynamics monitored at 580 and 720 nm, respectively, for tBuNPC nanoaggregate dispersed in aqueous solution.

(A) ESA dynamics monitored at 580 nm

Excitation energy (μJ/Pulse)	$[S_1(X)]_0$ (10^{21} cm^{-3})^a	k'_2 (10^{12} s^{-1})	$\tau_{exciton}$ (= $1/k_1$) (ps)	k_2 (10^{-9} cm^3 s^{-1})	R_a (nm)
10	1.2	0.78	50	1.4	1.34
8	0.96	0.59	50		
6	0.72	0.43	56		
4	0.48	0.25	60		

(B) Bleach dynamics monitored at 720 nm

Excitation energy (μJ/Pulse)	$[S_1(X)]_0$ (10^{21} cm^{-3})	k'_2 (10^{12} s^{-1})	$\tau_{exciton}$ (= $1/k_1$) (ps)	k_2 (10^{-9} cm^3 s^{-1})	R_a (nm)
10	1.2	0.77	50	1.5	1.06
8	0.96	0.49	50		
6	0.72	0.33	46		
4	0.48	0.20	42		

Exciton migration: Although exciton diffusion controls the exciton – exciton annihilation process, faster exciton migration is a primary requirement for efficient energy migration and transfer in photosynthetic reaction centers and also for larger efficiency in electronic devices. Therefore, the exciton diffusion length (L), which is defined as the distance travelled by the diffusing exciton, is one of the most important parameters for developing such devices. The annihilation rate constant, k_2, is related to the diffusion coefficient, D, and the annihilation radius, R_a, by equation (7.10) and the latter to the hopping time, τ_{hop}, by equation (7.11), assuming that the excitons are localized and moving mainly by an incoherent hopping process.[48,49] Here d indicates the intermolecular separation. Annihilation radius, R_a, may be defined as the radius of the sphere around a particular exciton, beyond which if another exciton is created, it would never be able to reach the former to participate in annihilation reaction. R_a value of an exciton in the nanoaggregate matrx may be estimated from the intercept on the X-axis for the plot of k_2' vs $[S_1(X)]_0$. In Table 7.4, we give the photophysical parameters of five phthalocyanine nanoaggregates investigated in this work.

$$k_2 = 8 \pi R_a D \qquad (7.10)$$

$$\tau_{hop} = \frac{d^2}{6D} \qquad (7.11)$$

Table 7.4: Photophysical and migration parameters of the S_1 excitonic state created in phthalocyanine nanoaggregates.

NA	$\tau_{exciton}$ (ps)	g (10^{-9} cm^3 s^{-1})	R_a (nm)	D (10^{-4} cm^2 s^{-1})	t_{hop} (ps)	L_D(nm)
tBuPC	32 ± 3	1.1 ± 0.2	1.2 ± 0.2	3.6 ± 0.2	2.96	2.6 ± 0.4
tBuNPC	50 ± 8	1.5 ± 0.2	1.2 ± 0.2	4.8 ± 0.9	2.22	3.7 ± 0.5
ZnPC	43 ± 5	5.6 ± 0.6	1.1 ± 0.1	20.1 ± 3.0	0.53	7.2 ± 0.6
Zn-tBuPC	30 ± 4	3.0 ± 0.3	1.3 ± 0.1	9.2 ± 1.0	1.16	4.1 ± 0.5
Zn-tBuNPC	45 ± 6	6.3 ± 0.4	1.3 ± 0.1	19.3 ± 2.0	0.55	7.2 ± 0.8

The typical errors in the measured parameters are ±10%

The large hopping rates ($k_{hop} = (\tau_{hop})^{-1} \sim 8.62 \times 10^{11}$ and 18.18×10^{12} s^{-1} for Zn-tBuPC and Zn-tBuNPC , respectively) obviously can be correlated with a very large energy transfer rate and strong excitonic interaction. These values have been used to estimate the diffusion length, L, which is defined as for the S_1 exciton,[13]

$$L = \sqrt{6 D \tau_{exciton}} \qquad (7.12)$$

Where, the coordination number is 6 for three dimensional structures.[13] Diffusion lengths of the S_1 excitons in nanoaggregate matrices of five phthalocyanines thus estimated are given in Table 7.4.

Comparison of the values of the diffusion coefficient and diffusion length between those having similar molecular structures or those with variation in molecular structures with respect to a particular structural feature leads us to make the following inferences: (1) By comparing these values for tBuPC and tBuNPC as well as for Zn-tBuPC and Zn-tBuNPC , we find that the diffusion coefficient of the S_1 exciton become largerand hence the diffusion length is longer as the π-conjugation is extended. (2) Comparison of these values for similar phtalocyanines and their zinc derivatives suggests that exciton diffusion length becomes larger by complexation with Zn. (3) Because of butyl substitution, aromatic moiety of the phthalocyanine becomes nonplanar and exciton diffusion length is reduced due to poor stacking pattern in the nanoaggregate. This explains why ZnPC is a better photonic material as compared to Zn-tBuPC. Following the trends of these physical parameters of exciton migration for those phthalocyanines listed in Table 4, one may infer that ZnPC and Zn-tBuNPC should be the better photonic materials with larger diffusion coefficients and longer diffusion lengths as compared to that of other phthalocyanine derivatives. However, it should be pointed out that diffusion length is limited to a few nanometers only (about 10 nm may be expected for the Zn-tBuNPC), which may limit their efficiency in light harvesting devices. The diffusion length is a function of both diffusion coefficient and exciton lifetime (equation 7.12). While the value of diffusion coefficient may reasonably be large, the exciton lifetime is only in the range of 30 – 50 ps, as opposed to their long lifetime (a few nanosecond) in monometic forms. The short lifetime of the excitons, which may be attributed to the presence of many disordered sites which act as trap centres for faster nonradiative deactivation for the excitons, limit the maximum distance, which an exciton may travel during its lifetime,.[35,36,50] To reduce the disordered trap state by changing preparation condition (such as solvent combination, reaction temperature, etc) may be a future course of action to increase the exciton lifetime to improve diffusion lengths for better viability of these materials in solar harvesting applications.

7.3. CONCLUSIONS

Excited state dynamics and exciton diffusion parameters of five phthalocyanine derivatives have been studied using sub-picosecond time-resolved transient absorption spectroscopic technique. Following photoexcitation of the monomer in the S_2 state, two ultrafast processes, namely the internal conversion to the S_1 state and the vibrational relaxation in the S_1 state are the major relaxation pathways populating the lowest vibrational level of the long lived

S_1 state. The S_1 state further found to decay with a time constant of few ns. On the other hand, dynamics of the excited states of the nanoaggregates are mainly governed by exciton - exciton annihilation and annihilation free natural decay which are completed within a few hundred picoseconds. From excitation intensity dependent ultrafast transient dynamics studies, diffusion coefficient and diffusion length of the excitons in nanoaggregates of the five phthalocyanine derivatives have been estimated which vary in the following order: ZnPC ~ Zn-tBuNPC > Zn-tBuPC > tBuNPC > tBuPC. Superior diffusion properties of Zn-tBuNPC is attributed to better intermolecular interaction facilitated by expanded aromatic conjugation and central zinc metal coordination and thus Zn-tBuNPC may find better suitability for better photovoltaic applications. The non -tBu substituted ZnPC possibly have much more better molecular packing due to the better approachability of the molecules to each other in NA form. Thus it also possesses faster exciton diffusion and longer exciton diffusion length. However, there is further scope in future to improve diffusion length of these materials by addressing the factors which limit exciton lifetime in the range of 40-50 ps and reducing the possibility of disordered molecular packing.

7.4. REFERENCES

1. Cui, H. Q.; Zhao, Y. S.; Yao, J. *Adv. Mat.* **2014**, *26*, 6852.
2. Medforth, C. J.; Wang, Z.; Martin, K. E.; Song, Y.; Jacobsen, J. L.; Shelnutt, J. A. *Chem. comm*. **2009**, 7261.
3. Zhang C.; Chen, P.; Dong, H.; Zhen, Y. Liu, M.; Hu, W. *Adv. Mat. 2015*, *27*, 5379.
4. Zhong, Y.; Wang, J.; Zhang, R.; Wei, W.; Wang, H.; Lu, X,; Bai, F.; Wu, H.; Haddad, R.; Fan, H. *Nano Lett*. **2014**, *14*, 7175.
5. Philp, D.; Stoddart, J. F. *Angew. Chem. Int. Ed.***1996**, *35*, 1154.
6. Wurthner, F.; Kaiser, T. E.; Saha-Moller C. R. *Angew. Chem. Int. Ed.* **2011**, *50*, 3376
7. Ward, M. D. *Chem. Soc. Rev.***1997**, *26***,** 365.
8. Ahrens, M. J.; Sinks, L. E.; Rybtchinski, B.; Liu, W.; Jones, B. A.; Giaimo, J. M.; Gusev, A. V.; Goshe, A. J.; Tiede, D. M.; Wasielewski, M. R. *J. Am. Chem. Soc***., 2004,** *126***,** 8284.
9. Pope, M.; Swenberg, C. E. *Electronic Processes in Organic Crystals*, 2nd ed. (Oxford University Press, New York), **1999**.
10. Sundström, V.; Gillbro, T.; Gadonas, R.; Piskarskas, A.; *J. Chem. Phys.***1988,** *89***,** 2754.
11. Scheblykin, I.; Varnavsky, O.; Bataiev, M.; Sliusarenko, O.; Van der Auweraer, M.; Vitukhnovsky, A.; *Chem. Phys. Lett.* **1998**, *298***,** 341.

12. Moll, J.; Harrison, W. J.; Brumbaugh, D. V.; Muenter, A. A. *J. Phys. Chem. A* **2000**,*104*, 8847.
13. Kakade, S.; Ghosh, R.; Palit, D. K. *J. Phys. Chem. C* **2013**, *116*, 15155.
14. Gulbinas, V.; Chachisvilis, M.; Valkunas, L.; Sundström, V. *J. Phys. Chem.***1996**, *100*, 2213.
15. Shirakawa, M.; Kawano, S.; Fujita, N.; Sada, K.; Shinkai, S. *J. Org. Chem.* **2013,** *68*, 5037.
16. Verma, S.; Ghosh, A.; Das, A.; Ghosh, H. N. *J. Phys. Chem. B*, **2010**,*114*, 8327.
17. Keuren, E. V.; Bone, A.; Ma, C. *Langmuir*, **2008**, *24*, 6079.
18. Yago, T.; Tamaki, Y.; Furube, A.; Katoh, R. *Phys. Chem. Chem. Phys.*, **2008,** *10*, 4435.
19. Furube, A.; Murai, M.; Tamaki, Y.; Watanabe, S.; Katoh, R.; *J. Phys. Chem. A* **2006,** *110*, 6465.
20. Farren, C.; FitzGerald, S.; Beeby, A.; Bryce, M. R. *Chem. Commun.***2002**, 572.
21. Tamaki, Y.; Asahi, T.; Masuhara, H.; *J. Phys. Chem. A*, **2002**, *106*, 2135.
22. Manna, B.; Ghosh, R.; Palit, D. K. *J. Phys. Chem. C,* **2015,** *119*, 10641.
23. Manna, B.; Ghosh, R.; Palit, D. K. *J. Phys. Chem. C,***2016**, *120*, 7299.
24. Ito, F.; Inoue, T.; Tomita, D.; Nagamura, T. *J. Phys. Chem. B*, **2009**, *113*, 5458.
25. Jakubikova, E.; Campbell, I. H.; Martin, R. L. *J. Phys. Chem. A*, **2011**, *115*, 9265.
26. Maligaspe, E.; Kumpulainen, T.; Lemmetyinen, H.; Tkachenko, N. V.; Subbaiyan, N. K.; Zandler, M. E.; D'Souza, . *J. Phys. Chem. A*, **2010**, *114*, 268.
27. Walter, M. G.; Rudine, A. B.; Wamser, C. C. *J. Porphyrins Phthalocyanines*, **2010**, *14*, 759.
28. Torre, G.; Vazquez, P.; Agullo-Lopez, F.; Torres, T. *Chem. Rev*. **2004**, *104*, 3723.
29. Nitschke, C.; O'Flaherty, S. M.; Kroll, M.; Blau, W. J. *J. Phys. Chem. B*, **2004,** *108*, 1287.
30. Ghosh, R.; Nandi, A.; Palit, D. K. *Phys Chem. Chem. Phys.* **2016**, *18*, 7661.
31. Middleton, C. T.; Cohen. B.; Kohler, B. *J. Phys. Chem. A*, **2007**, *111*, 10460.
32. Ghosh, R.; Palit, D. K. *J. Phys. Chem. A* **2012**, *116*, 1993.
33. Lunt, R. R.; Benziger, J. B.; Forrest, S. R. *Adv. Mater*. **2010**, *22*, 1233.
34. Terao, Y.; Sasabe, H.; Adachi, C. *Appl. Phys. Lett.* **2007**, *90*, 103515.
35. Rim, S.; Fink, R. F.; Schoneboom, J. C.; Erk, P.; Peumans, P. *Appl. Phys. Lett.* **2007**, *91*, 173504.
36. Siebbeles, L. D. A.; Huijser, A.; Savenije, T. J. *J. Mater. Chem*. **2009**, *19*, 6067.

37. Torre, G. D. I.; Vazquer, P.; Agullo-Lopez, F.; Torres, T. *Chem.Rev.* **2004**, *104*, 3723.

38. Ke, L.; Gasparini, N.; Min, J.; Zhang, H.; Adam, M.; Rechberger, S.; Forberich, K.; Zhang, C.; Spiecker, E.; Tykwinski, R. R.; Brabec, C. J.; Ameri, T. *J. Mat. Chem. A.* **2017**, *5*, 2550

39. Fornari, R. P.; Arago, J.; Troisi, A. *J. Phys. Chem. C.* **2016**, *120*, 7987.

40. Kurrle, D.; Pflaum, J. *Appl. Phys. Lett.* **2008**, *92*, 133306

41. Peumans, P.; Yakimov, A.; Forrest, S. R. *J. Appl. Phys.* **2003**, *93*, 3693

42. Banerjee, S.; Parhi, A. P.; Iyer, S. S. K.; Kumar, S. *Appl. Phys. Lett.* **2009**, *94*, 223303.

43. Bruno, A.; Reynolds, L. X.; Smith, C. D.; Nelson, J.; Haque, S. A. *J. Phys. Chem. C.* **2013**, *117*, 19832.

44. Paillotin, G.; Swenberg, C. E.; Breton, J.; Geacintov, N. E. *Biophysics J.* **1979**, *25*, 513.

45. Sundström, V.; Gillbro, T.; Gadonas, R.; Piskarskas, A. *J. Chem. Phys.* **1988**, *89*, 2754.

46. Valkunas, L.; Akesson, E.; Pullerits, T.; Sundstrom, V. *Biophys. J.* **1996**, *70*, 2373.

47. Edward, J. T. *J. Chem. Educ.* **1970**, *47*, 261.

48. Fornari, R. P.; Arago, J.; Troisi, A. *J. Phys. Chem. C.* **2016**, *120*, 7987

49. Makhnenko, O. V.; Blom, P. W. M.; Nguyen, T. Q. *Energy Environ. Sci.* **2015**, *8*, 1867.

50. Bruno, A.; Reynolds, L. X.; Smith, C. D.; Nelson, J.; Haque, S. A. *J. Phys. Chem. C.* **2013**, *117*, 19832.

CHAPTER 8

SUMMARY AND FUTURE DIRECTIONS

8.1. INTRODUCTION

Finally we come to the concluding chapter of the thesis. Scientific research can be compared to a never ending relay race, where one group carried out experiments and summarized there results, ideas and passed it to the scientific community; again some other groups take those ideas to progress in the field. Therefore, summary and future directives always possess a significant importance in a thesis. Here in this chapter, we will summarize the overall works carried out under this thesis and make an attempt to provide consolidated pictures of microscopic nature of the RTILs and the excitonic properties of the nanoaggregates, which may lead to the comments on the applicability of these materials in the real world. We will also try to address about the future prospects of these research fields, to which our group or other groups may contribute in the near future.

8.2. CHAPTER WISE SUMMARY

The first chapter basically summarizes some basic concepts of the two types of self assembly forming media, their photophysical properties and describes the objective of the thesis. On the other hand the second is focused on the experimental techniques used in thesis. The summary of experimental results are documented in the subsequent chapters are provided in the following discussion.

In Chapter 3, we mainly described the results of our investigations on the triplet energy transfer and electron transfer processes in RTILs and other conventional solvent media carried out using transients, triplet states or radical anions, which are very long lived. The first part of the work has established the fact predicated by Vauthey et al. and Maroncelli et al. that, diffusion controlled energy or electron transfer reaction may be observed in highly viscous RTIL media in the stationary quenching regime.[1,2] We observe that using long-lived transient donors, e.g. radical anion or molecule in excited triplet state; which have lifetimes in the μs time domain, the stationary quenching regime may be achieved and the diffusion controlled reaction may be observed in the conventional solvents as well as in RTIL media.

In the second part, observation of ET and TET rates involving neutral-neutral and neutral-ionic pairs in different RTILs with different alkyl substituents suggests that, as the chain length of the alkyl substituent increases, RTILs may form more prominent microscopic pockets in the media. The alkyl chains interact with each other and form a hydrophobic nonionic pocket and on the other hand the imidazolium cation and the counter anion part accumulate in the region to form the ionic pocket. When both the donor and acceptor are neutral, they mostly prefer to remain solvated in the nonionic pockets. The reactions also take place in these pockets and the rates of the reactions reflect the effect of micro-viscosity of these nonionic pockets. As the solvent is changed from C_2mim to C_{10}mim, the bulk viscosity of the solvent increases, but as the reaction occurs in the nonpolar microscopic pocket and the reaction rate remain almost comparable. As a result the resultant parameter k_{ET}/k_{Diff} or k_{TET}/k_{Diff} (k_{diff} estimated from bulk viscosity) shows an increase as the RTIL changes from C_2mim to C_{10}mim. We also investigated the same reaction in SDS micelle and we observe the rates of the reactions occurring in the miceller core region are comparable to those estimated for the neutral-neutral pairs in these RTILs. This suggests that the nonpolar pockets of RTILs possess microscopic viscosity comparable to the microscopic viscosity of the micelle core of SDS.

When one of the species is ionic, it prefers to be solvated in ionic region and the other one being neutral prefers to remain in the nonionic pocket. Thus during reaction, these two reactants required to diffuse in those two different microscopic pockets. As a result the overall microscopic viscosity effect becomes nullified and we observe a bulk viscosity controlled ET or TET reaction in those cases.

In Chapter 4, we have shown that using reprecipitation method we can easily synthesize disc shape anthracene nanoaggregates having sizes of ~260 nm and height ~40 nm. The nanoaggregates possess bulk crystal type β-phase of molecular packing, however with some amorphous character. The absorption and emission maxima of the 0 - 0 vibronic bands of the NA are red-shifted by about 20 nm as compared to the corresponding one in the solution form. Time-resolved emission studies suggest wavelength dependent dynamics, which originates from the distribution of the orientational heterogeneities in the aggregate leading to different types of defect sites and hence the excimeric states of different conformations. Transient absorption studies reveal nonexponential dynamics of both the singlet and triplet excitonic states due to exciton - exciton annihilation reaction at high excitation intensities. Exciton annihilation rate constants of the singlet and the triplet excitons have been determined as 3.7×10^{-9} cm^3 s^{-1} and 2.2×10^{-13} cm^3 s^{-1}, respectively and exciton diffusion lengths to be about 13.2 and 6.5 nm, respectively. The singlet exciton diffusion length in the nanoaggregate is comparable to that of the anthracene crystal and this suggests that the NA may also be considered as materials for efficient optoelectronic and photovoltaic devices. However, we observe drastic reduction in triplet exciton diffusion coefficient in the nanoaggregate form and it is explained considering slower triplet energy transfer mechanism via spin exchange process.

In Chapter 5, we have demonstrated that polyacene molecules, e.g. tetracene, perylene and pentacene, which have structural similarities with anthracene molecule, can easily be doped into the anthracene nanoaggregate. The average size and height of the doped nanoaggregates are comparable to that of the anthracene nanoaggregate itself. The small dopant concentration used here does not show significant feature of the dopant in the absorption spectrum. However, in the steady state emission studies, we observe that the donor emission reduces with increase in acceptor concentration and concomitant enhancement in acceptor emission has also been observed. The time resolved emission studies also ensure the resonance energy transfer process as we observe decay of donor emission and concomitant growth of acceptor emission. We used SV analysis to estimate the energy transfer rate constants. The fast energy transfer rates observed here could not be explained considering the single step Förster resonance energy transfer process. The exciton diffusion rate has further been estimated from the excitation intensity dependent exciton – exciton annihilation process. The observed energy transfer rate is close to the diffusion limited rate. Thus, we conclude that in these doped nanoaggregates, exciton diffusion assisted FRET process takes place and make the energy transfer process highly efficient.

In this case, the three dopents provide emission in three different wavelength regions of the visible spectrum. When we combinedly doped these three dopants in proper concentration proportion we observe white light emission from the doped nanoaggregates upon excitation with near UV light. This work also suggests that such doped nanoaggregates may provide better emission yield with colour tunability which may be useful for LED or display device systems.

In Chapter 6, we describe the photophysics of pyrene and perylene nanoaggrgates, which were also synthesized using reprecipitation method having average sizes of ~120 nm. The XRD experiments confirm the presence of α-crystalline phase in both cases along with minor amorphous nature. The steady state absorption of pyrene nanoaggregate mainly shows red shifted broad absorption feature, on the other hand perylene nanoaggregate shows broad absorption band with a blue shifted absorption maximum. Both the nanoaggregates show broad excimer emission. The time resolved fluorescence measurements lead us to the confirmation of the presence of emission from free excitonc states as well as shallow and deep trap excitonic states in these two nanoaggregates. The shallow trap to deep trap state transition undergoes through an energy barrier of 57 meV and 102 meV for pyrene and perylene nanoaggregates, respectively.

In nanoaggregated form, the free exciton lifetime found to be enhanced as compared to the corresponding α-crystalline form. It causes enhancement in the exciton diffusion length of free excitons in the nanoaggrgated form. The exciton diffusion lengths have been estimated to be 10 ± 2 nm and 20 ± 4 nm for perylene and pyrene nanoaggregates, respectively. The longer exciton diffusion length of a material makes it more superior for photovoltaic application.

In Chapter 7, we describe the work carried out with five phthalocyanine compounds. Phthalocyanine molecules mainly form non fluorescent H-type aggregates. In all these cases the excitonic lifetimes decrease by almost two orders of magnitude as compared to those of the molecules in the solution. Enhanced nonradiative decay path may be assigned to be a possible reason for this first decay. We have carried out ultrafast transient absorption measurements for the excitonic states of these nanoaggregates at different excitation intensities. Like in the case of anthracene, pyrene and perylene nanoaggregates, these nanoaggregates also show intensity dependent second order decay of the excitonic state population. These intensity dependent kinetics are fitted using mixed order decay model to estimate the exciton - exciton annihilation rate constants. The rates of diffusion controlled exciton annihilation process have further been used to extract the exciton diffusion parameter such as, exciton diffusion coefficients, hopping times, exciton diffusion lengths. These parameters further compared for these five phthalocyanine nanoaggregates.

We observe that introduction of bulky –^{t}Bu substituents at four peripheral positions causes less efficient molecular packing, evident from the XRD pattern, and hamper the exciton diffusion process. It causes shorter exciton diffusion length. The more extended π-conhugation leads to stronger intermolecular interaction and faster exciton hopping. Zn^{2+} ion complex formation also causes enhancement in the exciton diffusion length. Among these five materials ZnPC and ^{t}BuZnNPC possess longer exciton diffusion lengths and more promising material for photovoltaic device from charge separation efficiency point of view. These materials are non-fluorescent and don't have much scope for emission based device applications.

8.3. FUTURE DIRECTIONS

In the first part of this thesis we have mainly observed the energy transfer and electron transfer reactions with long lived transients in different RTIL media. We have started with these most common imidazolium based ionic liquids. However, other RTILs with different counter ions having superior application property can also be taken for such experiments to explore the microscopic properties. The molecular rotors which are considered as good microviscosity sensor can also be utilized to probe the microscopic viscosities of the local pockets of RTIL medium.[3-5]

This is also inferred that association of long alkyl substitution in the RTILs causes more prominent microscopic pocket formation in RTIL media. Thus we can use more elongated alkyl substitutents and observe the micelle type structure formation. We can also observe this property in aqueous or other solvent medium. The microscopic properties, microscopic viscosity also can be investigated observing the energy transfer or electron transfer process in those binary solvent medium.[4] These explorations may lead to more detail understanding about the RTIL medium and provide insights about the efficient applicability of these solvent systems.

In the second part, the excited state dynamics has been resolved for few polyacene molecules and few phthalocyanine derivatives. These are some primary works and we think there are plenty of scopes to explore in these fields. First we may explore exciton dynamics in other polyacene molecules and their derivatives. Specially polyacene molecules e.g. tetracene, pentacene, rubrene, perylenediimide have got huge attention for the possibility of observation of exciton fission process which may double the efficiency of organic solar cells.[7-15] Different substituents may be introduced in these polyacene molecules and we can observe the effect on photophysical properties and exciton dynamics upon aggregation of the molecules.[16,17]

There are also scopes to synthesize nanoaggregates having different sizes and shapes.[18] The effect of the morphology on the excited state properties may also be investigated As mentioned in this thesis, the molecular packing also may have significant effect on the photophysics of a material.[19] Therefore significant efforts should be provided to produce materials having different molecular packings and the effect may be monitored. Not only to the aggregates, similar studies may be conducted in the thin films and may be extended for device fabrication step.

In the case of phthalocaynine derivatives there are also verity of pthalocyanines which may be taken for similar experiments. It has been observed that these molecules form mainly H-type of aggregates. One can also try to synthesise the J-type of aggregates of these molecules and explore the photophysical properties.[20] These aggregates are also found to have very short lifetime than the solution form. In the H- type of nanoaggregates the radiative decay rate remain very low, this means the other nonradiative decay rates are very high in the nanoaggregate form. Nonradiative decay occurs through phonon modes, may be one possible reason for that. However, if this is true, then one can try to explore the factors which govern the nonradiative decay rate through the phonon modes.

Finally in organic chemistry there are enormous scopes to choose molecules having desired property or designed and synthesized them accordingly and similar photophysical studies can be carried out. Thus it seems a vast open research field, till remain unexplored, which can be elucidated in the near future by the researchers.

8.4. REFERENCES

1. Liang, M.; Kaintz, A.; Baker, G. A.; Maroncelli, M. *J. Phys. Chem. B.* **2012**, *116*, 1370.
2. Koch, M.; Rosspeintner, A.; Angulo, G.; Vauthey, E. *J. Am. Chem. Soc.***2012**, *134*, 3729.

3. Levitt, J. A.; Kuimova, M. K.; Yahioglu, G.; Chung, P. H.; Suhling K.; Phillips, D. J. *Phys. Chem. C*, **2009**, *113*, 11634.

4. Kuimova, M. K. *Phys. Chem. Chem. Phys*. **2012**, *14*, 12671.

5. Thompson, A. J.; Herling, T. W.; Kubankova, M.; Vysniauskas, A.; Knowles, T. P. J.; Kuimova, M. K. *J. Phys. Chem. B*, **2015**, *119*, 10170.

6. Sarkar, S.; Mandal, S.; Ghatak, C.; Rao, V. G.; Ghosh, S.; Sarkar, N. *J. Phys. Chem. B*, **2012**, *116*, 1335.

7. Wilson, M. W. B.; Rao, A.; Johnson, K.; Gélinas, S.; Pietro, R. D.; Clark, J.; Friend, R. H. J. *Am. Chem. Soc.*, **2013**, *135*, 16680.

8. Liu, H.; Wang, R.; Shen, L.; Xu, Y.; Xiao, M.; Zhang, C.; Li, X. *Org. Lett.*, **2017**, *19*, 580.

9. Korovina, N. V.; Das, S.; Nett, Z.; Feng, X.; Joy, J.; Haiges, R.; Krylov, A. I.; Bradforth, S. E.; Thompson, M. E. *J. Am. Chem. Soc.*, **2016**, *138*, 617.

10. Wilson, M. W. B.; Rao, A.; Ehrler, B.; Friend, R. H. *Acc. Chem. Res.*, **2013**, *46*, 1330.

11. Lee, J.; Jadhav, P.; Reusswig, P. D.; Yost, S. R.; Thompson, N. J.; Congreve, D. N.; Hontz, E.; Voorhis, T. V.; Baldo, M. A. *Acc. Chem. Res.*, **2013**, *46*, 1300.

12. Tabachnyk, M.; Karani, A. H.; Broch, K.; Pazos-Outón, L. M.; Xiao1, J. *APL Materials* **2016**, *4*, 116112.

13. Tabachnyk, M.; Ehrler, B.; Bayliss, S.; Friend, R. H.; Greenhama, N. C. *Appl. Phys. Lett.* **2013**, *103*, 153302.

14. Eaton, S. W.; Shoer, L. E.; Karlen, S. D.; Dyar, S. M.; Margulies, E. A.; Veldkamp, B. S.; Ramanan, C.; Hartzler, D. A.; Savikhin, S.; Marks, T. J.; Wasielewski, M. R. *J. Am. Chem. Soc.*, **2013**, *135*, 14701.

15. Mauck, C. M.; Brown, K. E.; Horwitz, N. E.; Wasielewski, M. R. *J. Phys. Chem. A*, **2015**, *119*, 5587.

16. Walker, B. J.; Musser, A. J.; Beljonne, D.; Friend, R. H. *Nature Chemistry* **2013**, *5*, 1019.

17. Stern, H. L.; Musser, A. J.; Gelinas, S.; Parkinson, P.; Herz, L. M.; Bruzek, M. J.; Anthony, J.; Friend, R. H.; Walker, B. J. *PNAS*, **2015**, *112*, 7656.

18. Yang, B.; Xiao, J.; Wong, J. I.; Guo, J.; Wu, Y.; Ong, L.; Lao, L. L.; Boey, F.; Zhang, H.; Yang, H. Y.; Zhang, Q. *J. Phys. Chem. C*, **2011**, *115*, 7924.

19. Manna, B.; Ghosh, R.; Palit, D. K. *J. Phys. Chem. C*. **2015**, *119*, 10641.
20. Adachi, K.; Chayama, K.; Watarai, H. *Langmuir*, **2006**, *22*, 1630.

SUPPLEMENTARY DATA

CHAPTER 3

S3.1: Structures of the chemical systems, for which the TET and ET processes have been studied and the RTIL solvents used in this work.

Triplet – triplet Energy Transfer (TET) **Electron Transfer (ET)**

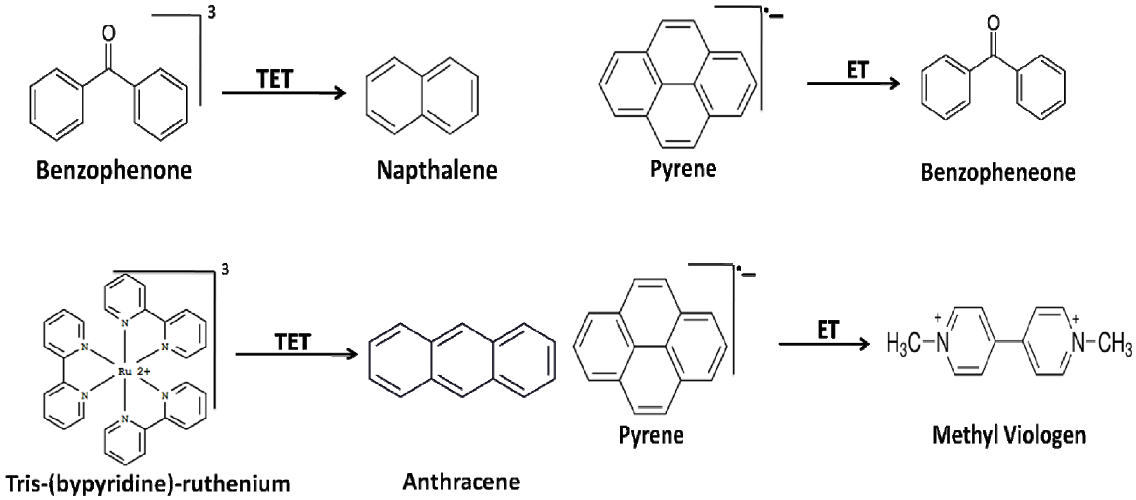

RTIL solvents:

C_2Mim: n = 1
C_4Mim: n = 3
C_6Mim: n = 5
C_{10}Mim: n = 9

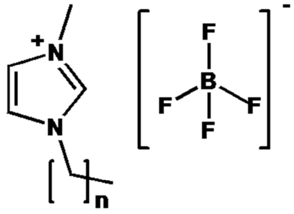

S3.2: Time resolved transient absorption spectra recorded following photoexcitation of (A) BP in C_4Mim and (B) RuBPY^{2+}in C_4Mim **Insets:** (A) The temporal profile recorded at 525 nm for the decay of the T_1 state of BP, (B) the decay of stimulated emission from the T_1 state of RuBPY^{2+}

recorded at 620 nm. Values of the lifetimes associated with the single exponential fit functions are also shown in the insets.

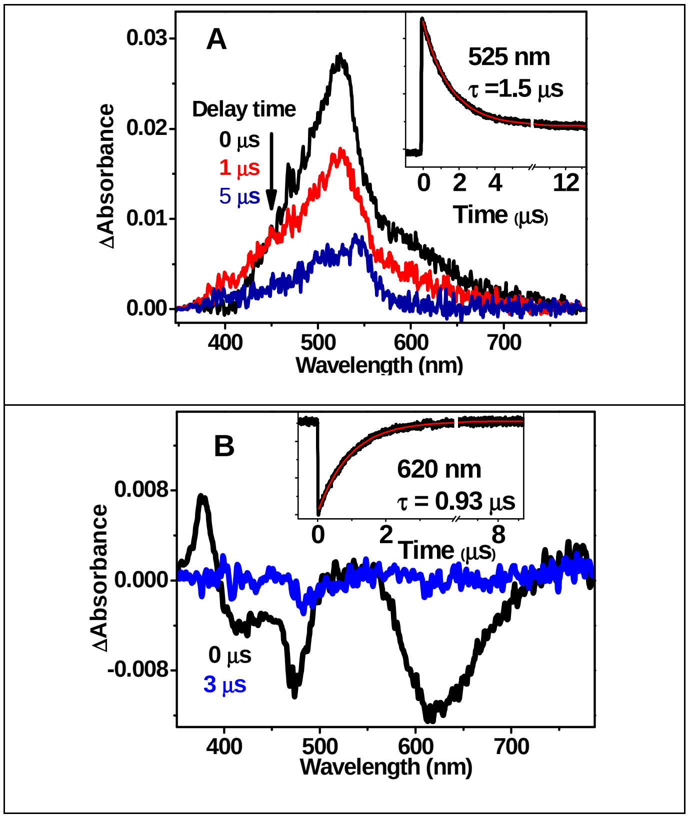

S3.3: Single exponential fit functions and residual distributions in the cases of the TET process for BP - NP pair in four RTIL solvents.

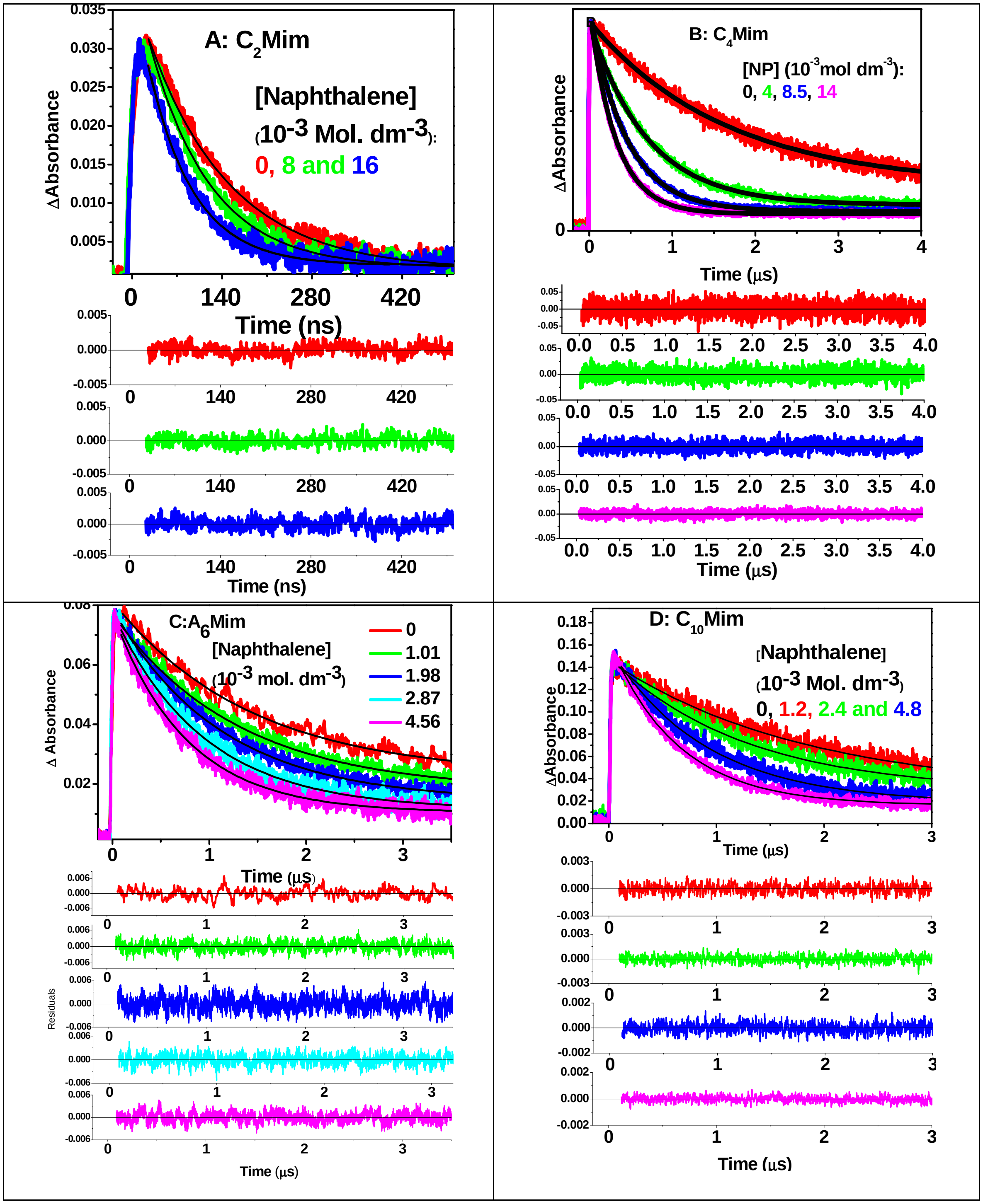

S3.4: Single exponential fit functions and residual distributions in the cases of the ET process for Py-BP pair in four RTIL solvents.

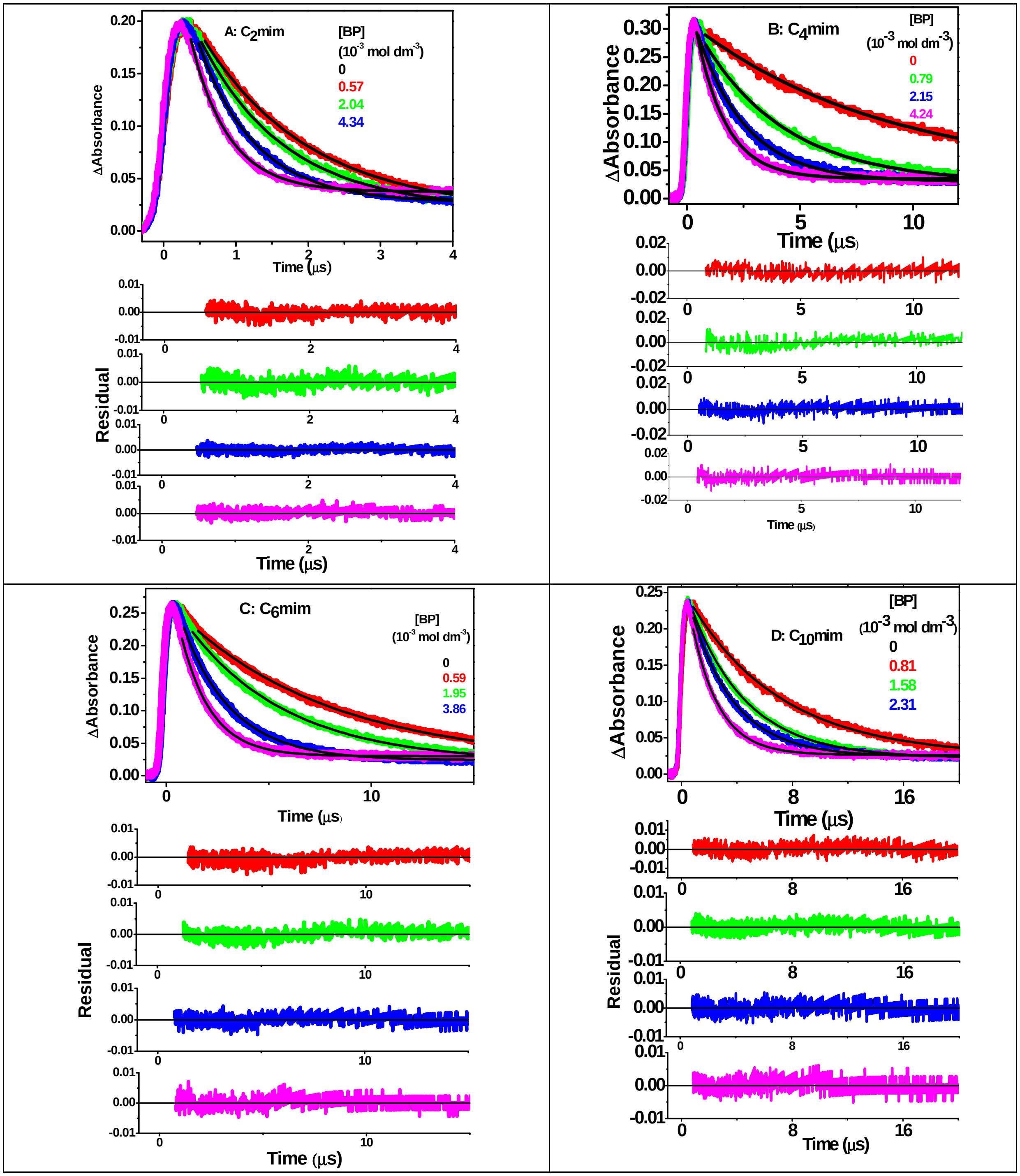

S3.5: The time resolved absorption spectra recorded following pulse radiolysis of methylviologen (MV^{2+}) in C_4Mim solvent.

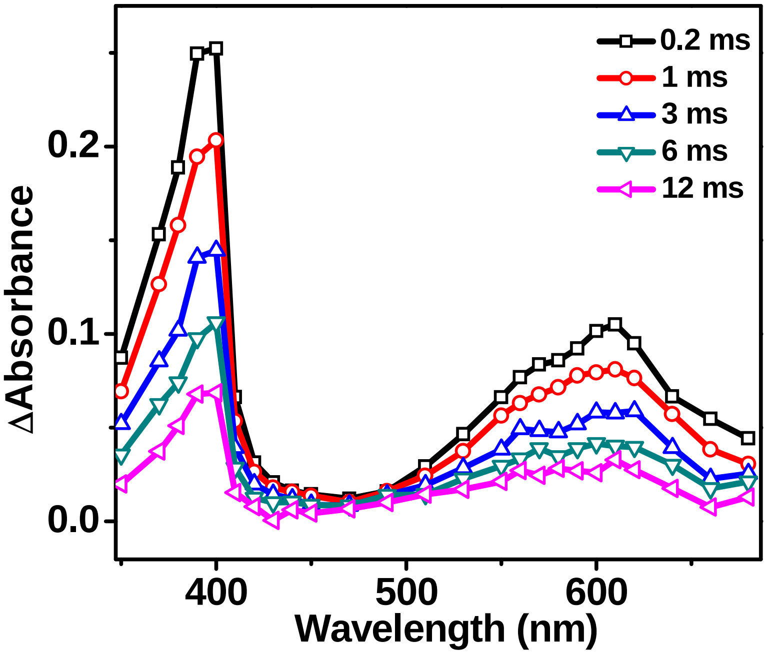

S3.6: Dependence of the transient quenching time domain on the bulk viscosity of the solvents.

Py-BP Pair		BP-NP Pair	
η (cP)	Time (ns)	η (cP)	Time (ns)
0.35	0.2	0.35	0.14
15.7	8.9	15.6	6.3
24	13.6	24	9.7
44	24.9	44.2	17.9
93	52.7	91.2	37
185	104.8	205.1	83.3
490	277.7	493.2	200.2

S3.7: Pyrene emission spectra recorded in four RTIL solvents Inset: showing emission spectra in cyclohexane, acetonitrile.

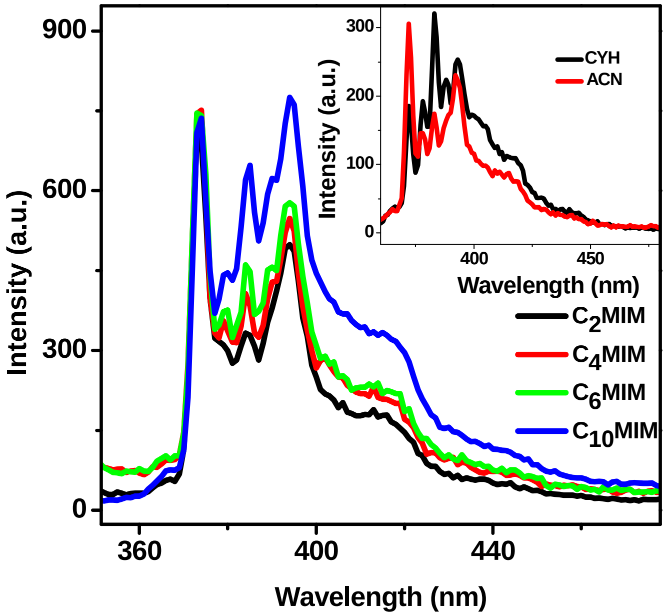

Table S2: The intensity ratios of 373 nm vs.385 nm emission of pyrene in these above solvents.

Solvent	CYH	ACN	C_2MIM	C_4MIM	C_6MIM	C_{10}MIM
I_{373}/I_{385}	0.58	1.77	2.12	1.86	1.65	1.13

I_{373}/I_{385}: TX100 ~0.95, SDS ~0.8, Methanol: 1.35, 2-propanol: 1.09 (Ref 68)

CHAPTER 4

S4.1: Derivation of the equations for the fitting of temporal profile

The rate of change of singlet exciton concentration can be written as (considering equation 1-3 and taking assumption that the [D] is constant with respect to time),

$$\frac{d[S_1]}{dt} = -k_1[S_1] - \frac{1}{2}k_2[S_1]^2$$

Let us take, x = 1/$[S_1]$

$$\frac{dx}{dt} = -\frac{1}{[S_1]^2}\frac{d[S_1]}{dt}$$

Hence, $$-[S_1]^2 \frac{dx}{dt} = -k_1[S_1] - \frac{1}{2}k_2[S_1]^2$$

$$\frac{dx}{dt} = k_1 x + \frac{1}{2}k_2$$

Or, $$\frac{dx}{dt} - k_1 x = \frac{1}{2}k_2$$

Integrating Factor = $e^{\int -k_1 dt} = e^{-k_1 t}$

Multiplying integrating factor both side, we get:

$$e^{-k_1 t}\frac{dx}{dt} - k_1 x e^{-k_1 t} = \frac{1}{2}k_2 e^{-k_1 t}$$

Integrating both side for 0 to t time limit,

$$\int_0^t d[xe^{-k_1 t}] = \int_0^t \frac{1}{2}k_2 e^{-k_1 t} dt$$

Or, $[xe^{-k_1 t}]_0^t = [-\frac{k_2}{2k_1}e^{-k_1 t}]_0^t$

Putting the value of x, and simplifying the equation we get,

$$[S_1] = \frac{[S_1]_0 e^{-k_1 t}}{1 + \frac{k_2}{2k_1}[S_1]_0\,[1 - e^{-k_1 t}]}$$

In the present case we can assume, k_{1t}<<1.

Therefore, $e^{-k_1 t} = 1 - k_1 t$ can be used in the above expression and we get,

$$[S_1] = \frac{[S_1]_0 e^{-k_1 t}}{1+\frac{k_2}{2}[S_1]_0 t} = \frac{[S_1]_0 e^{-k_1 t}}{1+k_2' t}$$

Where, $k_2' = \frac{k_2}{2}[S_1]_0$

The transient absorption signal also contained excimer formation signal.

$$S_1 + D \xrightarrow{k_3} E$$

The excimer formation associated with rate constant k_3.

Therefore for the above process, we can write the differential equation as follows,

$$\frac{d[E]}{dt} = k_3[S_1][D]$$

Now putting the value of $[S_1]$from the earlier calculation we get,

$$\frac{d[E]}{dt} = k_3 \frac{[S_1]_0 e^{-k_1 t}}{1 + k_2' t}[D]$$

Integrating both side for the 0 to t time limit we get,

$$[E] = k_3[D][S_1]_0 \int_0^t \frac{e^{-k_1 t}}{1 + k_2' t} dt = k_3[D][S_1]_0[te^{-k_1 t}\left(1 - \frac{1}{k_1^2} - \frac{1}{k_1^3}\right)]$$

As the value of k_1 is very large we can assume that,

$$\left(1 - \frac{1}{k_1^2} - \frac{1}{k_1^3}\right) = 1$$

Hence,

$$[E] = k_3[D][S_1]_0 te^{-k_1 t}$$

Therefore, the stimulated signal coming from the formation of excimer state will have similar formula with negative sign.

S4.2: Table: Parameters best-fitting to the temporal TA profiles recorded at 590 nm at different excitation intensities by using mixed order decay kinetics (equation 13)

Parameters	**12.1 μJ/pulse**	**9.05 μJ/pulse**	**6.85 μJ/pulse**	**4.64 μJ/pulse**	**3.31 μJ/pulse**
$[\Delta OD]_0$(mOD)	6.26 ± 0.05	5.82 ± 0.04	5.95 ± 0.03	5.55 ± 0.04	5.4 ± 0.02
k'_2 (10^{11} s^{-1})	4.28 ± 0.26	2.91 ± 0.17	2.11 ± 0.14	1.2 ± 0.09	0.748 ± 0.06
k'_1 (10^9 s^{-1})	3.06 ± 0.3	3 ± 0.2	2.96 ± 0.2	2.9 ± 0.3	2.87 ± 0.4
k'_3 (10^8 s^{-1})	1.04 ± 0.1	1.08 ± 0.1	1.1 ± 0.1	1.07 ± 0.1	1.01 ± 0.1
R (10^{-4})	-8 ± 0.5	-2 ± 0.4	-1 ±0.2	-1 ± 0.2	-1 ± 0.3

S4.3: Calculation of singlet exciton density, $[S_1]_0$

We have used pulse energy in the range of 3-13 μJ/pulse. Here we have shown the procedure of exciton density estimation for pulse energy 12.1 μJ.

The excitation pulse energy=12.1 μJ

Each photon has energy=hc/λ=4.966×10^{-19} J [λ=400 nm]

Per pulse number of incident photon =2.436×10^{13}

Absorbance of the sample=0.35 i.e. 55% of incident photon are absorbed or 1.34×10^{13} number of photon are absorbed per pulse.

Beam diameter=2r~0.5 mm, path length=d=2 mm

The volume of excitation region =$\pi r^2 d$=3.925×10^{-4} cm^3

Volume of aggregate=$\pi R^2 h$= 2.65x106 nm^3[R=130 nm, h=50 nm]

Volume of one anthracene molecule 0.342 nm^3 (estimated using the molecular volume calculation reference: *J. Phys. Chem.***1964**, *68*, 441)

Number of anthracene molecule present per aggregate $=7.76\text{x}10^{6}$

Number of anthracene molecule present in excitation region=Concentration x volume (in lit.) x $6.023 \text{ x } 10^{23}= 0.625\text{x}10^{-3}\text{x}3.925\text{x}10^{-7}\text{x}6.023\text{x}10^{23} =14.78\text{x}10^{13}$ [Sample Concentration =0.625 mM]

Total number of aggregate present in the excitation region= $14.78 \text{ x}10^{13}/ 7.76 \text{ x}10^{6} =1.9 \text{ x } 10^{7}$

Per aggregate number of photon absorbed=$1.34\text{x}10^{13}/ 1.9\text{x}10^{7} =0.705\text{x}10^{6}$

Exciton density=$0.705\text{x}10^{6}/2.65\text{x}10^{6}$ nm^{3} $=2.66 \text{ x } 10^{20}$ cm^{-3}

S4.4: Calculation of Triplet Exciton Yield

In general, triplet yield is estimated from the comparison of triplet-triplet absorption spectra with a reference compound having known triplet yield. However, this method requires prior knowledge of triplet-triplet absorption coefficient of the molecule of interest. In the present case, we don’t know the triplet-triplet absorption coefficient of nanoaggregate. We have chosen an alternative method, reported by Weisman et. al. (ref-77). It uses the delayed fluorescence contribution to estimate triplet yield. It does not require any reference material and prior knowledge about extinction coefficient of triplet-triplet absorption. It is an independent method and gives triplet yield with reasonable accuracy.

Fluorescence decay profile recorded following nanosecond laser excitation at 355 nm and the data were analyzed following the method reported by Weisman et. al.

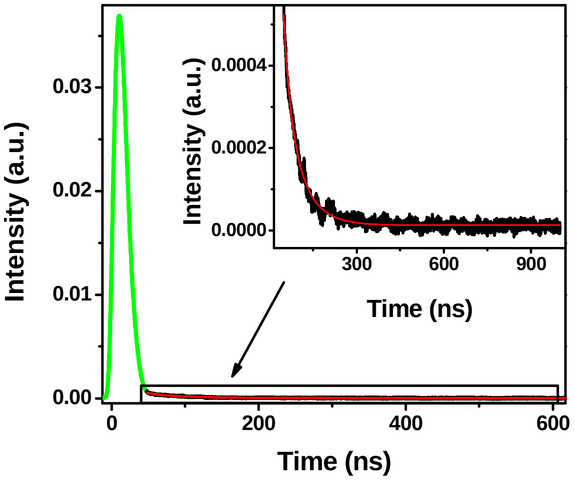

Delayed fluorescence part has been fitted using equation,

$$I_{Total} = I_0 X \frac{[exp(-k_1^T t)]}{(1 + k_2^T t)} + R$$

Fitting data for delayed fluorescence part : I_0=.00053, k_1^T=0.009 ns^{-1}, k_2^T=.0207 ns^{-1}, R=.000015

The triplet yield can be calculated using the given equation,

$$\Phi_T = \frac{5}{1 + Q\left(\frac{k_1^T \beta}{1 - \beta}\right)}$$

Where,

$\beta = \frac{k_2^T}{k_1^T + k_2^T}$=0.6971

Here Q=(Area under prompt fluorescence trace/$I_0^{Delayed}$) =1.707x 10^{-6} s

Putting the values of Q and β in the above equation we have estimated the triplet yield of 0.14, for anthracene nanoaggregate sample.

CHAPTER 5

S5.1: DLS (A, B and C) and AFM (D, E and F) data for TeAn, PnAn and ternary doped anthracene (MAn) nanoaggregates, respectively.

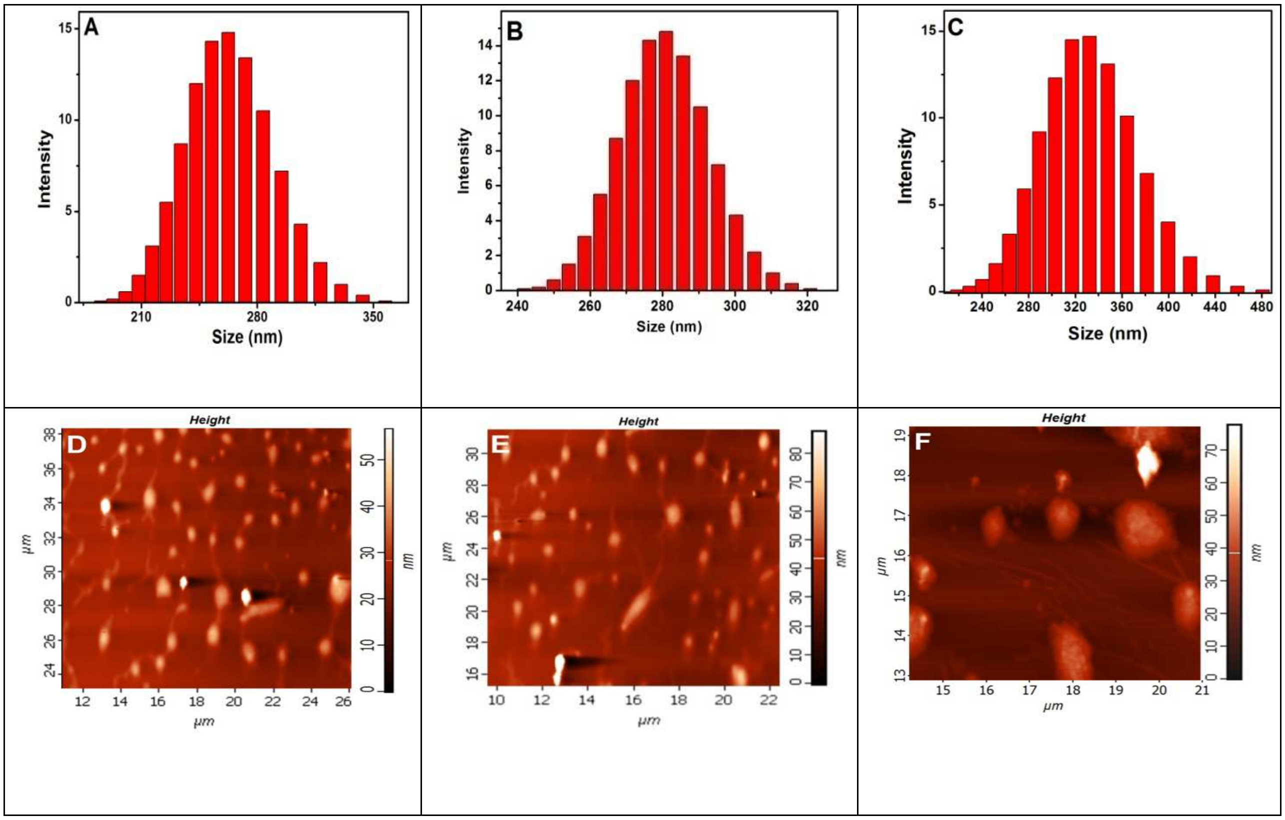

S5.2: Calculation of concentrations of the dopants in the nanoaggregates:

Approximation: All dopant molecules injected in the solution are accommodated inside the nanoaggregates. The dopant molecules are present in the nanoaggregates maintaining same concentration.

The acceptor/donor molar ratio is known (say 0.1% or 0.001)

The volume of the nanoaggregtaes are known [say, $\pi \times (140)^2 \times 50$ nm^3]

We have calculated the dopant concentration following these steps,

Per aggregate number of anthracne molecule = $\pi \times (140)^2 \times 50$ nm^3 / 0.343 nm^3 = 8.97×10^6

Hence per aggregate number dopant molecule = $8.97 \times 10^6 \times 0.001 = 8.97 \times 10^3$

Concentration of dopant = $8.97 \times 10^3 / \pi \times (140)^2 \times 50 \times 10^{-24} \times 6.023 \times 10^{23}$ mol. dm^{-3}

= 4.8 x 10^{-3} mol. dm^{-3}.

S5.3: Steady state absorption spectra of (A) TeAN and (B) PnAn nanoaggregates with three different concentrations of the dopant.

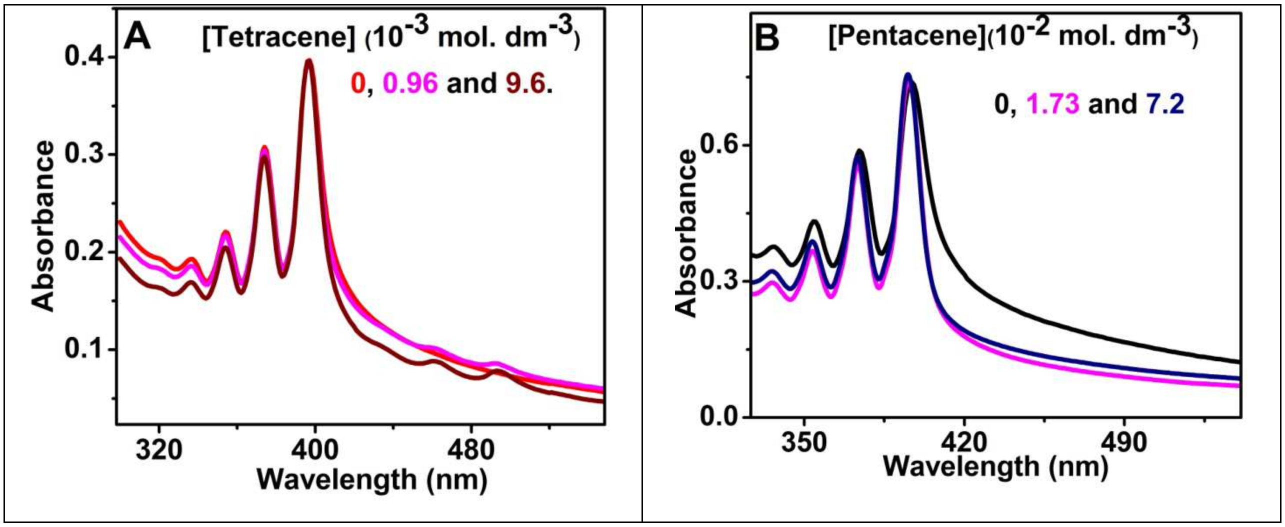

S5.4: Steady state emission spectra for (A) TeAn nanoaggregate and (B) PnAn nanoaggregate. ET efficiencies as a function of dopant concentrations for (C) TeAn and (D) PnAn nanoaggregates.

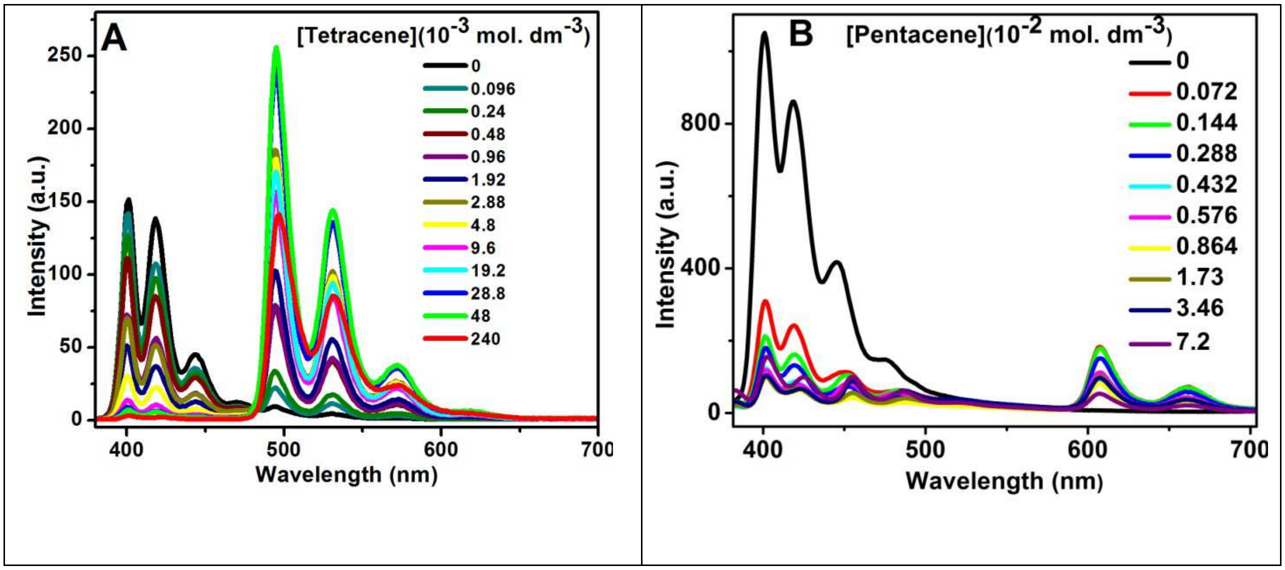

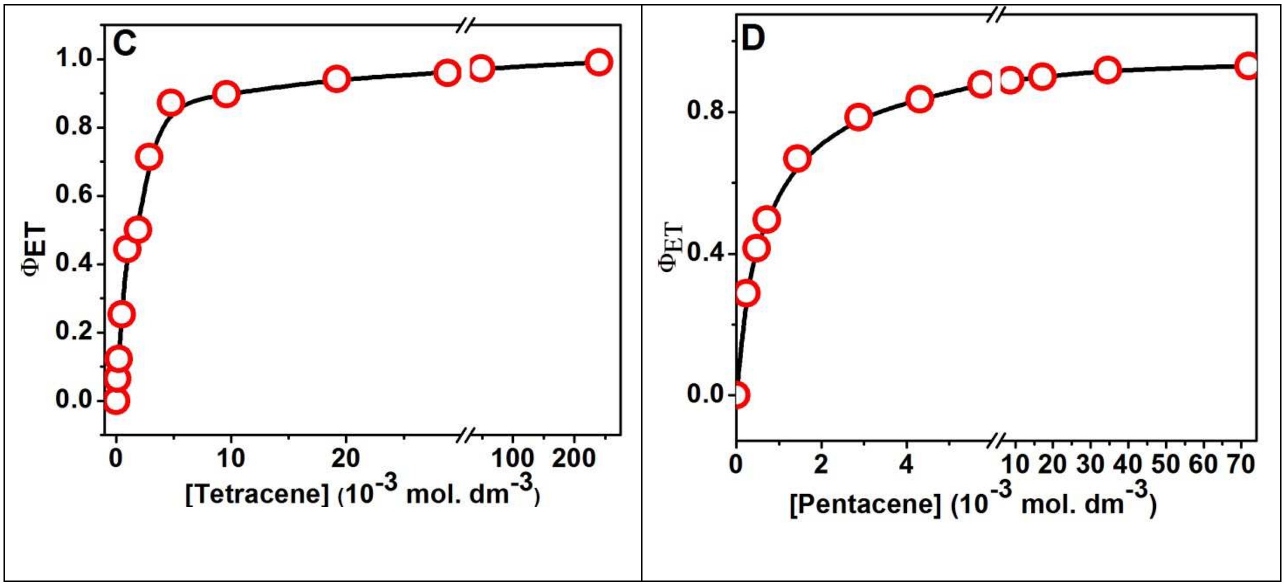

S5.5: Dependence of the emission yield of the doped binary anthracene nanoaggregates on the concentrations of the dopants.

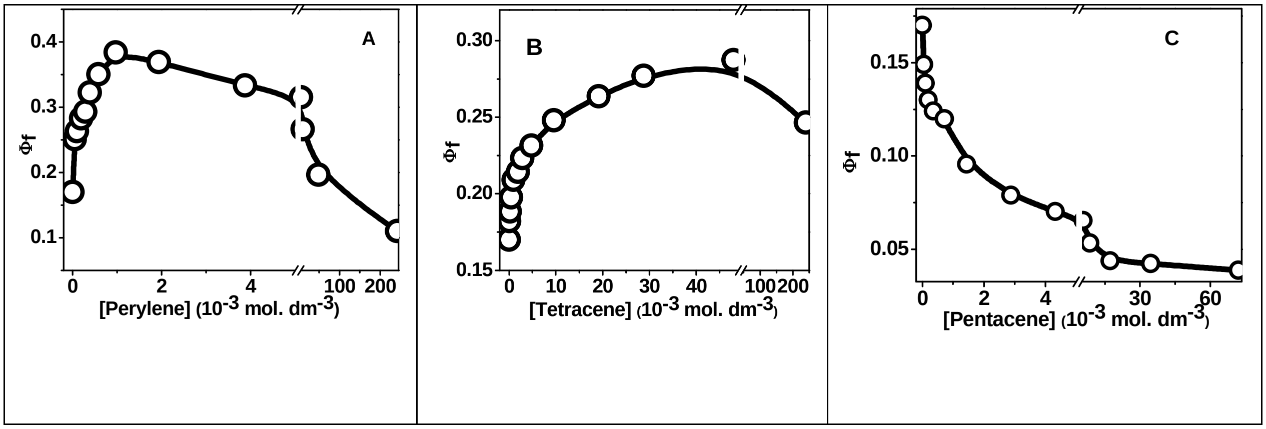

S5.6: Stern-Volmer plots for (A) TeAn and (B) PnAn nanoaggregate samples from the steady state emission data.

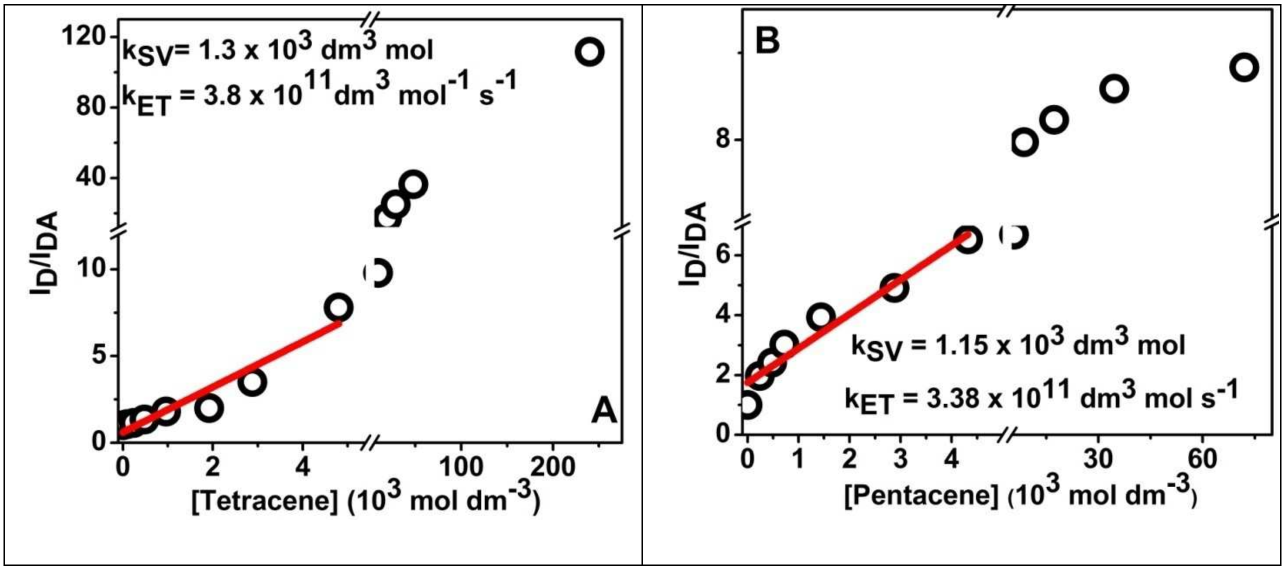

S5.7: Results of multi-exponential fittings of the temporal emission profiles recorded at 400 and 480 nm for undoped An and PeAn nanoaggregate samples.

A/D Ratio	**400 nm**	**480 nm**	$<\tau>_{400\ nm}$	$<\tau_D>/<\tau_{DA}>$
0 mM	τ_1 = 1.9 ns (0.31), τ_2 = 4.08ns (0.69)	-	3.4 ns	1
0.1 mM	τ_1 = 1.4 ns (0.33), τ_2 = 2.99 ns (0.67)	τ_1 = 1.3 ns (-0.09), τ_2 = 5.9 ns (0.47), τ_3 = 16.4 ns (0.62)	2.47	1.38
0.3 mM	τ_1 = 0.7 ns (0.21), τ_2 = 1.78 ns (0.7), τ_3 = 3.9 ns (0.09)	τ_1 = 0.4 ns (-0.05), τ_2 = 4.9 ns (0.34), τ_3 = 14.6 ns (66.5)	1.51	2.25
0.6 mM	τ_1 = 0.5 ns (0.37), τ_2 = 1.51 ns (0.6), τ_3 = 7 ns (0.03)	τ_1 = 0.49 ns (-0.03), τ_2 = 5.9 ns (0.39), τ_3 = 15.6 ns (0.64)	1.3	2.62
1.9 mM	τ_1 = 0.14 ns (0.19), τ_2 = 0.53 ns (0.69), τ_3 = 2.03 ns (0.12)	τ_1 = 0.22 ns (-0.01), τ_2 = 5.05 ns (0.37), τ_3 = 14.7 ns (0.64)	0.64	5.31
9.7 mM	τ_1 = 0.12 ns (0.25), τ_2 = 0.47 ns (0.69), τ_3 = 1.2 ns (0.06)	τ_1 = 0.2 ns (-0.01), τ_2 = 5.08 ns (0.4), τ_3 = 15.1 ns (0.61)	0.43	7.9`

S5.8: Temporal profiles recorded using TCSPC technique following photoexcitation of the undoped Anthracene and TeAn and PnAn nanoaggregate samples with different dopant concentrations at 374 nm. Temporal profiles have been recorded at 400 nm (A and C) for monitoring donor emission and at 495 nm (B) and 600 nm (D) for monitoring acceptor emission for TeAn and PnAn nanoaggregates, respectively.

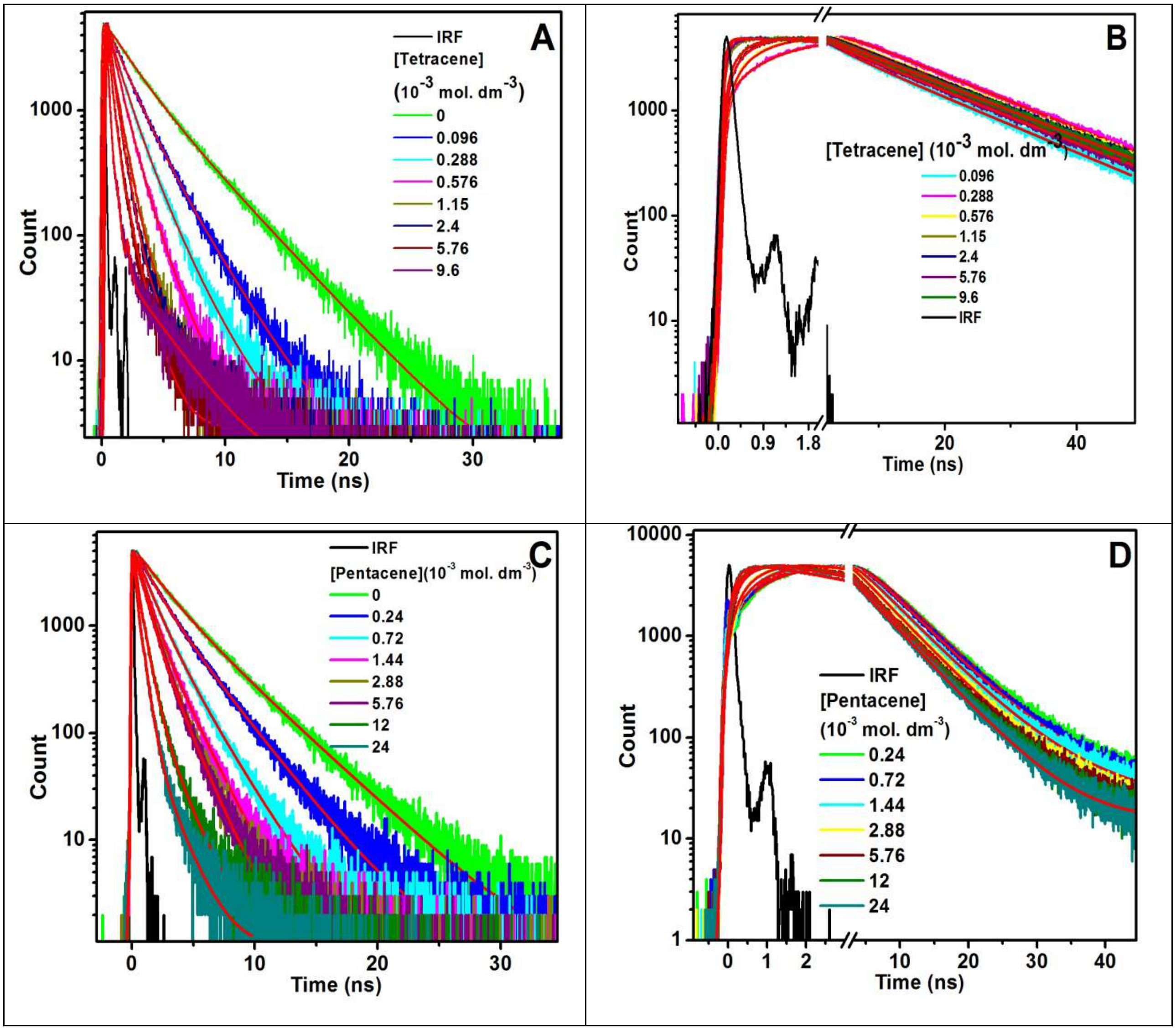

S5.9: The average lifetimes estimated from the fitting of the temporal profiles recorded at 400 nm and the fluorescence quenching efficiencies of the donor emission for PeAn, TeAn and PnAn nanoaggregates.

[Perylene] (10^{-3} mol. dm^{-3})	<τ> (ns)	ϕ_{ET}(TR)
0	3.4	-
0.1	2.46	0.27
0.3	1.74	0.49
0.6	1 3	0.62
1.2	0.93	0.73
2.3	0.66	0.81
5.8	0.51	0.85
9.6	0.38	0.89

PeAn Nanoaggrgate

[Tetracene] (10^{-3} mol. dm^{-3})	<τ> (ns)	ϕ_{ET}
0	3.4	-
0.3	2.01	0.4
0.5	1.62	0.52
1.0	1.45	0.58
2.9	1.04	0.694
4.8	0.723	0.787
19.2	0.49	0.86
48.0	0.31	0.91

TeAn nanoaggregate

[Pentacene] (10^{-3} mol. dm^{-3})	<τ> (ns)	ϕ_{ET}
0	3.4	-
0.2	2.66	0.22
0.7	1.73	0.491
1.4	1.35	0.614
2.9	1.14	0.67
5.8	0.7	0.78
12	0.64	0.82
24	0.43	0.87

PnAn nanoaggregate

S5.10: Stern-Volmer plots for (A) TeAn and (B) PnAn nanoaggregate samples from the average lifetime data (TCSPC experiments).

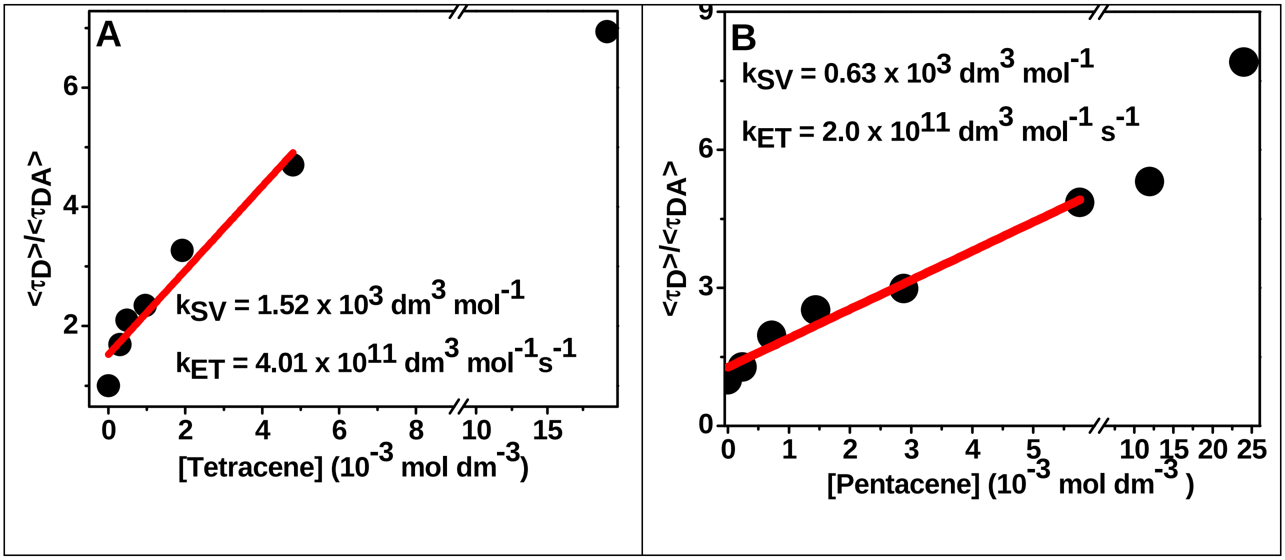

S5.11: Anthracene to Perylene energy transfer in THF.

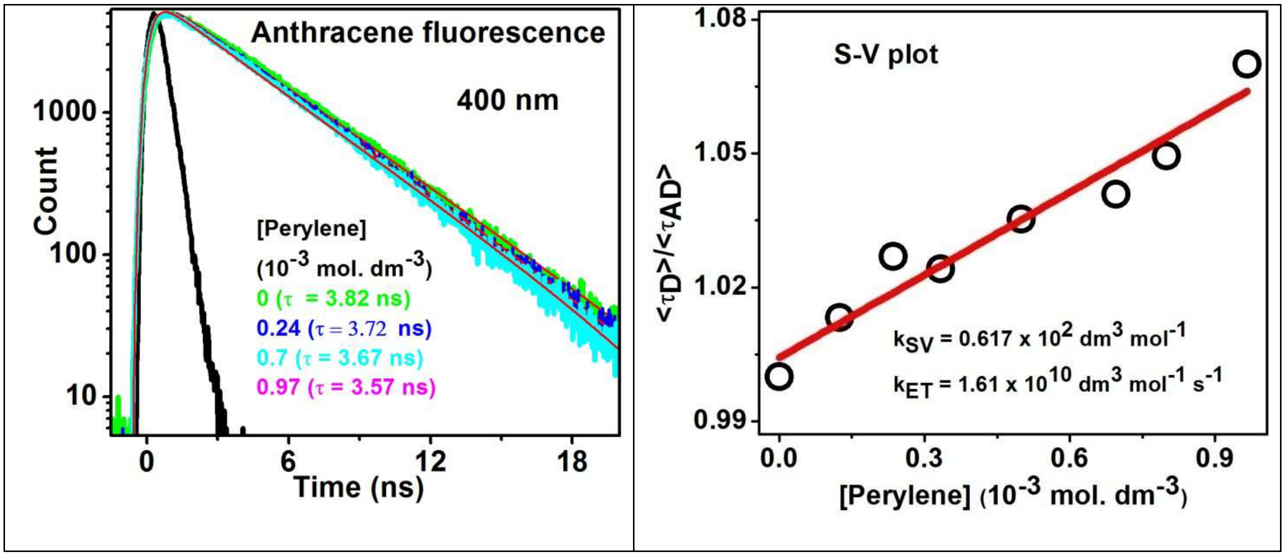

[Perylene] (10^{-3} mol. dm^{-3})	0	0.13	0.24	0.33	0.5	0.7	0.8	0.97
<τ> (ns)	3.82	3.77	3.72	3.73	3.69	3.67	3.64	3.57

S5.12: Fluorescence quenching of anthracene in THF by tetracene and pentacene.

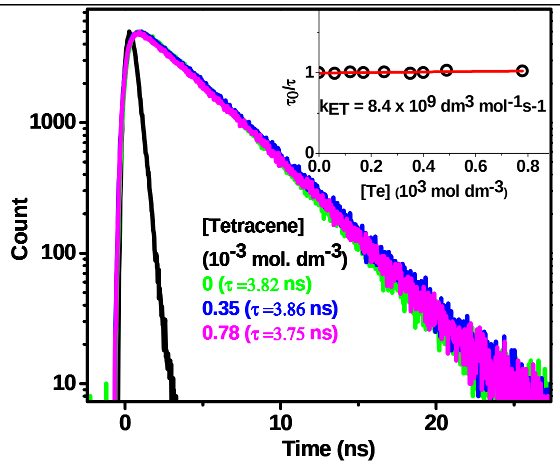

Anthracene to Tetracene energy transfer in THF

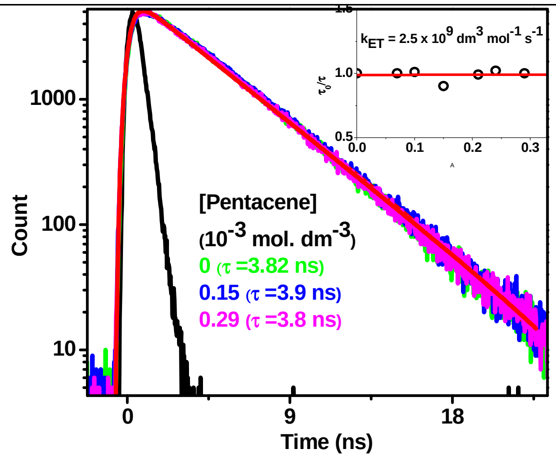

Anthracene to Pentacene energy transfer in THF

[Tetracene] (10^{-3} mol. dm^{-3})	0	0.06	0.12	0.17	0.25	0.35	0.4	0.49	0.78
<τ >(ns)	3.82	3.86	3.78	3.81	3.78	3.86	3.8	3.72	3.75
$<\tau_D>/<\tau_{DA}>$	1	0.99	1.01	1	1.01	0.99	1.0	1.03	1.02

[Pentacene] (10^{-3} mol. dm^{-3})	0	0.04	0.07	0.1	0.15	0.21	0.24	0.29
<τ >(ns)	3.82	3.87	3.81	3.78	3.9	3.84	3.76	3.8
$<\tau_D>/<\tau_{DA}>$	1	0.99	1.00	1.01	0.9	0.99	1.02	1.00

S5.13: Calculation of exciton density, Exciton annihilation rate constant and exciton diffusion length form exciton – exciton annihilation process.

We have used pulse energy in the range of 1- 6 μJ/pulse. Here we have shown the procedure of exciton density estimation for pulse energy 6 μJ.

The excitation pulse energy=6 μJ

Each photon has energy=hc/λ=4.966x10^{-19} J [λ=400 nm]

Per pulse number of incident photon =1.2 x10^{13}

Absorbance of the sample=0.35 i.e. 55% of incident photon are absorbed or 0.7 x10^{13} number of photon are absorbed per pulse.

Beam diameter=2r~0.5 mm, path length=d=2 mm

The volume of excitation region =$\pi r^2 d$= 3.925 x 10^{-4} cm^3

Volume of aggregate=$\pi R^2 h$= 3.07x10^6 nm^3[R=140 nm, h=50 nm]

Volume of one anthracene molecule 0.342 nm^3 (estimated using the molecular volume calculation reference: *J. Phys. Chem.***1964**, *68*, 441)

Number of anthracene molecule present per aggregate =8.97x10^6

Number of anthracene molecule present in excitation region=Concentration x volume (in lit.) x 6.023 x 10^{23}= 0.625x10^{-3}x3.925x10^{-7}x6.023x10^{23} =14.78x10^{13} [Sample Concentration =0.625 mM]

Total number of aggregate present in the excitation region= 14.78 x10^{13}/ 8.97 x10^6 =1.66 x 10^7

Per aggregate number of photon absorbed=0.7x10^{13}/ 1.66x10^7 =0.42x10^6

Exciton density=0.42x10^6/3.07x10^6 nm^3 =1.4x 10^{20} cm^{-3}.

Annihilation threshold of singlet exciton density= 0.16 x 10^{20} cm^{-3}

Annihilation radius (R_a) = 2.4 nm

Annihilation rate constant =(10.07/2) x 10^{11} = 5 x 10^{11} s^{-1}.

D = 5.3 x $10^{-4}$$cm^2$ .s^{-1}

Comparison of exciton diffusion coefficient from ET rate

In the present case the experimentally determined ET rate =6.21 x 10^{11} dm^3 mol^{-1} s^{-1} = 1.03 x 10^{-9} cm^3. s^{-1}.

$k_{ET} = 4\pi D R_{ET}$

D = 3.5x 10^{-4} cm^2. s^{-1} (assuming, $R_a = R_{ET}$)

S5.14: Stern-Volmer plots for (A) perylene (B) tetracene and (C) pentacene doped nanoaggregate samples from the average lifetime data obtained from fluorescence upconversion data.

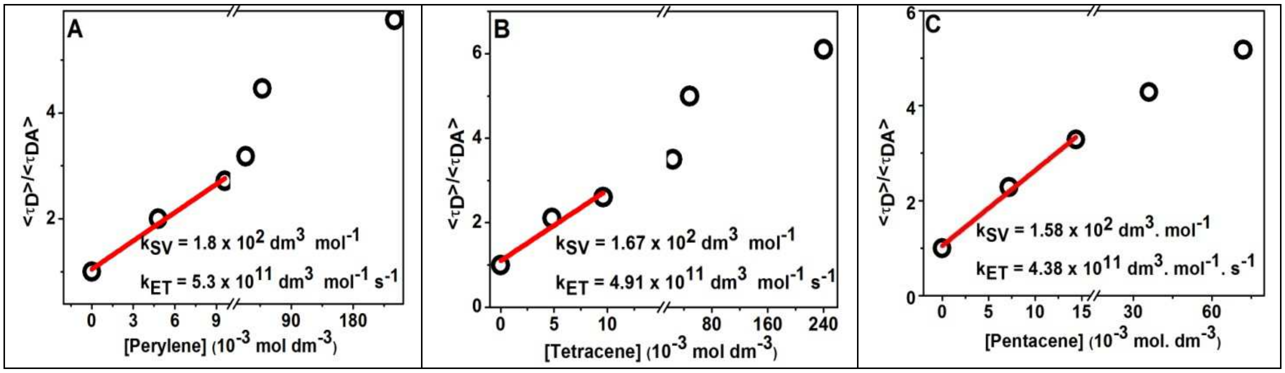

S5.15: Temporal profiles recorded after photoexcitation at 390 nm at 430 nm for different pentacene concentrations.

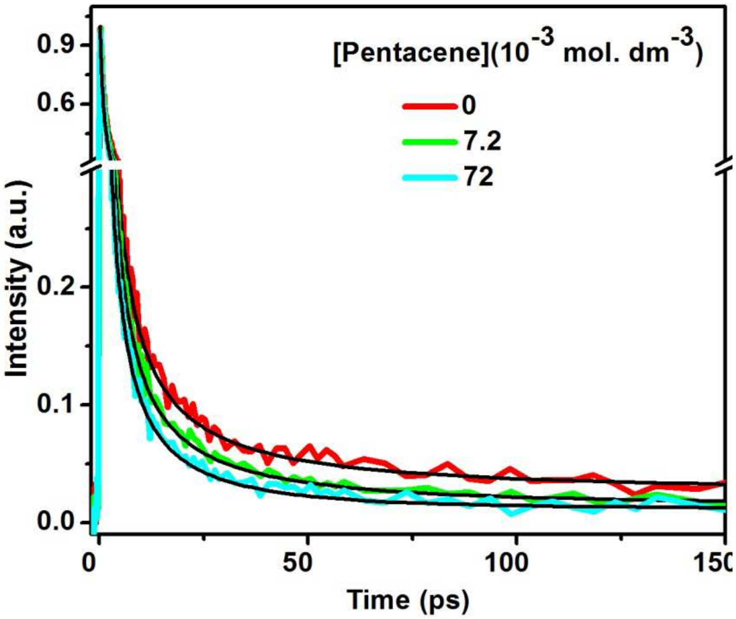

S5.16: Parameters associated with the best fit functions for the temporal profiles (see Figure 8), which were recorded at 430 nm using different dopant concentrations in TeAn nanoaggregate samples, generated using equation 8.

[Tetracene] (10^{-3} mol dm^{-3})	I_0	k'_{an} (10^{11} s^{-1})	τ (10^{-9} s^{-1})	R
0	1.12	0.79	0.36	0.026
4.8	1.07	0.73	0.17	0.01
24	1.09	0.79	0.14	0.01
48	1.05	0.86	0.10	0.02
240	1.03	0.91	0.07	0.012

S5.17: Parameters associated with the best fit functions for the temporal profiles (see Figure 8), which were recorded at 430 nm using different dopant concentrations in PnAn nanoaggregate samples, generated using equation 8.

[Pentacene] (10^{-3} mol dm^{-3})	I_0	k'_{an} (10^{11} s^{-1})	τ (10^{-9} s^{-1})	R
0	1.12	0.79	0.36	0.026
7.2	1.19	0.87	0.16	0.015
14.4	1.08	0.79	0.11	0.022
36	1.17	0.89	0.08	0.017
72	1.22	0.95	0.07	0.012

S5.18: Estimation of Förster radius (using PhotochemCAD software)

(A) Perylene doped anthracene nanoaggregate

Refractive index (n) 1.590
Orientation factor 0.476
Quantum yield 0.170
Fluorescence lifetime (ns) 3.400
Epsilon(Molar extinction coefficient) 29500.000
Wavelength for epsilon (nm) 437.000
Low wavelength (nm) 380.000
High wavelength (nm) 709.000
J value (overlap integral) in cm^6/mmol 5.474e-014
Forster distance: 29.113Å

(B) Tetracene doped anthracene nanoaggregate

Refractive index (n) 1.590
Orientation factor 0.476
Quantum yield 0.170
Epsilon(Molar extinction coefficient) 10000.000
Wavelength for epsilon (nm) 488.000
Low wavelength (nm) 380.000
High wavelength (nm) 717.000
J value (overlap integral) in cm^6/mmol 1.535e-014
Forster distance: 23.555 Å

(C) Pentacene doped anthracene nanoaggregate

Refractive index (n) 1.590
Orientation factor 0.476
Quantum yield 0.170
Epsilon(Molar extinction coefficient) 3800.000
Wavelength for epsilon (nm) 550.000
Low wavelength (nm) 380.000
High wavelength (nm) 728.000
J value (overlap integral) in cm^6/mmol 6.584e-015
Forster distance: 20.455 Å

S5.19: Calculation of average number of exciton produced per nanoaggregate during TCSPC experiment

Excitation source: Laser Diode

Wavelength: 375 nm. Energy per photon = $h\nu$ = 5.27 x 10^{19} J

Energy: 28pJ/pulse (very low energy could not measure with our existing facility so the energy/pulse valu taken from the technical specification of Horiba)

Total number photons present per pulse = 28 x 10^{-12} J/ $h\nu$ = 5.28 x 10^{7}

Absorbance of the nanoaggregate sample at excitation wavelength = 0.2. i.e. 37 % light photons are absorbed by the sample.

Total number of photons absorbed = 5.28 x 10^{7} x 0.37 =1.95 x 10^{7}

Preparation of nanoaggrgate: 200 μl of 10 mM anthracene in THF is injected

Total number of molecule present in solution (10 ml) = 200 x 10^{-6}x 10 x 6.023 x 10^{20} = 1.2 x 10^{18}

Beam radius at sample ~ 500μm

Volume of excitation region = π x $(0.05)^2$ x 1 = 7.85 x 10^{-3} ml

Number of molecule present in the excitation region = 1.2 x 10^{18} x 7.85 x 10^{-3} / 10 = 9.42 x 10^{14}

Per aggregate number of anthracene molecule = π x $(140)^2$ x 50 / 0.343 = 8.97 x 10^{6}

Here, radius of nanoaggrgate = 140 nm, height = 50 nm, anthracene molecular volume = 0.343 nm^3.

Number of aggregates present in the excitation region = 9.42 x 10^{14}/ 8.97 x 10^{6} = 1.05 x 10^{8}

Per aggregate number of exciton produced = 5.28 x 10^{7} / 1.05 x 10^{8} = 0.5

Hence, we can say that in most of the nanoaggregates only one exciton is produced per aggregate.

S5.20: Variation of ET efficiency with donor-acceptor distance

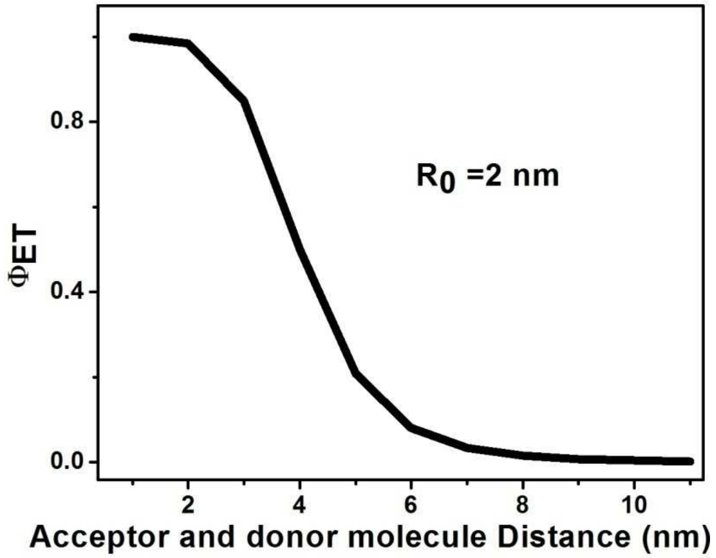

S5.21: Simulation procedure through Matlab software module

Our simulation follows these steps,

1) Estimation of the average number of acceptor molecules present per nanoaggregate for different concentration of the acceptor. (1870 number of acceptor molecules per nanoaggregate for 1 x 10^{-3} mol. dm^{-3} concentration)

2) The minimum distance between the acceptor and donor species = molecular radius of donor + molecular radius of acceptor = 0.9 nm (approximately).

3) We have generated random position of the donor or anthracne exciton inside one nanoaggregate (say j^{th} nanoaggregate). Then the acceptor positions are generated randomly inside this nanoaggregate. The distance between the donor and acceptor has been calculated. This distance must be greater than 0.9 nm. To impose this condition, we have rejected all such conditions where the evaluated distance between any donor and acceptor species is less than 0.9 nm. The condition where all the donor – acceptor distances are more than 0.9 nm are only considered for the next step of the simulation. Among these distances the minimum intermolecular distance between donor and acceptor species has been shorted and taken for k'_{ET} calculation.

Although the dipole-dipole interaction between donor and acceptor molecule can occur for all the donor-acceptor pairs inside a nanoaggregates, we expect energy transfer to a single acceptor molecule only. Because of the resonance energy transfer condition one donor should not donate its energy to multiple acceptors, simultaneously. The ET rate constant follows R^{-6} relationship. Therefore, we expect in most of the cases the energy transfer will take place to the nearest acceptor molecule. Thus we estimate the ET rate constant considering the minimum intermolecular distance (Rj) between the donor-acceptor pair.

4) Thousands of nanoaggregates remain present in the excitation region, during steady state and TCSPC study. The observed ET rate is actually the average feature for all those nanoaggregates. Therefore, to evaluate the similar condition, we have estimated the ET rate for 5000 cases (equivalent to N_P) and finally take the average value. Thus we obtained the final k'_{ET} value which is further used in equation 13 to estimate the Φ_{ET} for the system.

S5.22: Simulation of minimum average distance* and estimation of pseudo first order and second order energy transfer rate constants for different concentrations of perylene.

Concentration (10^{-3} Mol. dm^{-3})	<r> (nm)	$<r^6>$ (nm^6)	k'_{ET} (s^{-1})	k_{ET} (dm^3 mol^{-1} s^{-1})
2	6.25	2.43×10^5	9.3×10^6	4.7×10^9
10	3.52	5495.5	7.2×10^8	7.2×10^{10}
20	2.76	1153.1	5.7×10^9	2.8×10^{11}
40	2.19	333.9	1.7×10^{10}	4.2×10^{11}
100	1.48	14.28	2.6×10^{10}	2.6×10^{11}
240	1.34	8.16	5.4×10^{10}	2.3×10^{11}

S5.23: Emission spectra for undoped anthracene[A], perylene doped anthracene [P], tetracene doped anthracene [T], pentacene doped anthracene [Pn] and teranery doped anthracene [W] nanoaggregates (Excitation wavelength is 355 nm).

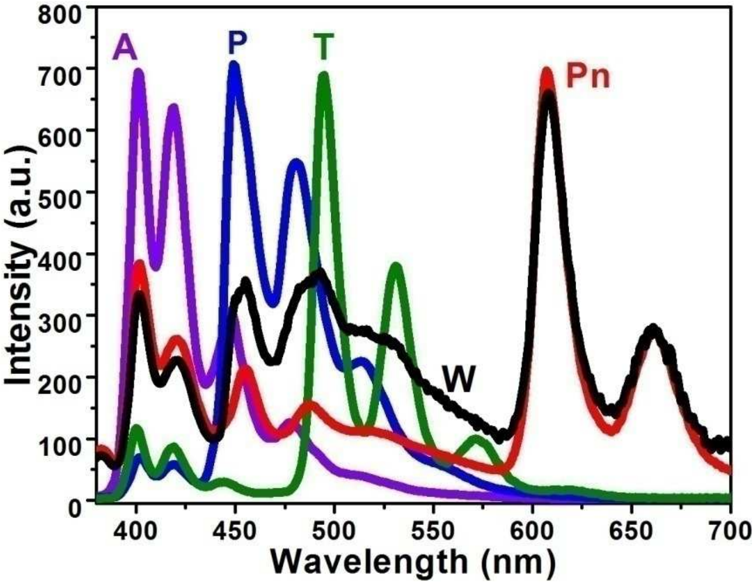

CHAPTER 6

S6.1: Tri-exponential fitting parameters of kinetics recorded at 630 nm for perylene nanoaggregates excited with different energy/pulse

Energy/Pulse	τ_1 (a_1)	τ_2 (a_2)	τ_3 (a_3)
11 μJ	0.43 ps (-10)	5 ps (-4)	180 ps (-2.5)
9 μJ	0.5 ps (-8.4)	6 ps (-4.5)	180 ps (-2.8)
6 μJ	0.6 ps (-7)	6.6 ps (-4.5)	180 ps (-4)
3 μJ	0.8 ps (-2.7)	8.6 ps (-4)	180 ps (-5.7)

S6.2: Fitting of kinetic traces recorded at different excitation intensities for 500nm and 700 nm for perylenenanoaggregate using equation 13and k'$_2$vs [S$_1$]$_0$ plots.

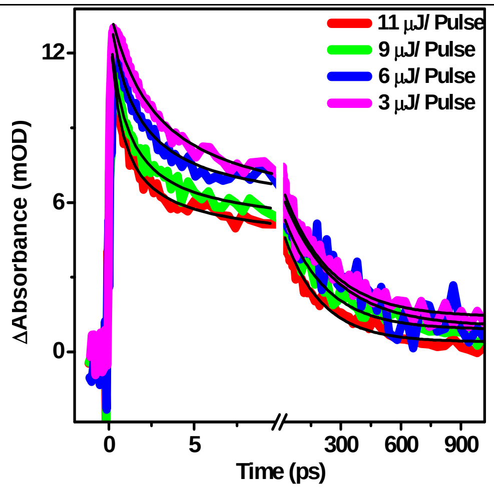

500 nm

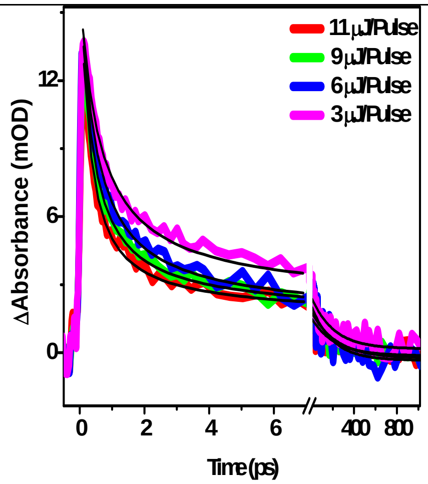

700 nm

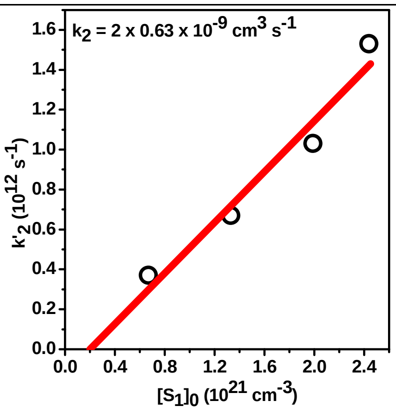

500 nm

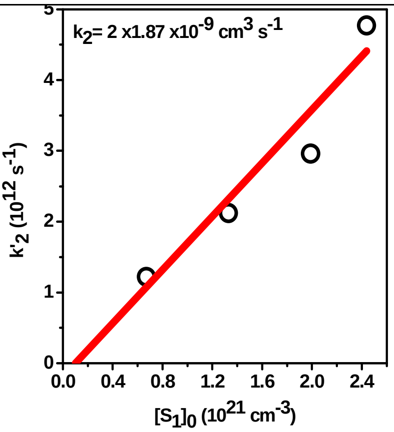

700 nm

S6.3: Calculation of singlet exciton density, $[S_1]_0$

We have used pulse energy in the range of 3-11 μJ/pulse for perylenenanoaggregate. Here we have shown the procedure of exciton density estimation for pulse energy 11 μJ.

The excitation pulse energy=11 μJ

Each photon has energy=hc/λ=$5.096\text{x}10^{-19}$ J [λ=390 nm]

Per pulse number of incident photon =$2.16\text{x}10^{13}$

Absorbance of the sample=0.4 i.e. 60% of incident photon are absorbed or $1.3\text{x}10^{13}$ number of photon are absorbed per pulse.

Beam diameter=2r~0.5 mm, path length=d=1 mm

The volume of excitation region =$\pi r^2 d$=$1.96\text{ x}10^{-4}$ cm^3

Volume of aggregate=$\pi R^2 h$= $7.9\text{x}10^5$ nm^3[R=60 nm, h=70 nm]

Volume of one anthracene molecule 0.226 nm^3 (estimated using the molecular volume calculation reference: *J. Phys. Chem.***1964**, *68*, 441)

Number of anthracene molecule present per aggregate =$3.5\text{x}10^6$

Number of anthracene molecule present in excitation region=Concentration x volume (in lit.) x 6.023 x 10^{23}= $0.2\text{x}10^{-3}\text{x}1.96\text{x}10^{-7}\text{x}6.023\text{x}10^{23}$ =$2.36\text{x}10^{13}$ [Sample Concentration =0.2mM]

Total number of aggregate present in the excitation region= 6.74 x 10^6

Per aggregate number of photon absorbed=$1.3\text{x}10^{13}$/ $6.74\text{x}10^6$ =$1.93\text{x}10^6$

Exciton density=$1.93\text{x}10^6/7.9\text{x}10^5$ nm^3 =2.44 x 10^{21} cm^{-3}

CHAPTER 7

S7.1: DLS data showing the size distribution of the nanoaggregates five phtalocyane derivatives.

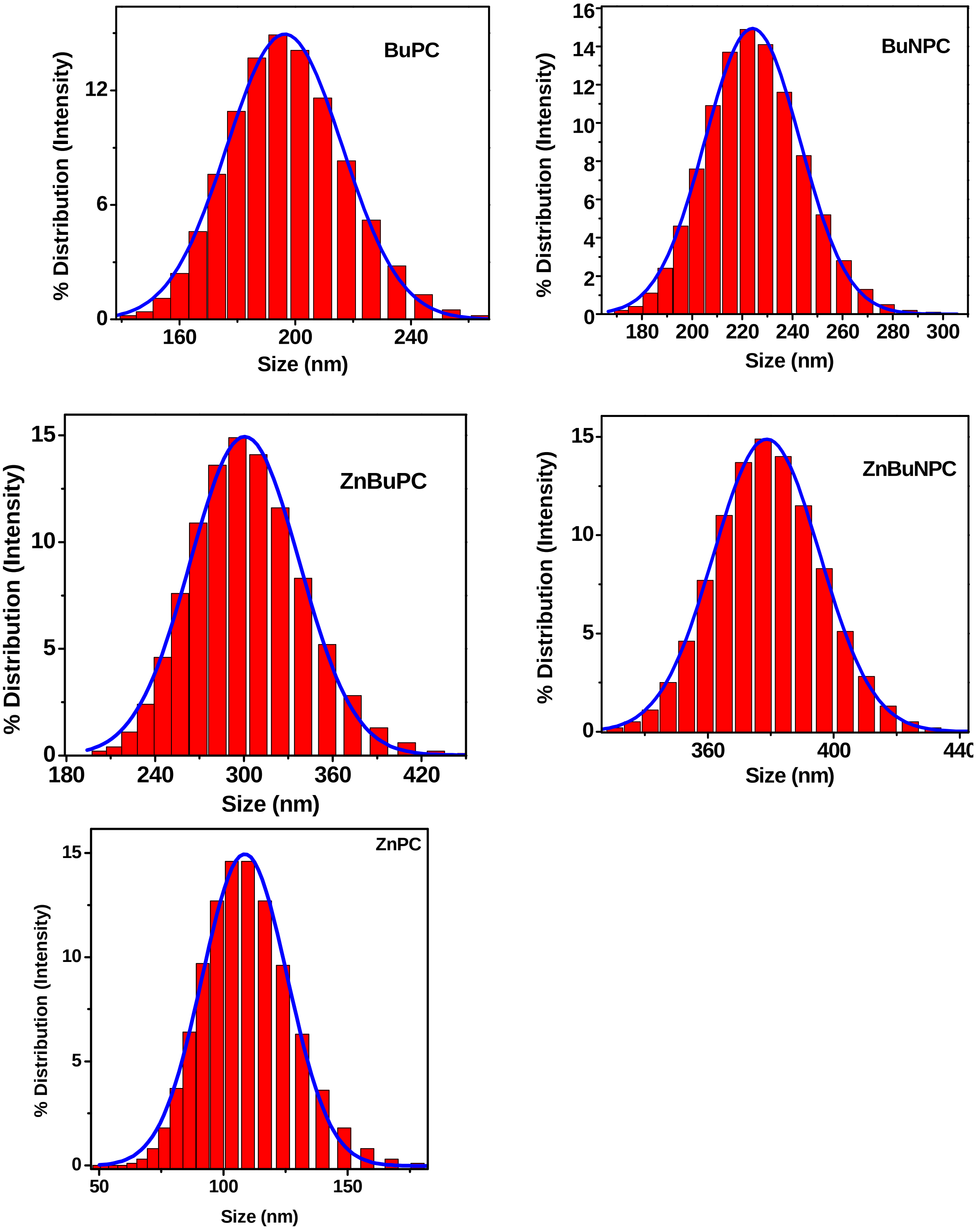

S7.2: AFM images of the nanoaggregates five phtalocyane derivatives

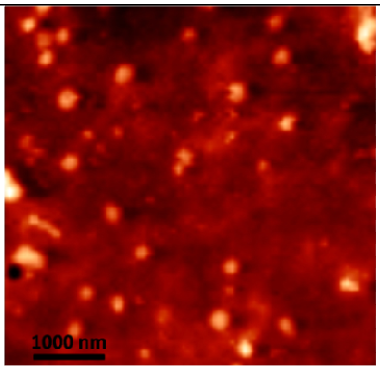 tBuPC	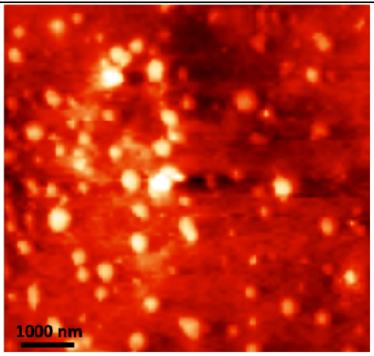 tBuNPC
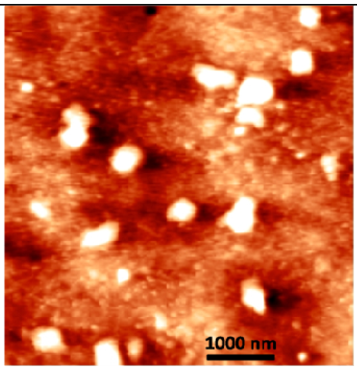 Zn-tBuPC	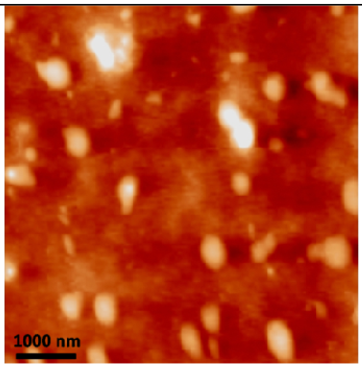 Zn-tBuNPC

Figure S7.3: Kinetics recorded for fluorescence emission for the five phthalocyanine derivatives and it fitting data.

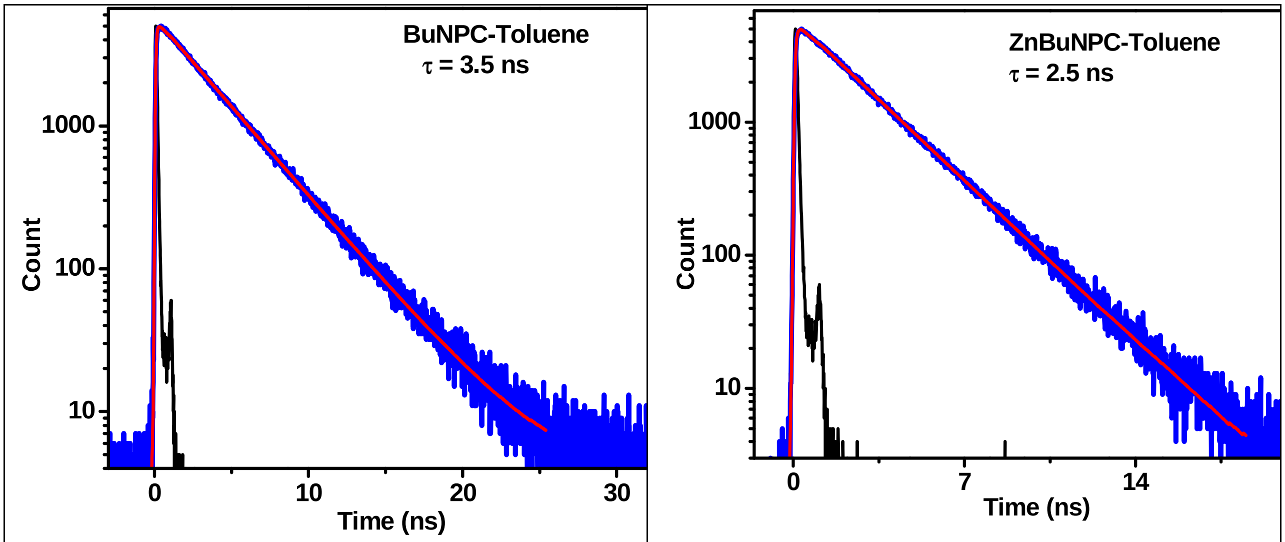

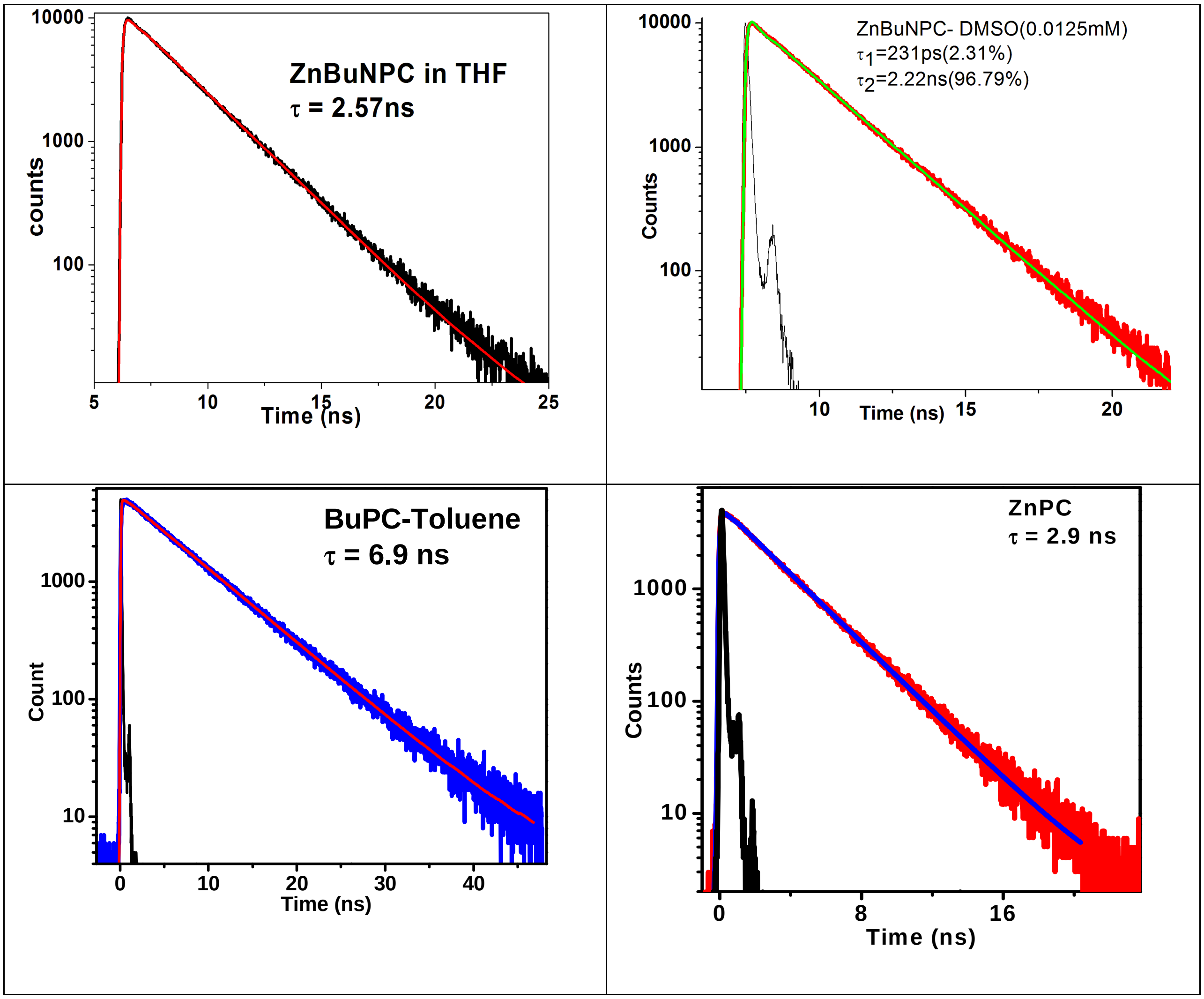

Figure S7.4: ZnBuNPC does not form nanoaggregate in non-aqueous solvents of even very high polarity, like DMSO

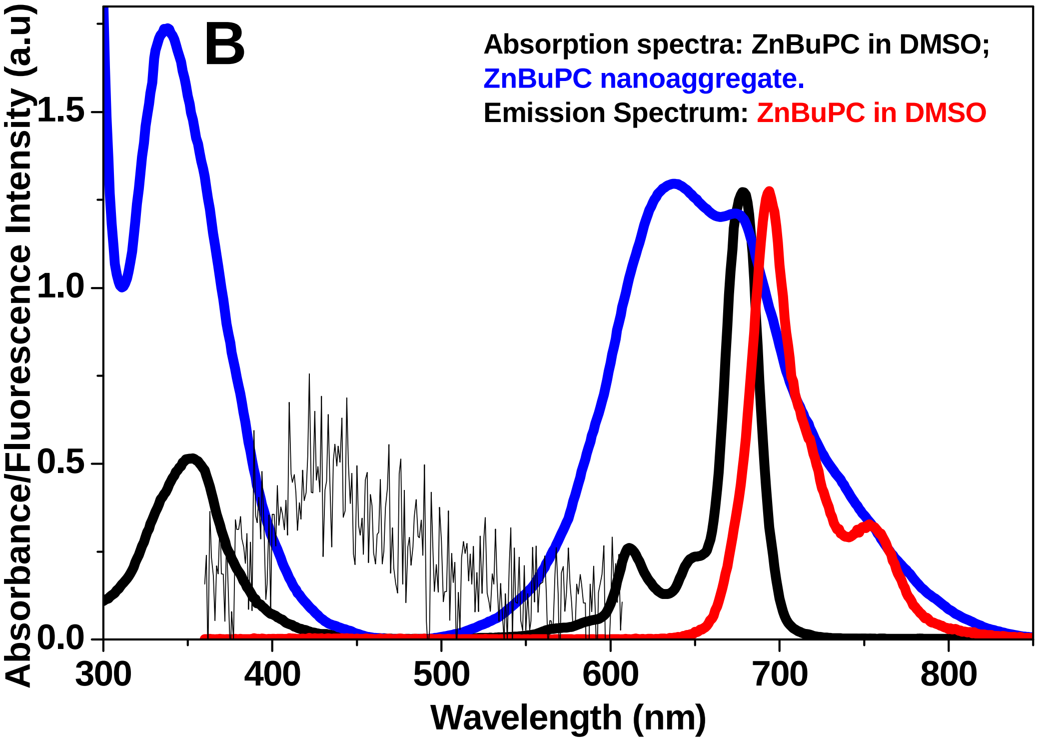

S7.5: Calculation of exciton density

We have used pulse energy in the range of 3-11 μJ/pulse. Here we have shown the procedure of exciton density estimation for pulse energy 10 μJ.

The excitation pulse energy=10 μJ

Each photon has energy=hc/λ=5.093 × 10^{-19} J [λ=390 nm]

Per pulse number of incident photon =1.96 × 10^{13}

Absorbance of the sample=0.1 i.e. 21.6% of incident photon are absorbed or 4.23 × 10^{12} number of photon are absorbed per pulse.

Beam diameter=2r~0.5 mm, path length=d=1 mm

The volume of excitation region =$\pi r^2 d$=1.96 × 10^{-4} cm^3

Volume of aggregate=$\pi R^2 h$ = 3.53 × 10^6 nm^3 [R=100 nm]

Volume of one NPC molecule 1.12 nm^3 (estimated using the molecular volume calculation reference: J. Chem. Educ. 1973)

Number of NPC molecule present per aggregate =3.15 × 10^6

Number of curcumin molecule present in excitation region=Concentration x volume (in lit.) × 6.023 × 10^{23}= 2.7 × 10^{-5} × 1.96 × 10^{-7}× 6.023 × 10^{23} =3.2 × 10^{12} [Sample Concentration =0.027 mM]

Total number of aggregate present in the excitation region= 3.2 × 10^{12}/ 3.15 ×10^{6} =1.02 × 10^{6}

Number of photons absorbed by each particle of the nanoaggregate = 4.23 × 10^{12}/ 1.02 ×10^{6} =4.15 × 10^{6}

Exciton density ($[S_1]_0$) = 4.15 × 10^{6}/ 3.53 ×10^{6} nm^3 =1.2 × 10^{21} cm^{-3}

S7.6: Calculation of Annihilation radius

The exciton density at threshold of annihilation for NPC NA (for fitting at 580 nm) = 0.1 x 10^{21} cm^{-3}

The threshold of annihilation is the X-axis intercept of k_2' vs $[S_1]_0$ plot.

At the annihilation threshold condition, two excitons are expected to be separated by a distance of 2 × annihilation radius (R_a) (assuming homogeneous distribution of excitons inside nanoaggregate)

If we assume homogeneous generation of excitons inside the nanoaggregate, then per exciton available volume = 1 cm^3 / 0.1 × 10^{21} = 10 nm^3

$$\frac{4\pi {R_a}^3}{3} = 10\ nm^3$$

R_a = 1.34 nm